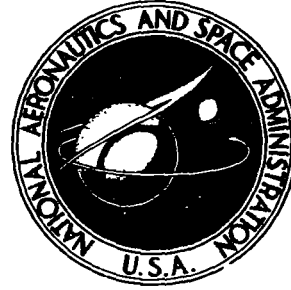


NASA
CR
1219
v.4
c.1

NASA CONTRACTOR REPORT



NASA CR

NASA CR-1423



LOAN COPY: RETURN TO
AFWL (WLD-2)
KIRTLAND AFB, N MEX

EXPERIMENTAL INVESTIGATION IN AN ANNULAR CASCADE SECTOR OF HIGHLY LOADED TURBINE STATOR BLADING Volume IV. Performance of Jet-Flapped Blade

by James L. Bettner

Prepared by
GENERAL MOTORS
Indianapolis, Ind.
for Lewis Research Center



NATIONAL AERONAUTICS AND SPACE ADMINISTRATION • WASHINGTON, D. C. • SEPTEMBER 1969



EXPERIMENTAL INVESTIGATION IN AN ANNULAR CASCADE SECTOR
OF HIGHLY LOADED TURBINE STATOR BLADING

Volume IV. Performance of Jet-Flapped Blade

By James L. Bettner

Distribution of this report is provided in the interest of information exchange. Responsibility for the contents resides in the author or organization that prepared it.

Prepared under Contract No. NAS 3-9404 by
GENERAL MOTORS
Indianapolis, Ind.

for Lewis Research Center

NATIONAL AERONAUTICS AND SPACE ADMINISTRATION

For sale by the Clearinghouse for Federal Scientific and Technical Information
Springfield, Virginia 22151 - CFSTI price \$3.00



FOREWORD

The research described herein, which was conducted by the Allison Division of General Motors, was performed under NASA Contract NAS 3-9404. The work was done under the technical management of Mr. Edward L. Warren and Mr. Stanley M. Nosek, Airbreathing Engines Division and Fluid System Components Division, respectively, NASA Lewis Research Center. The report was originally issued as Allison EDR 5315, Volume IV, March 1969.

TABLE OF CONTENTS

	<u>Page</u>
Summary and Conclusions	1
Introduction	3
Symbols.	5
Jet-Flapped Blade Performance	7
Velocity and Pressure Distribution.	9
Surface Velocity Distribution.	9
Surface Pressure Distribution	10
Flow Visualization Results	11
Downstream Gas Angle and Tangential Velocity	12
Average Downstream Gas Angle Radial Distribution	12
Mean Section Jet Momentum and Deflection Characteristics	13
Change in Tangential Velocity Across Blade Row	14
Contour Plots	15
Results at the Blade Trailing Edge (Station 3).	15
Results Downstream of the Blade Trailing Edge (Station 4).	16
Kinetic Energy Loss Coefficient	16
Downstream Gas Angle	17
Mass Averaged Loss and Boundary Layer Parameters	17
Results at the Blade Trailing Edge (Station 3).	17
Aerodynamic Loss Data	17
Boundary Layer Parameters	18
Results Downstream of the Blade Trailing Edge (Station 4)	19
Aerodynamic Loss Data	19
Boundary Layer Parameters	20
Summary of Jet-Flapped Blade Performance.	21
References	23
Tables	25
Figures	31



LIST OF TABLES

<u>Table</u>	<u>Title</u>	<u>Page</u>
I	Design data for the jet-flapped and plain blades	25
II	Experimental results for the jet-flapped and plain blades	26
III	Jet-flapped and plain blade mean section tangential force results	27
IV	Jet-flapped and plain blade measured and design change in tangential velocity across blade row . . .	28
V	Jet-flapped and plain blade trailing edge (Station 3) overall mass averaged loss data	29
VI	Jet-flapped and plain blade downstream (Station 4) overall mass averaged loss data	30

LIST OF ILLUSTRATIONS

<u>Figure</u>	<u>Title</u>	<u>Page</u>
1	Jet-flapped blade assembly	31
2	Jet-flapped blade internal and external profiles	32
3	Bench test results showing radial distribution of jet stream	33
4	Annular cascade test rig	34
5	Measured and predicted surface critical velocity ratio distribution for the jet-flapped blade (hub section)—0.022-in. jet slot	35
6	Measured and predicted surface critical velocity ratio distribution for the jet-flapped blade (mean section)—0.022-in. jet slot	36
7	Measured and predicted surface critical velocity ratio distribution for the jet-flapped blade (tip section)—0.022-in. jet slot	37
8	Measured and predicted surface critical velocity ratio distribution for the jet-flapped blade (hub section)—0.031-in. jet slot	38
9	Measured and predicted surface critical velocity ratio distribution for the jet-flapped blade (mean section)—0.031-in. jet slot	39
10	Measured and predicted surface critical velocity ratio distribution for the jet-flapped blade (tip section)—0.031-in. jet slot	40
11	Measured and predicted surface critical velocity ratio distribution for the jet-flapped blade (hub section)—0.040-in. jet slot	41
12	Measured and predicted surface critical velocity ratio distribution for the jet-flapped blade (mean section)—0.040-in. jet slot	42
13	Measured and predicted surface critical velocity ratio distribution for the jet-flapped blade (tip section)—0.040-in. jet slot	43
14	Measured and predicted surface critical velocity ratio distribution for plain blade hub section	44
15	Measured and predicted surface critical velocity ratio distribution for plain blade mean section	45
16	Measured and predicted surface critical velocity ratio distribution for plain blade tip section.	46
17	Measured surface static pressure distribution for the jet-flapped blade (mean section)—0.022-in. jet slot	47

<u>Figure</u>	<u>Title</u>	<u>Page</u>
18	Measured surface static pressure distribution for the jet-flapped blade (mean section)—0.031-in. jet slot	48
19	Measured surface static pressure distribution for the jet-flapped blade (mean section)—0.040-in. jet slot	49
20	Flow visualization results for the jet-flapped blade with 0.022-in. jet slot and 0.81% secondary flow ($C_{jm} = 0.0133$)	50
21	Flow visualization results for the jet-flapped blade with 0.022-in. jet slot and 1.69% secondary flow ($C_{jm} = 0.0355$)	51
22	Flow visualization results for the jet-flapped blade with 0.022-in. jet slot and 2.61% secondary flow ($C_{jm} = 0.0619$)	52
23	Flow visualization results for the jet-flapped blade with 0.031-in. jet slot and 1.50% secondary flow ($C_{jm} = 0.0297$)	53
24	Flow visualization results for the jet-flapped blade with 0.031-in. jet slot and 2.04% secondary flow ($C_{jm} = 0.0450$)	54
25	Flow visualization results for the jet-flapped blade with 0.031-in. jet slot and 2.82% secondary flow ($C_{jm} = 0.0671$)	55
26	Flow visualization results for the jet-flapped blade with 0.040-in. jet slot and 1.97% secondary flow ($C_{jm} = 0.0406$)	56
27	Flow visualization results for the jet-flapped blade with 0.040-in. jet slot and 3.03% secondary flow ($C_{jm} = 0.0651$)	57
28	Flow visualization results for the jet-flapped blade with 0.040-in. jet slot and 3.89% secondary flow ($C_{jm} = 0.0823$)	58
29	Plain blade flow visualization results for inlet hub static-to-total pressure ratio of 0.74 (design value)	59
30	Circumferential variation of downstream gas angle with secondary flow rate at 12.58-in. radial position for 0.022-in. slot	60

<u>Figure</u>	<u>Title</u>	<u>Page</u>
31	Average measured and predicted radial variation of downstream gas angle for jet-flapped blade with 0.022-in. slot	61
32	Average measured and predicted radial variation of downstream gas angle for jet-flapped blade with 0.031-in. slot	62
33	Average measured and predicted radial variation of downstream gas angle for jet-flapped blade with 0.040-in. slot	63
34	Average measured and predicted radial variation of the plain blade downstream gas angle	64
35	Variation of mean section gas angle and blade force with jet momentum coefficient	65
36	Variation of mean section gas angle and blade force with secondary flow rate	66
37	Variation of the jet contribution to the total mean section lift with percentage of secondary flow rate	67
38	Jet momentum and deflection characteristics for mean section of jet-flapped blade	68
39	Variation of position and shape of the jet-flapped blade wake with an increase in the amount of secondary flow	69
40	Plain blade Station 3 total pressure distribution for radial position ($R = 12.97$ in.)	70
41	Contours of kinetic energy loss coefficient across one jet-flapped blade passage at Station 3 (0.022-in. slot and $0.81\% \dot{m}_j/\dot{m}_p$)	71
42	Contours of kinetic energy loss coefficient across one jet-flapped blade passage at Station 3 (0.022-in. slot and $1.69\% \dot{m}_j/\dot{m}_p$)	72
43	Contours of kinetic energy loss coefficient across one jet-flapped blade passage at Station 3 (0.022-in. slot and $2.61\% \dot{m}_j/\dot{m}_p$)	73
44	Contours of kinetic energy loss coefficient across one jet-flapped blade passage at Station 3 (0.031-in. slot and $1.50\% \dot{m}_j/\dot{m}_p$)	74
45	Contours of kinetic energy loss coefficient across one jet-flapped blade passage at Station 3 (0.031-in. slot and $2.04\% \dot{m}_j/\dot{m}_p$)	75
46	Contours of kinetic energy loss coefficient across one jet-flapped blade passage at Station 3 (0.031-in. slot and $2.82\% \dot{m}_j/\dot{m}_p$)	76

<u>Figure</u>	<u>Title</u>	<u>Page</u>
47	Contours of kinetic energy loss coefficient across one jet-flapped blade passage at Station 3 (0.040-in. slot and 1.97% \dot{m}_j/\dot{m}_p)	77
48	Contours of kinetic energy loss coefficient across one jet-flapped blade passage at Station 3 (0.040-in. slot and 3.03% \dot{m}_j/\dot{m}_p)	78
49	Contours of kinetic energy loss coefficient across one jet-flapped blade passage at Station 3 (0.040-in. slot and 3.89% \dot{m}_j/\dot{m}_p)	79
50	Contours of kinetic energy loss coefficient across one plain blade passage at Station 3	80
51	Contours of kinetic energy loss coefficient at Station 4 for the jet-flap blade (0.022-in. slot and 0.79% \dot{m}_j/\dot{m}_p)	81
52	Contours of kinetic energy loss coefficient at Station 4 for the jet-flap blade (0.022-in. slot and 1.65% \dot{m}_j/\dot{m}_p)	82
53	Contours of kinetic energy loss coefficient at Station 4 for the jet-flap blade (0.022-in. slot and 2.57% \dot{m}_j/\dot{m}_p)	83
54	Contours of kinetic energy loss coefficient at Station 4 for the jet-flap blade (0.031-in. slot and 1.50% \dot{m}_j/\dot{m}_p)	84
55	Contours of kinetic energy loss coefficient at Station 4 for the jet-flap blade (0.031-in. slot and 2.02% \dot{m}_j/\dot{m}_p)	85
56	Contours of kinetic energy loss coefficient at Station 4 for the jet-flap blade (0.031-in. slot and 2.47% \dot{m}_j/\dot{m}_p)	86
57	Contours of kinetic energy loss coefficient at Station 4 for the jet-flap blade (0.040-in. slot and 1.97% \dot{m}_j/\dot{m}_p)	87
58	Contours of kinetic energy loss coefficient at Station 4 for the jet-flap blade (0.040-in. slot and 3.08% \dot{m}_j/\dot{m}_p)	88
59	Contours of kinetic energy loss coefficient at Station 4 for the jet-flap blade (0.040-in. slot and 3.85% \dot{m}_j/\dot{m}_p)	89
60	Contours of kinetic energy loss coefficient at Station 4 for the plain blade	90
61	Contours of downstream gas angle measured from axial for the jet-flap blade (0.022-in. slot and 0.79% \dot{m}_j/\dot{m}_p)	91

<u>Figure</u>	<u>Title</u>	<u>Page</u>
62	Contours of downstream gas angle measured from axial for the jet-flap blade (0.022-in. slot and 1.65% \dot{m}_j/\dot{m}_p)	92
63	Contours of downstream gas angle measured from axial for the jet-flap blade (0.022-in. slot and 2.57% \dot{m}_j/\dot{m}_p)	93
64	Contours of downstream gas angle measured from axial for the jet-flap blade (0.031-in. slot and 1.50% \dot{m}_j/\dot{m}_p)	94
65	Contours of downstream gas angle measured from axial for the jet-flap blade (0.031-in. slot and 2.02% \dot{m}_j/\dot{m}_p)	95
66	Contours of downstream gas angle measured from axial for the jet-flap blade (0.031-in. slot and 2.47% \dot{m}_j/\dot{m}_p)	96
67	Contours of downstream gas angle measured from axial for the jet-flap blade (0.040-in. slot and 1.97% \dot{m}_j/\dot{m}_p)	97
68	Contours of downstream gas angle measured from axial for the jet-flap blade (0.040-in. slot and 3.08% \dot{m}_j/\dot{m}_p)	98
69	Contours of downstream gas angle measured from axial for the jet-flap blade (0.040-in. slot and 3.85% \dot{m}_j/\dot{m}_p)	99
70	Contours of downstream gas angle measured from axial for the plain blade at Station 4	100
71	Radial variation of circumferentially mass averaged $\bar{\epsilon}$ at Station 3—0.022-in. slot	101
72	Radial variation of circumferentially mass averaged $\bar{\epsilon}$ at Station 3—0.031-in. slot	102
73	Radial variation of circumferentially mass averaged $\bar{\epsilon}$ at Station 3—0.040-in. slot	103
74	Radial variation of circumferentially mass averaged $\bar{\epsilon}$ at Station 3—plain blade	104
75	Variation of overall mass averaged kinetic energy loss coefficient with percent secondary flow rate at the jet-flapped blade trailing edge.	105
76	Radial variation of circumferentially mass averaged $\bar{\omega}$ at Station 3—0.022-in. slot	106
77	Radial variation of circumferentially mass averaged $\bar{\omega}$ at Station 3—0.031-in. slot	107
78	Radial variation of circumferentially mass averaged $\bar{\omega}$ at Station 3—0.040-in. slot	108
79	Variation of overall mass averaged total pressure loss coefficient with percent secondary flow rate at the jet-flapped blade trailing edge.	109

<u>Figure</u>	<u>Title</u>	<u>Page</u>
80	Variation of trailing edge (Station 3) overall mass averaged total pressure loss coefficient with mean section jet momentum coefficient	110
81	Radial variation of boundary layer displacement thickness at Station 3—0.022-in. slot	111
82	Radial variation of boundary layer displacement thickness at Station 3—0.031-in. slot	112
83	Radial variation of boundary layer displacement thickness at Station 3—0.040-in. slot	113
84	Shape factor distribution at Station 3—0.022-in. slot	114
85	Radial variation of boundary layer shape factor at Station 3—0.031-in. slot	115
86	Radial variation of boundary layer shape factor at Station 3—0.040-in. slot	116
87	Radial variation of boundary layer shape factor at Station 3—plain blade	117
88	Circumferentially mass averaged kinetic energy loss coefficient distribution at Station 4—0.022-in. slot	118
89	Circumferentially mass averaged kinetic energy loss coefficient distribution at Station 4—0.031-in. slot	119
90	Circumferentially mass averaged kinetic energy loss coefficient distribution at Station 4—0.040-in. slot	120
91	Circumferentially mass averaged kinetic energy loss coefficient distribution at Station 4—plain blade	121
92	Variation of overall mass averaged kinetic energy loss coefficient with percent secondary flow rate at Station 4 (2 in. downstream of blade trailing edge)	122
93	Circumferentially mass averaged total pressure loss coefficient distribution at Station 4—0.022-in. slot	123
94	Circumferentially mass averaged total pressure loss coefficient distribution at Station 4—0.031-in. slot	124
95	Circumferentially mass averaged total pressure loss coefficient distribution at Station 4—0.040-in. slot	125
96	Variation of overall mass averaged total pressure loss coefficient with percent secondary flow rate at Station 4 (2 in. downstream of blade trailing edge)	126
97	Radial variation of boundary layer displacement thickness at Station 4—0.022-in. slot	127

<u>Figure</u>	<u>Title</u>	<u>Page</u>
98	Radial variation of boundary layer displacement thickness at Station 4—0.031-in. slot	128
99	Radial variation of boundary layer displacement thickness at Station 4—0.040-in. slot	129
100	Radial variation of boundary layer shape factor at Station 4—0.022-in. slot	130
101	Radial variation of boundary layer shape factor at Station 4—0.031-in. slot	131
102	Radial variation of boundary layer shape factor at Station 4—0.040-in. slot	132
103	Radial variation of boundary layer shape factor at Station 4—plain blade.	133

EXPERIMENTAL INVESTIGATION IN AN ANNULAR CASCADE SECTOR
OF HIGHLY LOADED TURBINE STATOR BLADING

Volume IV. Performance of Jet-Flapped Blade

by J. L. Bettner

Allison Division of General Motors

SUMMARY AND CONCLUSIONS

A jet-flapped blade has been tested in a six-blade annular cascade. Three jet slot sizes of 0.022, 0.031, and 0.040 in. with three secondary flow rates for each slot have been investigated. The combinations of jet slot height and secondary flow rates produced a range of mean section jet momentum coefficient, C_{jm} , values of up to 0.08. The momentum coefficient is the ratio of jet-to-total momentum that exists at the blade trailing edge and is defined as

$$C_{jm} = \frac{\dot{m}_j U_a}{1/2 (\dot{m}_j U_a + \dot{m}_p W_{m3})}$$

Experimental results are compared with those for a plain blade designed to the same loading level as the jet-flapped blade but with greater solidity. The axial chord solidity, C_x/s , for the plain blade was 1.29, whereas it was only 1.18 for the jet-flapped blade.

Flow visualization results revealed that flow separation was essentially prevented all the way to the trailing edge region of the center blades of the cascade with jet flow rate and jet slot size combinations that corresponded to $C_{jm} \approx 0.03$. See Figures 21 and 23.

In general, the presence of the jet flap effected a larger mean section tangential blade force than the design value. The design value was achieved with a C_{jm} slightly less than 0.03 which corresponded to jet-to-primary flow rates of about 1.3% (Figures 35 and 36). The plain blade was over 16% deficient in achieving the design mean section tangential force.

The jet flap produced a greater amount of mainstream gas turning toward the tangential direction than the design value. The jet was more effective in deflecting the mainstream flow than was anticipated during the airfoil design phase of this investigation.

The mean section of the jet-flapped blade exceeded the design change in tangential velocity across the blade row for all combinations of jet slot size and secondary flow rate. In some cases, particularly at the low secondary flow rates, the hub and tip sections were deficient in achieving the design change in tangential velocity. This deficiency was overcome by increasing the amount of secondary flow.

For an unexplained reason, the 0.031-in. jet slot size data were different from that for the 0.022 or 0.040-in. jet slots. Not only was the radial loss distribution different (i. e., the 0.031-in. jet had a high loss region at the tip, while the hub was the region of large loss on the 0.022- and 0.040-in. jet slot configurations) but the loss level was larger for the 0.031-in. jet than for either the 0.022- or 0.040-in. jets.

If the 0.031-in. jet slot loss data are ignored, a jet-flapped blade trailing edge loss level equivalent to that of the plain blade was obtained at a jet momentum coefficient level of 0.025 (Figure 80). The conclusion reached is that the jet-flapped blade prevented flow separation and achieved the design blade force and gas turning requirements at a trailing edge loss level that was no larger than that for the plain blade which was deficient in satisfying all of these aerodynamic requirements.

The jet-flapped blade is a promising boundary layer control device for highly loaded turbine blades. Since the gas angle downstream of a jet-flapped blade row can be varied by changing C_j , the jet-flap concept also holds promise as a turbine flow path geometry aerodynamic controlling device.

INTRODUCTION

Increasing interest in developing lightweight, highly loaded gas turbine engines confronts the designer with the problem of maintaining a high level of engine performance. A major cause of performance loss in present engines is the condition of the gas flow separating from the blading surfaces. When flow separation is experienced in a blade passage, there is a loss in available kinetic energy, mixing losses are increased, and the desired change in tangential momentum of the gas is not attained. The use of boundary layer control devices offers a possible means of preventing flow separation in maintaining performance in turbomachinery. The NASA-Lewis Research Laboratory contracted the Allison Division of General Motors to conduct an experimental research program to evaluate the aerodynamic performance of highly loaded turbine stator blades incorporating several kinds of boundary layer control devices. The following four concepts are being investigated:

- Vortex generators
- Tandem airfoils
- Jet-flapped blowing
- Tangential jet blowing

This report covers the performance evaluation of the jet-flap concept of boundary layer control. Three jet heights, with three secondary flow rates for each jet height, were investigated. Blade surface static pressure and velocity distributions along with flow visualization results, aerodynamic loss, and boundary layer data are presented.

The analysis and design of all the blade configurations are presented in Volume I. The program base-line level of aerodynamic performance generated by a plain blade and the subsequent evaluation of a corotating vane and a triangular plow type vortex generators with respect to plain blade performance are established in Volume II. Volume III presents the aerodynamic evaluation of the tandem blade. The aerodynamic performance of the tangential jet blades is presented in Volume V.



SYMBOLS

C_x	blade axial chord, in.
C_j	jet momentum coefficient
D_s	suction surface diffusion factor, $1 - \frac{W/W_{cr})^2}{W/W_{cr})_{max}}$
\bar{e}	kinetic energy loss coefficient
F	force, lb_f
H	boundary layer shape factor
\bar{hb}	jet-flap slot size, in.
l	blade length, in.
\dot{m}	mass flow rate, lb_m/sec
o	throat dimension, in.
P	pressure, psia
R	radial position, in.
s	blade spacing, in.
T	temperature, $^{\circ}R$
t_e	blade trailing edge radius, in.
t_l	blade leading edge radius, in.
U_a	jet velocity, fps
W	mainstream flow velocity, fps
X	axial coordinate
β	gas angle measured from tangential, degrees
Δ	change in variable
δ_o	ratio of inlet air total pressure to standard sea level conditions
δ^*	dimensionless boundary layer displacement thickness
ξ	slot angle relative to engine centerline, degrees
Θ	jet deflection, degrees
Θ_{cr}	squared ratio of critical velocity at blade row inlet to critical velocity at standard sea level temperature
θ^*	dimensionless boundary layer momentum thickness
θ	circumferential position, degrees
ρ	density, lb_m/ft^3
σ	blade solidity, C_x/s
τ	jet efflux angle, degrees
ψ	gas angle measured from axial, degrees

\bar{w} total pressure loss coefficient

Subscripts

o station at stator inlet
1 station at blade throat
2 station immediately upstream of trailing edge inside blade passage
3 station immediately downstream of blade trailing edge
4 station two inches (measured in the axial direction) downstream of the blade trailing edge

Baro barometric conditions
cr conditions at Mach number of unity
f force
h hub
i incompressible
j jet
m mass, mean
ma mass averaged
oa overall
p primary
ps pressure surface
s secondary
sep separation
ss suction surface
st static
T total
t tip
u tangential velocity
y tangential direction
w/o without

JET-FLAPPED BLADE PERFORMANCE

A jet-flapped blade employs a high velocity jet which emanates from the trailing edge pressure surface. The interaction of this jet with the main-stream flow effects an acceleration on, thereby delaying flow separation from, the suction surface and a deceleration on the pressure surface in the aft region of the airfoil. The net effect is to produce a turbine blade capable of greater work capacity than an unblown or conventional airfoil.

The six-blade annular cascade assembly of jet-flapped airfoils is presented in Figure 1. The blade section profiles and relative position with adjacent airfoils is shown in Figure 2.

The cavity inside the blades was fed through the hub section from a plenum chamber located below the blade base. Bench tests on individual jet-flapped blades demonstrated that the secondary jet flow had a large positive radial component. The blades were designed on the premise that when a particle of jet fluid left the jet slot at a particular radial location, it remained at the radial location and moved only in the axial-tangential plane. It was necessary to modify the internal geometry of the airfoils to minimize this radial component to produce a more satisfactory distribution of jet velocity at the blade trailing edge. This was accomplished by blanking off the rear portion of the available flow area at the hub section which forced the flow to pass axially through a porous metal baffle that was positioned along the blade length. The baffle is shown installed in the blade in Figure 2. Since the blade was capped at the tip section, the secondary flow tended to stagnate on the upstream side of the baffle, pass through the holes in the baffle in an axial direction, and then flow out through the jet slot. A 0.030-in. diameter hole was drilled in the hub section blank material to keep from starving the hub cavity region of secondary flow. String tufts were attached to the trailing edge section surface of an individual blade which was bench tested in still air surroundings. The radial distribution of the string tufts (Figure 3) when the blade cavity was pressurized indicated that the secondary jet flow left the jet slot in essentially the axial-tangential plane.

Blade 3 was instrumented with static pressure taps primarily on the hub, mean, and tip section suction surface, while blade 4 was similarly instrumented on its pressure surface. This arrangement of static pressure taps permitted definition of the blade surface static pressure distribution through the center passage of the cascade. Design data for the jet-flapped blade and the plain blade are given in Table I. The plain blade experimental results established the program base-line level of performance and are presented in Reference 1. Experimental data for all of the jet-flap configurations and the plain blade are presented in Table II. The leading edges of blades 1 and 6 were matched to a set of inlet guide walls, contoured to generate a free-vortex flow immediately upstream of the blade row. The

plain blade was tested both with and without contoured exit guide walls. No exit guide walls were used on the jet-flapped blade tests. Details of the guide walls and the test rig are given in Reference 2. The aft end of the test rig with a plain blade mounted in position is shown in Figure 4.

As shown in Figure 29 of Reference 2, the design values for each jet slot were to be:

<u>Jet slot size (in.)</u>	<u>Jet flow (%)</u>
0.022	3.5
0.031	4.4
0.040	5.3

However, the constricting effect of the jet on blade flow passage area prevented attainment of these design jet flow rates without exceeding an allowable cavity pressure. With no jet flow, the test facility conditions were adjusted to obtain the correct critical velocity ratio, W/W_{cr}^0 , immediately upstream of the blade row. As jet flow was admitted to the passage, the flow area was progressively reduced which caused the inlet W/W_{cr} to decrease from the correct value. To reestablish the correct inlet W/W_{cr} , an increase in plenum pressure and primary flow rate was required. The increase in primary flow resulted in a reduced percentage of jet-to-primary flow. To correct this \dot{m}_j/\dot{m}_p deficiency, the blade cavity pressure had to be increased. However, this forced an increase in plenum conditions so that the correct flow conditions into the blade row would be maintained. This combination of events continued until the maximum allowable blade cavity pressure was obtained. The percentage of jet flow that existed when the maximum allowable blade cavity pressure was obtained was taken to be the largest of the three secondary flow rates to be investigated for each jet slot size.

Testing was accomplished by passing three jet flow rates through three jet slot sizes. The jet flow rate and slot size configurations were as follows:

<u>Jet slot size (in.)</u>	<u>Jet-to-primary flow rate (%)</u>
0.022	0.81
	1.69
	2.61
0.031	1.50
	2.04
	2.82

<u>Jet slot size (in.)</u>	<u>Jet-to-primary flow rate (%)</u>
0.040	1.97
	3.03
	3.89

Information concerning the kind of instrumentation and associated accuracy is presented in Reference 2. Actual conduct of the test and data reduction procedure is delineated in Reference 1.

VELOCITY AND PRESSURE DISTRIBUTIONS

Surface Velocity Distribution

Hub, mean, and tip section surface velocity distribution results for the three jet slot sizes and their respective secondary flow rates are presented in Figures 5 through 13. The plain blade results are shown in Figures 14, 15, and 16. The agreement between the predicted and measured jet-flap results was somewhat disappointing in that none of the computed hub, mean, or tip section maximum suction surface velocities were attained. This lack of agreement is attributed to deficiencies in the calculation procedure which tends to give optimistic results in regions of high surface curvature (Reference 1).

Surface velocity data are shown for zero secondary flow. The data obtained at the mean section (Figures 6, 9, and 12) indicate that from the 75% axial chord to the trailing edge the critical velocity ratio has essentially a constant value of about 0.77. This condition is attributed to the flow separating from the suction surface at 75% of the axial chord and not re-attaching. Flow visualization results (discussed later) showed that, at least on blade 3 (where the suction surface static pressure taps were located), the addition of even the smallest amounts of secondary flow delayed separation of the fluid from the suction surface to nearly the very trailing edge region of the blade. The observation considering the suction surface velocity distributions of Figures 6, 9, and 12 shows that once flow separation has been eliminated the change in velocity distribution around the airfoil is not so substantial with increasing secondary flow rate.

As the amount of secondary flow was increased for all slot sizes, an acceleration of the flow was promoted in the trailing edge region on the suction surface, while a deceleration was promoted on the pressure surface. There are two mechanisms at work to effect this simultaneous acceleration and deceleration of the flow on the blading surfaces. First, the addition of the secondary mass flow, with its constricting effect on the mainstream flow passage area, caused the mainstream flow to accelerate. This acceleration was further augmented around the very aft suction surface

trailing edge region by entrainment of the mainstream into the jet at the jet and mainstream boundaries. Second, the mainstream flow was essentially stagnated in the trailing edge pressure surface region by the jet, which was blowing nearly normal to the pressure surface, and the mainstream flow. The net result of these effects is an increased area under the W/W_{cr} (or P_{st}/P_{T_0}) versus C_x curves reflecting an increase in work capacity of the airfoil.

The 3.03 and 3.89% secondary flow data for the 0.040-in. slot configuration are particularly interesting. At the hub section, the Figure 11 results for both secondary flow rates show that the flow accelerates on the suction surface through $W/W_{cr} = 1.0$ and continues to accelerate to the trailing edge. At the mean section, Figure 12 shows that the velocity level is essentially a constant value of $W/W_{cr} = 1.0$ over the rear half of the blade for both secondary flow rates. For the tip section of Figure 13, the 3.03 and 3.89% secondary flow rates both show the critical velocity ratio to be unity over about the middle 25% of the axial chord. There are slight differences in the hub, mean, and tip pressure surface velocity distributions in the trailing edge region for the two different secondary flow rates. The interesting feature in this is that both the 3.03 and 3.89% secondary flow rate values give essentially the same hub, mean, and tip suction surface velocity distributions. Based on the ratio of trailing edge static pressure-to-cavity total pressure, the jet slot was choked for both the 3.03 and 3.89% secondary flow rates. The average Mach number at the jet exit for the 1.97, 3.03, and 3.89% secondary flow rates was 0.73, 1.01, and 1.12, respectively. It appears that the jet stream contour for the 3.03% secondary flow rate effectively formed a channel boundary with the blade aft end suction surface to produce the supersonic, transonic, and mixed flows at the hub, mean, and tip sections, respectively. However, by increasing the secondary flow rate to 3.89% of the mainstream, an increase in jet momentum was not represented which could substantially alter that jet stream contour which was produced by the 3.03% secondary flow rate. Therefore, virtually the same surface velocity distributions resulted for both secondary flow rates.

Surface Pressure Distribution

The surface static pressure distributions that correspond to the velocity distributions of Figures 6, 9, and 12 are presented as Figures 17, 18, and 19, respectively. The tangential force per unit blade length was computed by passing a smooth curve through the static pressure data points and by graphically determining the resulting area between the P_{st} versus C_x curves. There is some question as to just how the static pressure behaves in the trailing edge region on the pressure surface as the secondary flow rate is varied. Nevertheless, mean section blade loads were computed as the

sum of (1) the lift caused by the static pressure distributions of Figures 17, 18, and 19 plus (2) the change in the tangential component of the jet momentum. These blade forces are presented in Table III. In general, the presence of the jet flap effected a larger tangential blade force than the design value.

The effectiveness of a jet flap is examined in terms of a jet momentum coefficient. This coefficient is a measure of the momentum of the jet to the momentum of the total blade passage gas stream. In the present investigation, this coefficient is expressed in terms of the flow conditions that existed at the blade trailing edge—

$$C_{jm} = \frac{\dot{m}_j U_a}{1/2 (\dot{m}_j U_a + \dot{m}_p W_{m3})} \quad (1)$$

Figure 36 shows that the design mean section tangential force was attained with only about 1.3% secondary flow. This corresponds to having a mean section jet momentum coefficient of slightly less than 0.03. The plain blade, however, was 16.05% low in achieving the design value of mean section unit tangential blade force.

FLOW VISUALIZATION RESULTS

Application of the lampblack-mineral oil flow visualization technique demonstrated that the jet-flap concept was effective in preventing flow separation from the blade suction surface. These results are shown in Figures 20 through 28 for each of the three secondary flow rates used in conjunction with the three slot sizes. Flow visualization results for the plain blade are illustrated in Figure 29. It can be seen that the flow separation pattern exhibited strong circumferential and radial variations on the plain blade. These patterns also existed with small values of secondary flow for the jet-flapped blade. Blade 3 formed the suction surface while blade 4 formed the pressure surface of the center passage of the cascade. The effect of the jet flap on inhibiting or preventing flow separation from the suction surface of blade 3 in the cascade center passage was of primary interest. Examination of the photographs shown in Figures 20 through 28 indicates that secondary flow injection rates of 1.69% through the 0.022-in. jet slot, 1.50% through the 0.031-in. jet slot, and 1.97% through the 0.040-in. jet slot essentially delayed flow separation to the trailing edge of blade 3. These flow and slot size combinations correspond to a 0.030 to 0.040 range in mean section jet momentum coefficient. Increasing the amount of secondary flow progressively overcame the circumferential variation of flow conditions and eliminated flow separation from all of the airfoils of the cascade.

DOWNSTREAM GAS ANGLE AND TANGENTIAL VELOCITY

Average Downstream Gas Angle Radial Distribution

A radial-circumferential survey of total temperature, total pressure, and gas angle was performed in a plane located two inches downstream of the blade trailing edge. A typical circumferential variation with increasing secondary flow rate at a fixed radial position is presented in Figure 30. In general, the gas angle (measured from axial) tends to increase with increasing secondary flow. It may also be observed that when viewed aft-looking-forward the circumferential position of the blade wakes moves in the counterclockwise direction as the secondary flow rate is increased.

Gas angle data like that shown in Figure 30 were area averaged over each circumferential sweep performed to obtain only the radial variation of gas angle as a function of slot size and secondary flow rate combinations. These data are presented in Figures 31, 32, and 33 for the 0.022-, 0.031-, and 0.040-in. jet slot size configurations, respectively. Included in these figures is the theoretical distribution of downstream gas angle for the respective secondary flow rates.

The testing program consisted of setting the primary and secondary flow conditions on point and conducting the radial-circumferential boundary layer survey at the blade trailing edge (Station 3). The boundary layer probe was then replaced by the combination total pressure-temperature-angle probe and another flow survey was performed two inches downstream of the trailing edge (Station 4). The flow conditions for the Station 4 survey were as close as possible to those that existed during the trailing edge boundary layer survey. With the 0.031-in. jet slot configuration, however, 2.82% secondary flow existed for the trailing edge boundary layer survey and 2.47% secondary flow existed for the downstream temperature-pressure-angle survey. Because of this, the hub, mean, and tip gas angles, which were measured during the downstream survey, were extrapolated to values that should have existed had the secondary flow been actually 2.82% instead of only 2.47% of the mainstream flow. These data are shown in Figure 32.

In general, examination of Figures 31, 32, and 33 shows that the presence of the jet flap effected a considerably greater amount of turning toward the tangential direction than did the design value. This design value was based on a 4% loss in total pressure through the cascade and included the effects of mass addition. Similar plain blade results (Figure 34) show that the plain blade did not achieve the radial distribution of downstream angle without the assistance of the downstream guide walls to guide the gas flow out of the cascade. This is in agreement with the plain blade flow visualization results which demonstrated that flow separation occurred. The gas left the plain blade suction surface before the required turning had been accomplished and, therefore, did not achieve the correct downstream gas angle distribution.

Increasing the amount of secondary flow through the 0.022- and 0.031-in. jet slot generally shows a progressive increase in gas turning across the blade span. However, for the 0.040-in. jet slot, there was no increase and perhaps even a decline in the amount of gas turning as the secondary flow rate was increased from 3.08 to 3.85% of the mainstream flow. This observation is consistent with the surface velocity distribution results presented in Figures 11, 12, and 13.

These gas angle data are plotted against the jet momentum coefficient and are shown in Figure 35. Tangential blade forces for the jet-flapped blade along with the design and the plain blade angle and blade force results are also illustrated. The same results are presented as a function of percent secondary flow rate in Figure 36. As previously mentioned under Surface Pressure Distribution, the mean blade section loads were computed as the sum of the lift caused by the static pressure distribution plus the change in the tangential component of the jet momentum and are given in Table III. This can be expressed as

$$F_{y_{m_T}} / l = \rho_j U_a^2 \cos \xi \overline{hb} + \int (P_{st_{ps}} - P_{st_{ss}}) dx \quad (2)$$

Table III also presents the contribution of the jet change in tangential momentum to the total mean section blade lift. These results are presented in Figure 37 as a function of percent secondary flow. The contribution of the jet increases nearly linearly with percent secondary flow up to about 5% for the range of secondary flows covered in this investigation.

Figure 35 shows that the design tangential lift force was achieved with a jet momentum coefficient value of about 0.03. This value (Figure 36) corresponds to a secondary flow rate of about 1.3%. Also shown in Figure 36 is the variation of the design downstream gas angle with percentage of secondary flow. At $\dot{m}_j / \dot{m}_p = 1.3\%$, the angle measurements show the jet flap was overturning the gas 2.5 to 3 degrees beyond the design value. The conclusion reached on this point is that the jet was more effective in turning the mainstream flow than had been anticipated during the design phase of this blade.

The plain blade was 16.05% low in achieving the design value of tangential force and it did not satisfy the design gas turning requirements.

Mean Section Jet Momentum and Deflection Characteristics

Determination of how much gas deflection capability the jet had downstream of the blade mean section throat was made by assuming the blade turned the

gas to the design throat angle, ψ_1 , and subtracting this design throat angle from the measured downstream gas angle data of Figures 35 and 36—i. e.,

$$\Theta = \psi_4 - \psi_1 \quad (3)$$

The procedure which determined $\psi_1 = 39.34$ degrees is delineated in Reference 2.

These gas deflection results are plotted against the mean section C_j (based on blade cavity to Station 3 flow conditions) and are illustrated in Figure 38. The jet efflux angle at the blade mean section was 85 degrees. The definition of C_j has been altered slightly herein as compared with that used in Reference 2.

In Reference 2, C_j was defined as

$$C_j = \frac{\rho_j U_a^2 \overline{hb}}{1/2 \rho_1 W_{m1}^2 \ell} = \frac{\rho_j U_a^2 \overline{hb} \ell}{1/2 \rho_1 W_{m1}^2 \ell} = \frac{\dot{m}_j U_a}{1/2 \dot{m}_p W_{m1}} \quad (4)$$

The 1/2 in the denominator is a carryover from earlier isolated airfoil studies (Reference 3).

Since the jet aerodynamic properties were determined by the blade cavity total pressure to the mean section trailing edge static pressure expansion ratio, the momentum quantity in the denominator of the C_j expression should include effects of both the jet and primary gas streams—Equation (1). The magnitude of the jet momentum term in the denominator is such that the values of C_{jm} , whether computed by Equation (1) or (4), differ by only a few percent. Comparison of Figure 38 with Figure 33 of Reference 2 shows that the jet was more effective in deflecting the main-stream flow than had been anticipated in the design phase for this blade.

Change in Tangential Velocity Across Blade Row

The jet-flapped and plain blades were designed to the same change in tangential velocity across the blade row. Based on the inlet and exit critical velocity ratio, including loss and downstream gas angle measurements, the experimental change in tangential velocity was computed and is compared with the plain blade and design values in Table IV. Positive and negative deviations in Table IV represent, respectively, greater than and less than

design values of ΔW_u across the blade row. The mean section of the jet-flapped blade exceeded the design ΔW_u for all combinations of jet slot size and secondary flow rate. This was the result of two effects acting together: (1) the combination of the blade and jet turned the mainstream flow more toward the tangential direction than the design value and (2) the loss level at the mean section was low. At the hub and tip section, the large loss level made, in some cases, the jet-flapped blade deficient in achieving the design value of ΔW_u . Increasing the amount of secondary flow both at the hub and tip for a given jet slot size progressively eliminated in all cases (except at the hub for the 0.022-in. jet slot) this deficiency in achieving the design change in tangential velocity across the blade row. The plain blade fell short at all radial stations in satisfying the design ΔW_u .

CONTOUR PLOTS

Results at the Blade Trailing Edge (Station 3)

Total pressure radial-circumferential surveys were performed immediately behind the blade trailing edge for the purpose of determining the Station 3 loss and boundary layer characteristics for each blade configuration.

A typical result for the jet-flapped 0.022-in. jet slot blade with three values of secondary flow at a radial location of 12.97 in. is shown in Figure 39. Similar data for the plain blade are illustrated in Figure 40.

Progressive increase in the amount of secondary flow appeared to shrink the wake in the circumferential direction and stretch it in the axial direction. When viewed aft-looking-forward, the circumferential movement of the wake was in the counterclockwise direction. It should be noted that the wake of the jet-flapped blade for zero secondary flow probably was much larger than that for the plain blade, since the trailing edge thicknesses were 0.100 and 0.035 in. for the jet-flapped and plain blades, respectively. The experimental results of Reference 4 showed that with a trailing edge discharge (i. e., $\tau \approx 0$ degrees) a jet-to-free-stream velocity ratio of 2.0 was required before an excess of total pressure was observable in the blade wake. In the present investigation, the maximum value of jet-to-free-stream velocity ratio and $\tau = 85$ degrees were only 1.23 and no total pressure excess was observed. All combinations of jet slot sizes and secondary flow rates resulted in the conventional type of blade wakes depicted in Figure 39.

Kinetic energy loss coefficients were computed from the results of the total pressure surveys and are presented as contour plots in Figures 41 through 49 for the three jet slot sizes. Plain blade \bar{e} data are shown in Figure 50. The jet-flap \bar{e} contours show that for a given jet slot size the circumferential extent of the high loss wake region is reduced as the amount of secondary flow was increased. It is interesting to note that the contour

plot data show that the blade wakes are considerably larger for the 0.031-in. jet slot than for either the 0.022-in. or the 0.040-in. jet slots. Also, it is shown later that the circumferentially mass averaged loss coefficients for the 0.031-in. jet were larger than those for either the 0.022- or 0.040-in. jet slot blade configurations. The reason for this apparent anomaly is not clear. Mechanical rework and testing procedures were identical for each of the three slot size configurations. Also, there is nothing in the flow visualization results to suggest that the 0.031-in. jet slot configuration was markedly different in the aerodynamic sense from either the 0.022- or 0.040-in. jet slot configurations. The only indication of peculiar flow conditions for the 0.031-in. jet slot blade is suggested by the inlet velocity ratio conditions presented in Table II. Even though the velocity ratio level at the inlet hub section was the same for all jet-flap tests— $W/W_{cr} = 0.7$ —the tip value was nearly 0.58 for the 0.022- and 0.040-in. slot configurations but only about 0.54 for the 0.031-in. jet slot. The reason for this is not known since all configurations used the same inlet guide walls.

The $\bar{\epsilon}$ loss contour plots reveal that the loss was largest at the hub section for the 0.022- and 0.040-in. jet slots, but for the 0.031-in. jet slot the hub loss region was small compared to what existed at the tip. It is likely that the lower inlet velocity level (i. e., lower energy level) for the 0.031-in. jet slot tip section resulted in a tip section flow field that was more susceptible to the tip section secondary flow and end wall loss effects than either the 0.022- or 0.040-in. jet slot configurations.

Results Downstream of the Blade Trailing Edge (Station 4)

Kinetic Energy Loss Coefficient

Contours of kinetic energy loss coefficient are presented in Figures 51 through 59 for the jet-flapped blade and in Figure 60 for the plain blade. The highly skewed appearance of the jet-flap loss contours is the result of the large amount of gas turning from the axial direction. All of the jet-flap configurations have a very large loss region near the hub section at this axial station. This was because the jet and mainstream were excessively turned toward the tangential direction so that the flow separated from the convex rig hub casing wall.

Examination of the $\bar{\epsilon}$ contour plots reveals that the loss level is reduced at the radial span locations approximately 12.0, 13.5, and 15.0 in. This is generally true regardless of the jet slot and flow rate combinations. The reason for this is unclear. There may be some connection between the loss level observed and the fact that jet slot support ties were located at those radial locations. There was, however, no indication of any peculiar loss behavior at the radial stations in question computed at the blade trailing edge and which are shown as Figures 41 through 49.

Downstream Gas Angle

Contour plots of the gas angle, measured from the axial direction two inches downstream of the trailing edge, are shown in Figures 61 through 69 for the three jet-flapped blade slot sizes. Figure 70 illustrates the plain blade gas angle contour plot. The theoretical radial distribution of the gas angle, based on a 4% loss in total pressure across the cascade and including the effects of mass addition, is shown as the right-hand ordinate of Figures 61 through 70. The overturning of the gas from the axial direction, particularly near the hub section, is apparent for the jet-flapped blade as the jet slot size and secondary flow rate were increased. The only region in which the plain blade experienced design or overdesign turning was near the hub section.

MASS AVERAGED LOSS AND BOUNDARY LAYER PARAMETERS

Results at the Blade Trailing Edge (Station 3)

Aerodynamic Loss Data

Circumferentially mass averaged values of $\bar{\epsilon}$ at each radial depth were computed by Equation (6) of Reference 1 and are shown for the jet-flapped and plain blades in Figures 71 through 74. The numerical integrations were performed in the circumferential direction encompassing the points of minimum total pressure in the wakes of blades 3 and 4.

For a given slot size, the $\bar{\epsilon}$ results show that, at least in the midspan region of the blade, for the range of secondary flow rates investigated herein increasing the amount of secondary flow decreased the circumferentially mass averaged loss level. Also, these mass averaged loss data substantiate the observation made concerning the loss contour plots. That observation was that the loss level appears largest at the hub section for the 0.022- and 0.040-in. jet slot sizes but is largest at the tip for the 0.031-in. jet. The loss data of Figure 74 show that the plain blade had regions of large loss in the midspan and tip regions. The hub section loss, however, was quite small. An overall flow passage mass averaged value of kinetic energy loss was computed at the trailing edge and is presented in Figure 75 as a function of the amount of secondary flow in the jet stream. These data are also listed in Table V. The 0.022- and 0.040-in. jet slot data appear to correlate fairly well with the amount of secondary flow but the 0.031-in. jet slot data do not. All of these data, however, show that for a given slot size the loss tends to be reduced as the amount of secondary flow is increased. The plain blade Station 3 $\bar{\epsilon}_{oa_{ma}}$ value is also shown in Figure 75 for comparison purposes. As previously noted, the loss level for the jet-flapped blade with zero secondary flow was probably larger than for the plain blade because of the increased size of the trailing

edge of the jet-flapped blade. The large trailing edge was required to accommodate the jet flap. Circumferentially mass averaged values of the total pressure loss coefficient, $\bar{\omega}$, are presented as a function of radial position for the various jet slot sizes and flow rates in Figures 76, 77, and 78. These $\bar{\omega}$ data exhibit all of the same characteristics as did the \bar{e} loss coefficients. The overall mass averaged values of $\bar{\omega}$ are presented as a function of secondary flow rate in Figure 79 and mean section jet momentum coefficient in Figure 80. If the 0.031-in. jet slot size data are ignored and a least squares straight line is fitted through the 0.022- and 0.040-in. jet slot size data, Figure 79 shows that a jet-flap trailing edge loss level equivalent to that of the plain blade was attained with 1.25% secondary flow. This jet flow rate corresponds to a mean section jet momentum coefficient of about 0.025. A further increase in the amount of secondary flow produced a loss level that was less than that for the plain blade.

Boundary Layer Parameters

Radial variation of the displacement thickness and the boundary layer shape factor are shown in Figures 81 through 86 for the various jet-flapped blade configurations. Similar plain blade data are shown in Figure 87. In general, the momentum thickness, obtained from $\theta^* = \delta^*/H$, was nearly independent of the effects of varying jet slot size and amount of secondary flow rate. This was not the case for the displacement thickness which was quite sensitive to the variations of jet slot size and amounts of secondary flow. It can be noted that for a given slot size across nearly the entire radial span of the blade that the displacement thickness shrank or thinned out rather markedly as the secondary flow was increased. As the jet flap progressively prevented flow separation from the suction surface and shrank the size of the blade wake, the size of the displacement thickness, which reflects a blockage of the flow path area, was likewise reduced in size.

The boundary layer shape factor ($H = \delta^*/\theta^*$) results of Figures 84, 85, and 86 show the effects of the jet-flap configurations simultaneously on δ^* and θ^* . It can be seen that δ^* has the controlling influence on H since θ^* was nearly unaffected by jet slot size and flow rate combinations. Using Equation (18) of Reference 1, the free-stream conditions at the trailing edge of the blade, and $H_i = 1.8$, an estimate of the magnitude of H for separation in the midspan region, is shown in Figures 84, 85, and 86. If the experimental values of H lie above this estimated H value for flow separation, the flow may have separated from the blading surfaces. If the experimental values fall below the estimated level, flow separation probably did not occur. These results demonstrate, as do all of the previous results, that for a given slot size increasing the amount of secondary flow progressively inhibited flow separation from the blading surfaces. The results of Figures 84, 85, and 86 do not show any strong correlation between the jet slot size flow rate combination and the prevention of flow separation. For the 0.022-in. slot size, a jet flow rate larger than 2.61% ($C_j = 0.062$) would be required to prevent flow separation all along the blade span. Whereas, for the 0.031-in.

slot, only a secondary flow rate of between 1.5 and 2.0% ($C_j = 0.029$ to 0.045) was necessary. With the 0.040-in. jet slot size, a jet flow rate of between 2.0 and 3.0% ($C_j = 0.041$ to 0.065) was then required to produce experimental H values that were less than the critical value for predicted flow separation. The shape factor data presented herein include the effects of the boundary layer buildup on both the suction and pressure surfaces. Since the presence of the jet flap was to prevent separation on the suction surface but effected a wide variance between the flow conditions both on the suction and pressure surfaces in the trailing edge region, the jet slot size flow rate combination might have correlated with the shape factor spanwise distribution for no flow separation if the shape factor had been only the suction surface shape factor. The plain blade shape factor data of Figure 87 along with other aerodynamic measurements and flow visualization results show that the plain blade was operating with much of the blade surface covered with a separated flow.

Results Downstream of the Blade Trailing Edge (Station 4)

Aerodynamic Loss Data

Circumferentially mass averaged kinetic energy loss coefficients were computed at each of the 10 surveyed radial positions for each jet-flap configuration and are shown in Figures 88, 89, and 90. Similar plain blade results are included as Figure 91 for comparison purposes.

The obvious result of these $\bar{\epsilon}$ data is that the loss level in the hub region is so large that it propagates into and distorts the loss distribution in the midspan region. As stated earlier, the high loss level at the hub section is attributed to the flow separating off the rig hub casing wall at this axial station. The observation made earlier from the Station 4 loss contour plots that the loss distribution exhibited a peculiar behavior at radial locations of about 12.0, 13.5, and 15.0 in. is made further evident by the data presented in Figures 89 and 90. The circumferentially mass averaged loss level was consistently less at least at the radial positions of 13.5 and 15.0 in. than it was over the rest of the blade span.

Even though the very high loss level at Station 4 is largely attributed to the flow separating from the hub casing wall, overall mass averaged $\bar{\epsilon}$ loss coefficients were nevertheless computed and are shown in Figure 92 as a function of percent secondary flow rate. These data are also tabulated in Table VI. Comparison of the overall mass averaged loss coefficient calculations of Figure 75 with those of Figure 92 shows that the combined effect of jet mixing with the free-stream flow plus flow separation from the hub casing wall produced a loss level two inches downstream of the trailing edge that was nearly twice what it was at the trailing edge.

Station 4 total pressure loss coefficient data were circumferentially mass averaged at each radial depth surveyed and are illustrated in Figures 93, 94, and 95 for the three slot sizes investigated. Overall mass averaged values of $\bar{\omega}$ are shown as a function of percent secondary flow rate in Figure 96. These results exhibited all of the trends and characteristics as did the Station 4 kinetic energy loss coefficient data of Figures 88, 89, and 90.

Boundary Layer Parameters

Boundary layer displacement thicknesses were computed at Station 4 for the various jet-flapped blade configurations and are presented in Figures 97, 98, and 99 for the 0.022-, 0.031-, and 0.040-in. jet slot sizes. At this axial station, the effect of jet slot and secondary flow rate combination is slight on both the displacement and momentum thicknesses. They are slightly stronger on the displacement thickness. For a specific jet slot size, there is a decrease in δ^* , particularly at the radial positions near $R = 13.5$ and 15.0 in., with increasing secondary flow rate.

The radial variation of boundary layer shape factor, $H = \delta^*/\theta^*$, is shown in Figures 100, 101, and 102 for the various jet-flapped blade configurations and in Figure 103 for the plain blade. H was reasonably uniform over the outer 2/3 portion of the blade. Also, the level of the shape factor depended somewhat on the slot size and jet flow rate combination. For the 0.022- and 0.040-in. jet slot size, the level of H decreased with increasing secondary flow rate to a value in some instances less than 1.0. These cases of $H < 1.0$ occurred with the largest secondary flow rates at the radial positions where the loss was observed to be small—i. e., $R = 12.0, 13.5,$ and 15.0 in. A similar behavior of H for the intermediate jet slot size was not observed. The behavior of H in the midspan region with the 0.031-in. jet slot varied from about 1.3 to 1.2 and back to 1.3 as the jet flow was increased from 1.50 to 2.02 to 2.47%.

SUMMARY OF JET-FLAPPED BLADE PERFORMANCE

1. As the amount of secondary flow was increased for all slot sizes, an acceleration of the main flow was promoted on the suction surface while, at the same time, a deceleration was promoted on the pressure surface. Once the jet slot choked there was no significant change in the surface velocity distribution with increased jet flow.
2. In general, the presence of the jet flap effected a larger mean section tangential blade force than the design value. The design value was achieved with only about 1.3% secondary flow. This corresponded to a mean section jet momentum coefficient C_{jm} (the ratio of jet to mainstream momentum) of about 0.03. The mean section tangential force varied nearly linearly with C_{jm} . The plain blade was over 16% deficient in achieving the design mean section tangential force.
3. The flow visualization results revealed that flow separation was prevented from the center blades of the cascade with secondary flow rate and jet slot size combinations that corresponded to a mean section jet momentum coefficient in the 0.03 to 0.04 range.
4. Greater than design gas turning was consistently obtained for the jet-flap tests. The combination of the blade and jet was more effective in turning the mainstream flow than was anticipated during the airfoil design phase. Because of flow separation, the plain blade was unable to achieve the design gas turning.
5. Mainstream gas turning was, in general, increased by increasing C_{jm} ; thus, the jet-flapped blade can aerodynamically control flow path geometry.
6. The mean section of the jet-flapped blade exceeded the design change in tangential velocity across the blade row for all combinations of jet slot size and secondary flow rate.
7. A progressive increase in the jet flow shrank the blade wake in the circumferential direction and stretched it in the axial direction.
8. The radial velocity distribution immediately upstream of the blade row was essentially identical for both the 0.022- and 0.040-in. jet slot configurations. For an unexplained reason, the velocity level into the tip section of the 0.031-in. configuration was less than either

of the other two slot sizes. The loss for the 0.031-in. jet differed in two respects from that for either the 0.022- or 0.040-in. jet slot sizes.

- For the 0.022- and 0.040-in. jet slot sizes the loss was largest at the hub, while for the 0.031-in. jet the loss was largest at the tip.
 - The loss level for the 0.031-in. jet was higher than that for either the 0.022- or 0.040-in. jet slot sizes.
9. If the 0.031-in. jet slot loss data are ignored (which may be justifiable since the inlet condition differed from the rest of the blades tested), a jet-flapped blade trailing edge loss level equivalent to that of the plain blade was obtained with a jet momentum coefficient of about 0.025. The jet-flapped blade, which had a solidity of about 0.91 of the plain blade, prevented flow separation and achieved the design blade force and gas turning requirements with a mean section jet momentum coefficient of 0.03 at a loss level which was no larger than that for the plain blade. Because of flow separation, the plain blade satisfied neither the design loading nor the gas turning requirements. The mean section jet momentum coefficient of about 0.03 corresponded to a secondary flow rate of about 1.3% of the primary flow.

REFERENCES

1. Bettner, J. L.: Experimental Investigation in an Annular Cascade Sector of Highly Loaded Turbine Stator Blading. vol II, Performance of Plain Blade and Effect of Vortex Generators. NASA CR-1323, March 1969.
2. Bettner, J. L.: Experimental Investigation in an Annular Cascade Sector of Highly Loaded Turbine Stator Blading. vol I, Analyses and Design. NASA CR-1219, July 1968.
3. Spence, D. A.: The Two-Dimensional Jet-Flap. An Exact Solution in Closed Form of Small C_j , and an Interpolation Formula Up to $C_j = 10$. Royal Aircraft Establishment Great Britain. Report No. Aero 2568, 1956.
4. Brocher, E. F.: "The Jet-Flap Compressor Cascade." ASME Transactions, Journal of Basic Engineering. vol 83. September 1961, pp. 401-407.



Table I.
Design data for the jet-flapped and plain blades.

Symbol	Units	Jet-flapped blade			Plain blade		
		Hub	Mean	Tip	Hub	Mean	Tip
C_x	in.	1.2285	1.4555	1.6835	1.365	1.5925	1.820
s	in.	1.01267	1.22967	1.44678	1.01267	1.22967	1.44678
σ		1.213	1.185	1.164	1.348	1.293	1.258
tl	in.	0.04	0.04	0.04	0.0546	0.0637	0.0728
te	in.	0.05	0.05	0.05	0.0175	0.0175	0.0175
β_o	degrees	36.08	41.66	46.37	36.08	41.66	46.37
ψ_1	degrees	45.16	39.34	34.09	47.85	43.02	38.80
$W/W_{cr})_o$		0.703	0.623	0.572	0.703	0.623	0.572
$\frac{W_{ss}}{W_{cr}})_{\max, w/o \text{ jet}}$		1.380	1.210	1.095	1.350	1.189	1.082
$W/W_{cr})_4$		0.812	0.721	0.662	0.799	0.707	0.647

Table II.
Experimental results for the jet-flapped and plain blades.

Jet slot size, in.	Jet-flapped blade									Plain blade	
	0.022			0.031			0.040				
Secondary flow, %	0.0	0.81	1.69	2.61	1.50	2.04	2.82	1.97	3.03	3.89	
Actual primary flow rate, lb _m /sec	1.364	1.320	1.400	1.440	1.400	1.420	1.473	1.520	1.680	1.620	1.240
Equivalent primary flow rate, lb _m /sec	1.057	1.044	1.069	1.032	1.024	1.024	1.001	1.086	1.078	1.043	0.996
Plenum total pressure, in. of Hg abs	38.165	39.145	40.905	42.855	40.959	41.468	44.108	41.760	46.470	46.650	37.481
Barometric pressure, in. of Hg abs	29.565	29.495	29.505	29.555	29.559	29.568	29.508	29.165	29.168	29.105	29.306
P_{T_0}/P_{st4H}	1.324	1.355	1.420	1.496	1.414	1.434	1.536	1.472	1.638	1.672	1.288
P_{T_0}/P_{Baro}	1.291	1.327	1.386	1.450	1.386	1.402	1.495	1.432	1.593	1.603	1.279
Plenum total temperature, °R	508	556	566	547	520	518	521	516	515	523	525
θ_{cr}	0.979	1.072	1.091	1.054	1.002	0.998	1.004	0.995	0.993	1.008	1.012
δ_0	1.275	1.308	1.367	1.432	1.369	1.386	1.474	1.396	1.553	1.559	1.253
Actual secondary flow rate, lb _m /sec	0.0	0.0107	0.0237	0.0376	0.0210	0.0290	0.0450	0.030	0.051	0.063	---
Blade cavity total pressure, in. of Hg abs	---	34.41	42.05	51.50	39.06	43.62	53.16	41.52	51.92	59.21	---
Blade cavity total temperature, °R	---	550	565	549	513	510	530	522	515	517	---
P_{T_1}/P_{T_0}	---	0.879	1.028	1.202	0.954	1.052	1.205	0.994	1.117	1.269	---
Inlet W/W_{cr}											
Hub	0.702	0.702	0.705	0.708	0.706	0.701	0.701	0.703	0.704	0.702	0.703
Mean	0.637	0.642	0.643	0.646	0.627	0.622	0.623	0.644	0.651	0.643	0.633
Tip	0.569	0.578	0.577	0.579	0.542	0.536	0.538	0.582	0.595	0.581	0.569

Jet-flapped and plain blade trailing edge (Station 3)
overall mass averaged loss data.

Table III.
Jet-flapped and plain blade mean section tangential force results.

Jet flap		Mean section static pressure force, $F_{y_{mst}}$ (lb _f /in.)	Mean section jet momentum force, $F_{y_{mj}}$ (lb _f /in.)	Total mean section force, $F_{T_m} = F_{y_{mst}} + F_{y_{mj}}$ (lb _f /in.)	$F_{y_{mj}}/F_{y_{mst}}$ (%)	Flow rate per passage, \dot{m}_p (lb _m /sec)	$F_{y_{mT}}/\dot{m}_p \sqrt{e_{cr}}$ ($\frac{\text{lb}_f/\text{in.}}{\text{lb}_m/\text{sec}}$)
Slot size (in.)	\dot{m}_j/\dot{m}_p (%)						
0.022	0.0	7.910	0.0	7.910	0.0	1.364	5.864
	0.81	8.664	0.102	8.766	1.17	1.320	6.414
	1.69	9.526	0.205	9.731	2.11	1.400	6.654
	2.61	10.474	0.315	10.789	2.93	1.440	7.298
0.031	1.50	9.635	0.237	9.873	2.41	1.400	7.045
	2.04	9.903	0.318	10.221	3.10	1.420	7.205
	2.82	10.781	0.464	11.244	4.12	1.473	7.618
0.040	1.97	10.210	0.334	10.544	3.18	1.520	6.955
	3.03	12.966	0.593	13.559	4.38	1.680	8.100
	3.89	12.801	0.686	13.487	5.09	1.620	8.292
Plain blade		6.98	---	6.98	---	1.24	5.600
Design value		7.04	---	7.04	---	1.05	6.705

Table IV.
 Jet-flapped and plain blade measured and design change
 in tangential velocity across blade row.

		Jet-flapped blade									Plain blade	Design value
		0.022-in. jet slot			0.031-in. jet slot			0.040-in. jet slot				
		0.81	1.69	2.61	1.50	2.04	2.82	1.97	3.03	3.89		
		1143.28	1190.89	1236.77	1368.81	1336.59	1396.75	1280.92	1385.43	1361.27	1136.01	1247.87
on)		-8.38	-4.57	-0.89	-9.69	+7.11	+11.93	+2.65	+11.02	+9.09	-8.96	
		1049.17	1111.57	1151.23	1065.89	1105.14	1174.27	1086.38	1248.60	1237.79	940.59	1027.65
on)		+2.09	+8.17	+12.02	+3.72	+7.54	+14.27	+5.71	+21.50	+20.45	-8.47	
		814.86	867.37	895.51	803.55	883.89	922.84	827.81	1028.88	964.34	776.91	873.71
on)		-5.73	-0.62	+2.12	-8.03	+1.16	+5.62	-5.25	+17.76	+8.82	-11.08	

Table VI.
 Jet-flapped and plain blade downstream (Station 4)
 overall mass averaged loss data.

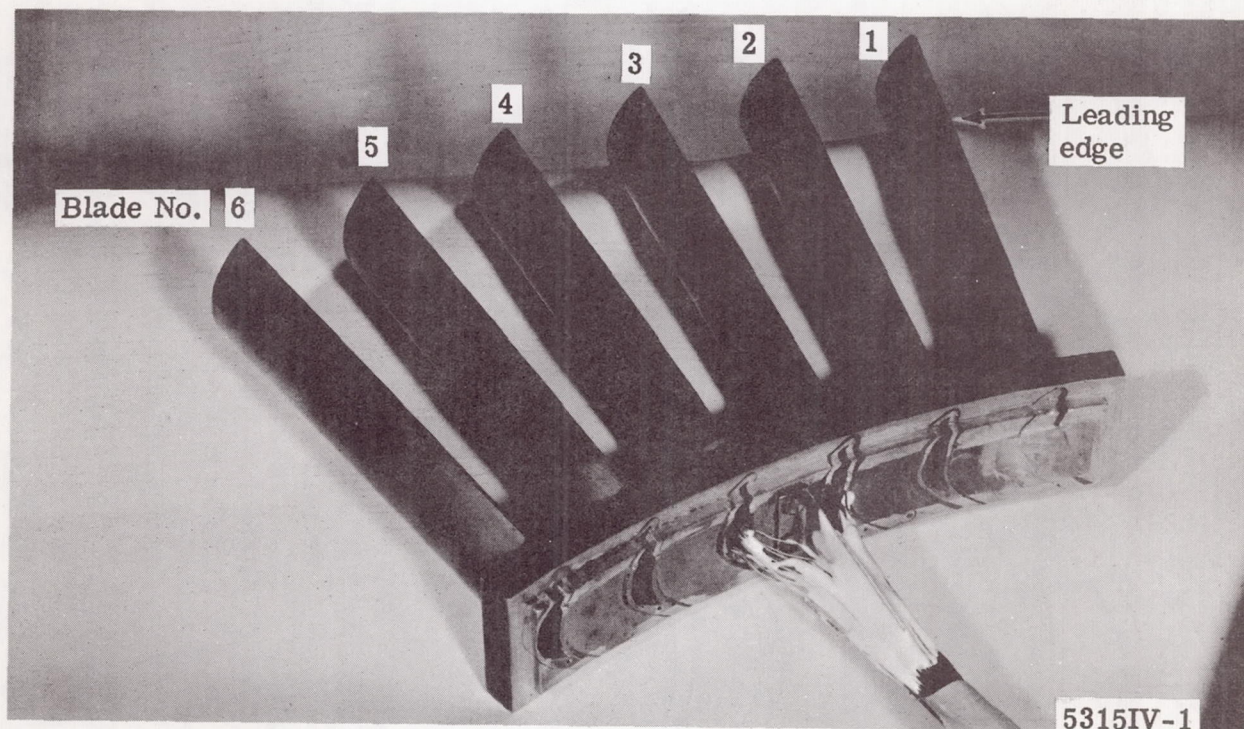
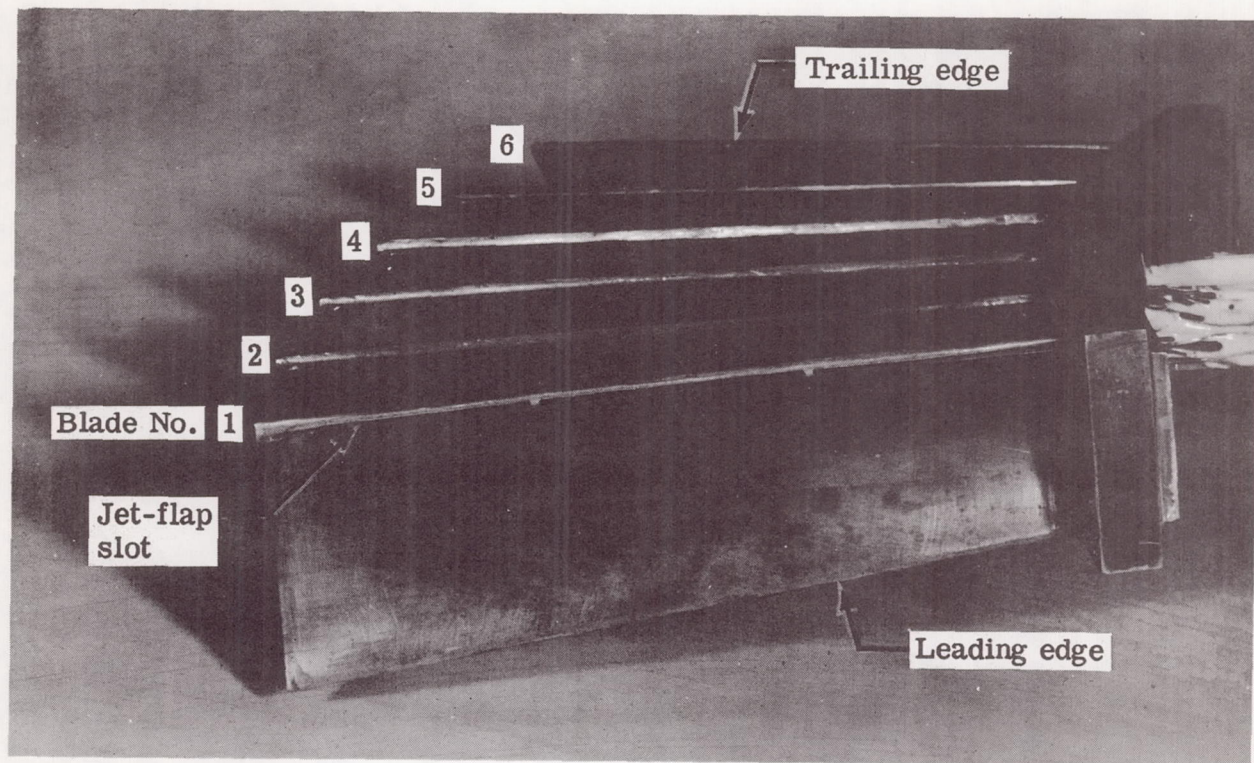
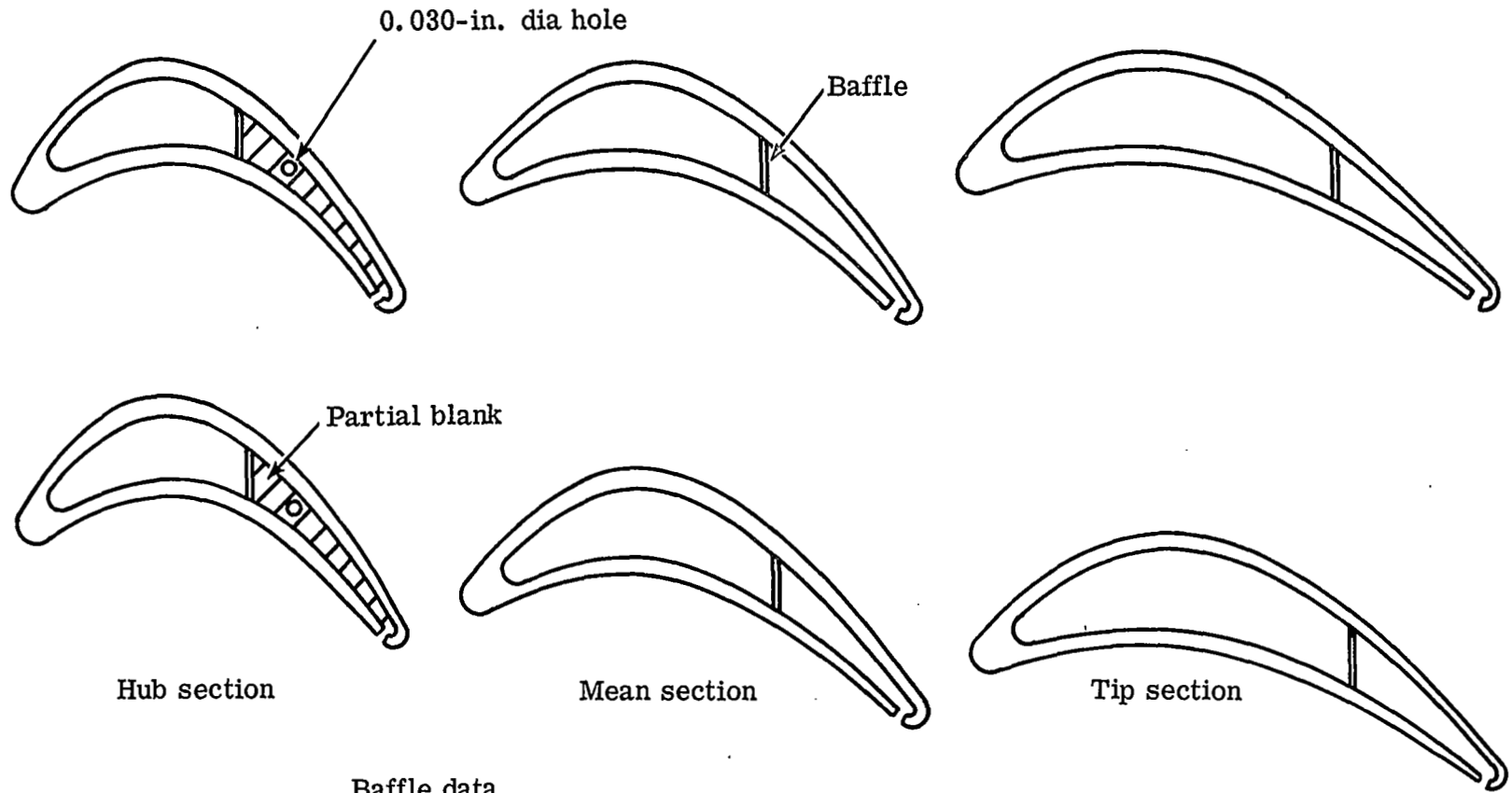


Figure 1. Jet flapped blade assembly.



<u>Baffle data</u>	
Material	316 SS
Thickness	0.014 in.
Hole size, dia	0.015 in.
Center distance	0.031 in.

5315IV-2

Figure 2. Jet-flapped blade internal and external profiles.

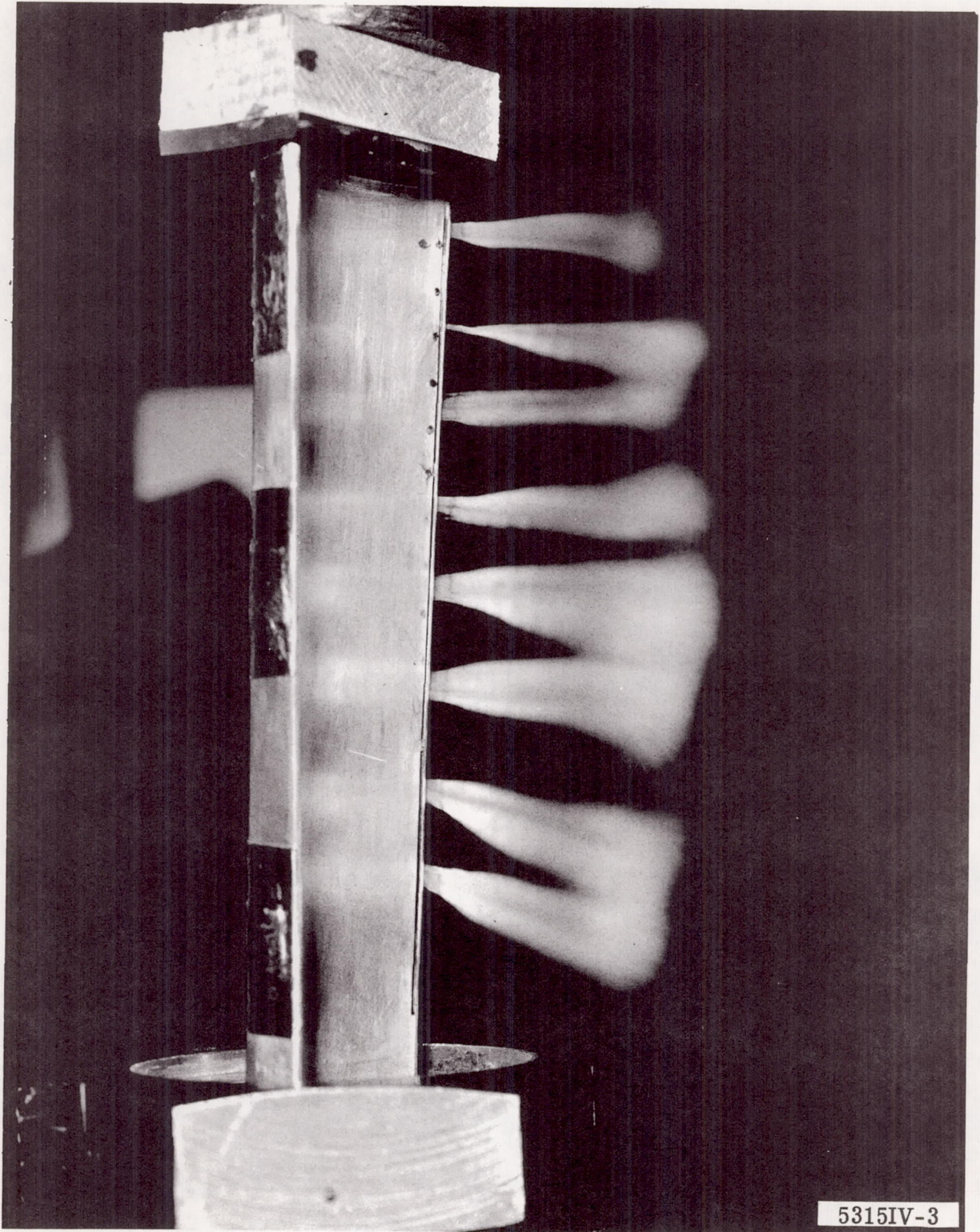


Figure 3. Bench test results showing radial distribution of jet stream.

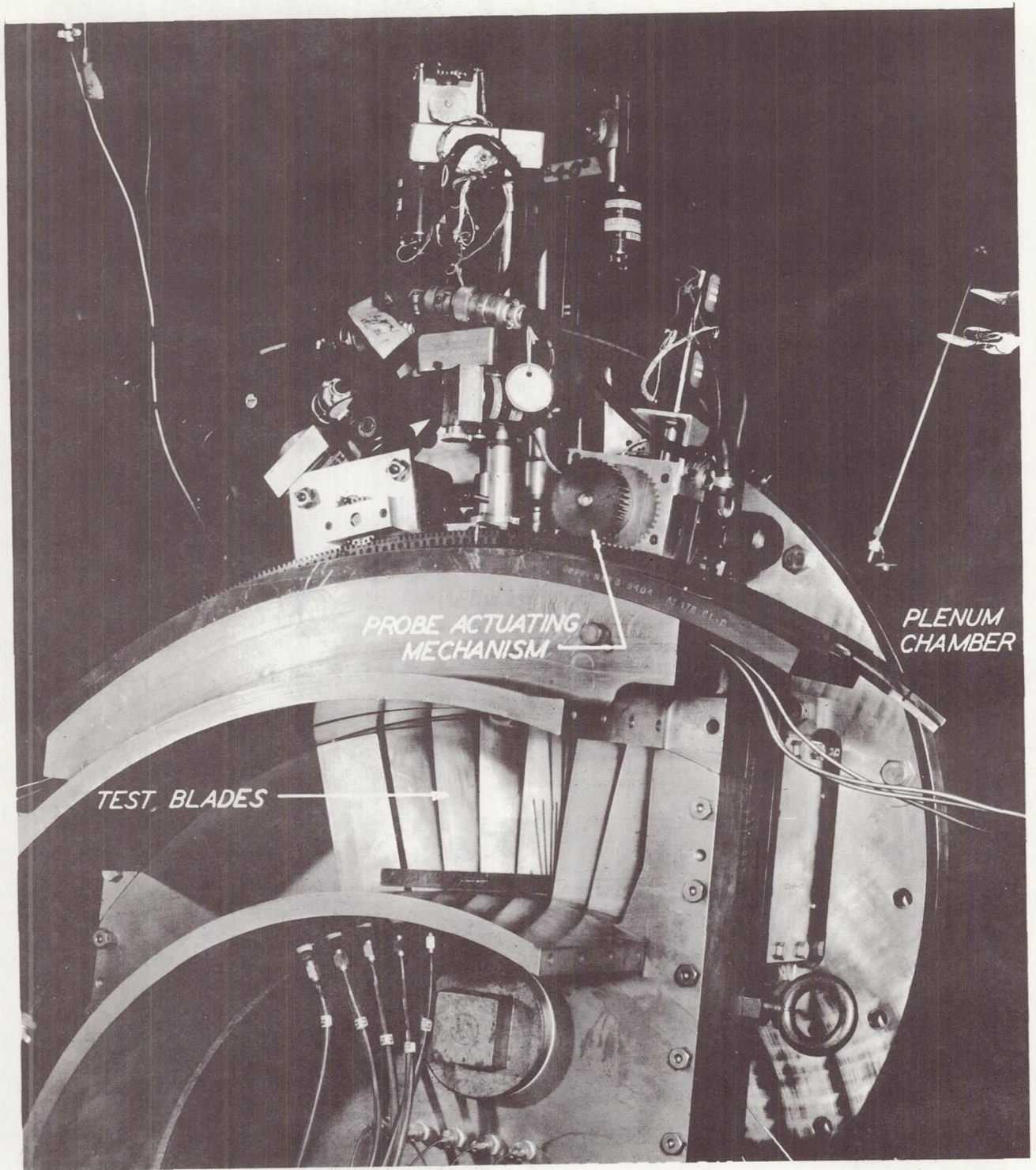
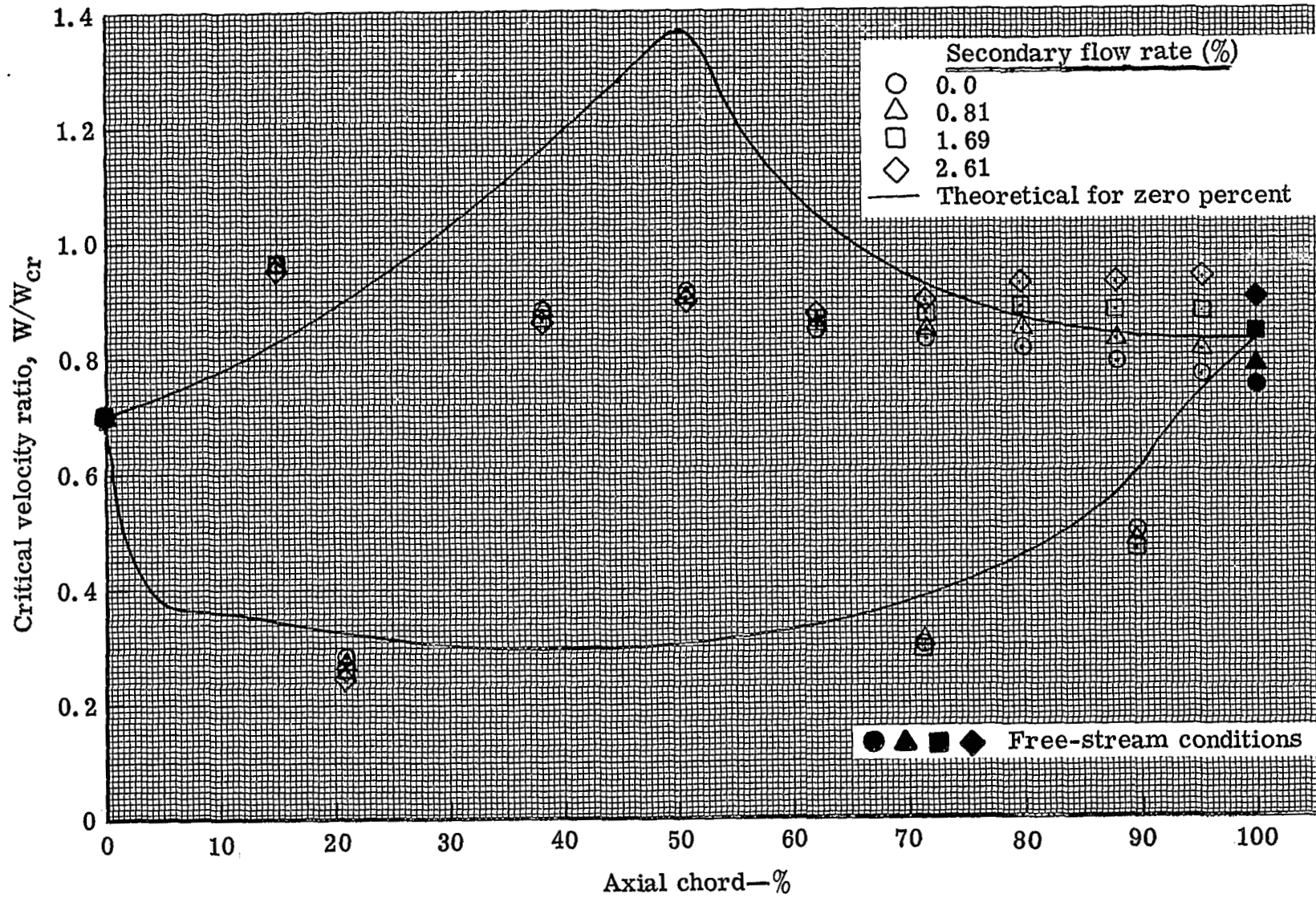
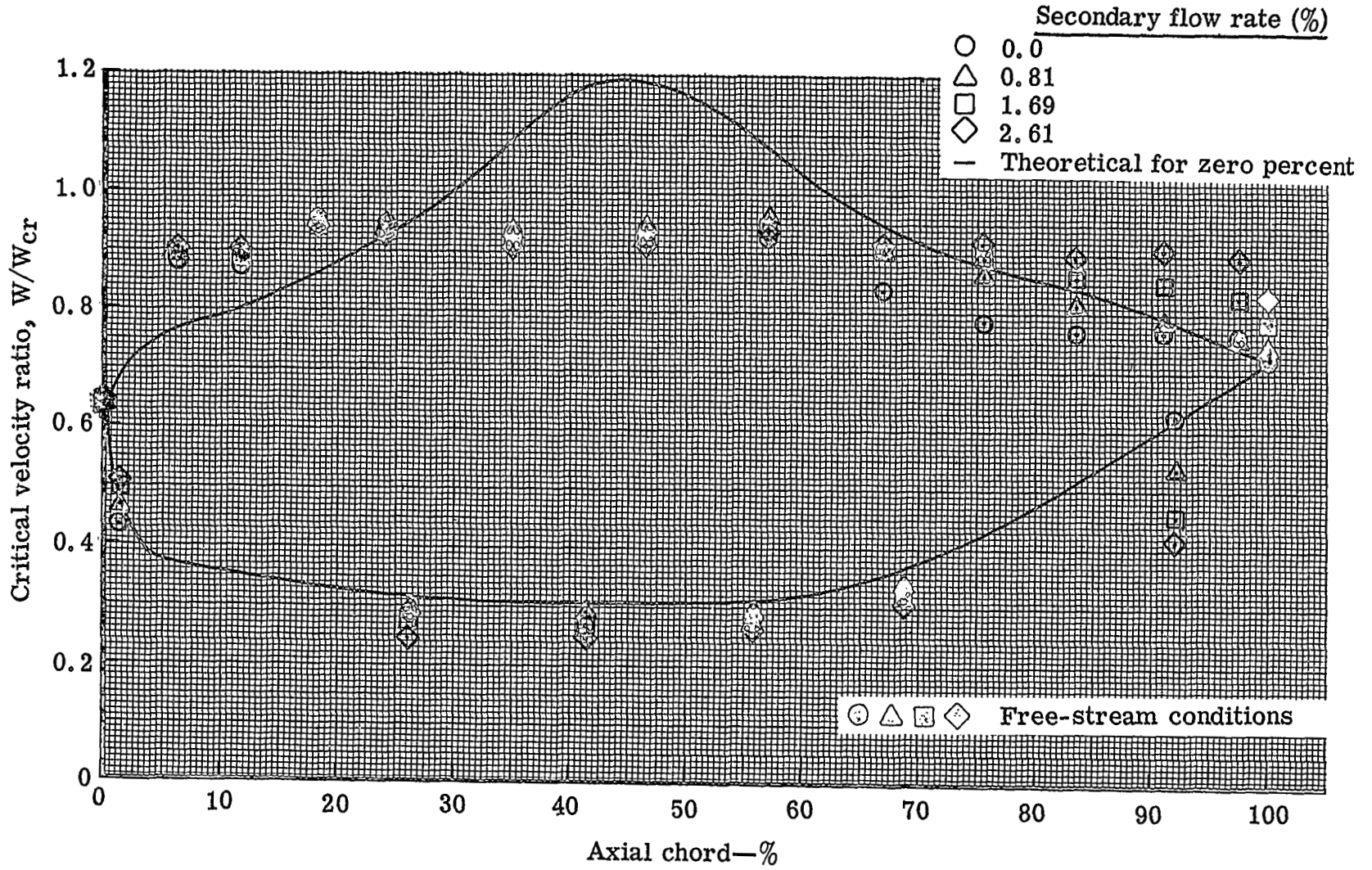


Figure 4. Annular cascade test rig.



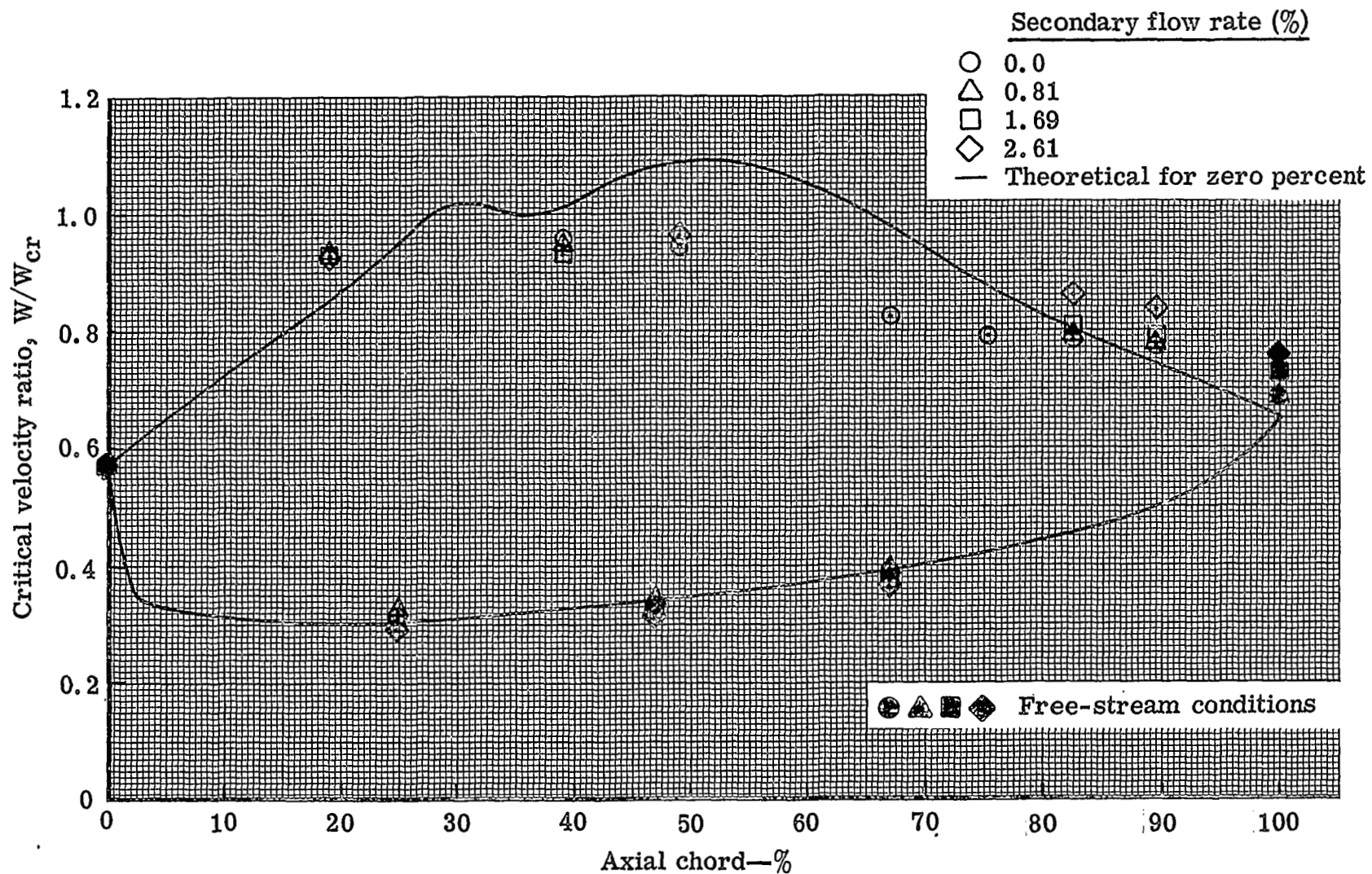
5315IV-5

Figure 5. Measured and predicted surface critical velocity ratio distribution for the jet-flapped blade (hub section)—0.022-in. jet slot.



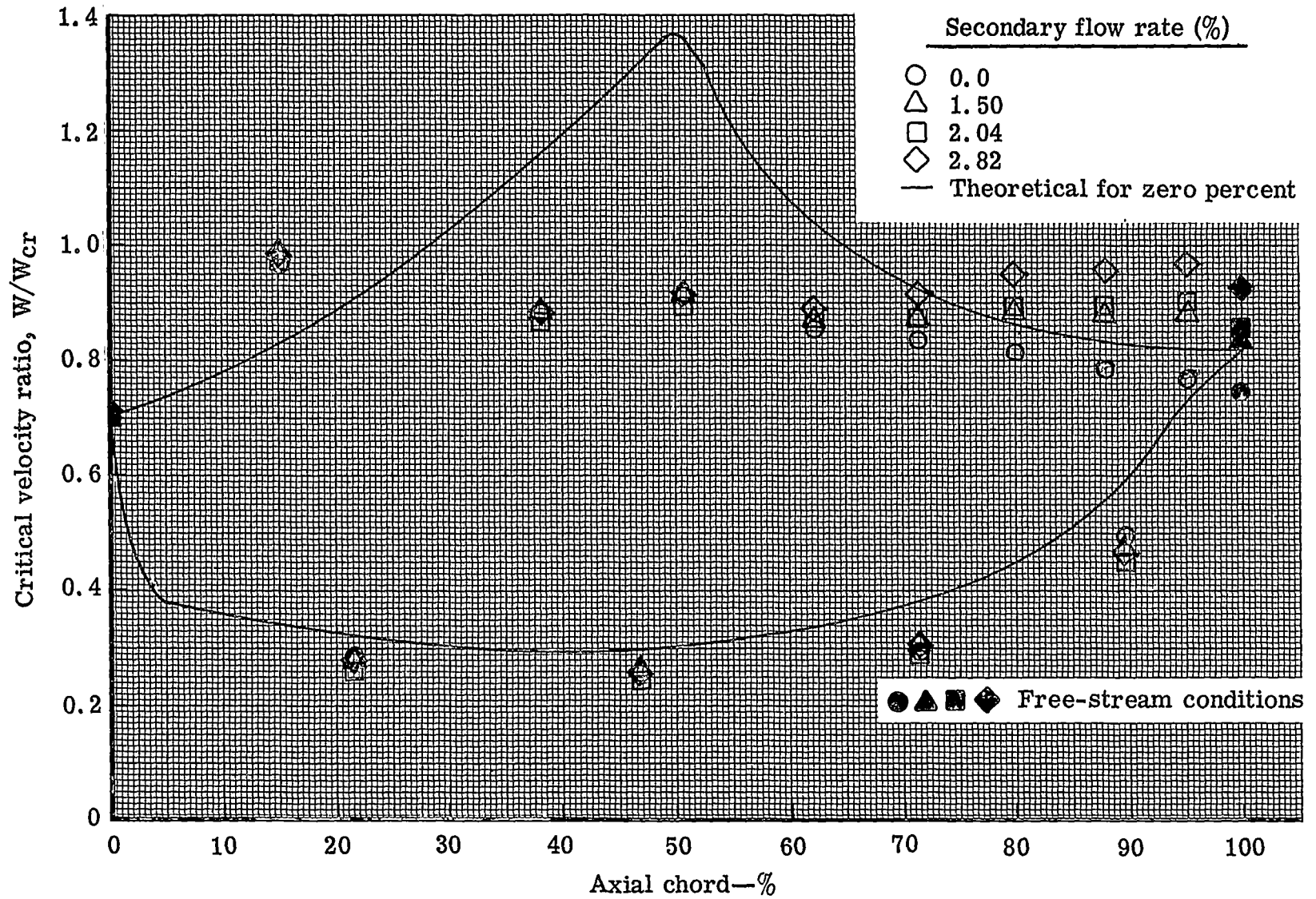
5315IV-6

Figure 6. Measured and predicted surface critical velocity ratio distribution for the jet-flapped blade (mean section)—0.022-in. jet slot.



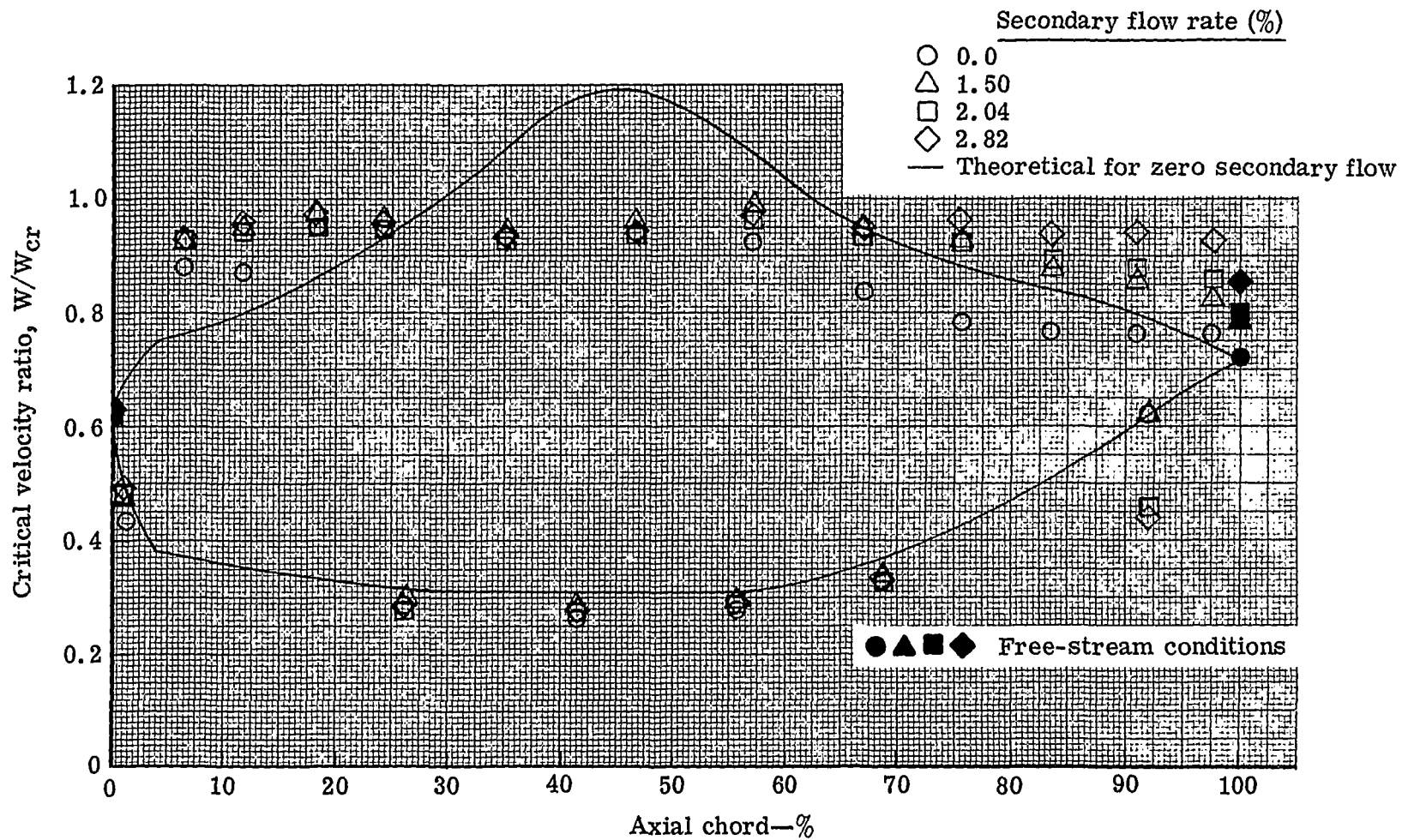
5315IV-7

Figure 7. Measured and predicted surface critical velocity ratio distribution for the jet-flapped blade (tip section)—0.022-in. jet slot.



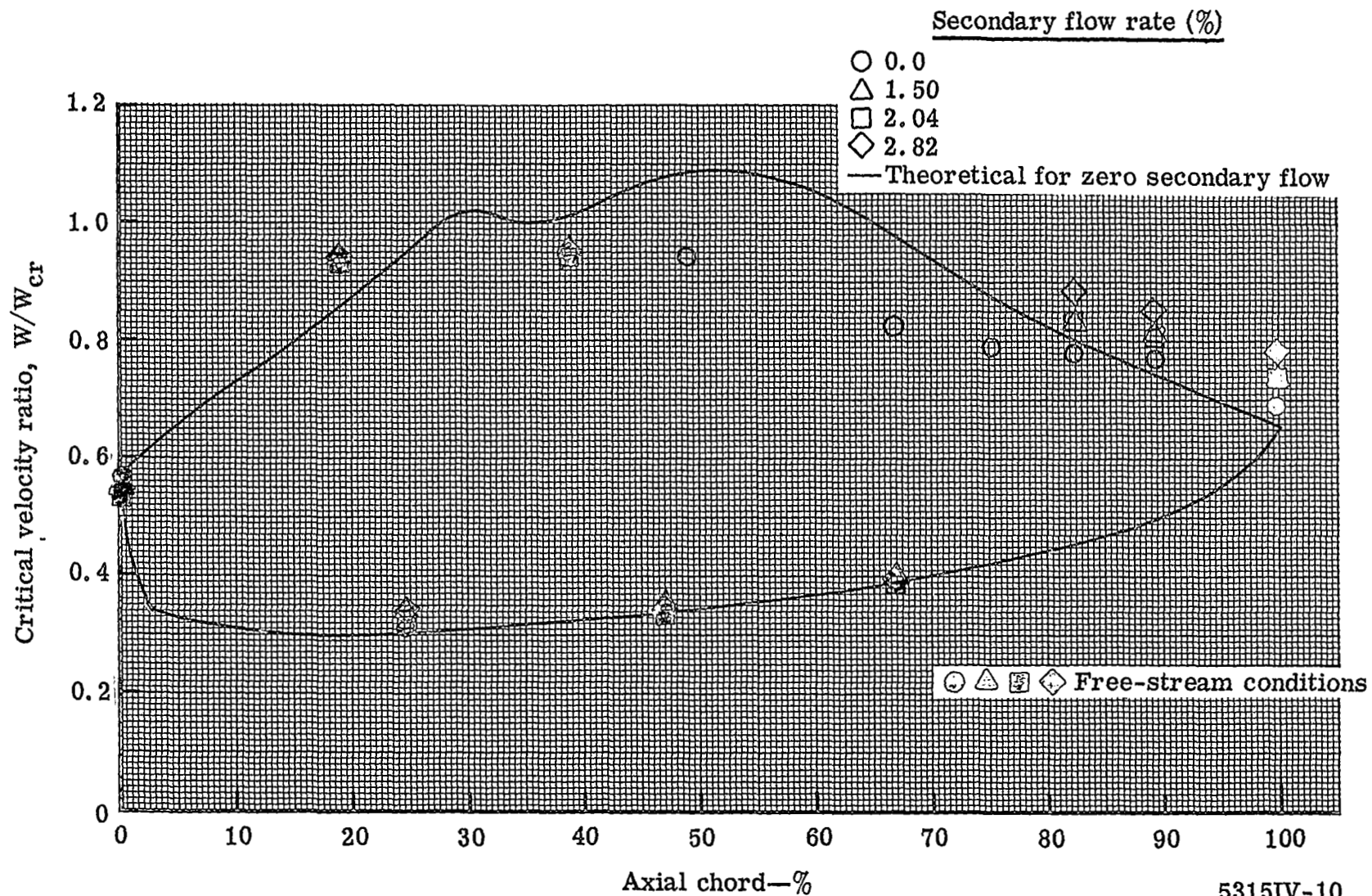
5315IV-8

Figure 8. Measured and predicted surface critical velocity ratio distribution for the jet-flapped blade (hub section)—0.031-in. jet slot.



5315IV-9

Figure 9. Measured and predicted surface critical velocity ratio distribution for the jet-flapped blade (mean section)—0.031-in. jet slot.



5315IV-10

Figure 10. Measured and predicted surface critical velocity ratio distribution for the jet-flapped blade (tip section)—0.031-in. jet slot.

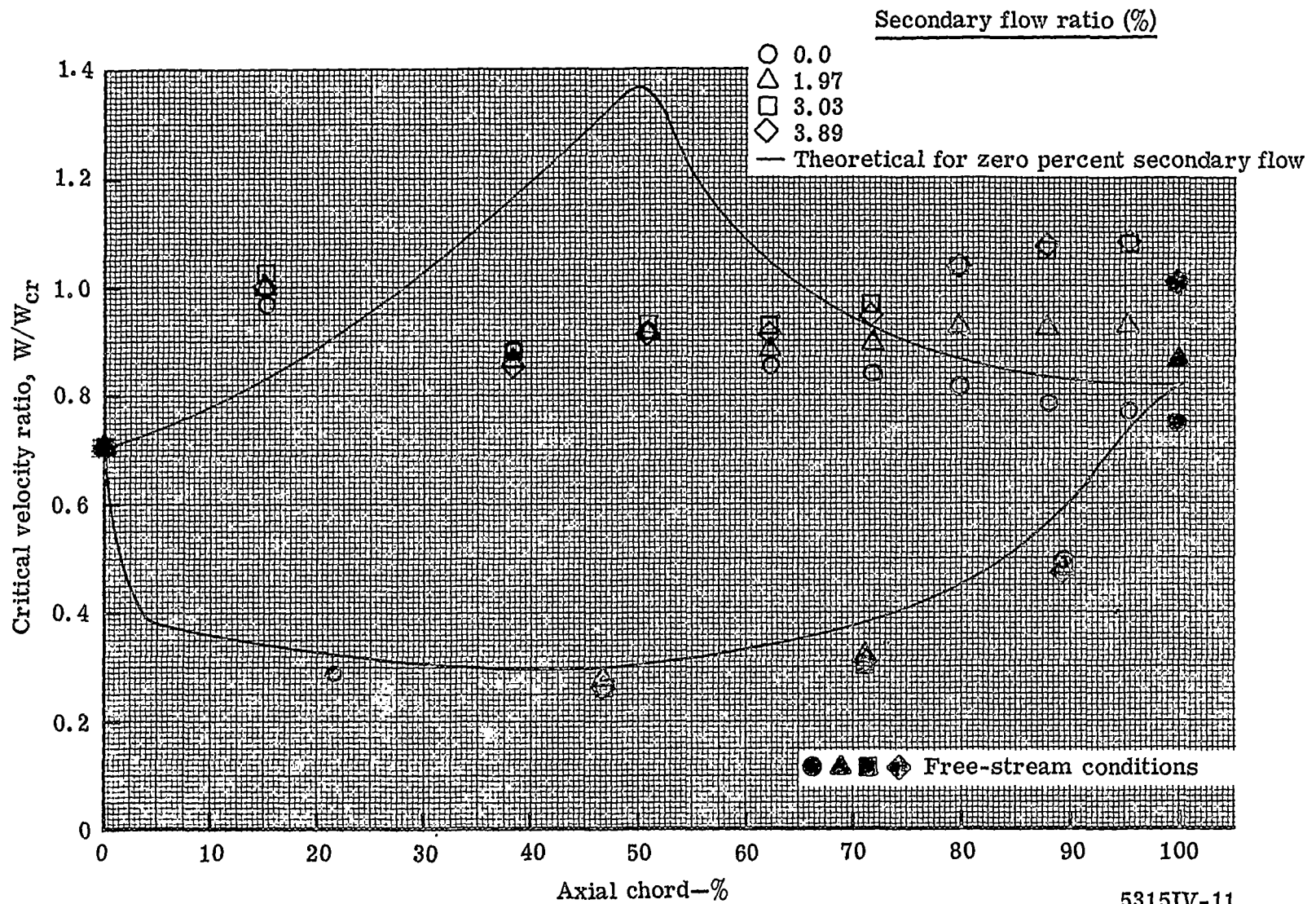
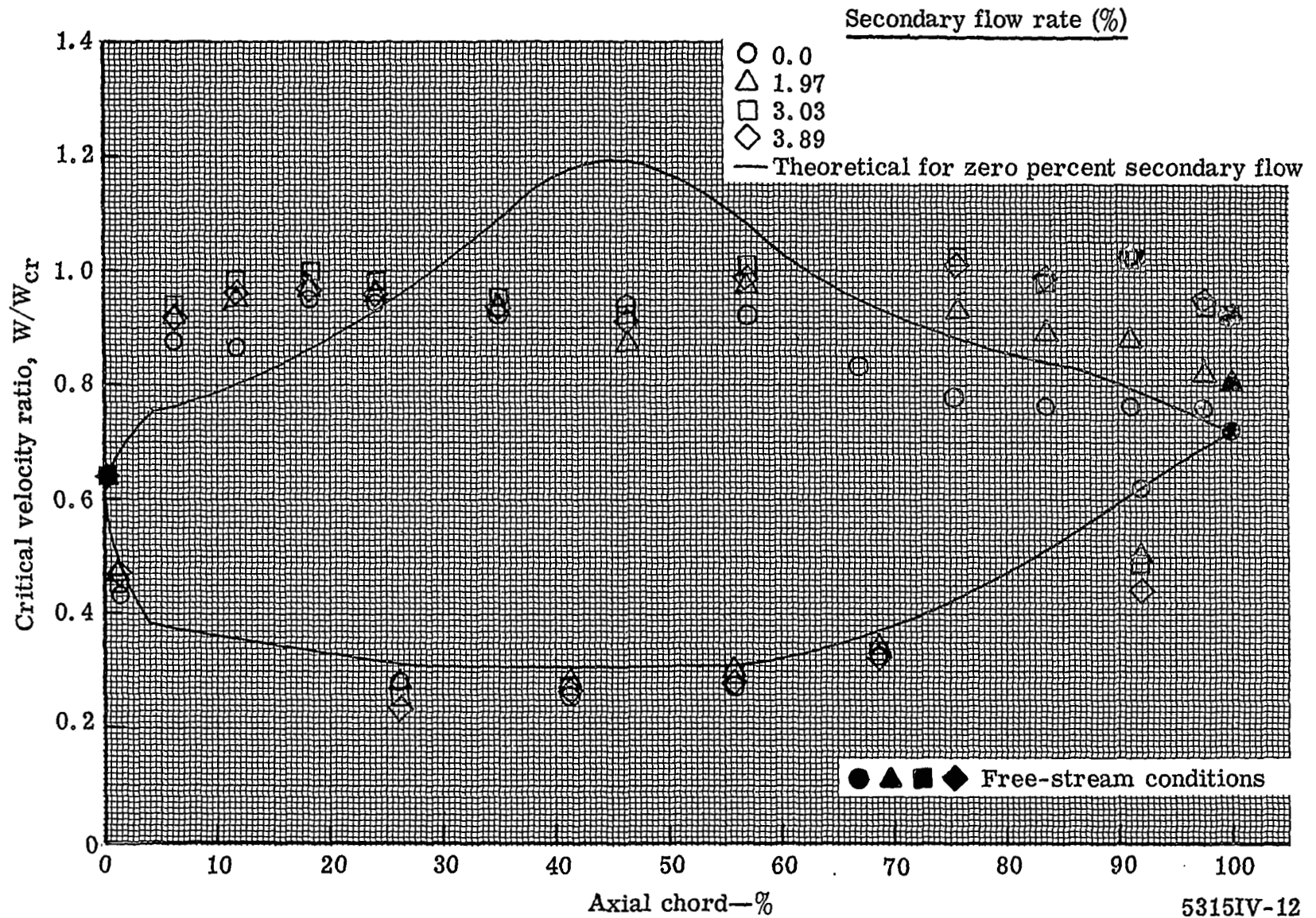
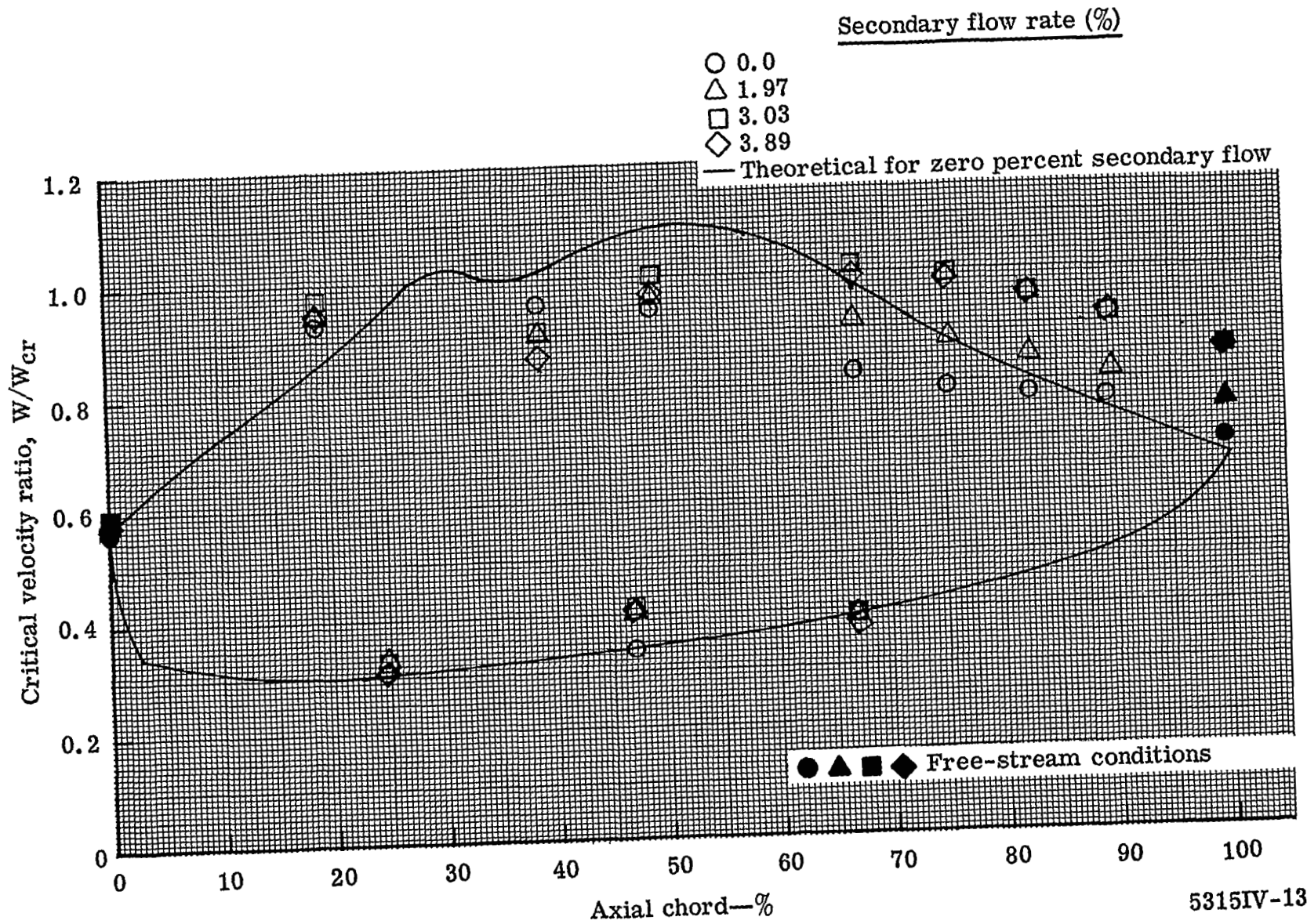


Figure 11. Measured and predicted surface critical velocity ratio distribution for the jet-flapped blade (hub section)—0.040-in. jet slot.



5315IV-12

Figure 12. Measured and predicted surface critical velocity ratio distribution for the jet-flapped blade (mean section)—0.040-in. jet slot.



5315IV-13

Figure 13. Measured and predicted surface critical velocity ratio distribution for the jet-flapped blade (tip section)—0.040-in. jet slot.

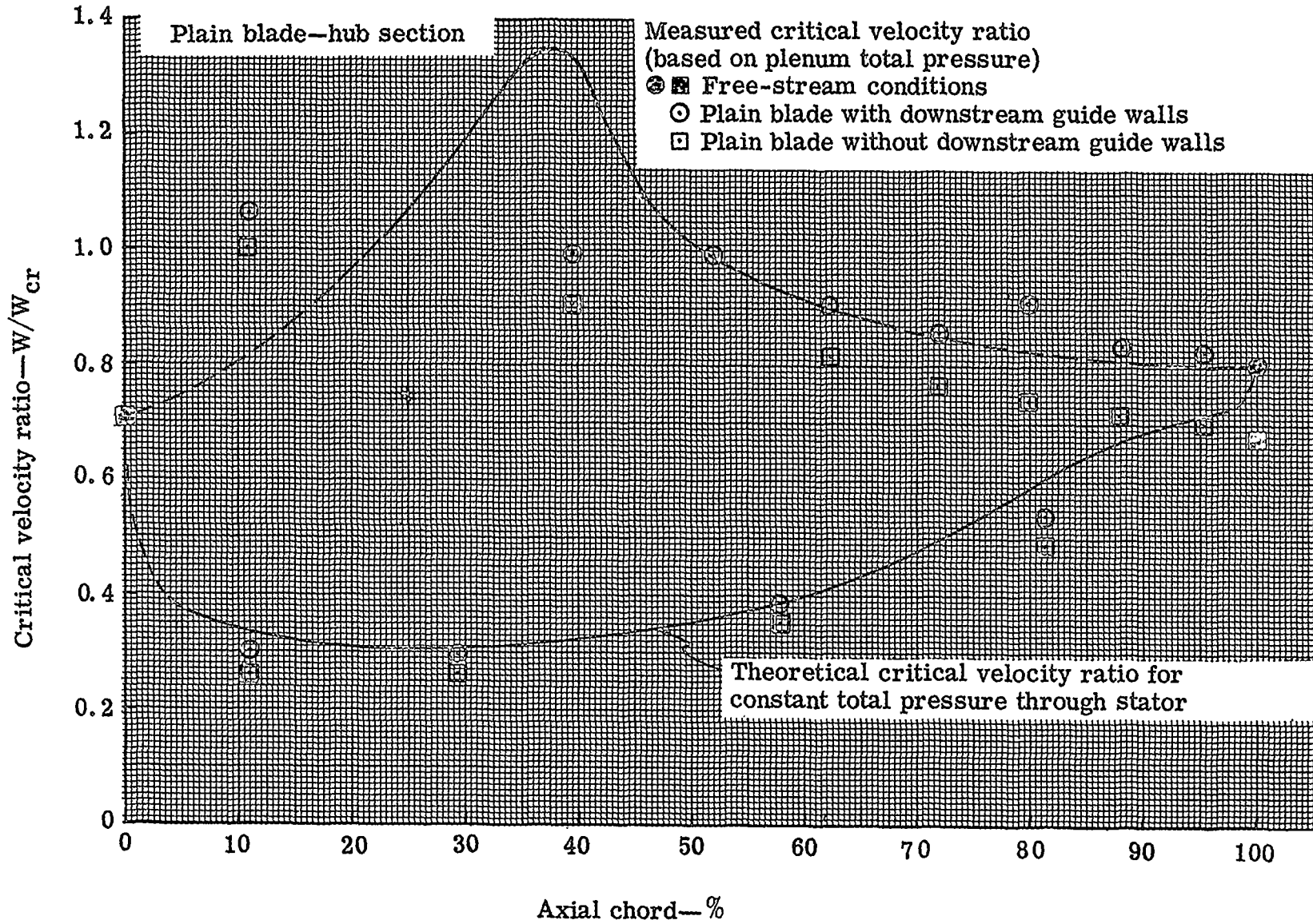


Figure 14. Measured and predicted surface critical velocity ratio distribution for plain blade hub section

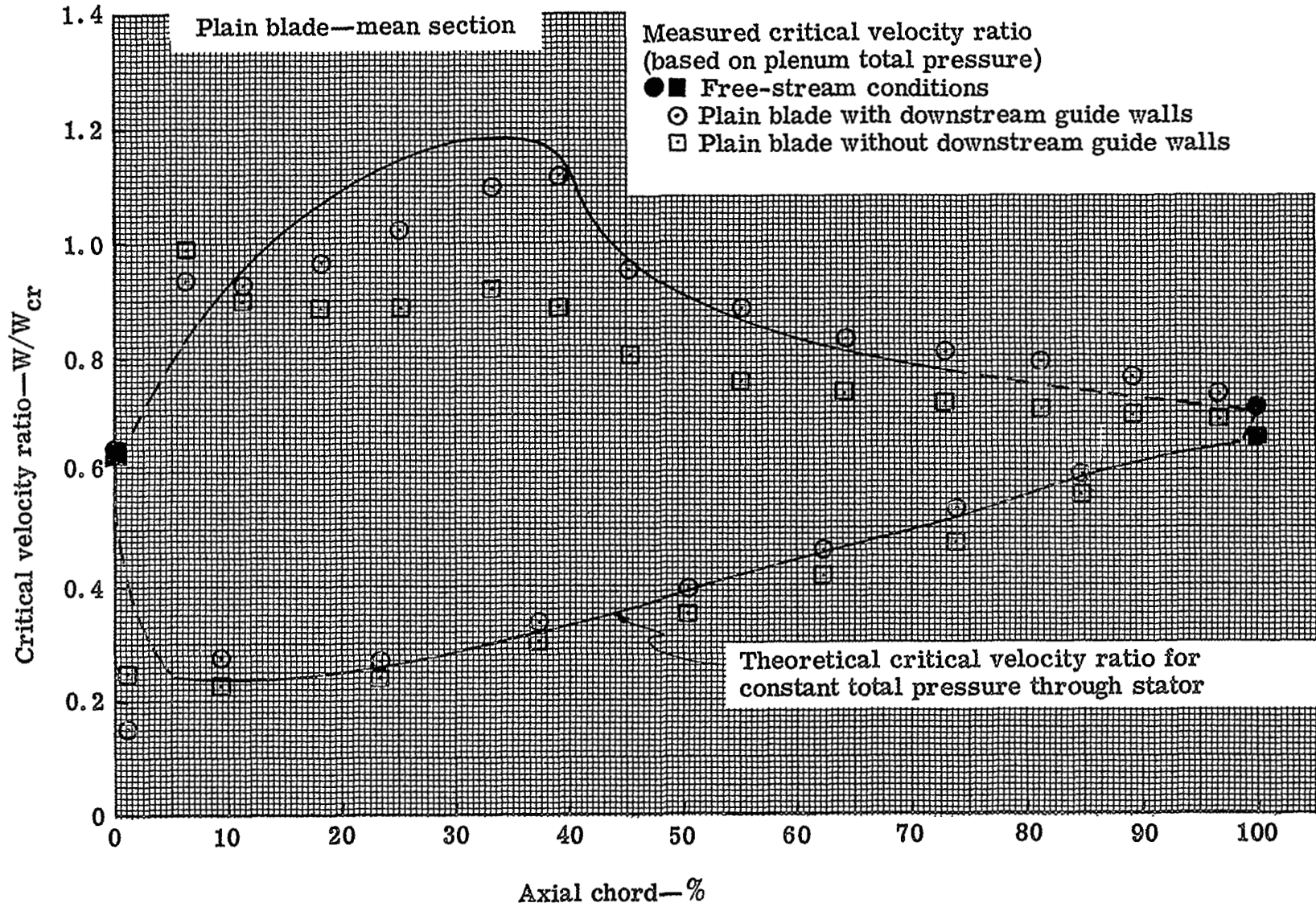


Figure 15. Measured and predicted surface critical velocity ratio distribution for plain blade mean section.

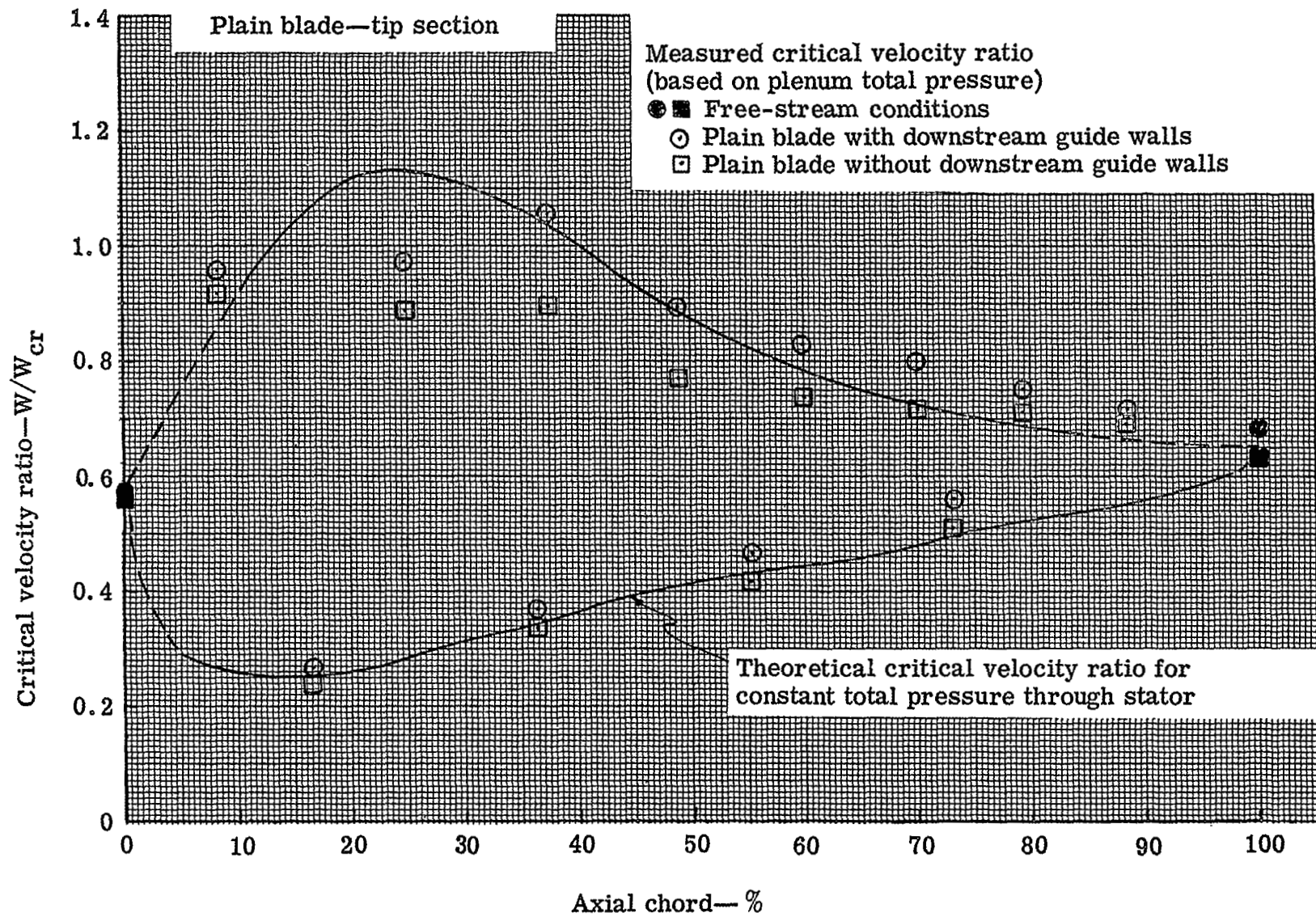
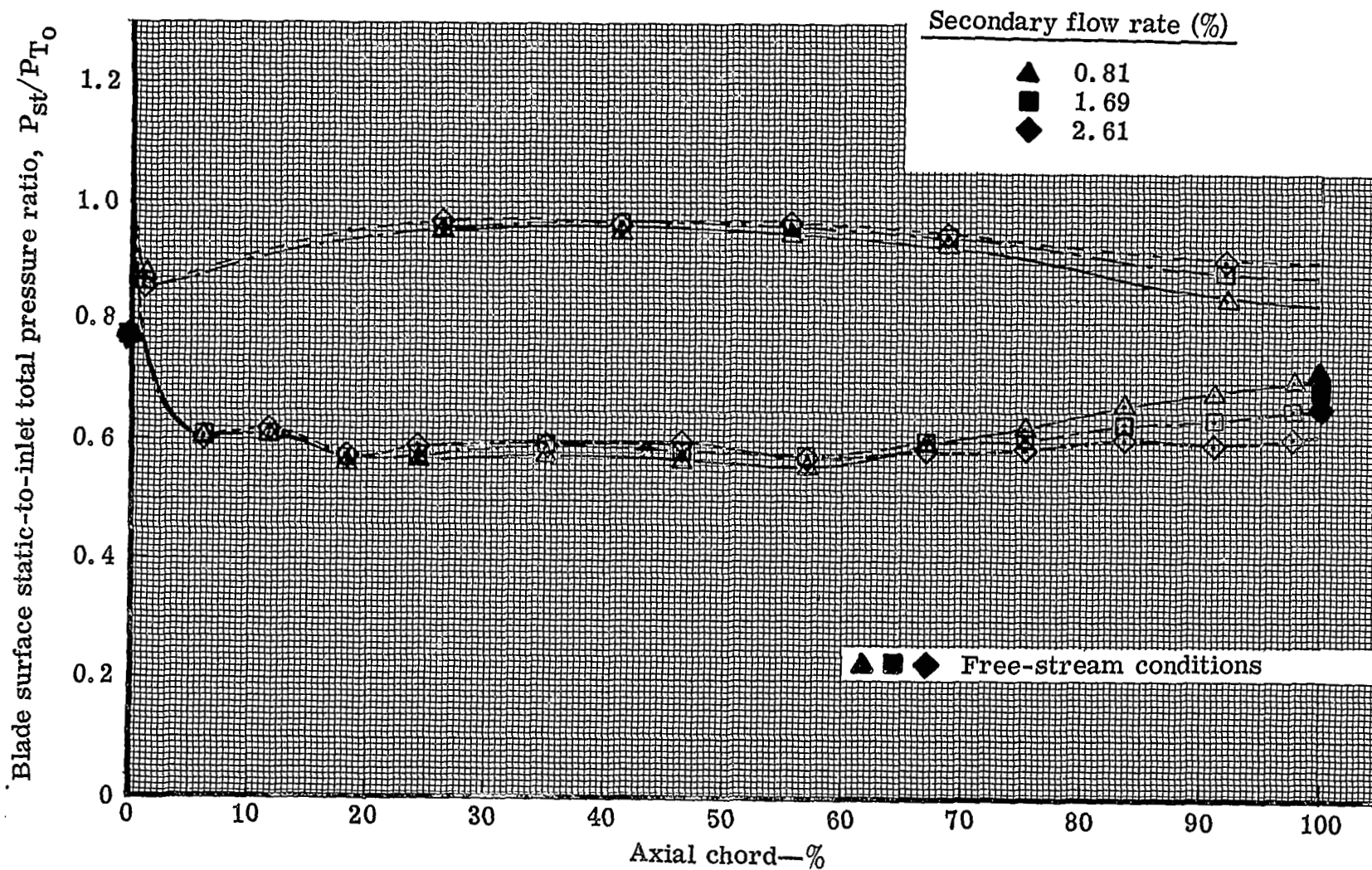
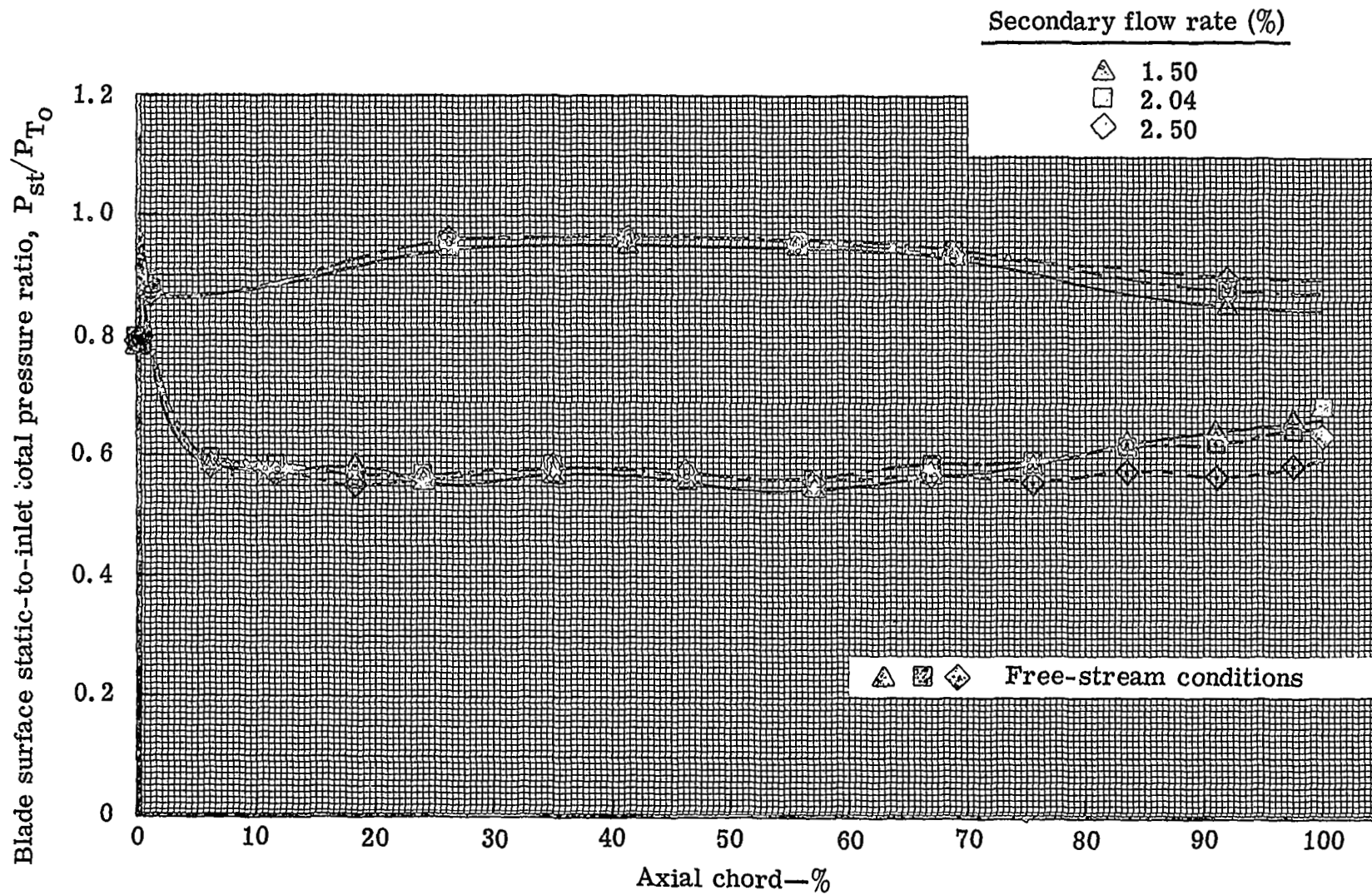


Figure 16. Measured and predicted surface critical velocity ratio distribution for plain blade tip section.



5315IV-17

Figure 17. Measured surface static pressure distribution for the jet-flapped blade (mean section)-0.022-in. jet slot.



5315IV-18

Figure 18. Measured surface static pressure distribution for the jet-flapped blade (mean section)—0.031-in. jet slot.

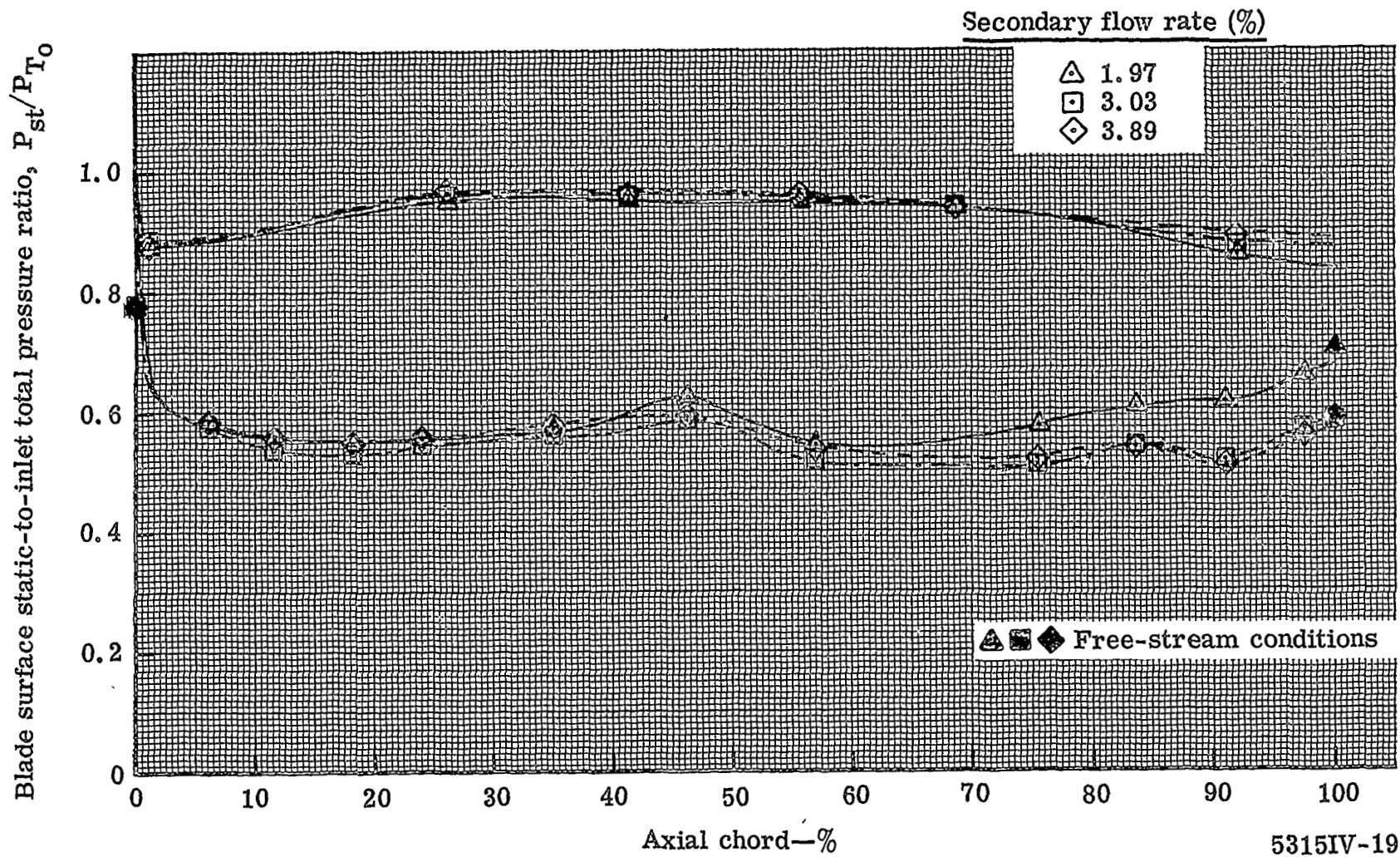
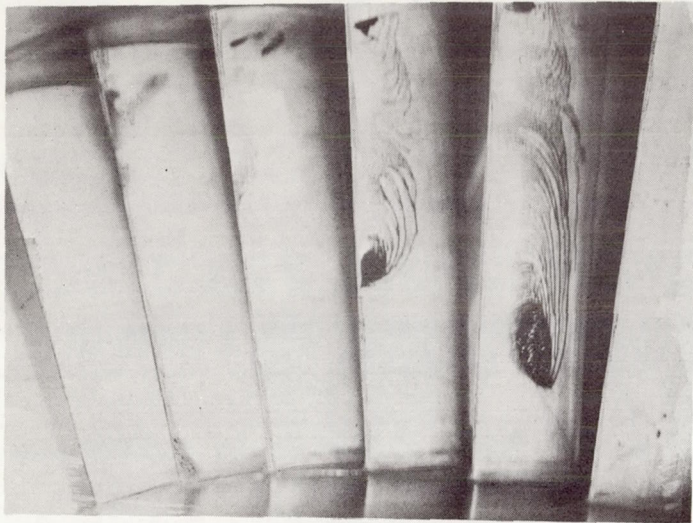
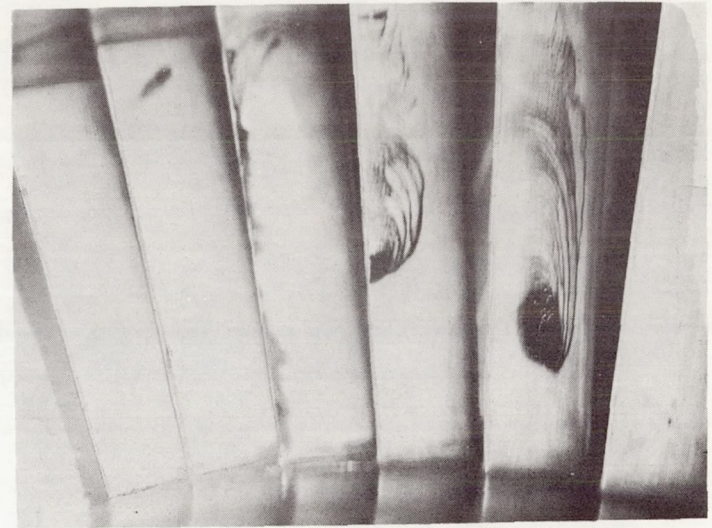


Figure 19. Measured surface static pressure distribution for the jet-flapped blade (mean section)—0.040-in. jet slot.



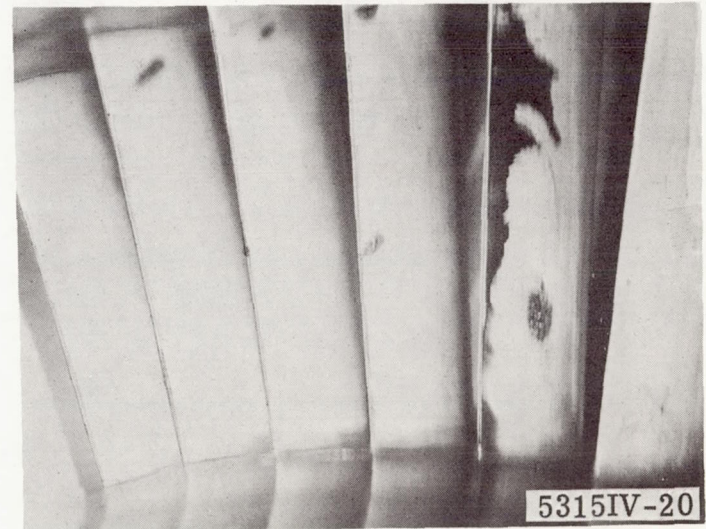
Vane No. 2



Vane No. 3



Vane No. 4

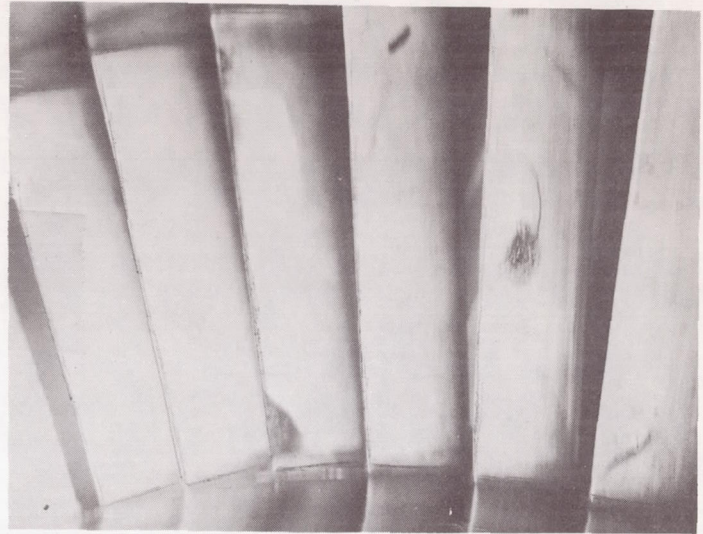


Vane No. 5

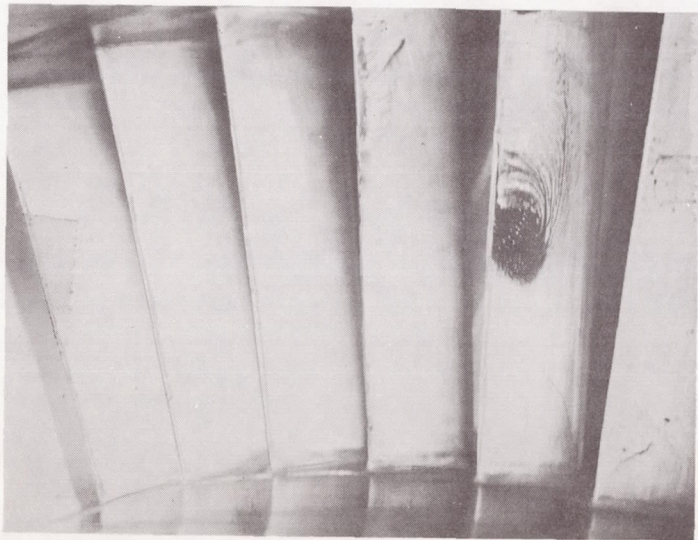
Figure 20. Flow visualization results for the jet-flapped blade with 0.022-in. jet slot and 0.81% secondary flow ($C_{jm} = 0.0133$).



Vane No. 2



Vane No. 3

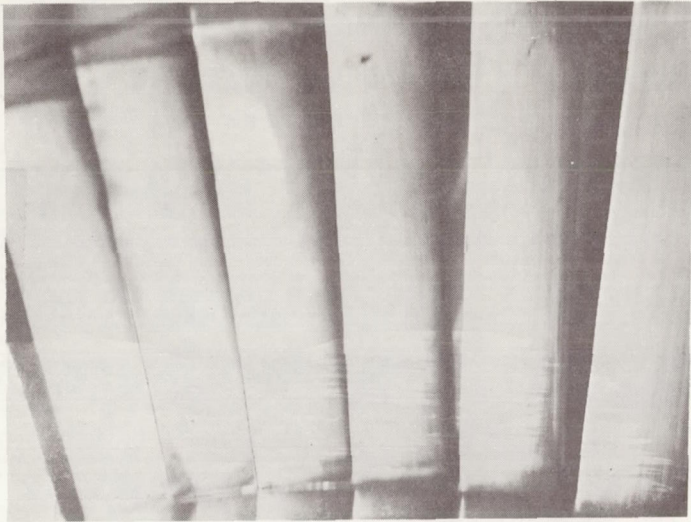


Vane No. 4

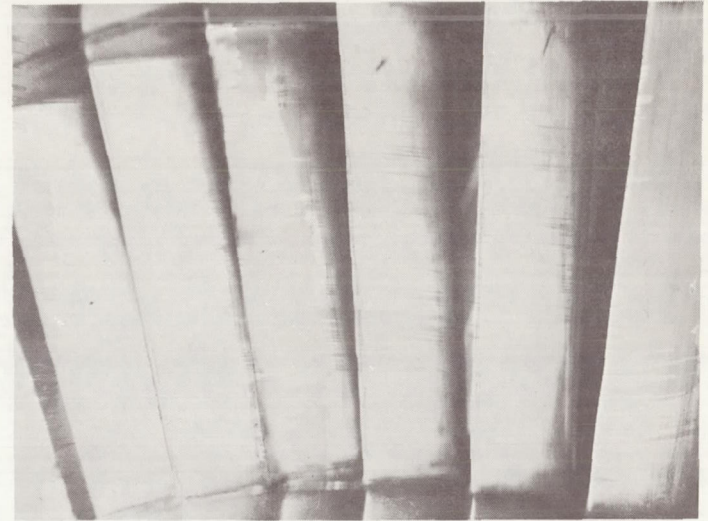


Vane No. 5

Figure 21. Flow visualization results for the jet-flapped blade with 0.022-in. jet slot and 1.69% secondary flow ($C_{jm} = 0.0355$).



Vane No. 2



Vane No. 3

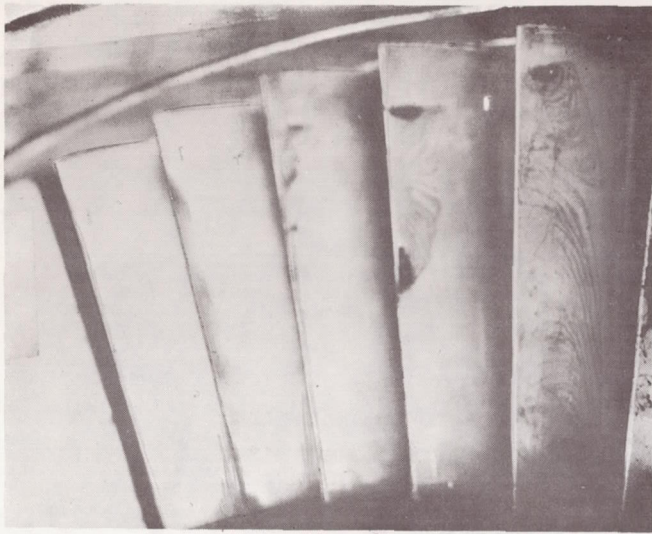


Vane No. 4

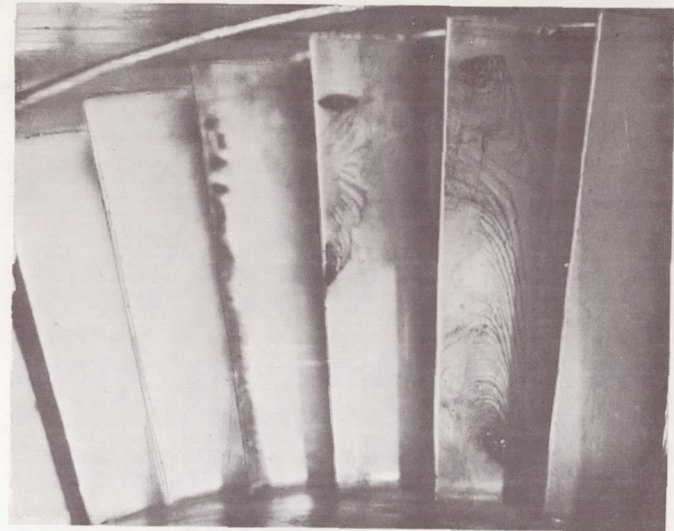


Vane No. 5

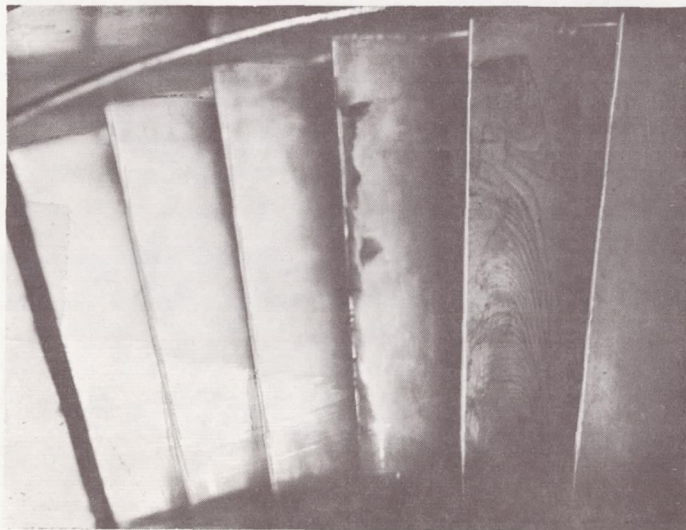
Figure 22. Flow visualization results for the jet-flapped blade with 0.022-in. jet slot and 2.61% secondary flow ($C_{jm} = 0.0619$).



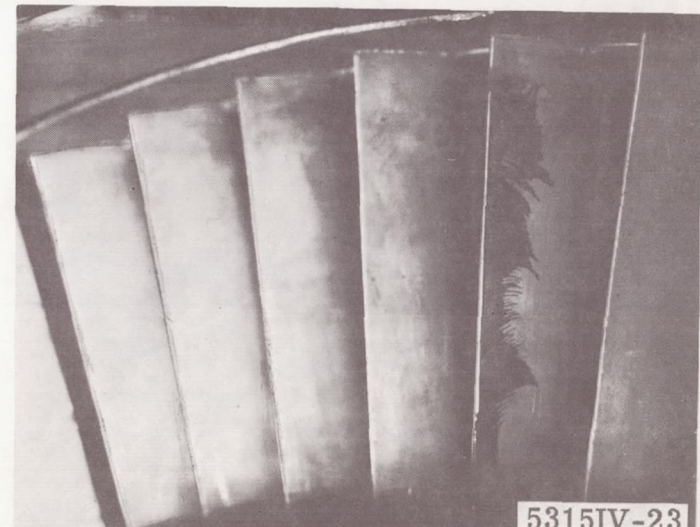
Vane No. 2



Vane No. 3



Vane No. 4



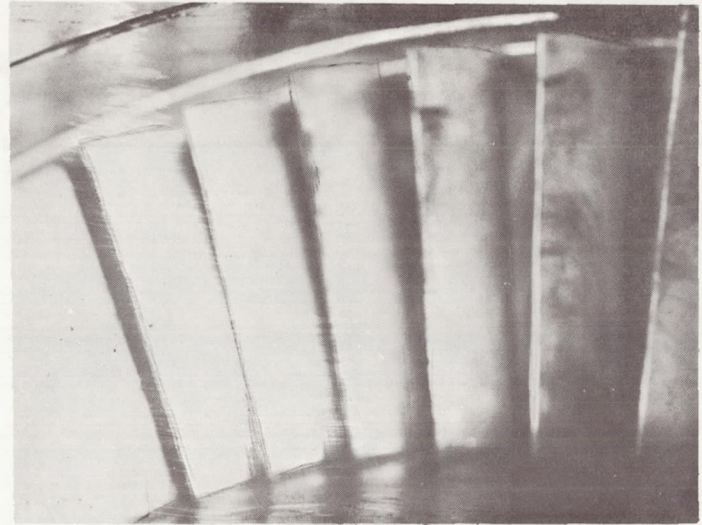
Vane No. 5

5315IV-23

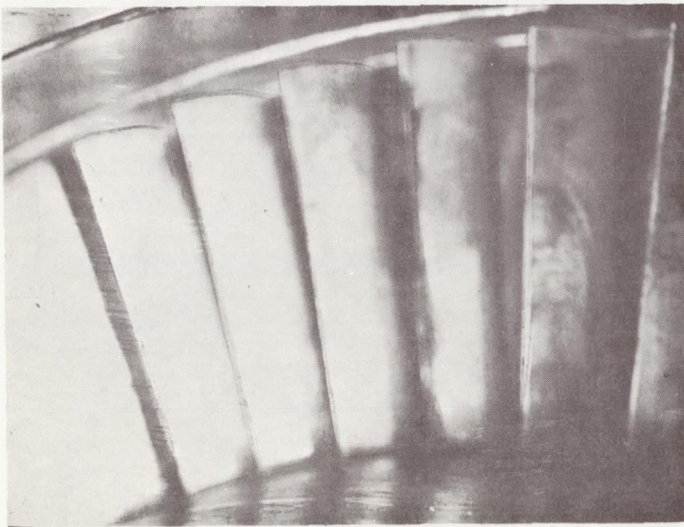
Figure 23. Flow visualization results for the jet-flapped blade with 0.031-in. jet slot and 1.50% secondary flow ($C_{j_m} = 0.0297$).



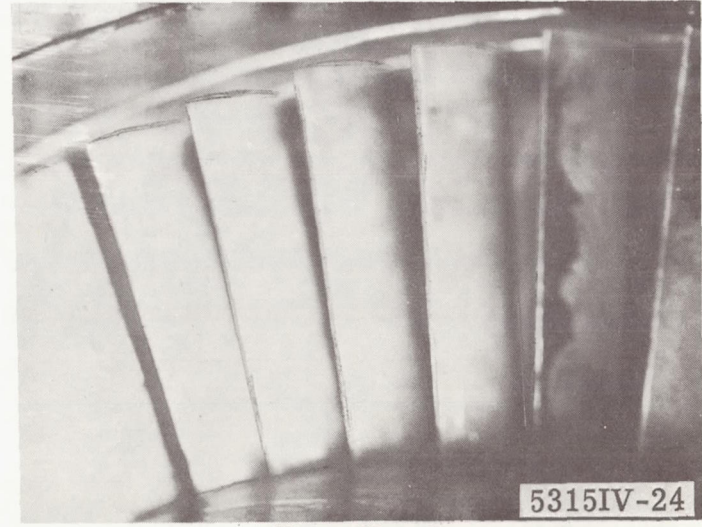
Vane No. 2



Vane No. 3



Vane No. 4

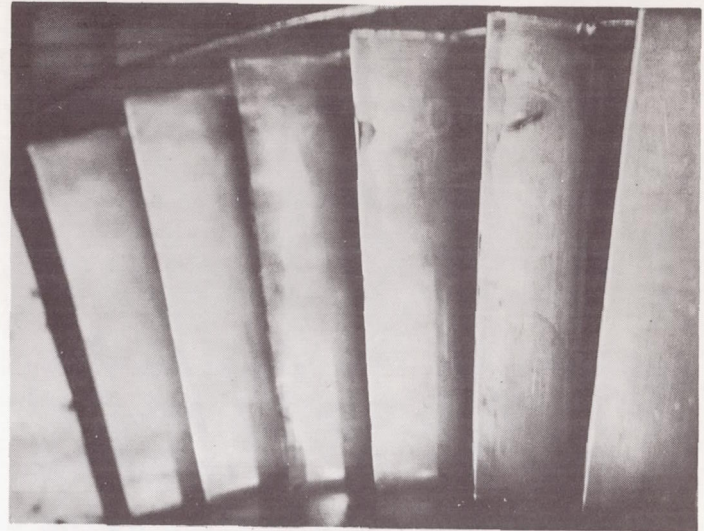


Vane No. 5

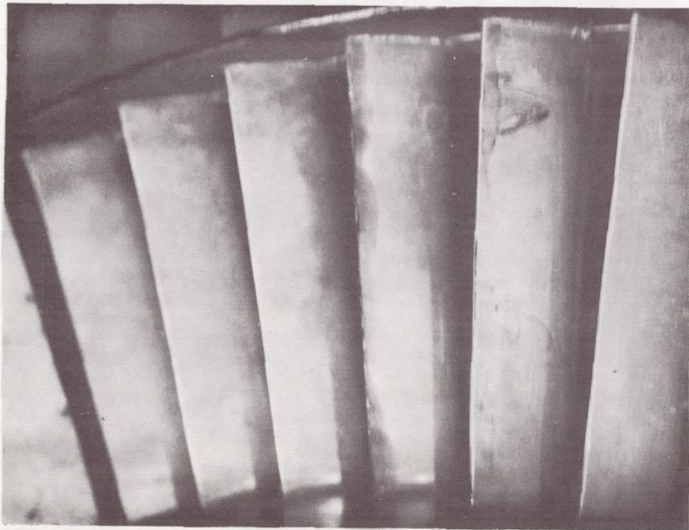
Figure 24. Flow visualization results for the jet-flapped blade with 0.031-in. jet slot and 2.04% secondary flow ($C_{j_m} = 0.0450$).



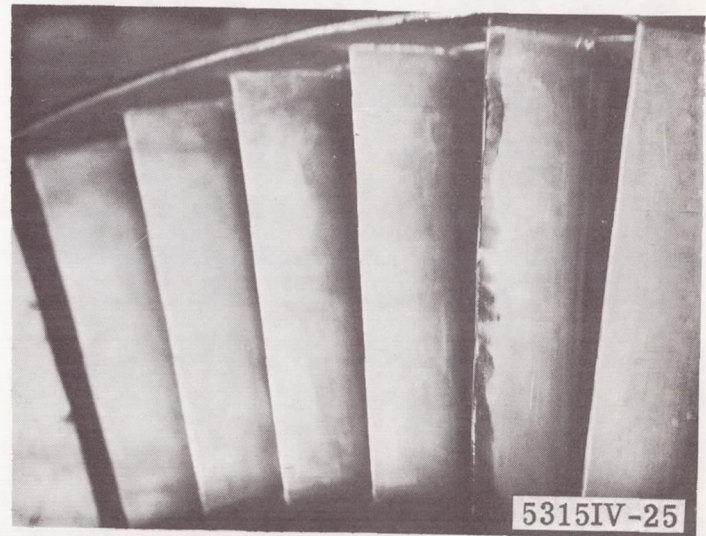
Vane No. 2



Vane No. 4



Vane No. 3



Vane No. 5

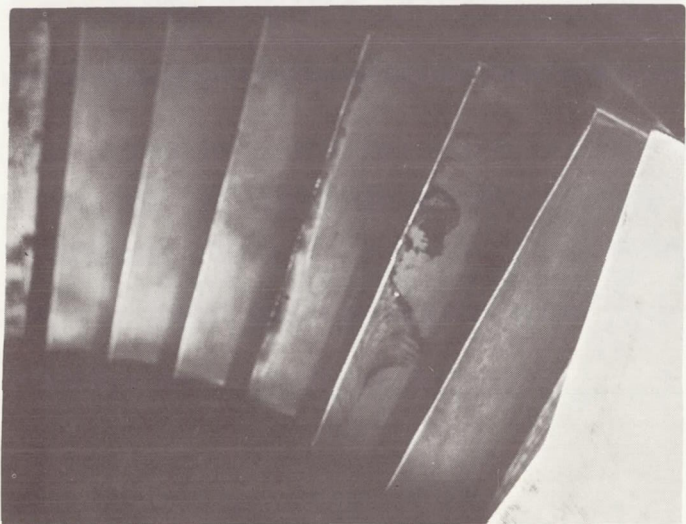
Figure 25. Flow visualization results for the jet-flapped blade with 0.031-in. jet slot and 2.82% secondary flow ($C_{jm} = 0.0671$).



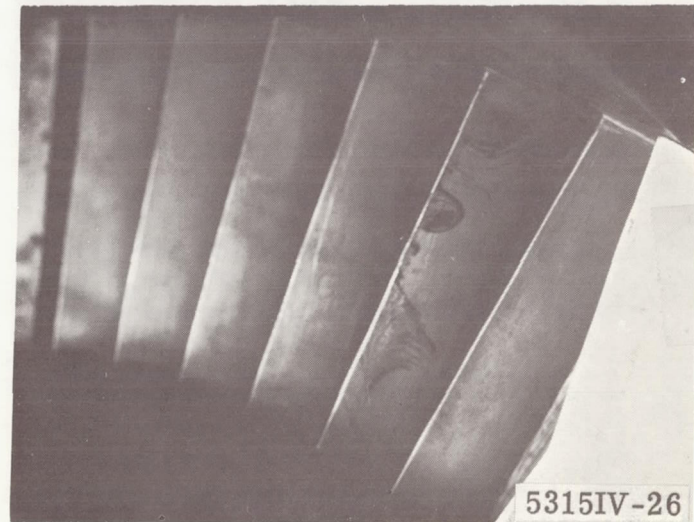
Vane No. 2



Vane No. 3



Vane No. 4

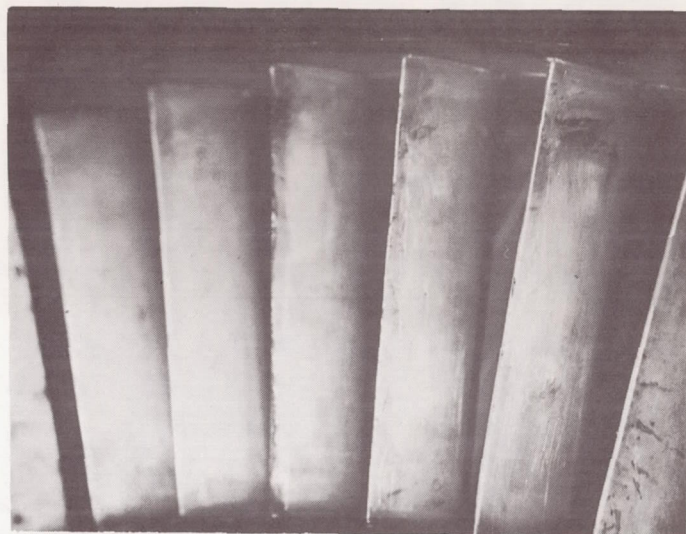


Vane No. 5

Figure 26. Flow visualization results for the jet-flapped blade with 0.040-in. jet slot and 1.97% secondary flow ($C_{j_m} = 0.0406$).



Vane No. 2



Vane No. 3

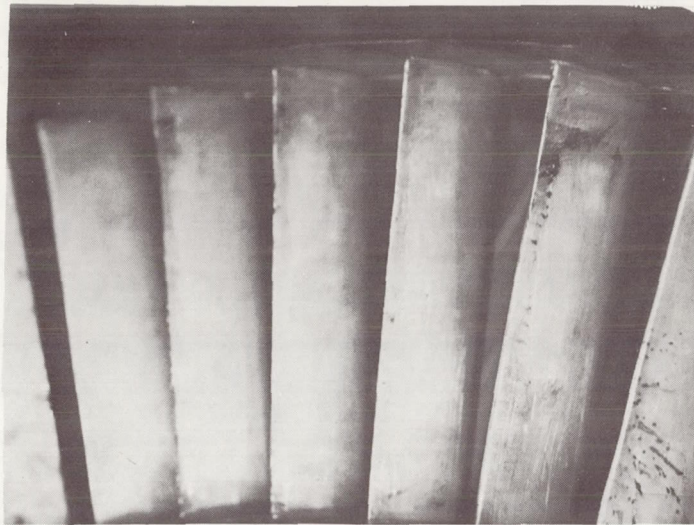


Vane No. 4



Vane No. 5

Figure 27. Flow visualization results for the jet-flapped blade with 0.040-in. jet slot and 3.03% secondary flow ($C_{j_m} = 0.0651$).



Vane No. 2



Vane No. 3

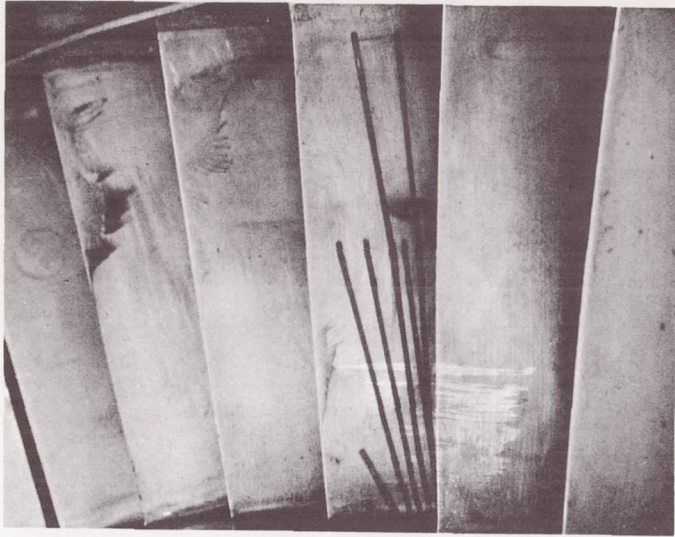


Vane No. 4

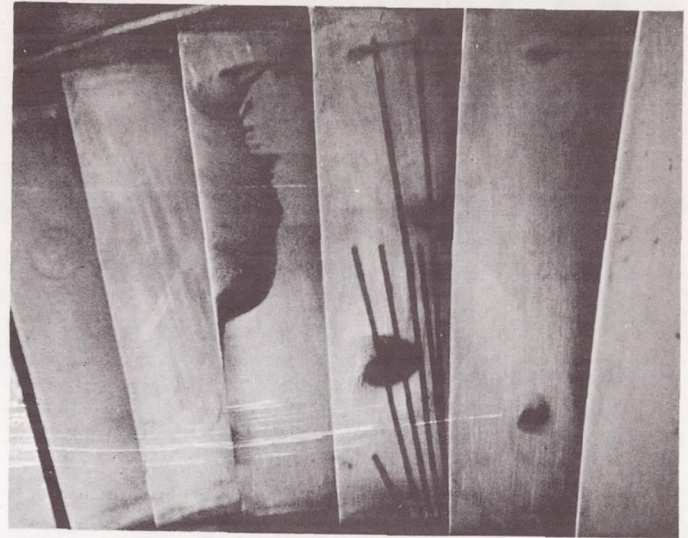


Vane No. 5

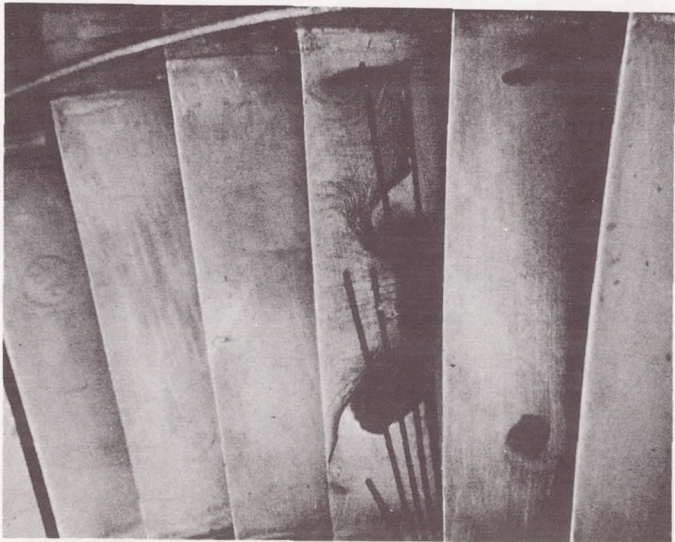
Figure 28. Flow visualization results for the jet-flapped blade with 0.040-in. jet slot and 3.89% secondary flow ($C_{j_m} = 0.0823$).



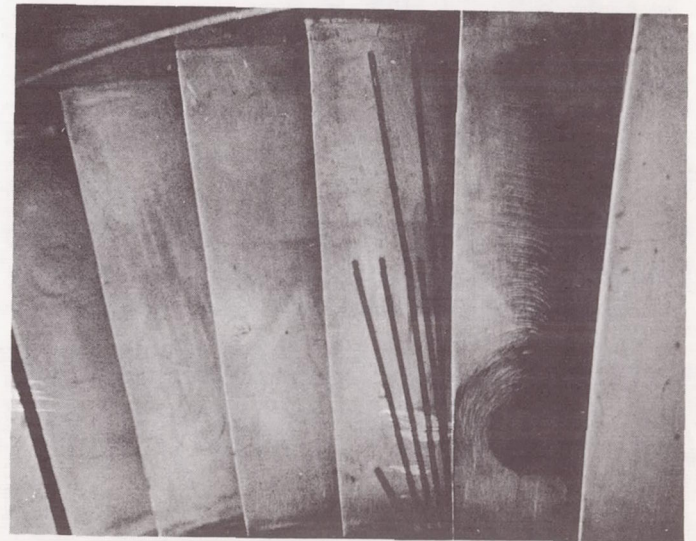
Vane No. 2



Vane No. 3



Vane No. 4



Vane No. 5

Figure 29. Plain blade flow visualization results for inlet hub static-to-total pressure ratio of 0.74 (design value).

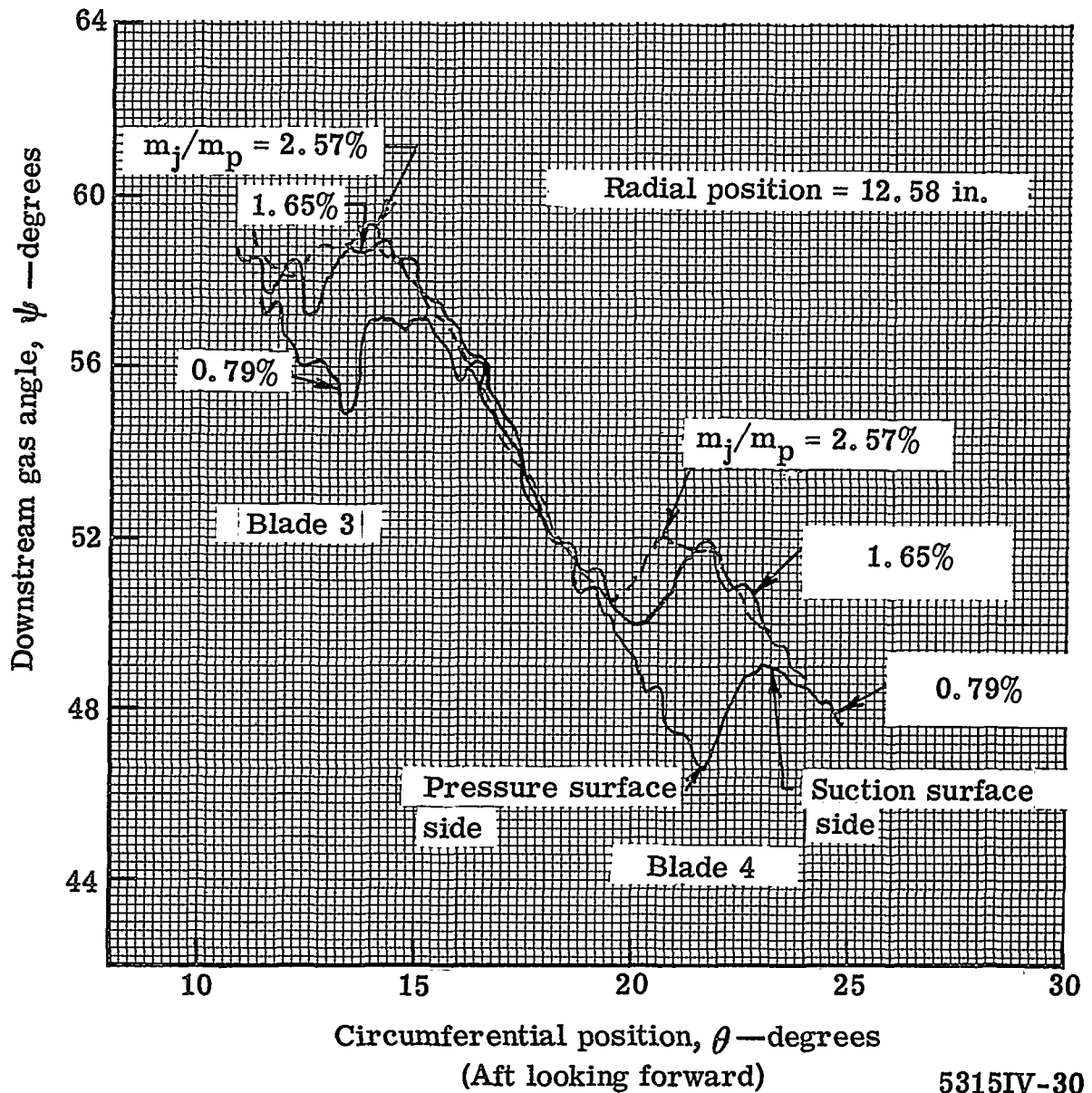
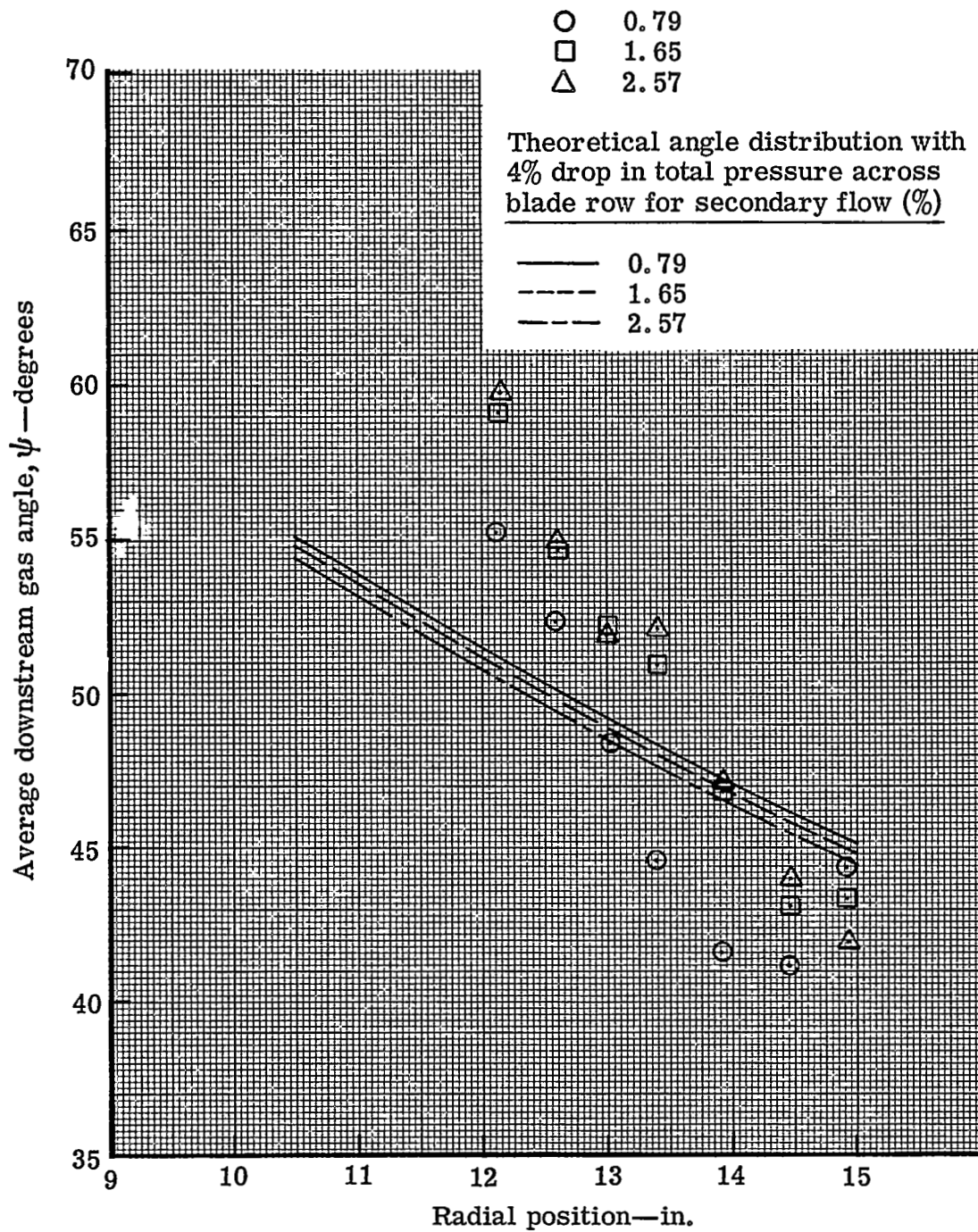


Figure 30. Circumferential variation of downstream gas angle with secondary flow rate at 12.58-in. radial position for 0.022-in. slot.

Experimental results for secondary flow (%)



5315IV-31

Figure 31. Average measured and predicted radial variation of downstream gas angle for jet-flapped blade with 0.022-in. slot.

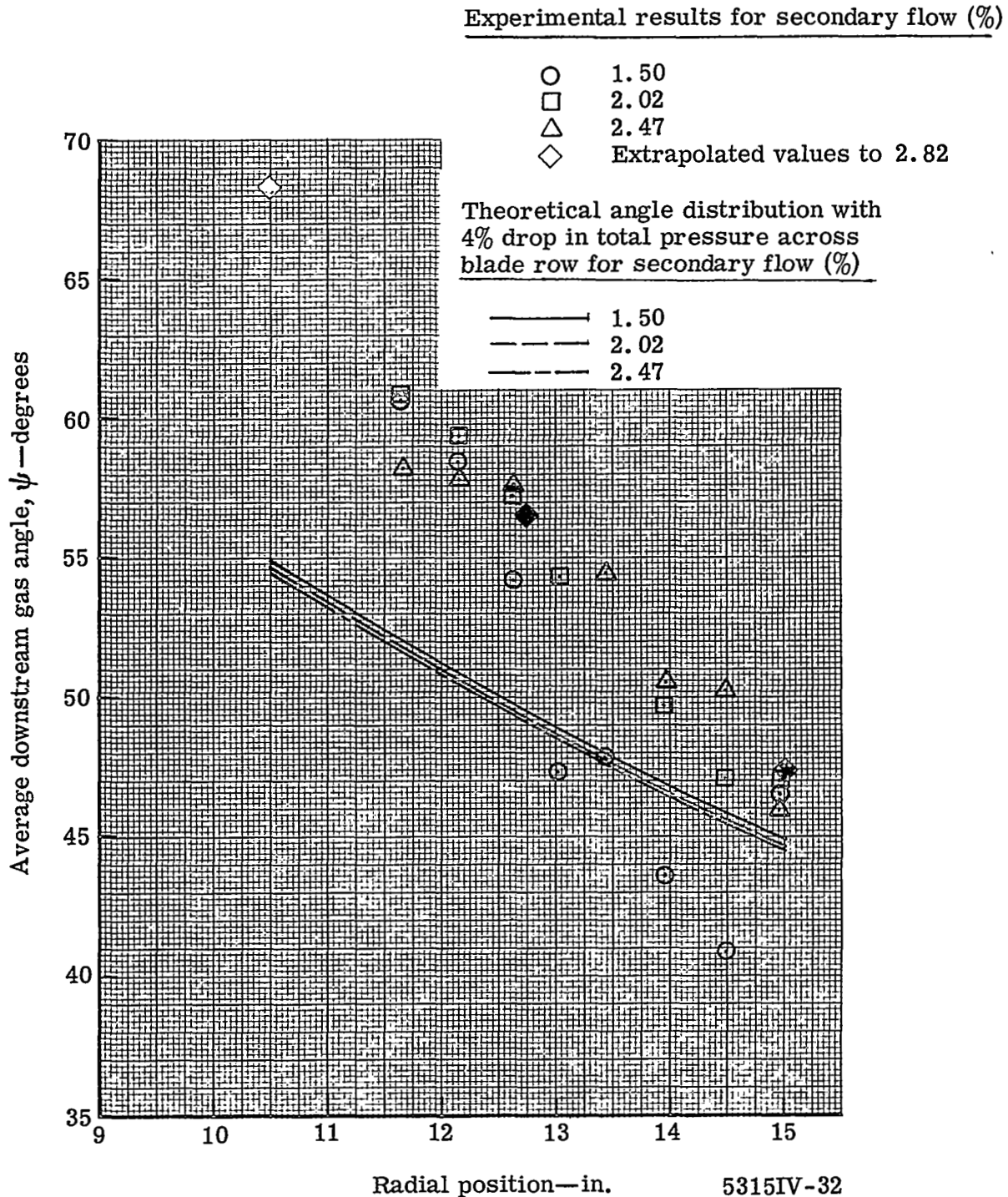


Figure 32. Average measured and predicted radial variation of downstream gas angle for jet-flapped blade with 0.031-in. slot.

Experimental results for secondary flow (%)

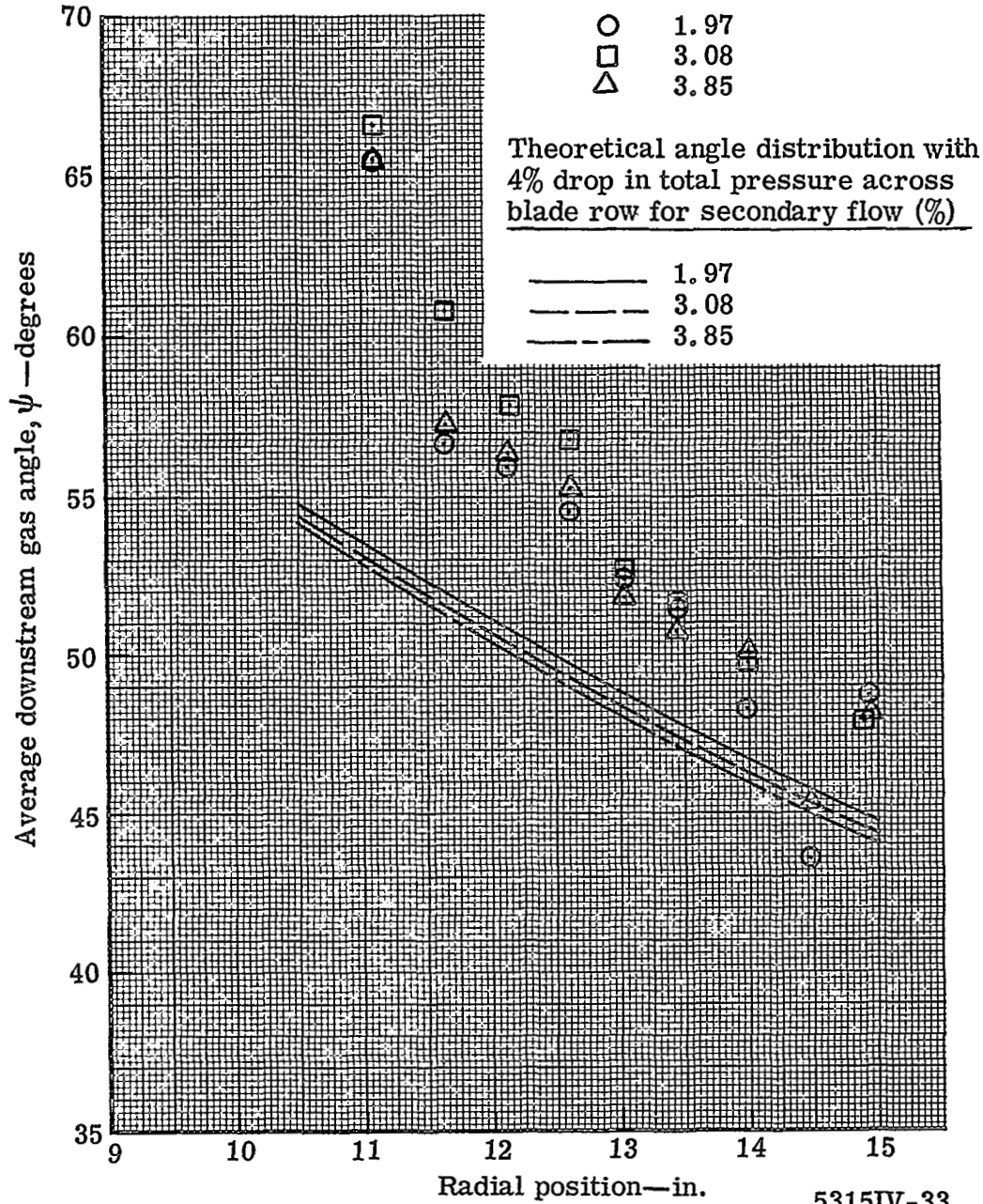
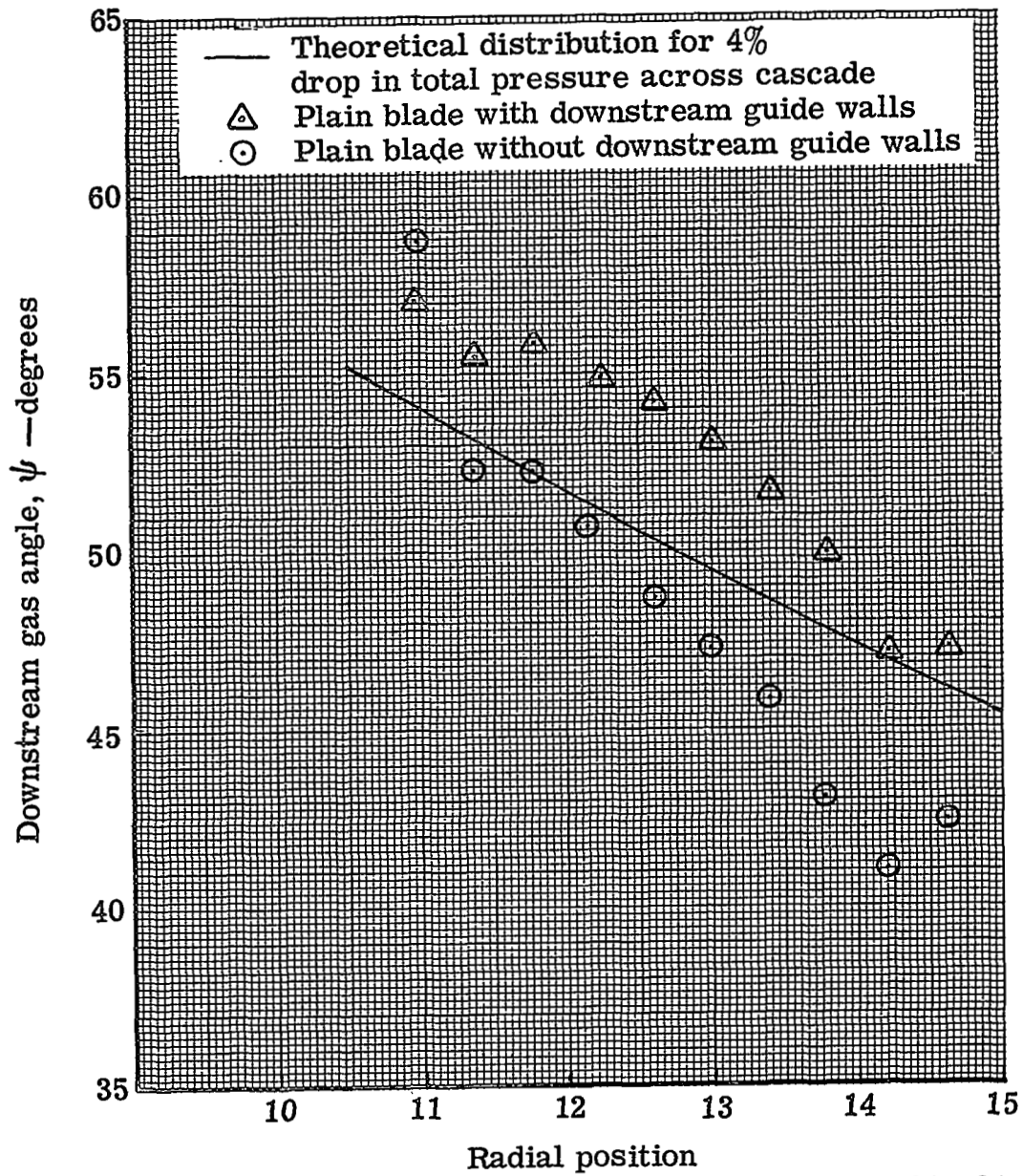
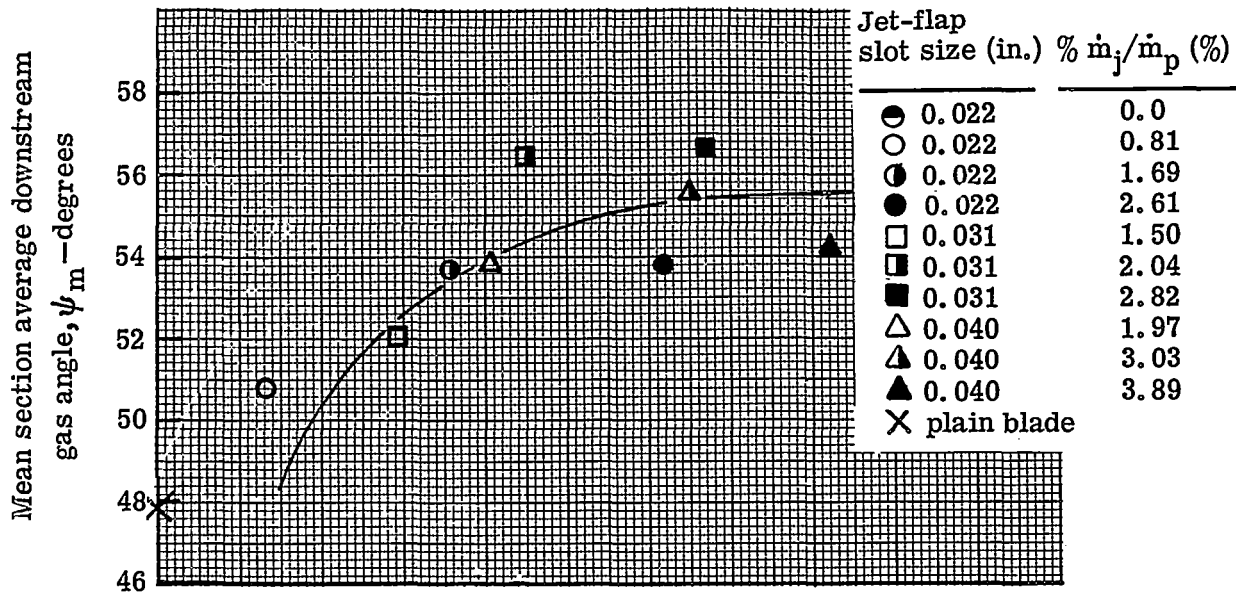


Figure 33. Average measured and predicted radial variation of downstream gas angle for jet-flapped blade with 0.040-in. slot.

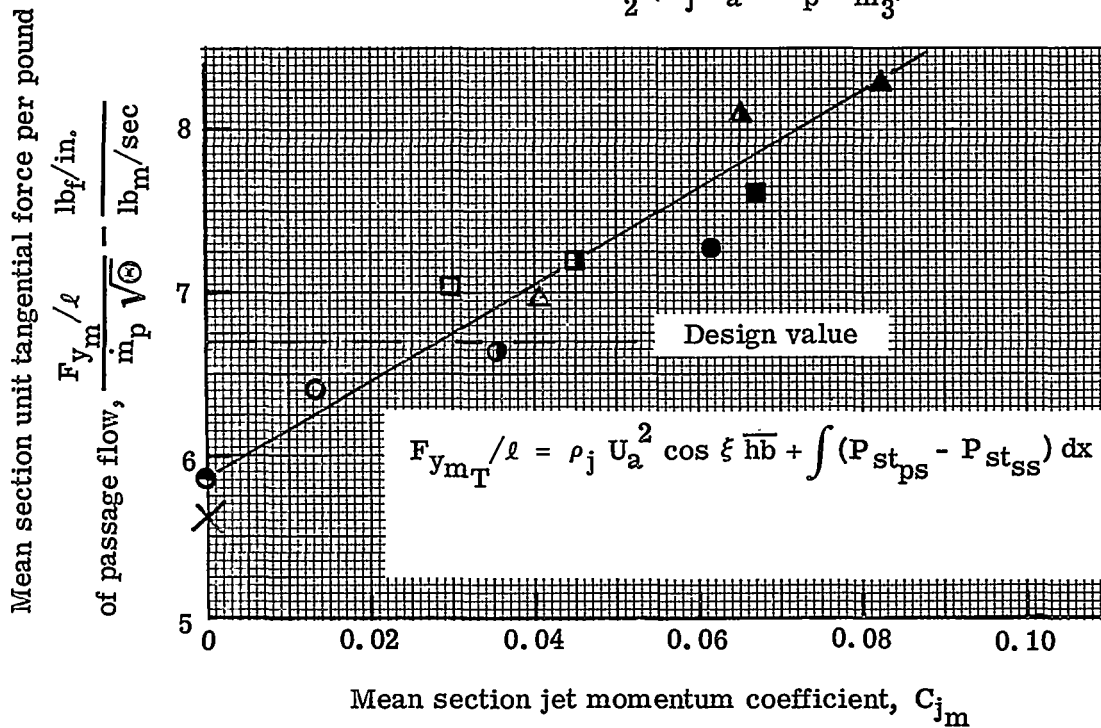


5315-20

Figure 34. Average measured and predicted radial variation of the plain blade downstream gas angle.



$$C_{j_m} = \frac{\dot{m}_j U_a}{\frac{1}{2} (\dot{m}_j U_a + \dot{m}_p W_{m_3})}$$



5315IV-35

Figure 35. Variation of mean section gas angle and blade force with jet momentum coefficient.

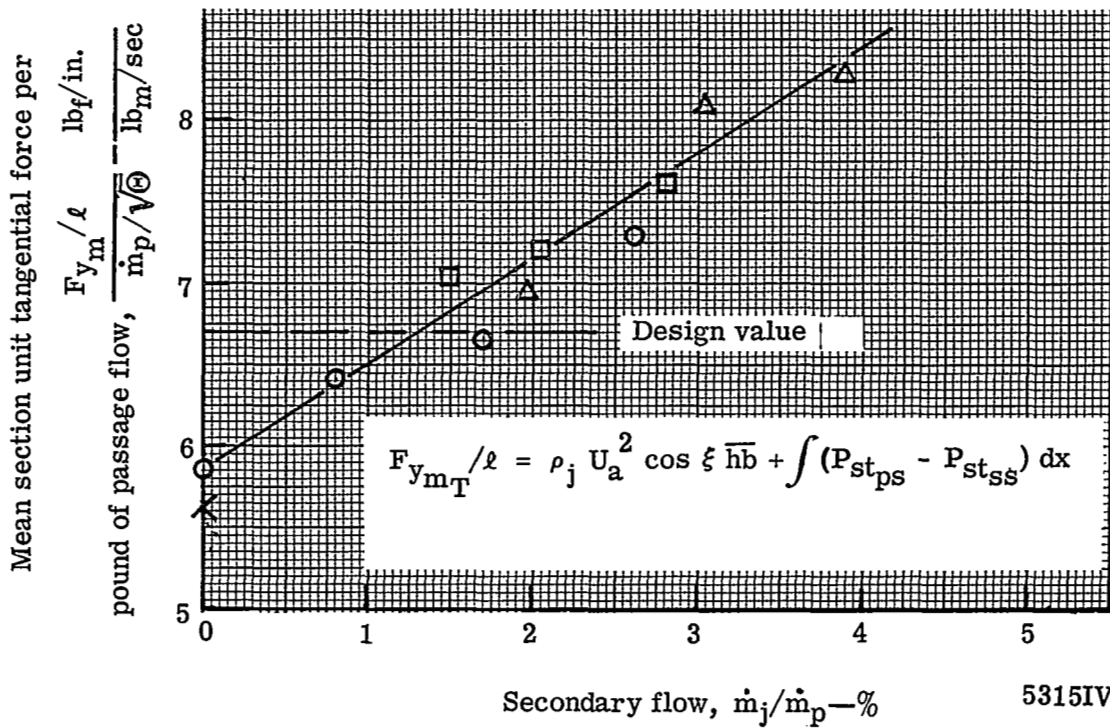
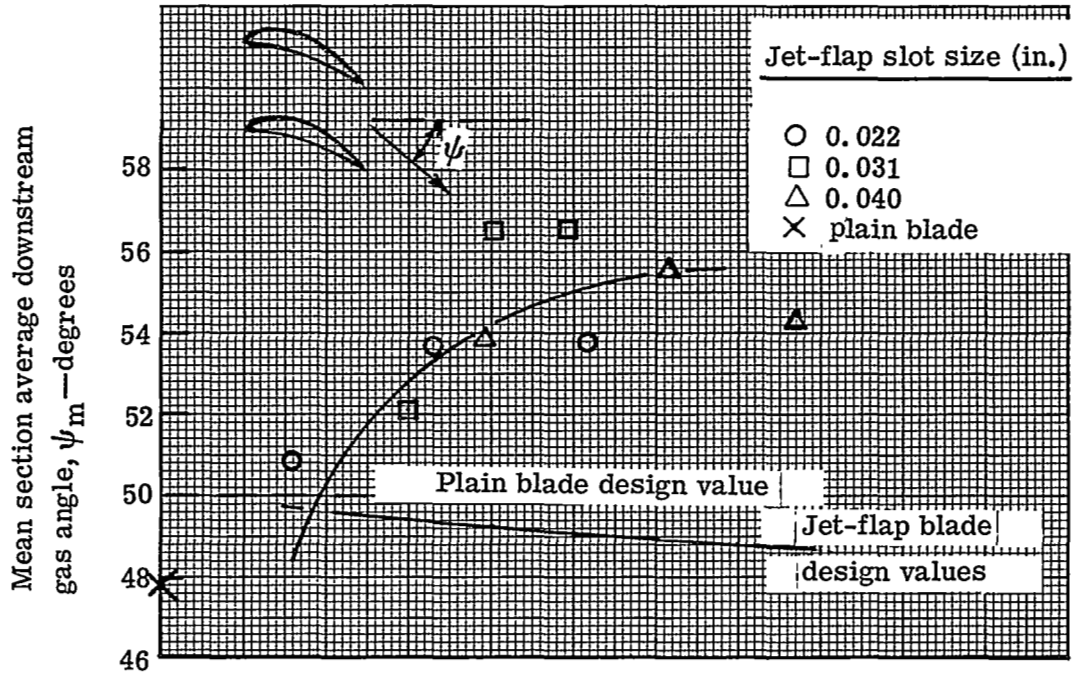


Figure 36. Variation of mean section gas angle and blade force with secondary flow rate.

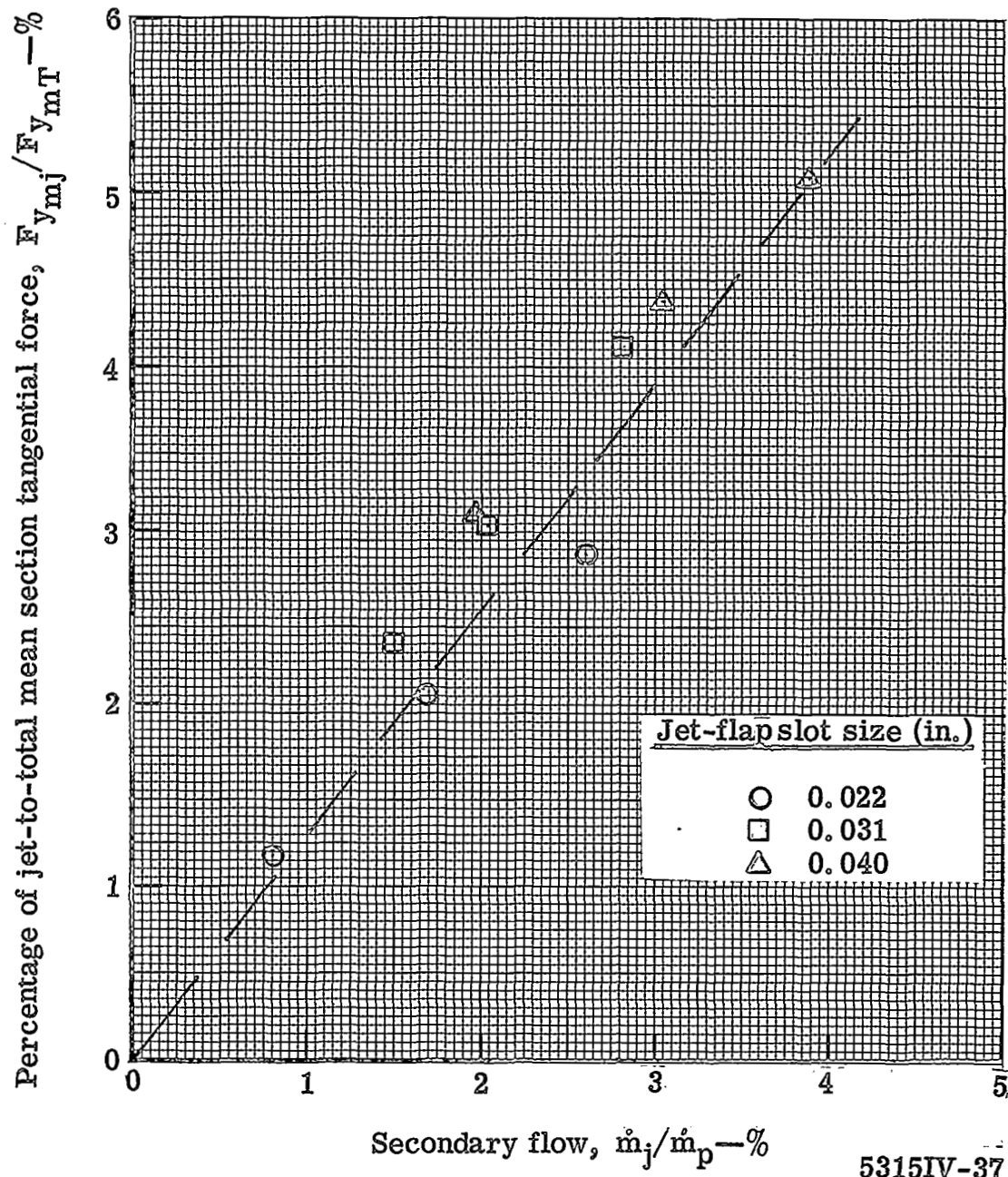


Figure 37. Variation of the jet contribution to the total mean section lift with percentage of secondary flow rate.

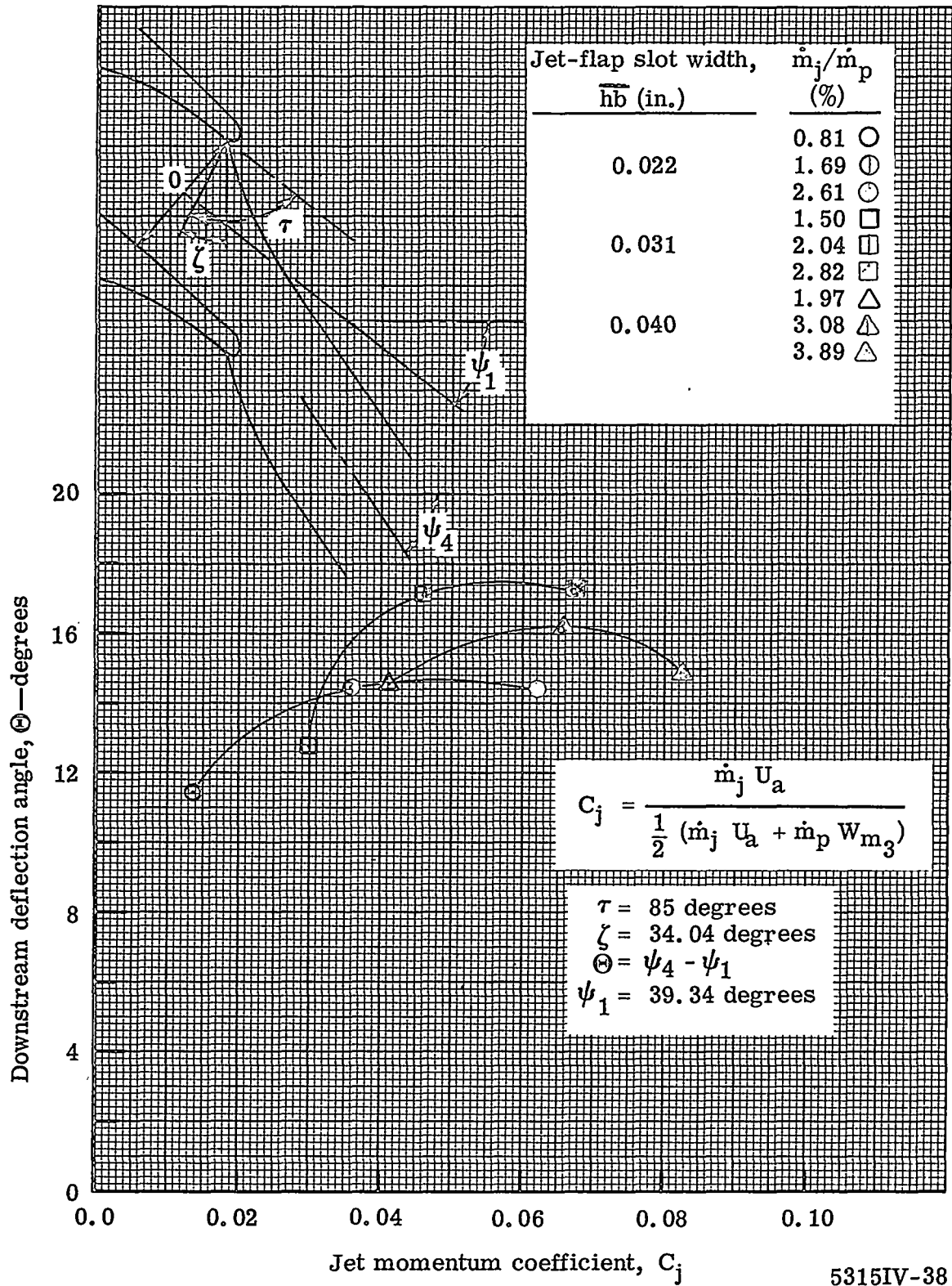


Figure 38. Jet momentum and deflection characteristics for mean section of jet-flapped blade.

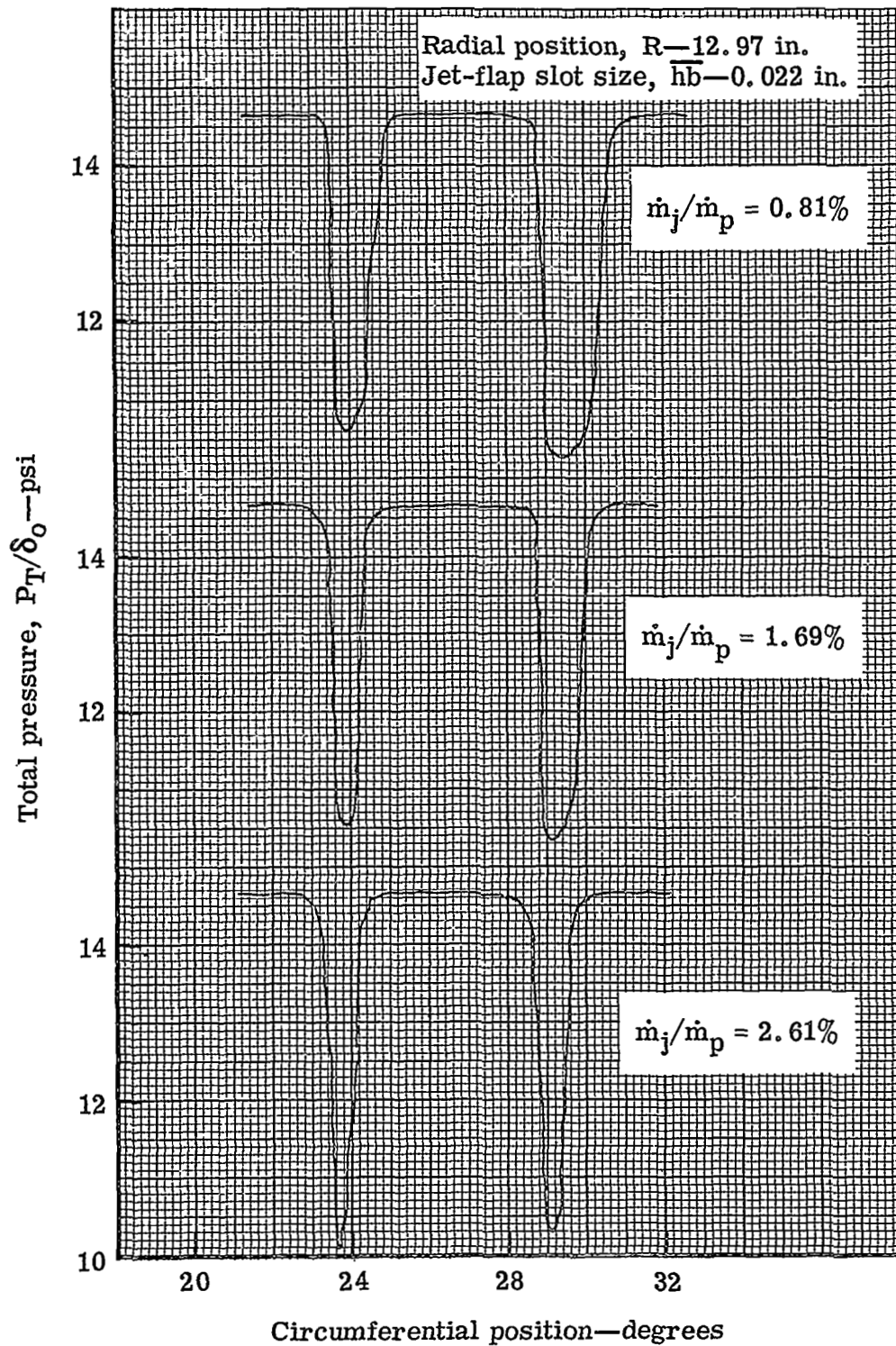
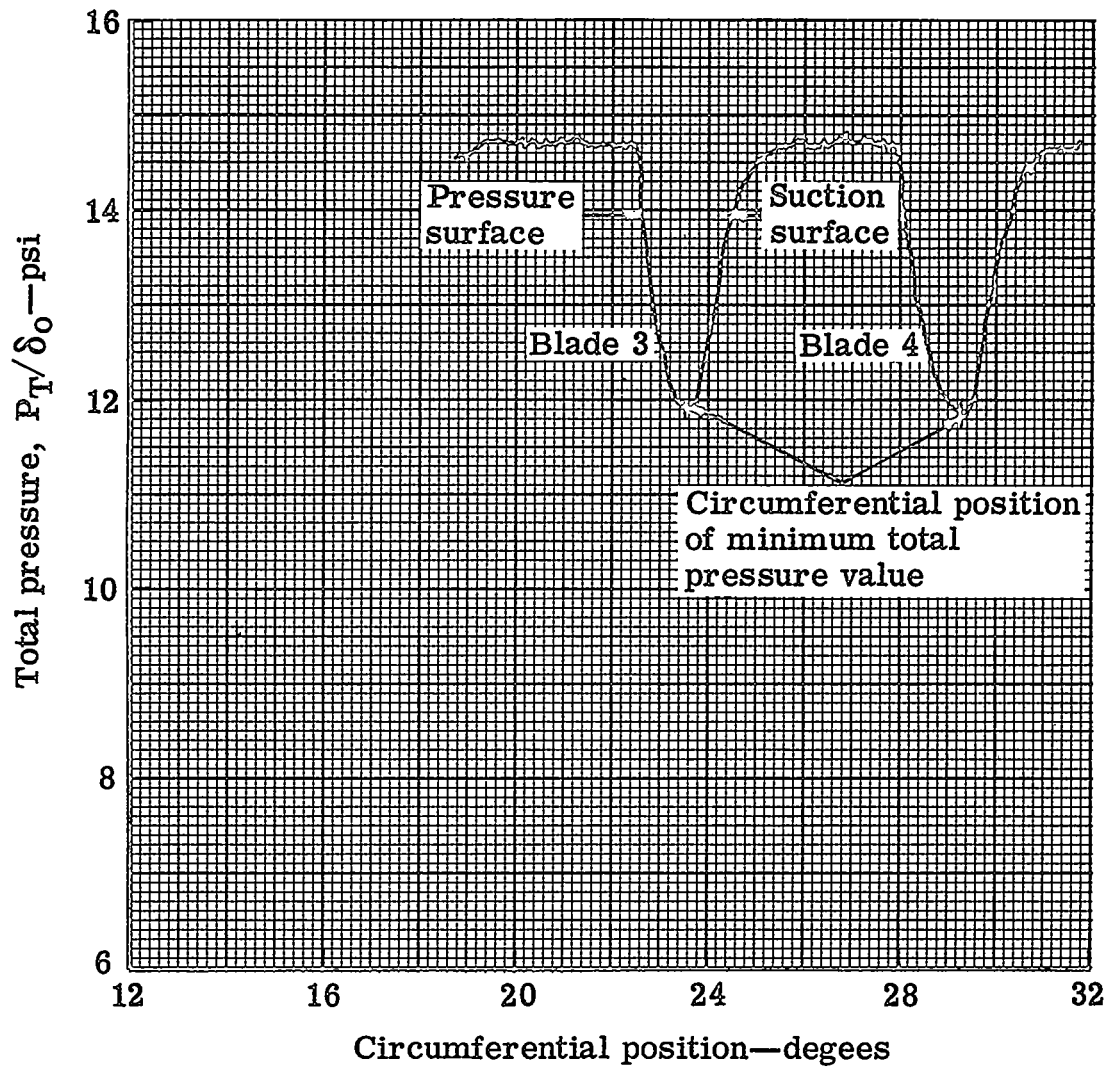


Figure 39. Variation of position and shape of the jet-flapped blade wake with an increase in the amount of secondary flow.



5315III-23

Figure 40. Plain blade Station 3 total pressure distribution for radial position ($R = 12.97$ in.).

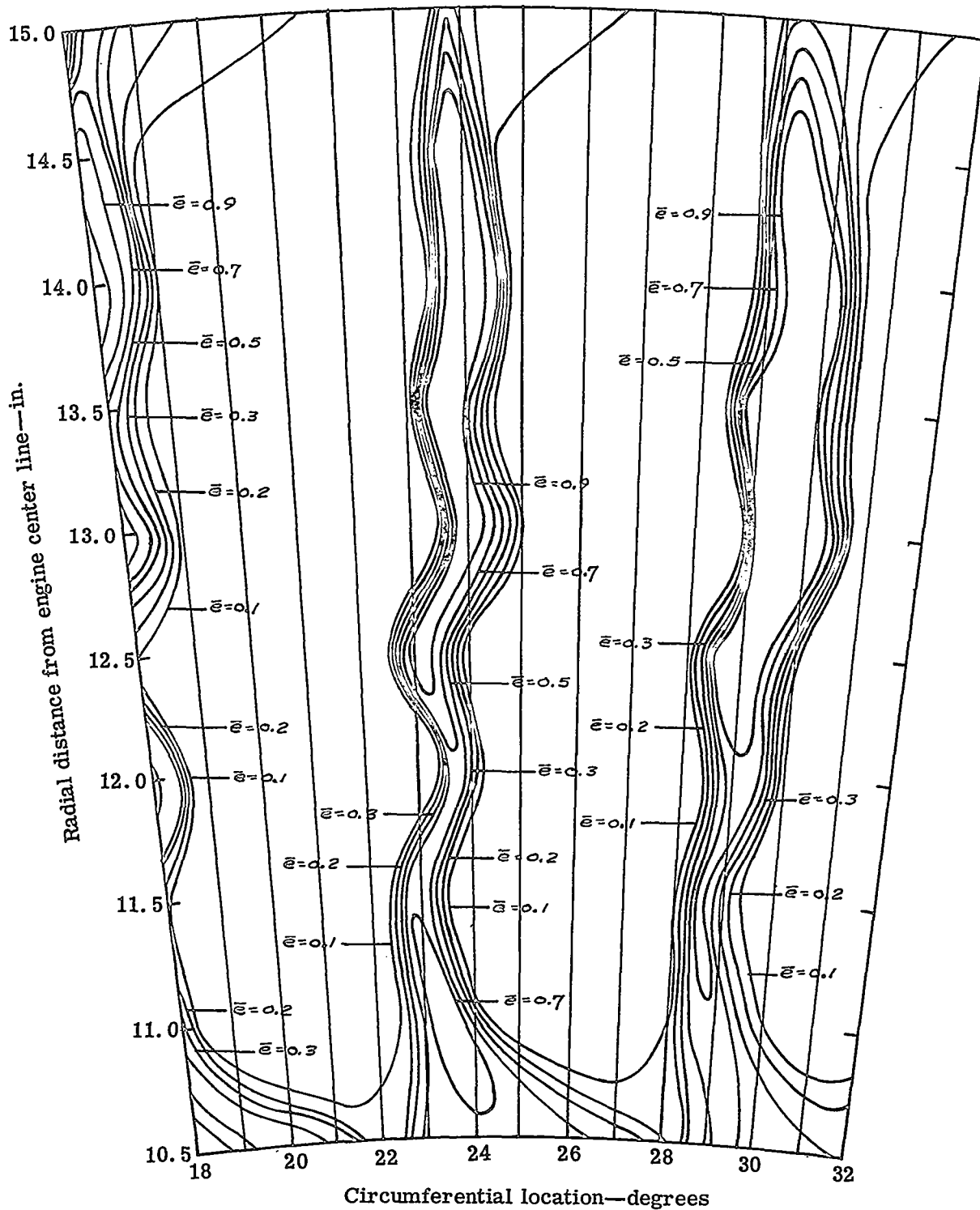
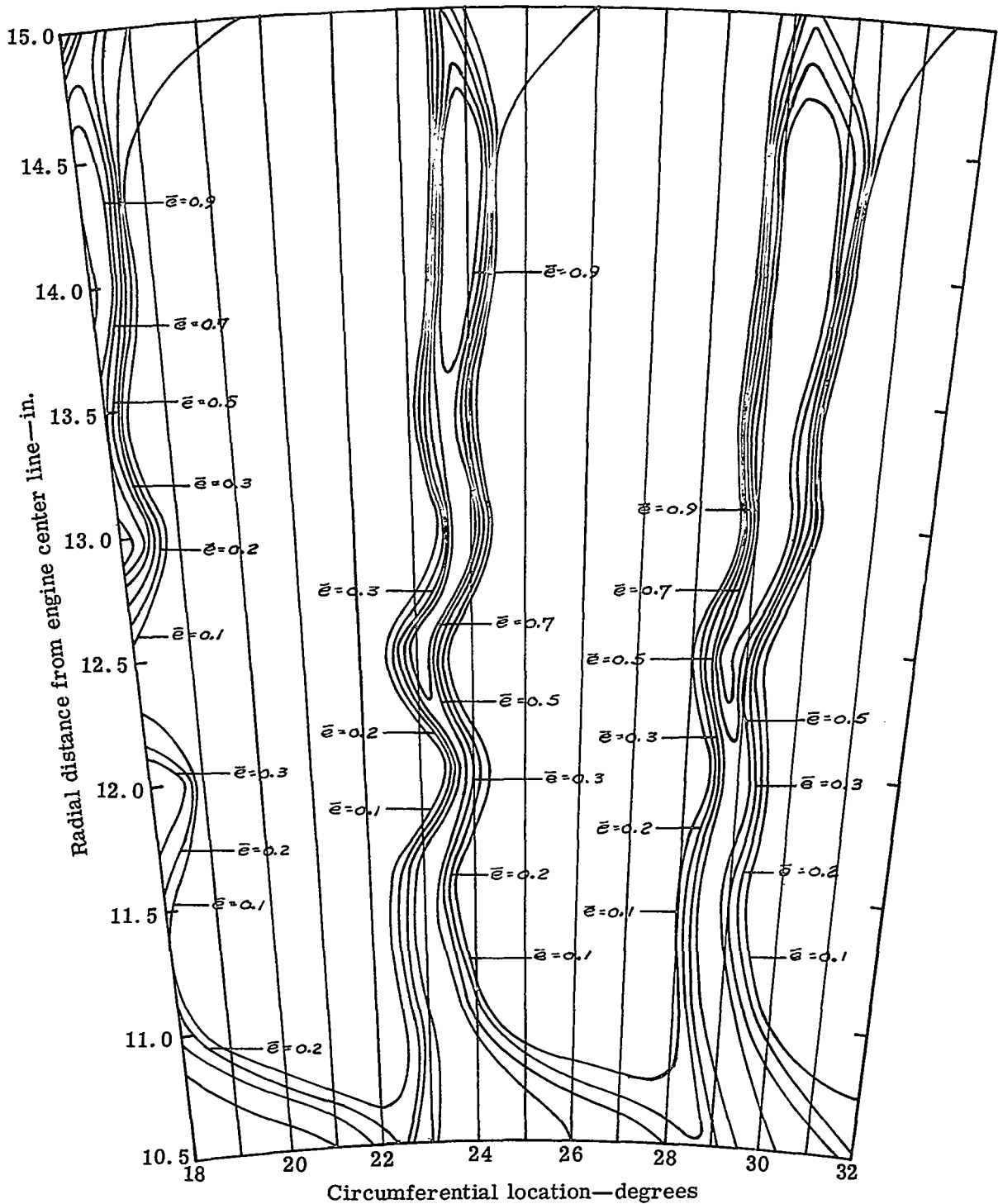
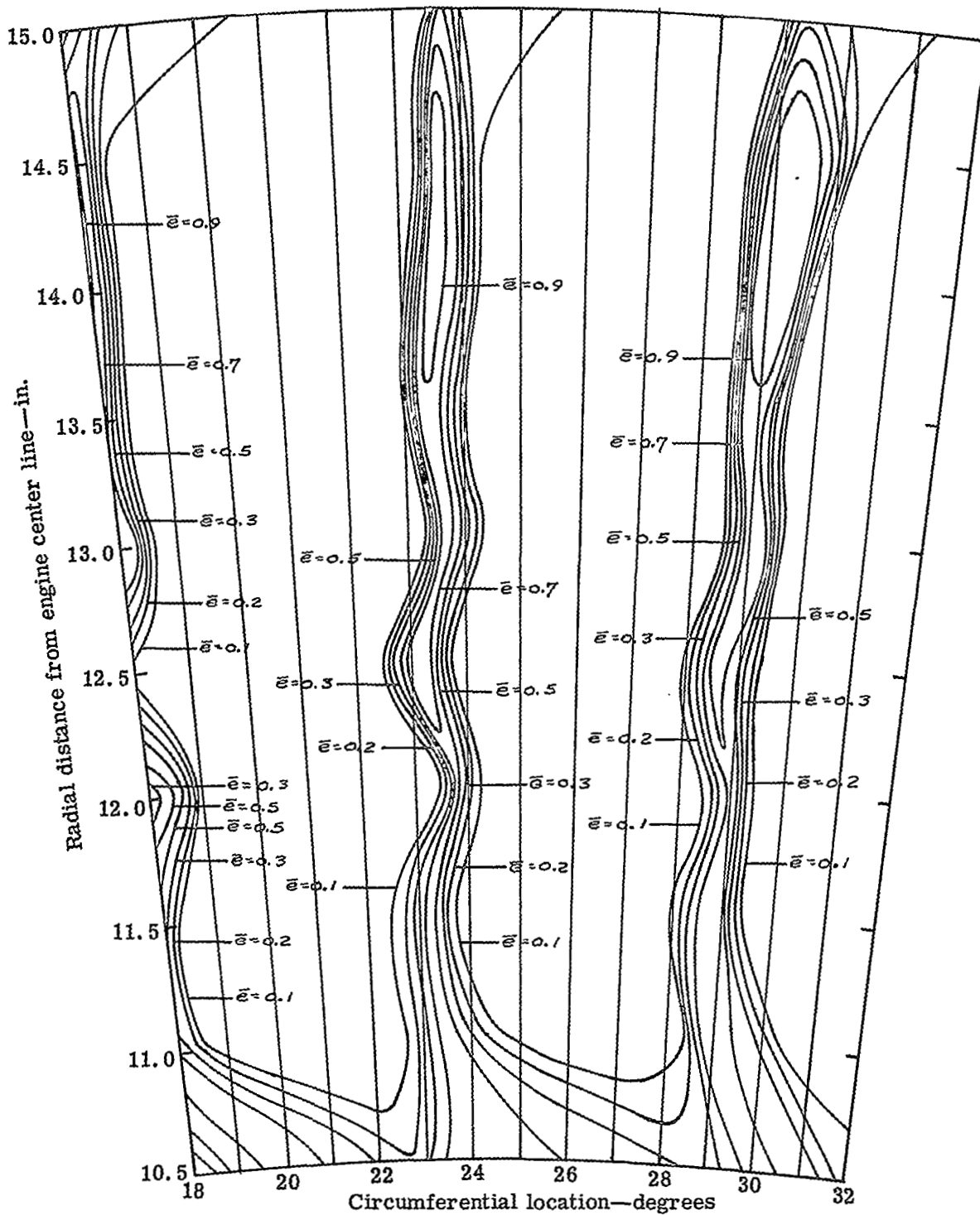


Figure 41. Contours of kinetic energy loss coefficient across one jet-flapped blade passage at Station 3 (0.022-in. slot and 0.81% \dot{m}_j/\dot{m}_p).



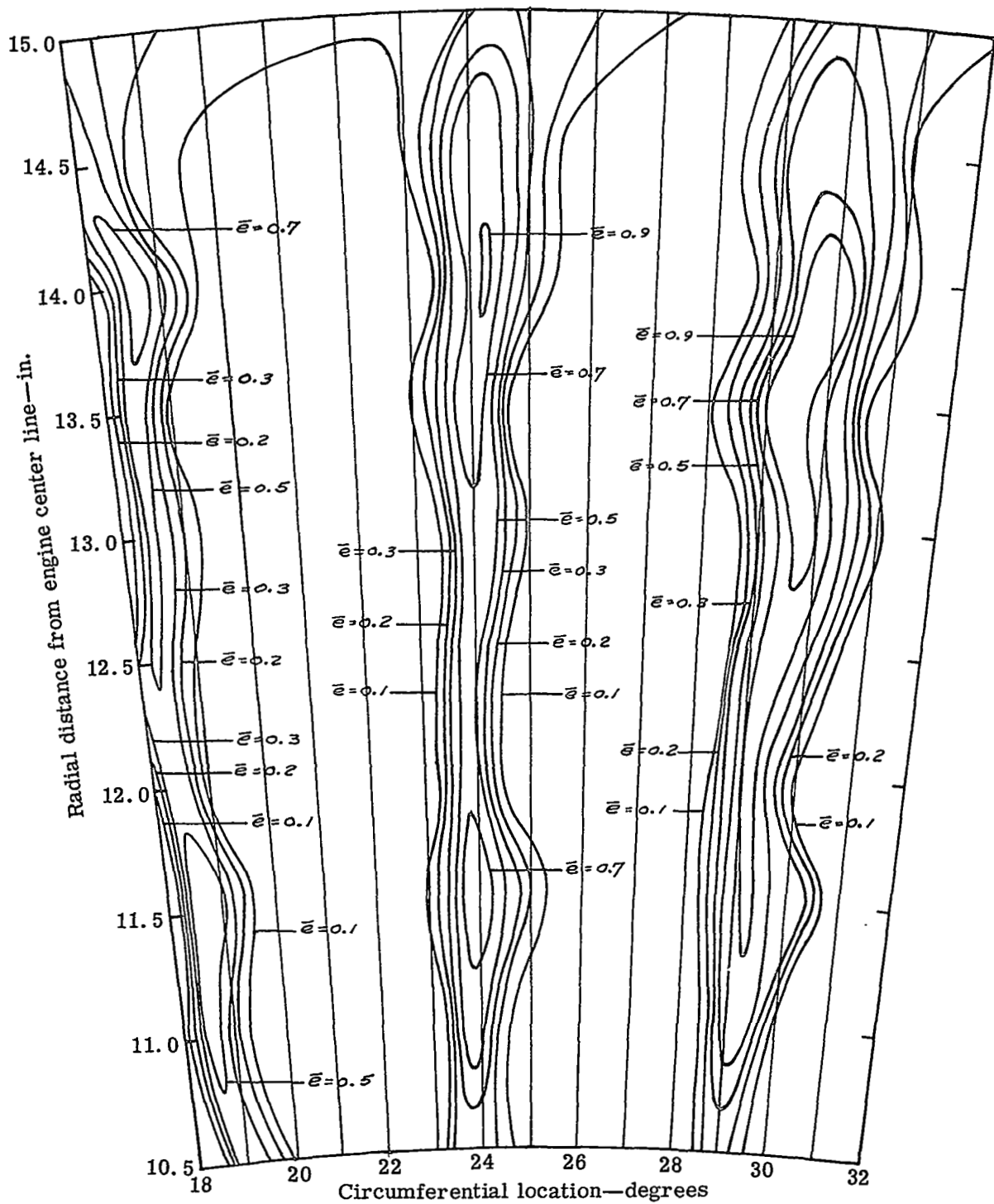
5315IV-42

Figure 42. Contours of kinetic energy loss coefficient across one jet-flapped blade passage at Station 3 (0.022-in. slot and 1.69% \dot{m}_j/\dot{m}_p).



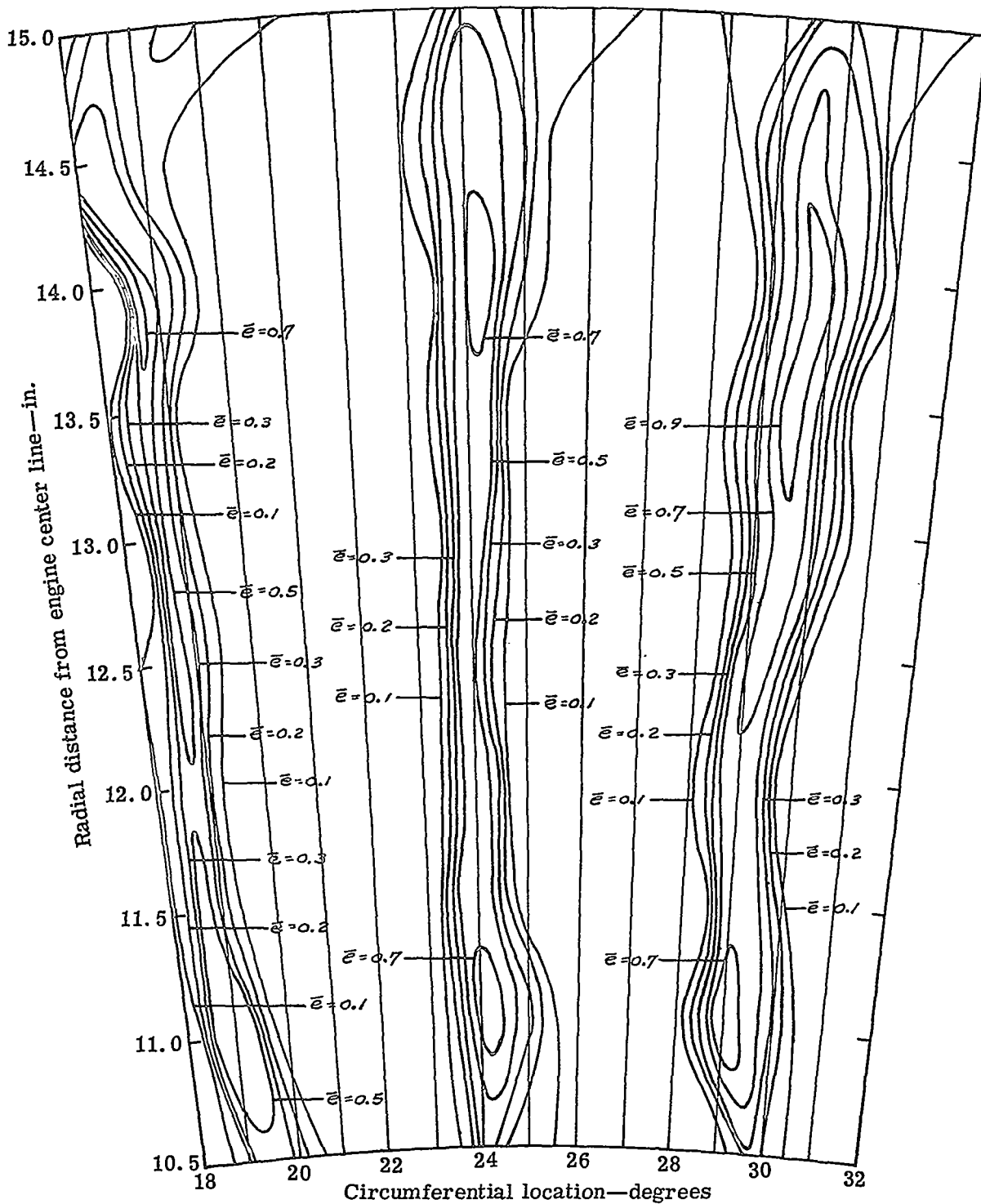
5315IV-43

Figure 43. Contours of kinetic energy loss coefficient across one jet-flapped blade passage at Station 3 (0.022-in. slot and 2.61% \dot{m}_j/\dot{m}_p).



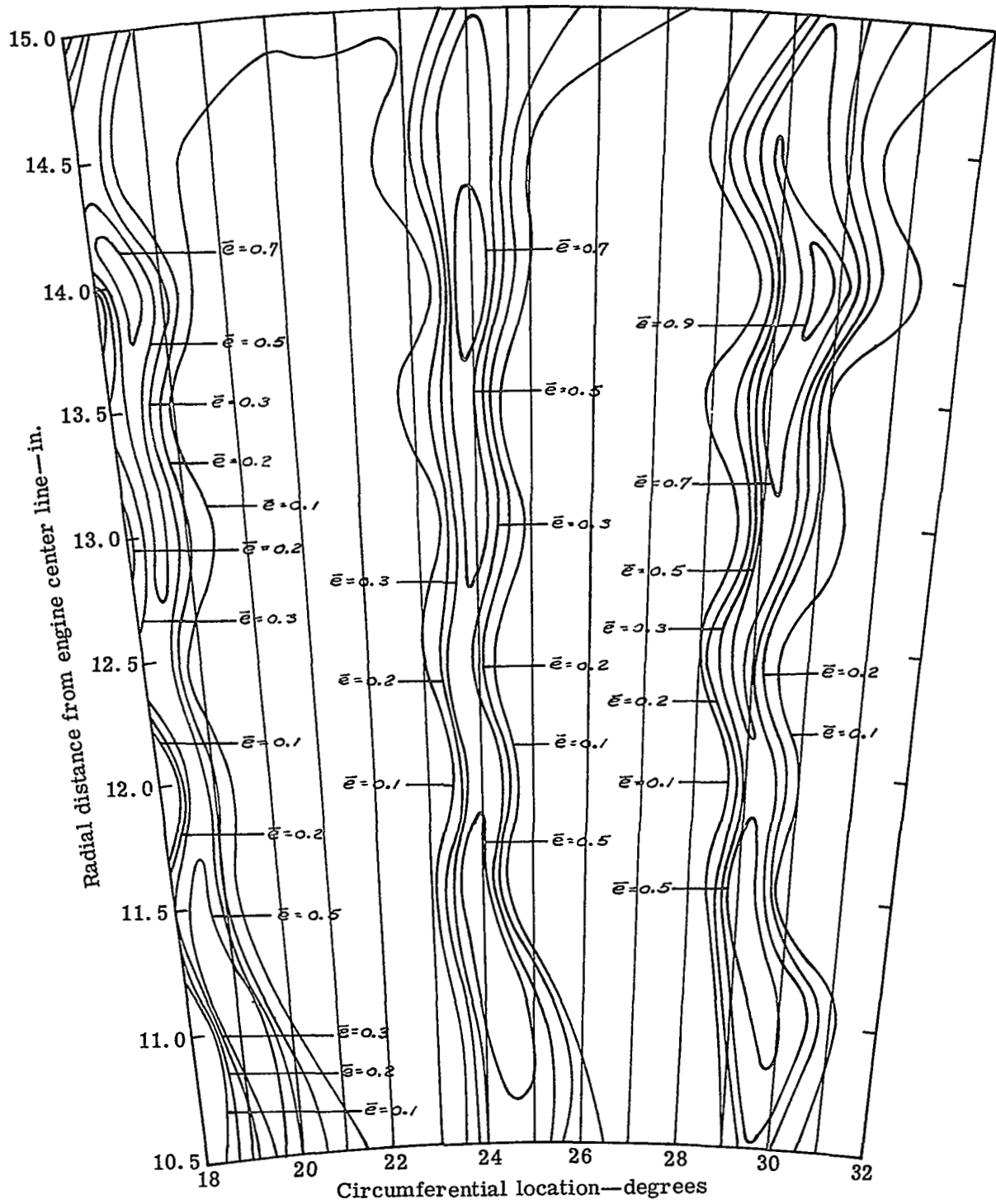
5315IV-44

Figure 44. Contours of kinetic energy loss coefficient across one jet-flapped blade passage at Station 3 (0.031-in. slot and 1.50% \dot{m}_j/\dot{m}_p).



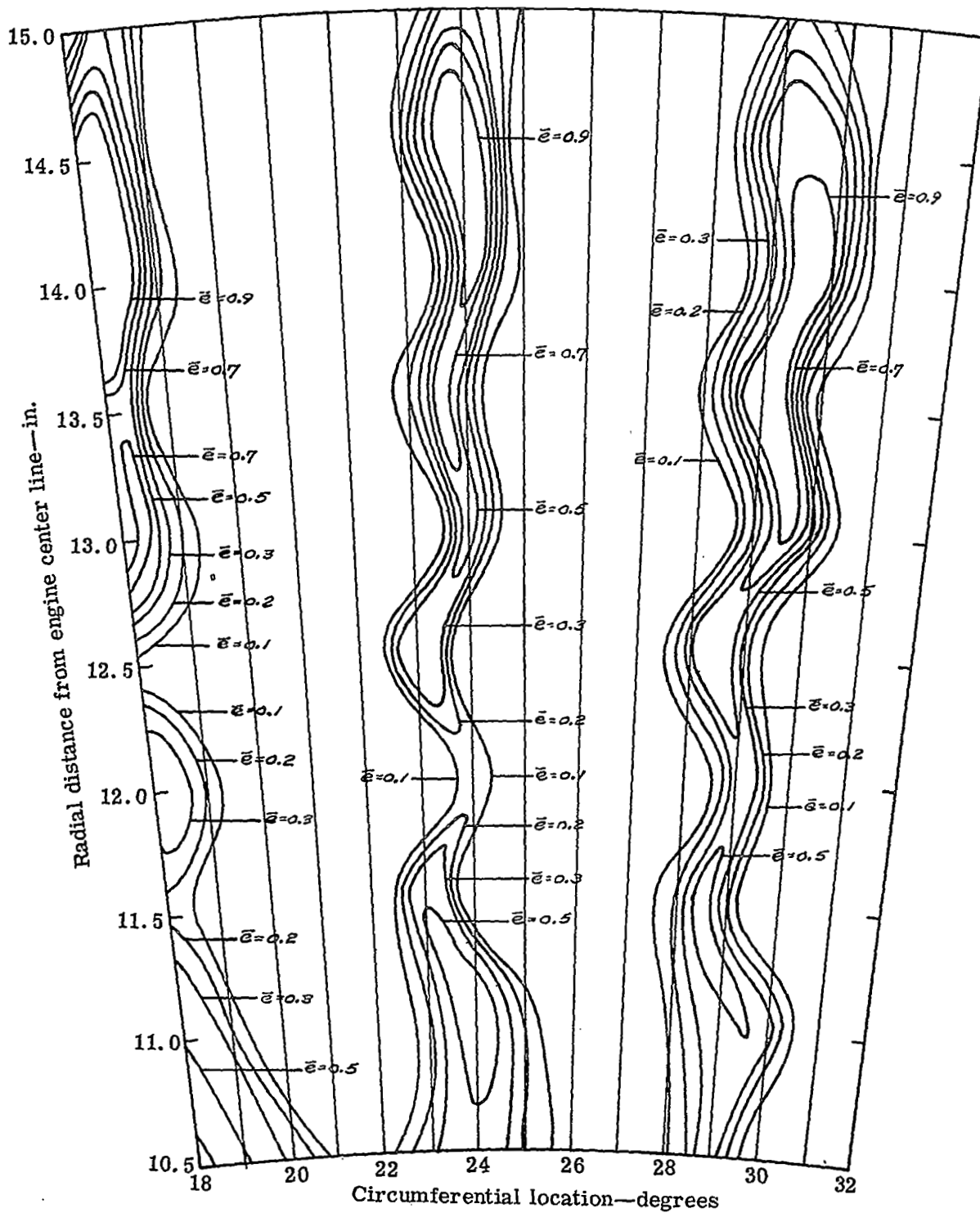
5315IV-45

Figure 45. Contours of kinetic energy loss coefficient across one jet-flapped blade passage at Station 3 (0.031-in. slot and $2.04\% \dot{m}_j/\dot{m}_p$).



5315IV-46

Figure 46. Contours of kinetic energy loss coefficient across one jet-flapped blade passage at Station 3 (0.031-in. slot and 2.82% \dot{m}_j/\dot{m}_p).



5315IV-47

Figure 47. Contours of kinetic energy loss coefficient across one jet-flapped blade passage at Station 3 (0.040-in. slot and $1.97\% \dot{m}_j/\dot{m}_p$).

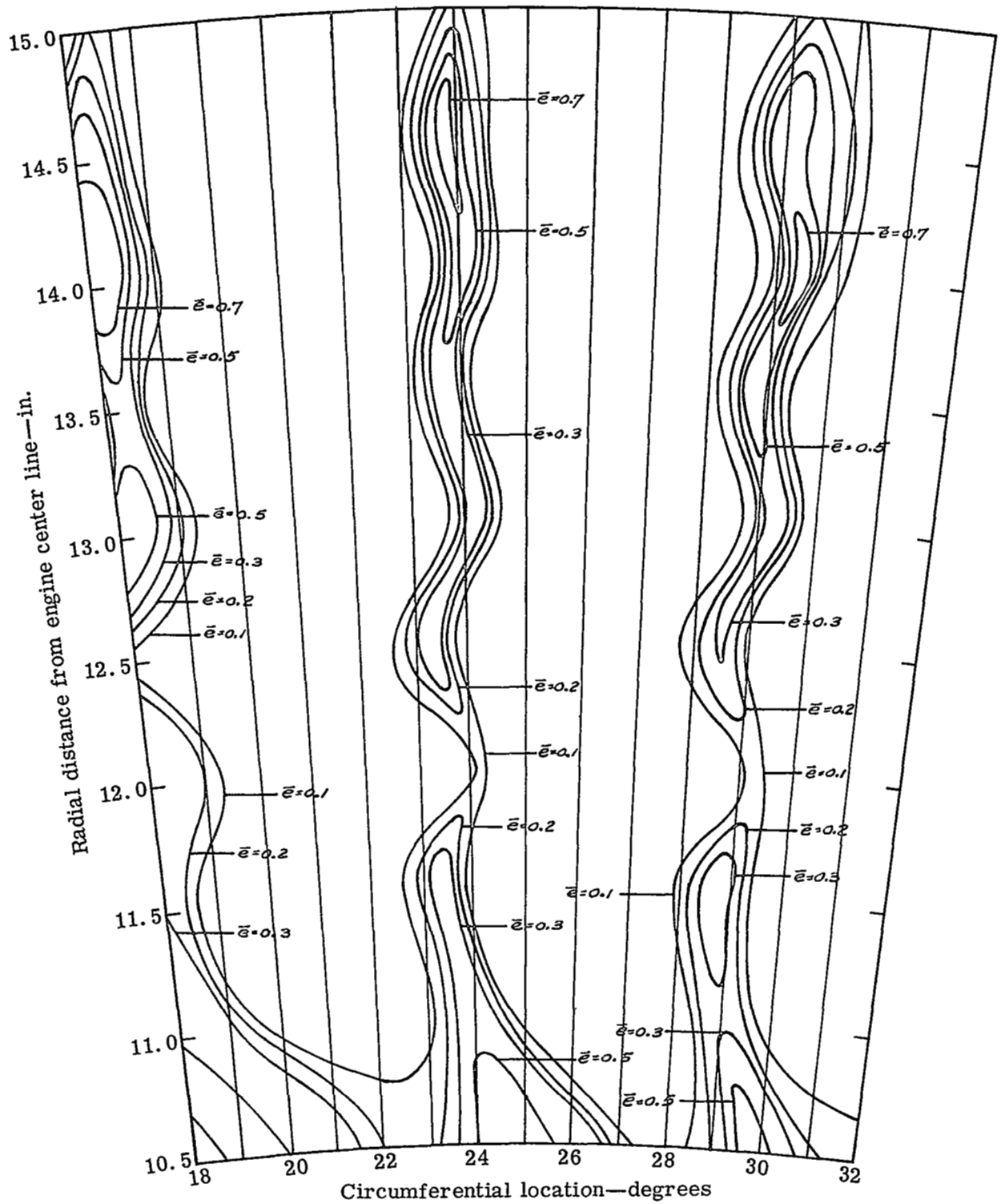
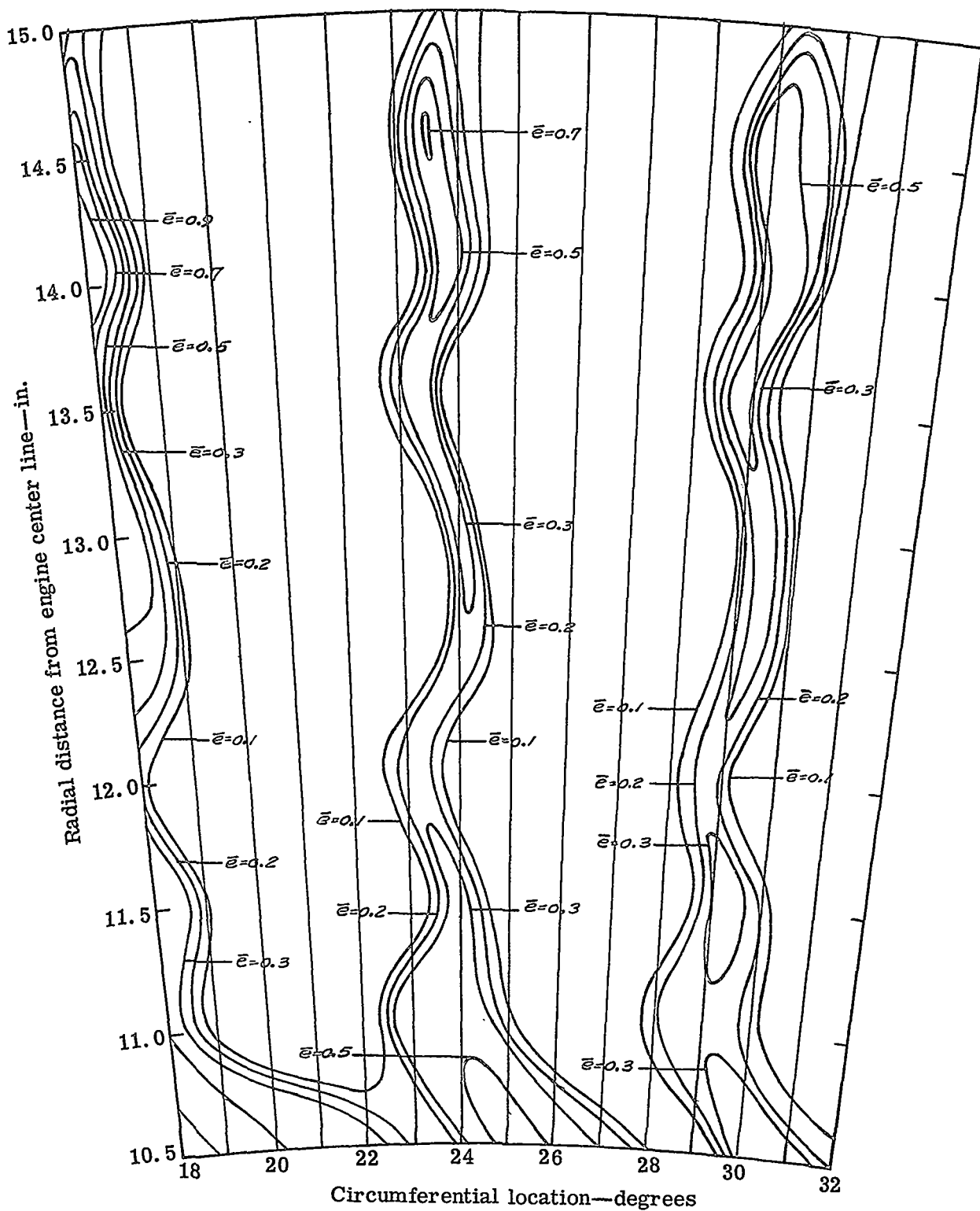
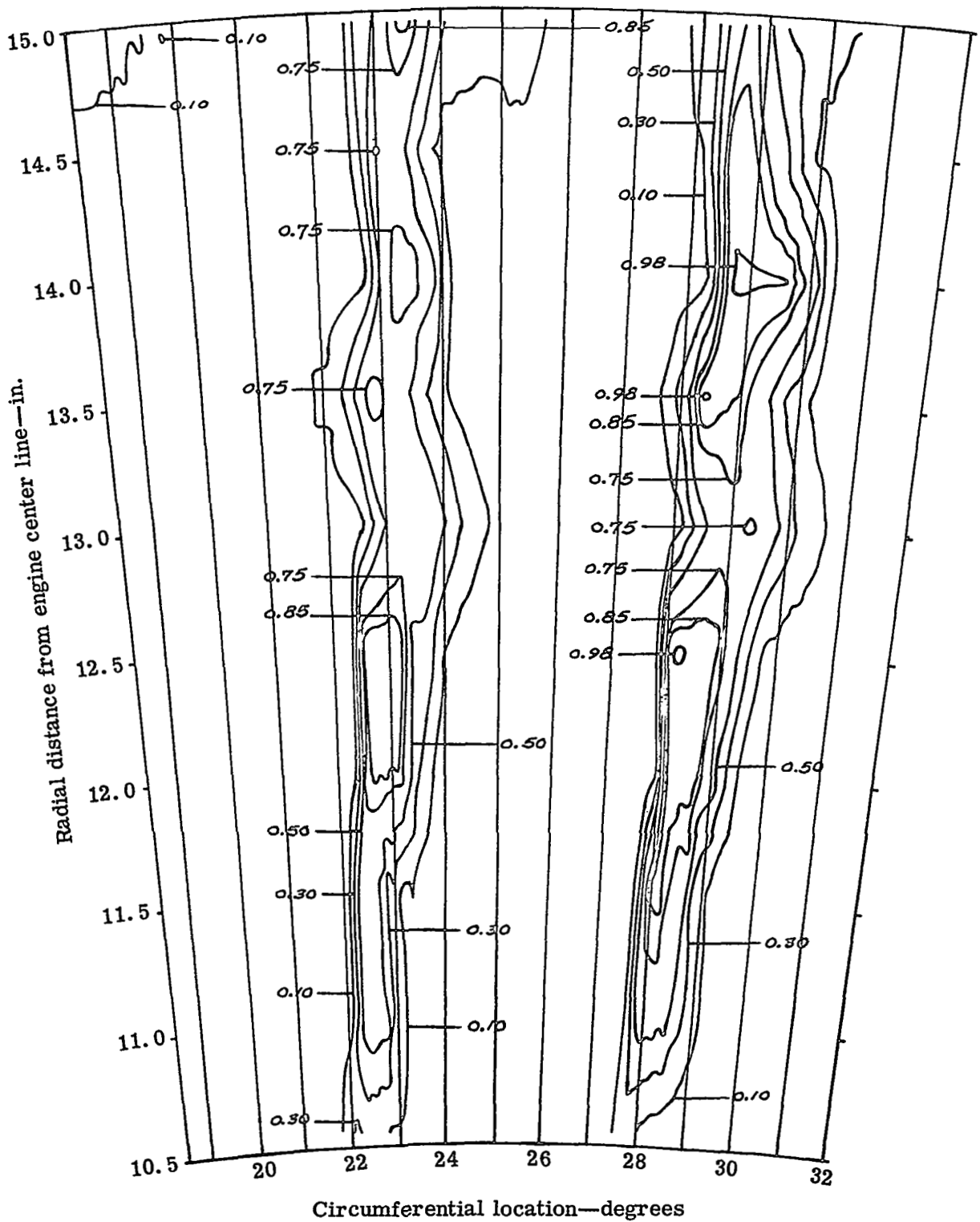


Figure 48. Contours of kinetic energy loss coefficient across one jet-flapped blade passage at Station 3 (0.040-in. slot and $3.03\% \dot{m}_j/\dot{m}_p$).



5315IV-49

Figure 49. Contours of kinetic energy loss coefficient across one jet-flapped blade passage at Station 3 (0.040-in. slot and 3.89% \dot{m}_j/\dot{m}_p).



5315

Figure 50. Contours of kinetic energy loss coefficient across one plain blade passage at Station 3.

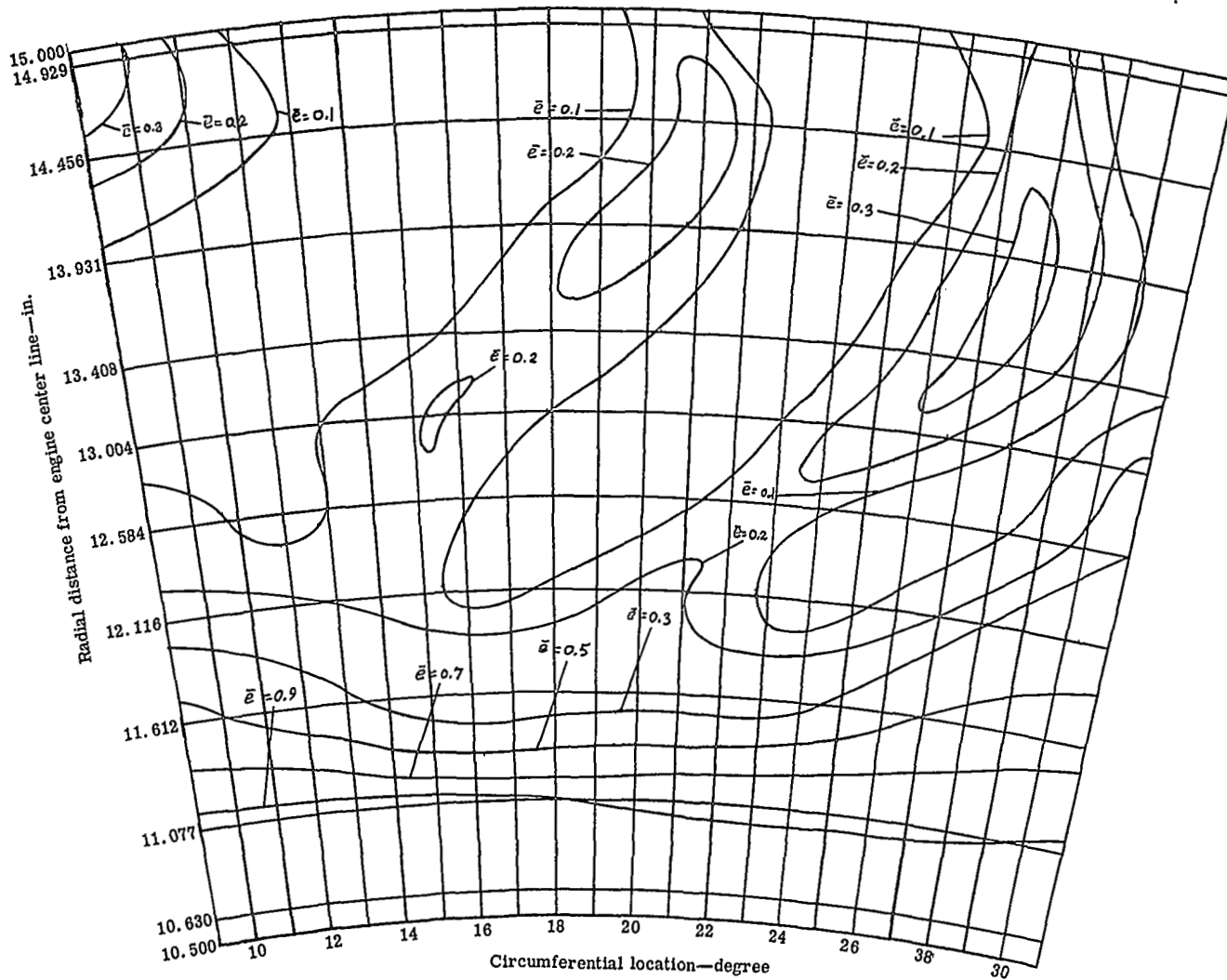


Figure 51. Contours of kinetic energy loss coefficient at Station 4 for the jet-flap blade (0.022-in. slot and $0.79\% \dot{m}_j/\dot{m}_p$).

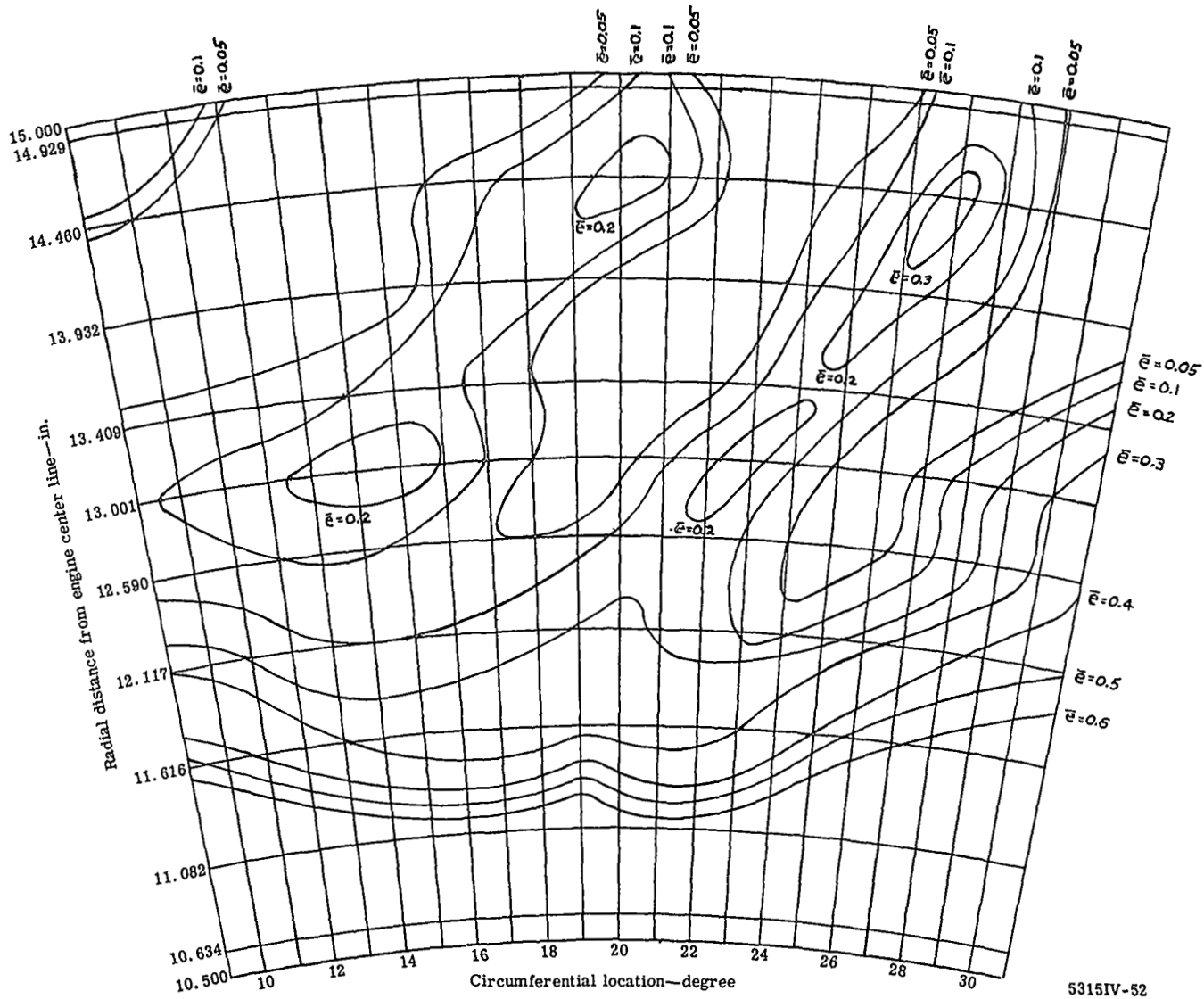
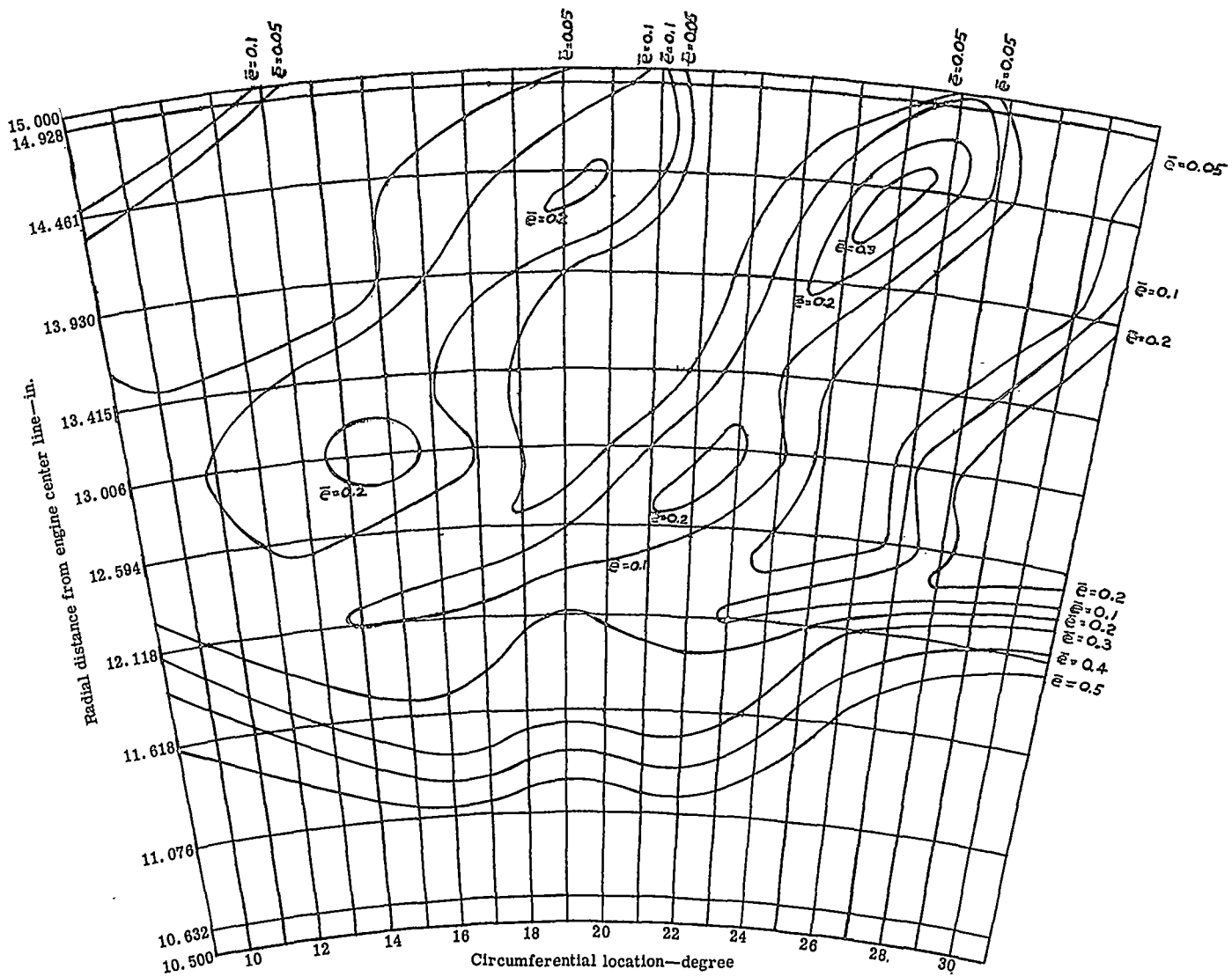


Figure 52. Contours of kinetic energy loss coefficient at Station 4 for the jet-flap blade (0.022-in. slot and 1.65% \dot{m}_j/\dot{m}_p).



5315IV-53

Figure 53. Contours of kinetic energy loss coefficient at Station 4 for the jet-flap blade)
 (0.022-in. slot and $2.57\% \dot{m}_j / \dot{m}_p$).

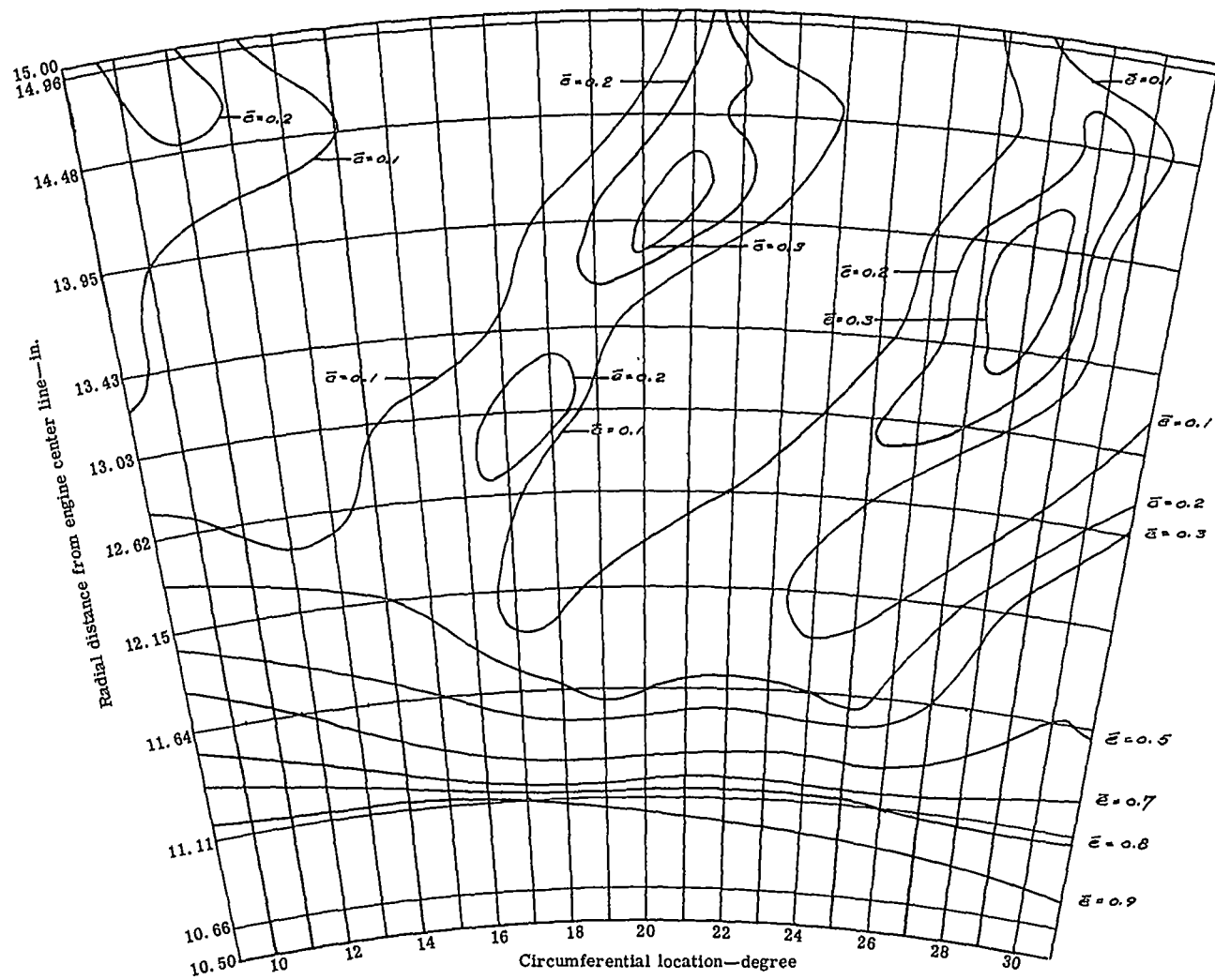
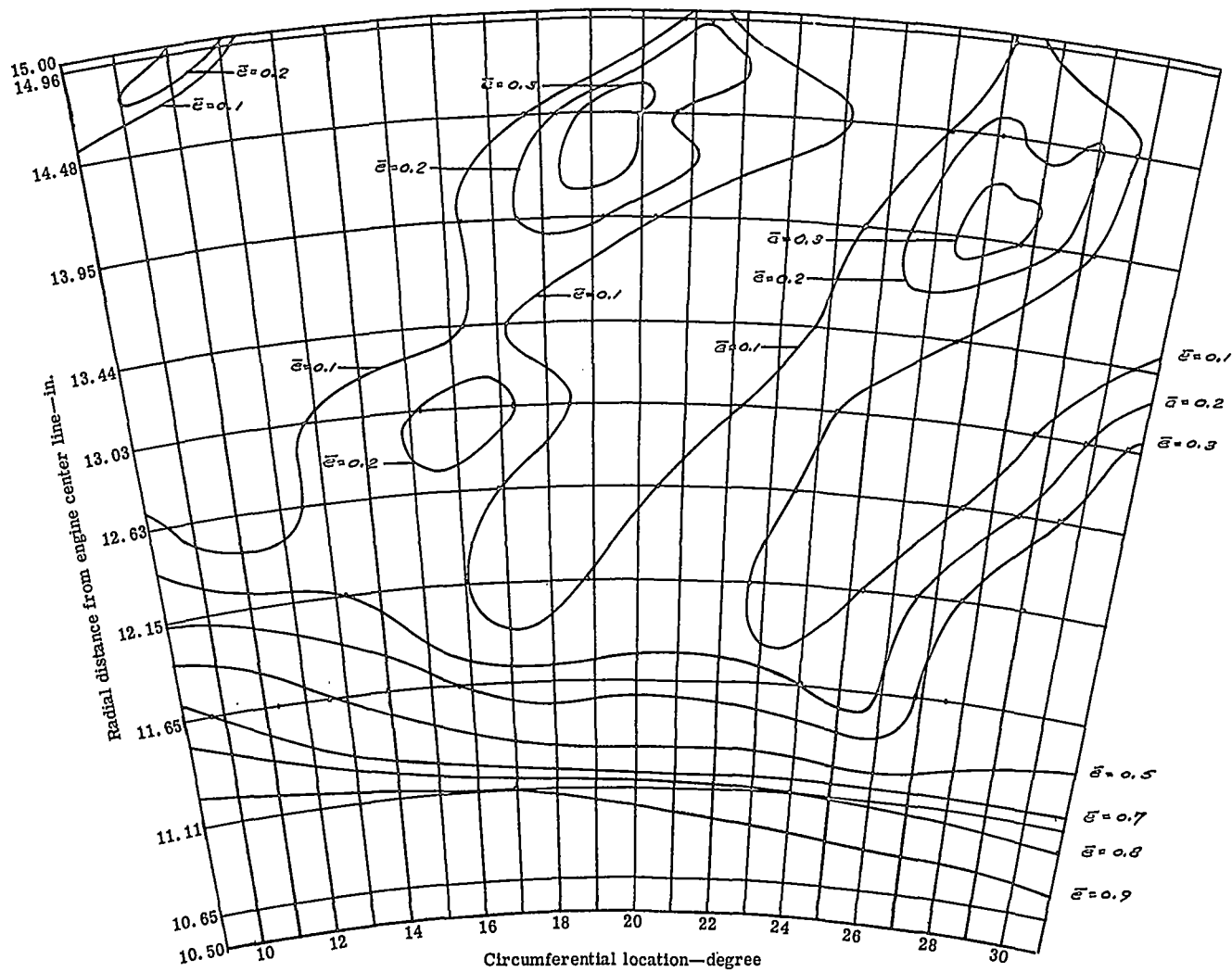


Figure 54. Contours of kinetic energy loss coefficient at Station 4 for the jet-flap blade (0.031-in. slot and $1.50\% \dot{m}_j/\dot{m}_p$).



5315IV-55

Figure 55. Contours of kinetic energy loss coefficient at Station 4 for the jet-flap blade (0.031-in. slot and 2.02% \dot{m}_j/\dot{m}_p).

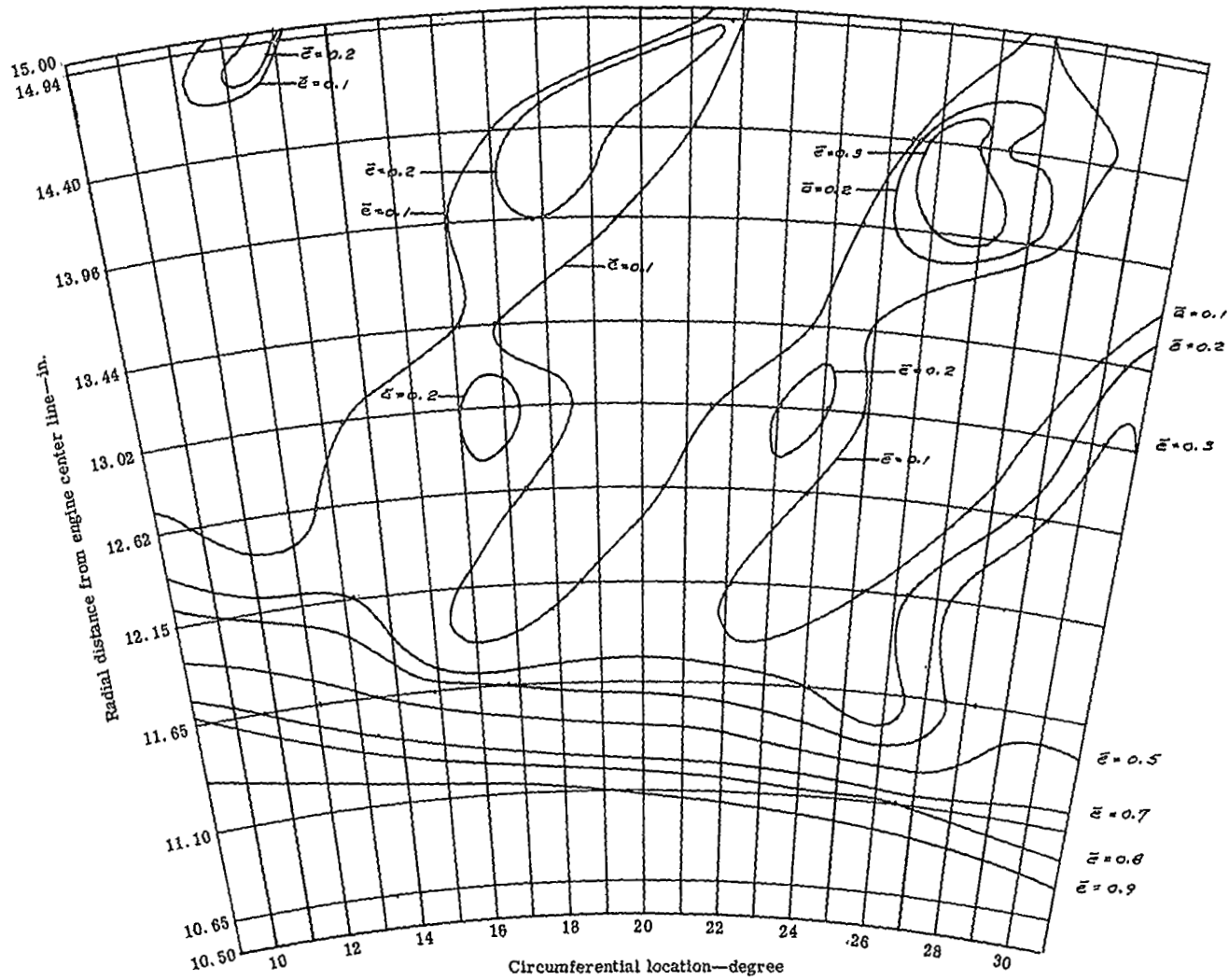
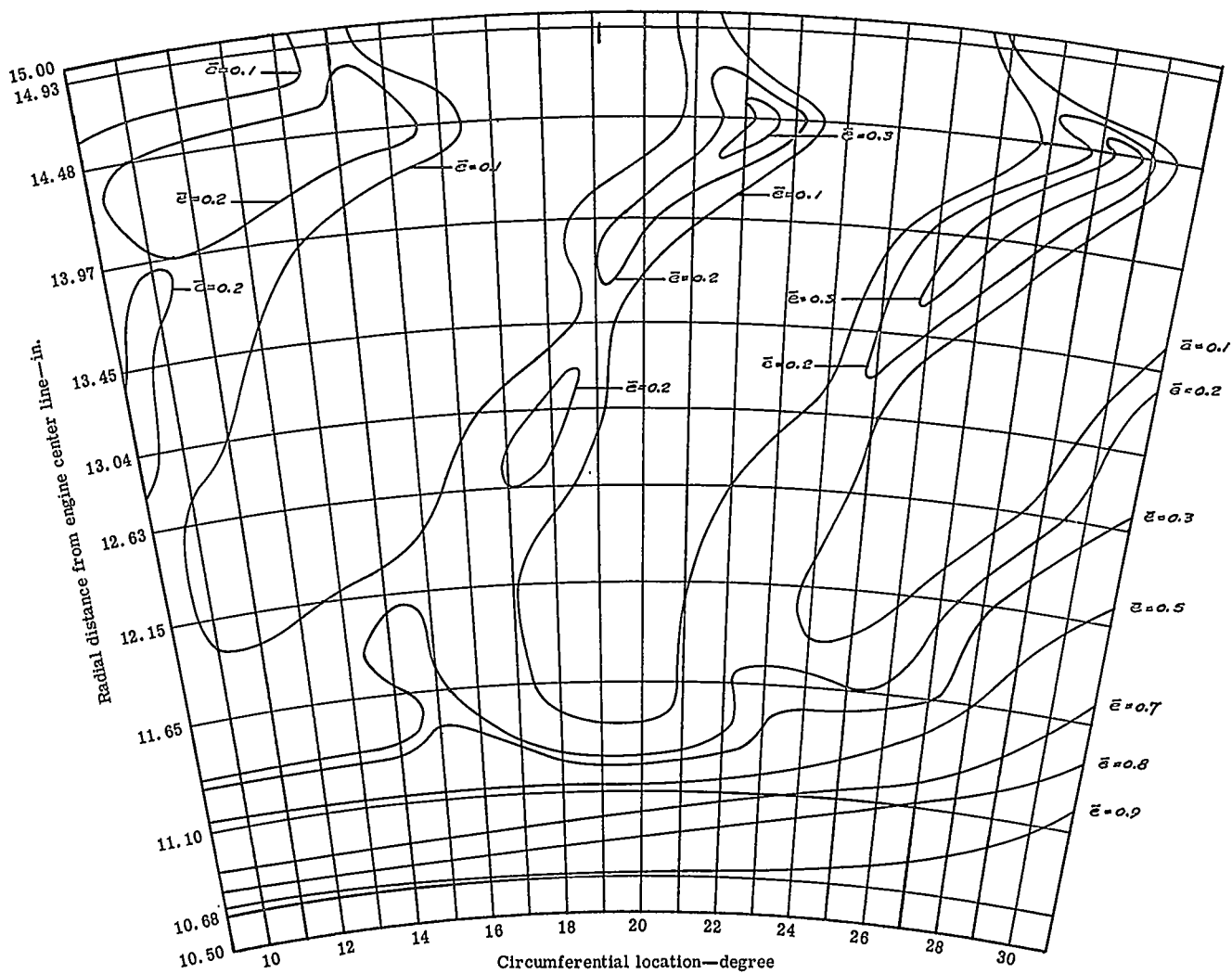


Figure 56. Contours of kinetic energy loss coefficient at Station 4 for the jet-flap blade (0.031-in. slot and $2.47\% \dot{m}_j/\dot{m}_p$).



5315IV-57

Figure 57. Contours of kinetic energy loss coefficient at Station 4 for the jet-flap blade (0.040-in. slot and $1.97\% \dot{m}_j/\dot{m}_p$).

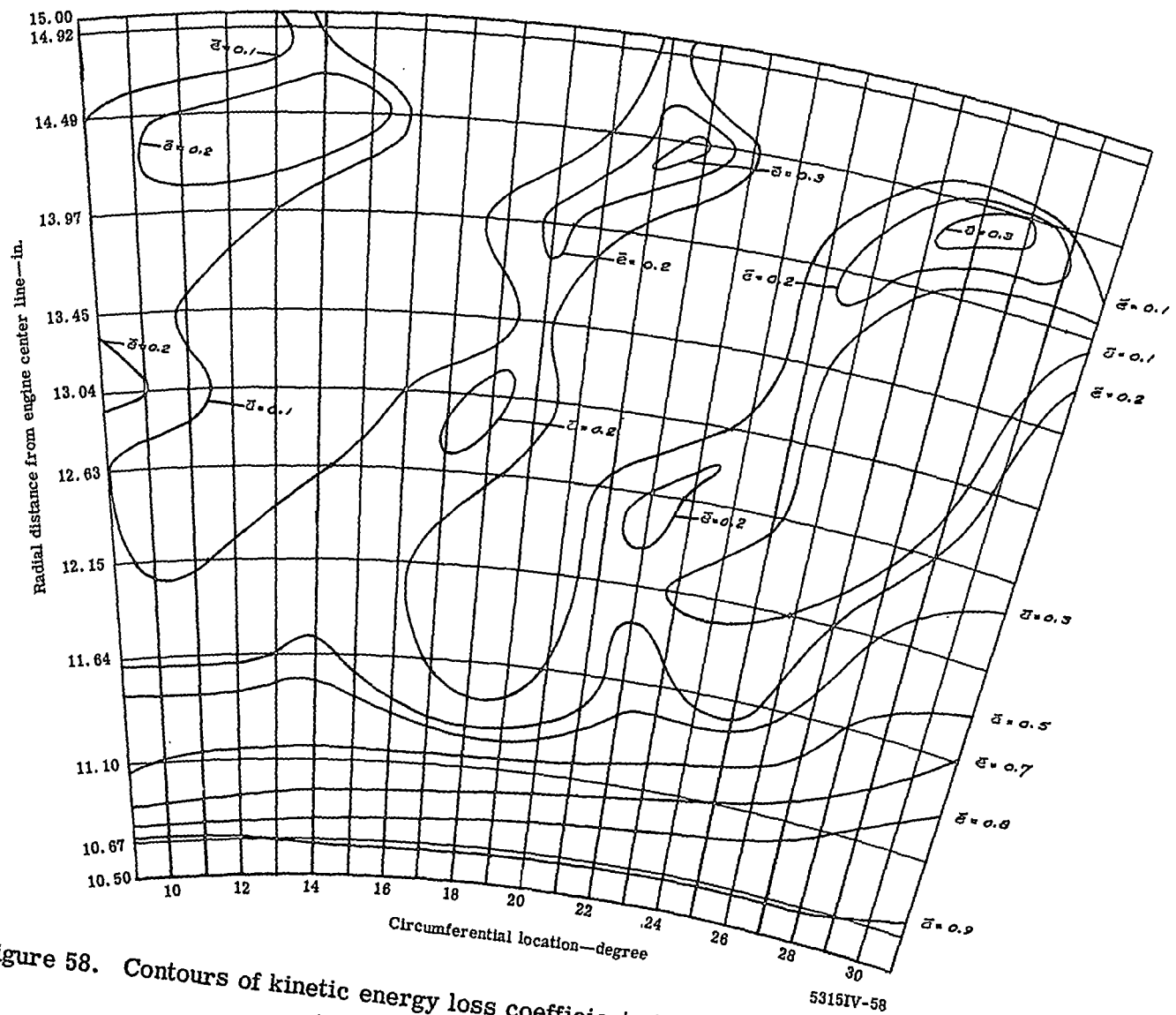
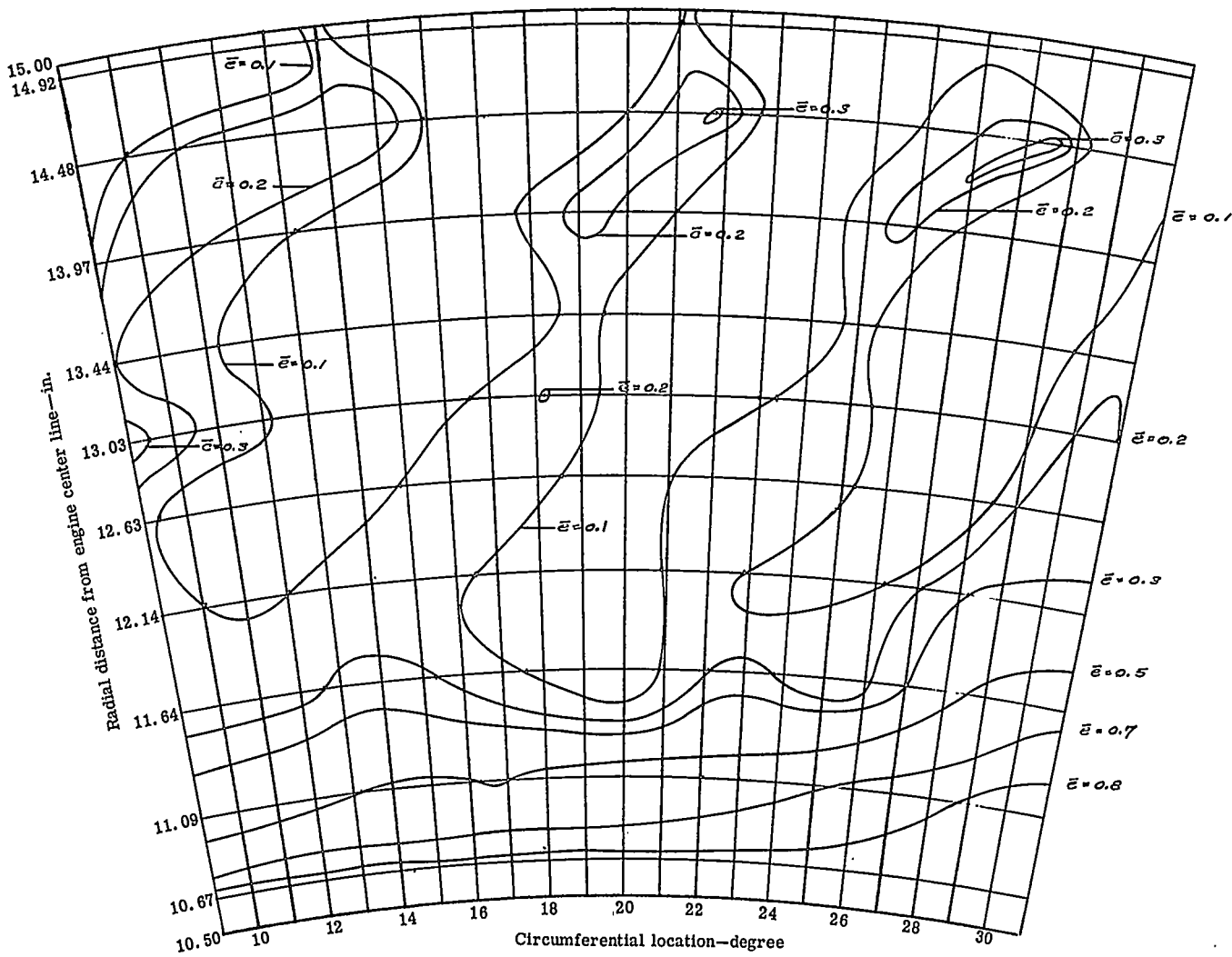
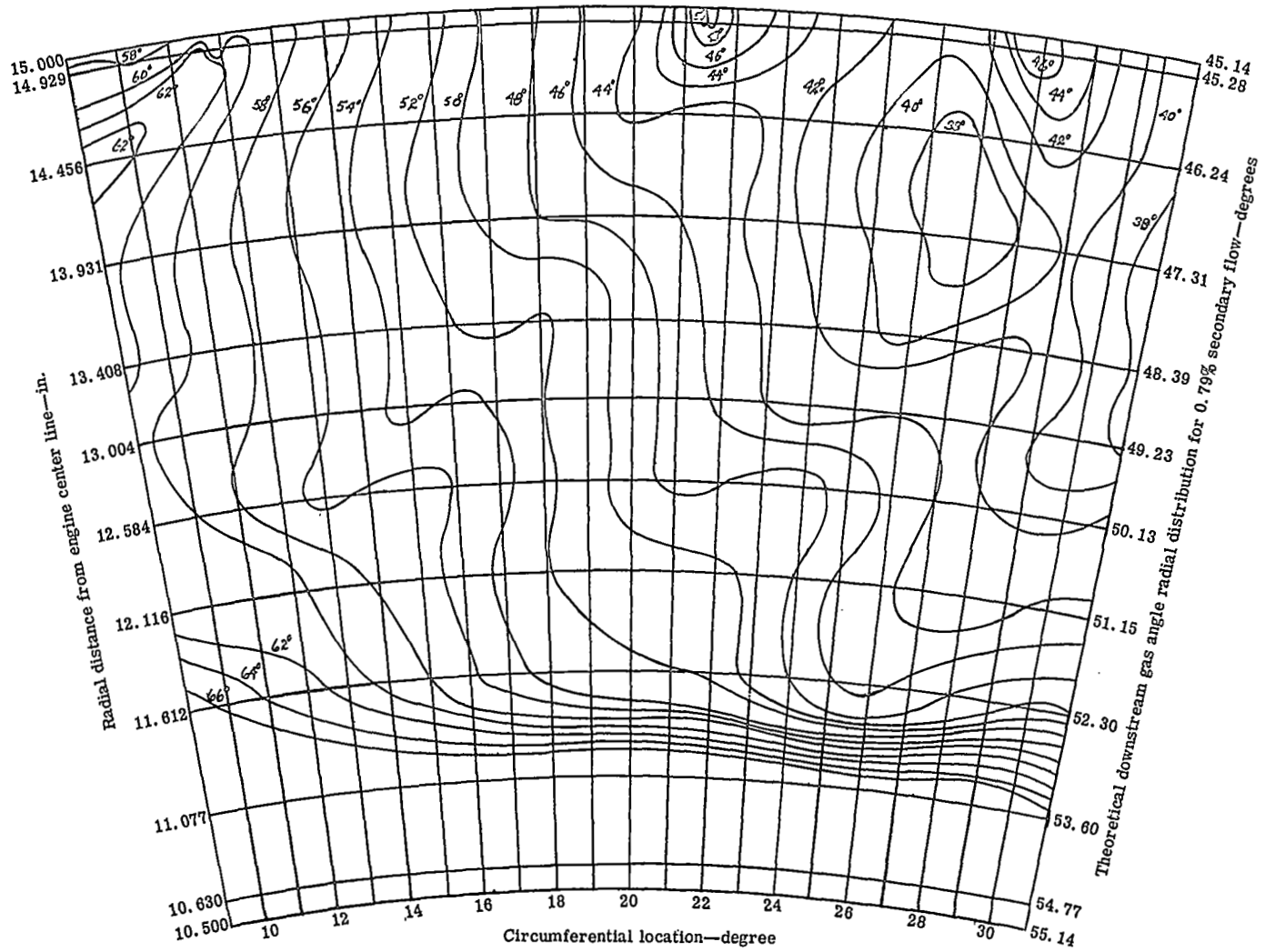


Figure 58. Contours of kinetic energy loss coefficient at Station 4 for the jet-flap blade (0.040-in. slot and $3.08\% \dot{m}_j/\dot{m}_p$).



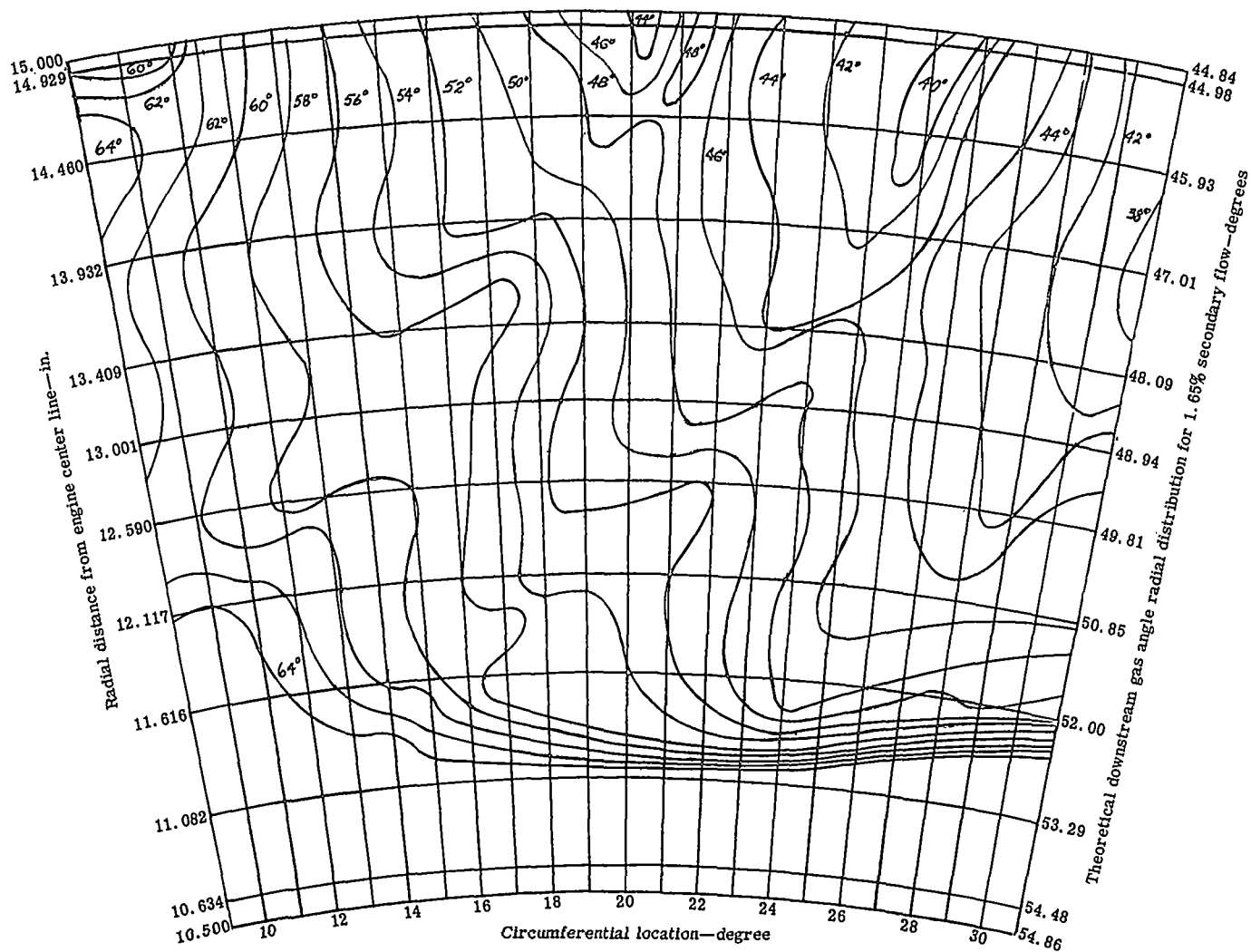
5315IV-59

Figure 59. Contours of kinetic energy loss coefficient at Station 4 for the jet-flap blade (0.040-in. slot and 3.85% \dot{m}_j/\dot{m}_p).



5315IV-61

Figure 61. Contours of downstream gas angle measured from axial for the jet-flap blade (0.022-in. slot and $0.79\% \dot{m}_j/\dot{m}_p$).



5315IV-62

Figure 62. Contours of downstream gas angle measured from axial for the jet-flap blade (0.022-in. slot and 1.65% \dot{m}_j/\dot{m}_p).

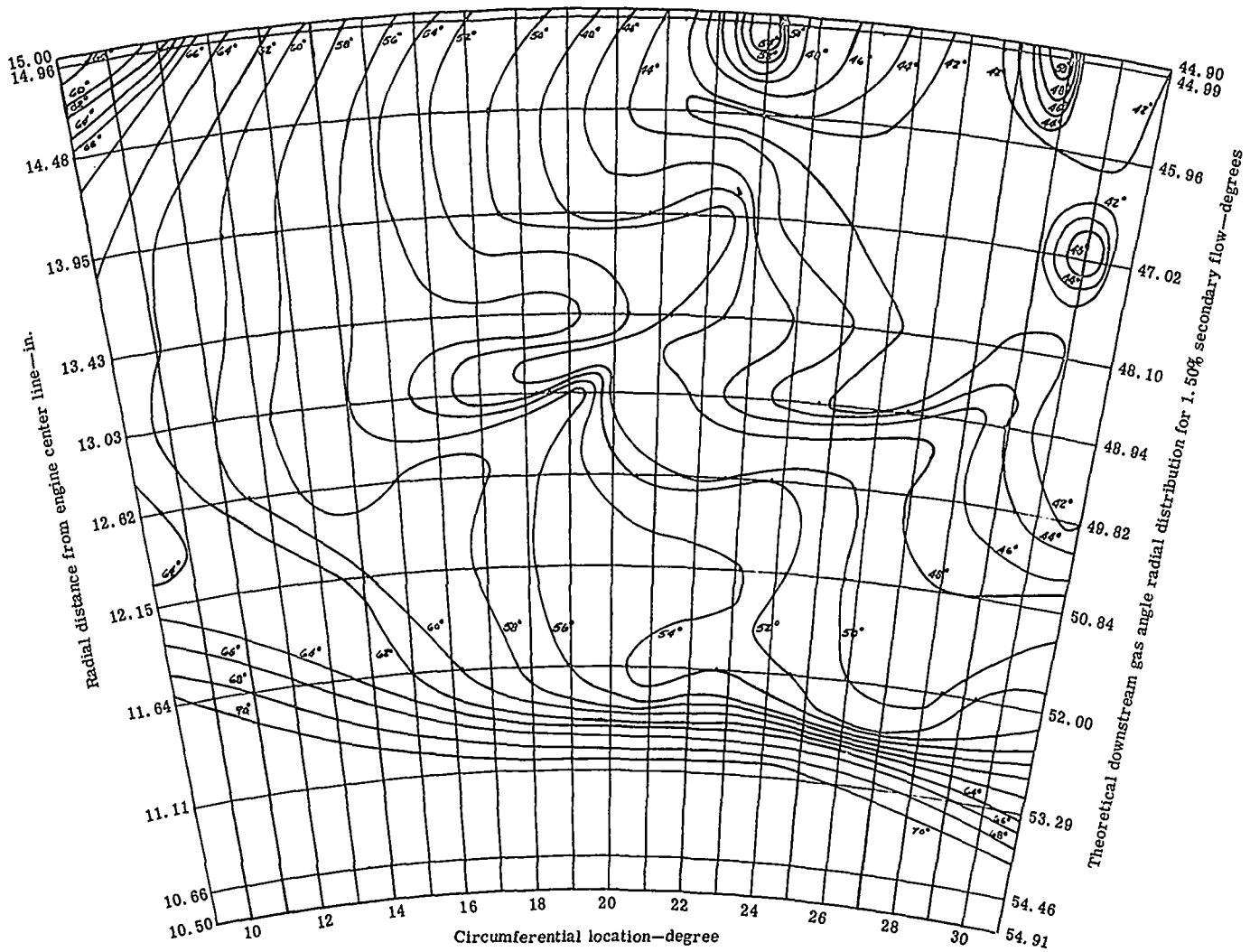


Figure 64. Contours of downstream gas angle measured from axial for the jet-flap blade (0.031-in. slot and 1.50% \dot{m}_j/\dot{m}_p).

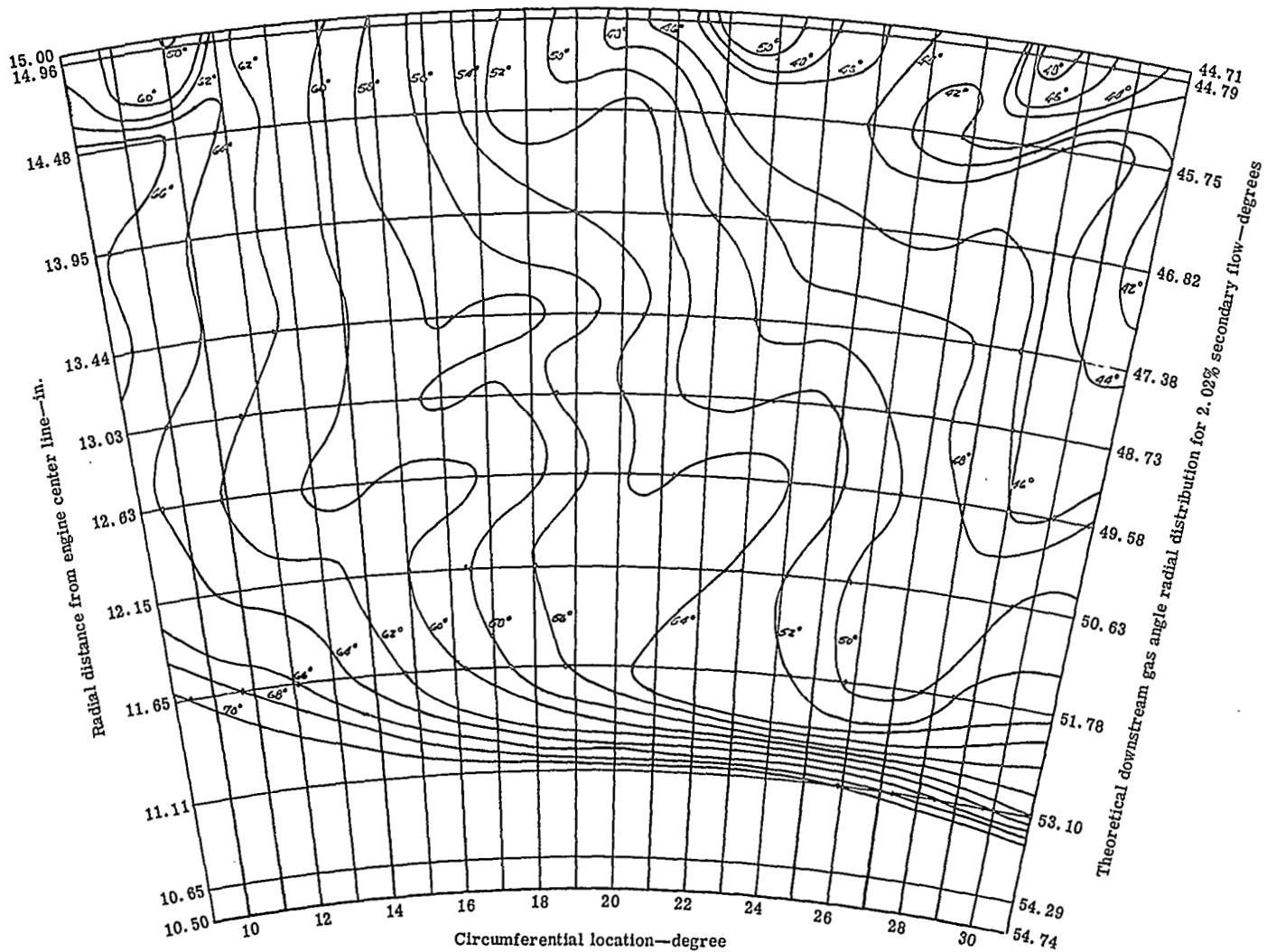


Figure 65. Contours of downstream gas angle measured from axial for the jet-flap blade (0.031-in. slot and 2.02% \dot{m}_j/\dot{m}_p).

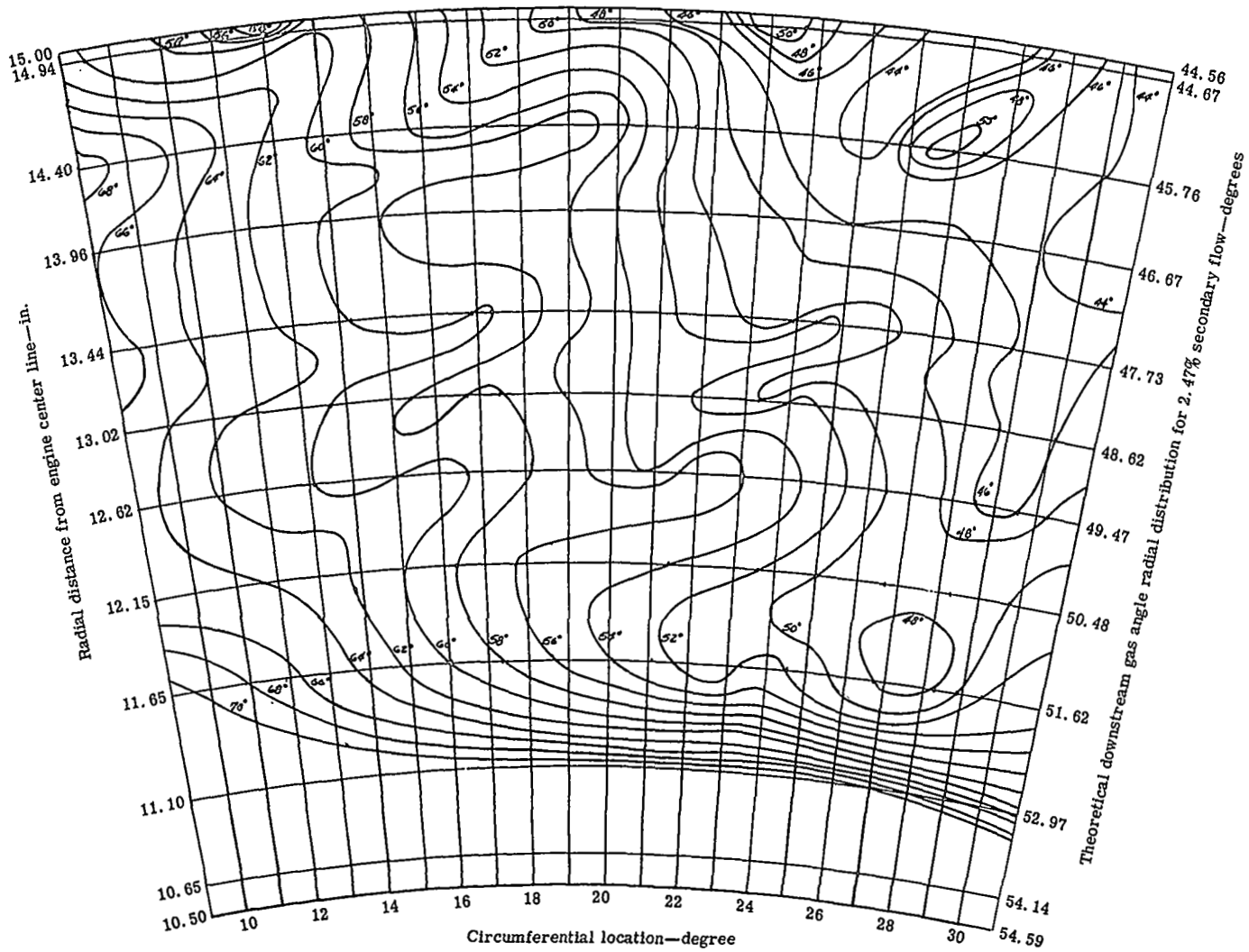


Figure 66. Contours of downstream gas angle measured from axial for the jet-flap blade (0.031-in. slot and $2.47\% \dot{m}_j/\dot{m}_p$).

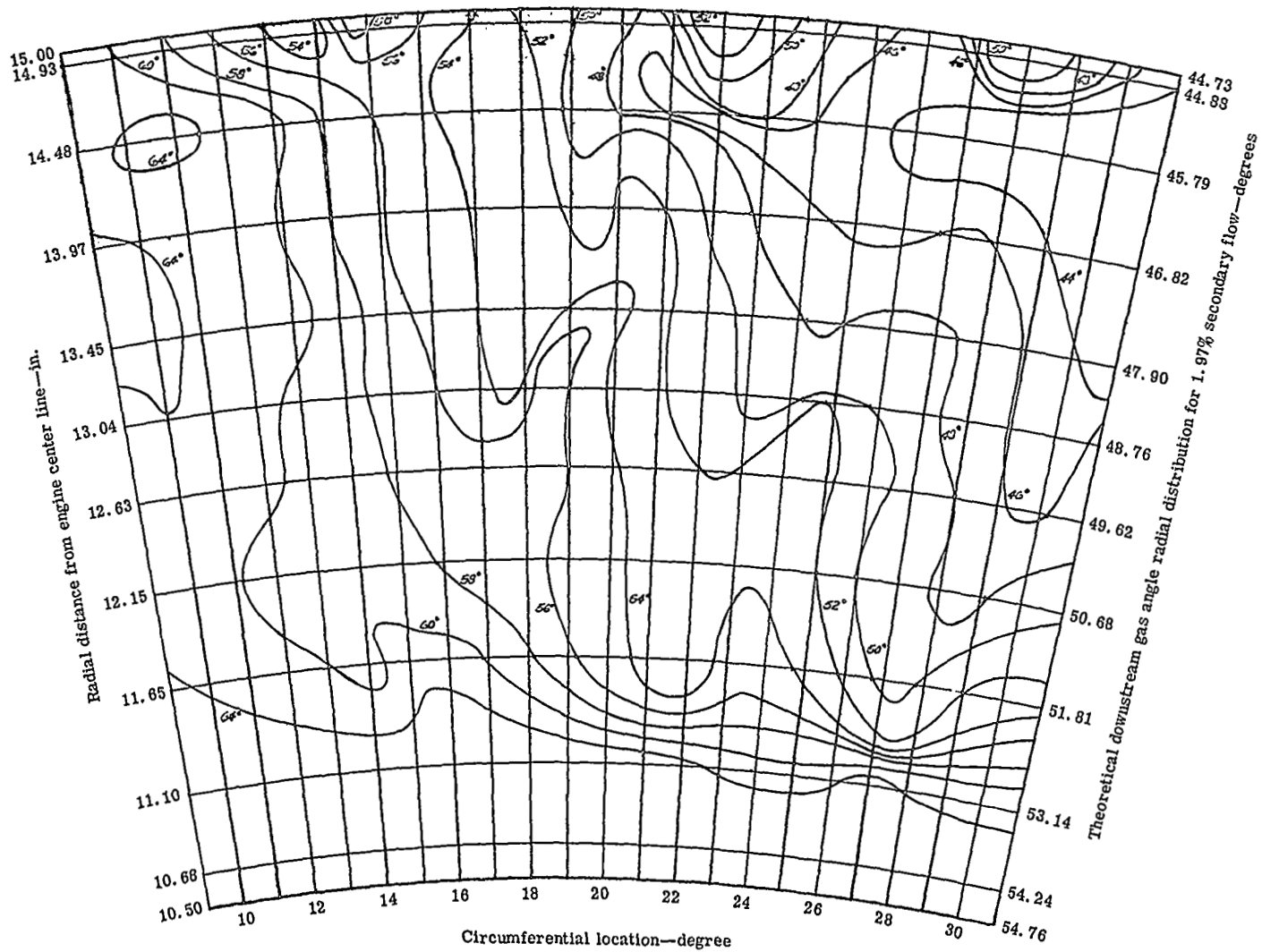


Figure 67. Contours of downstream gas angle measured from axial for the jet-flap blade (0.040-in. slot and 1.97% \dot{m}_j/\dot{m}_p).

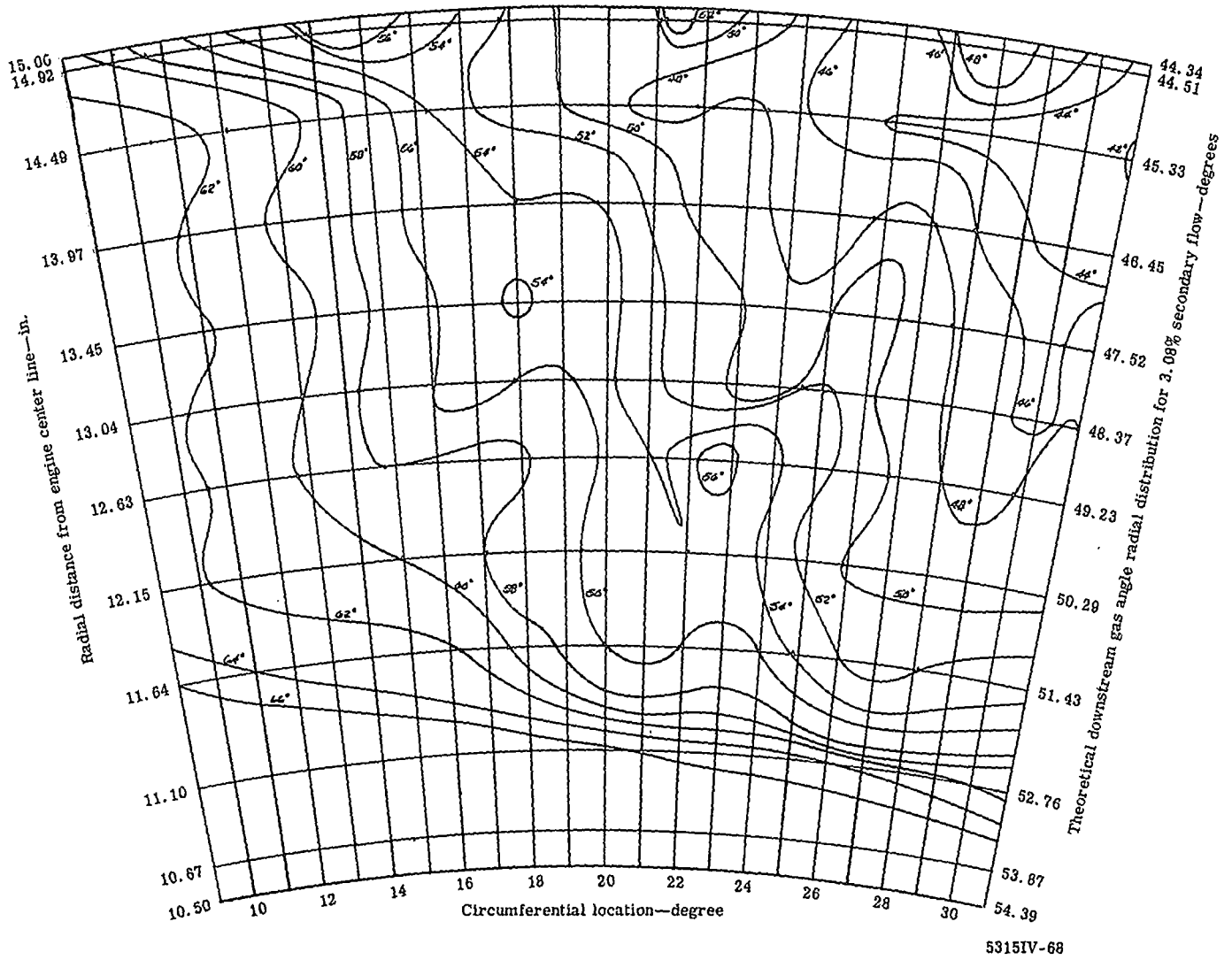
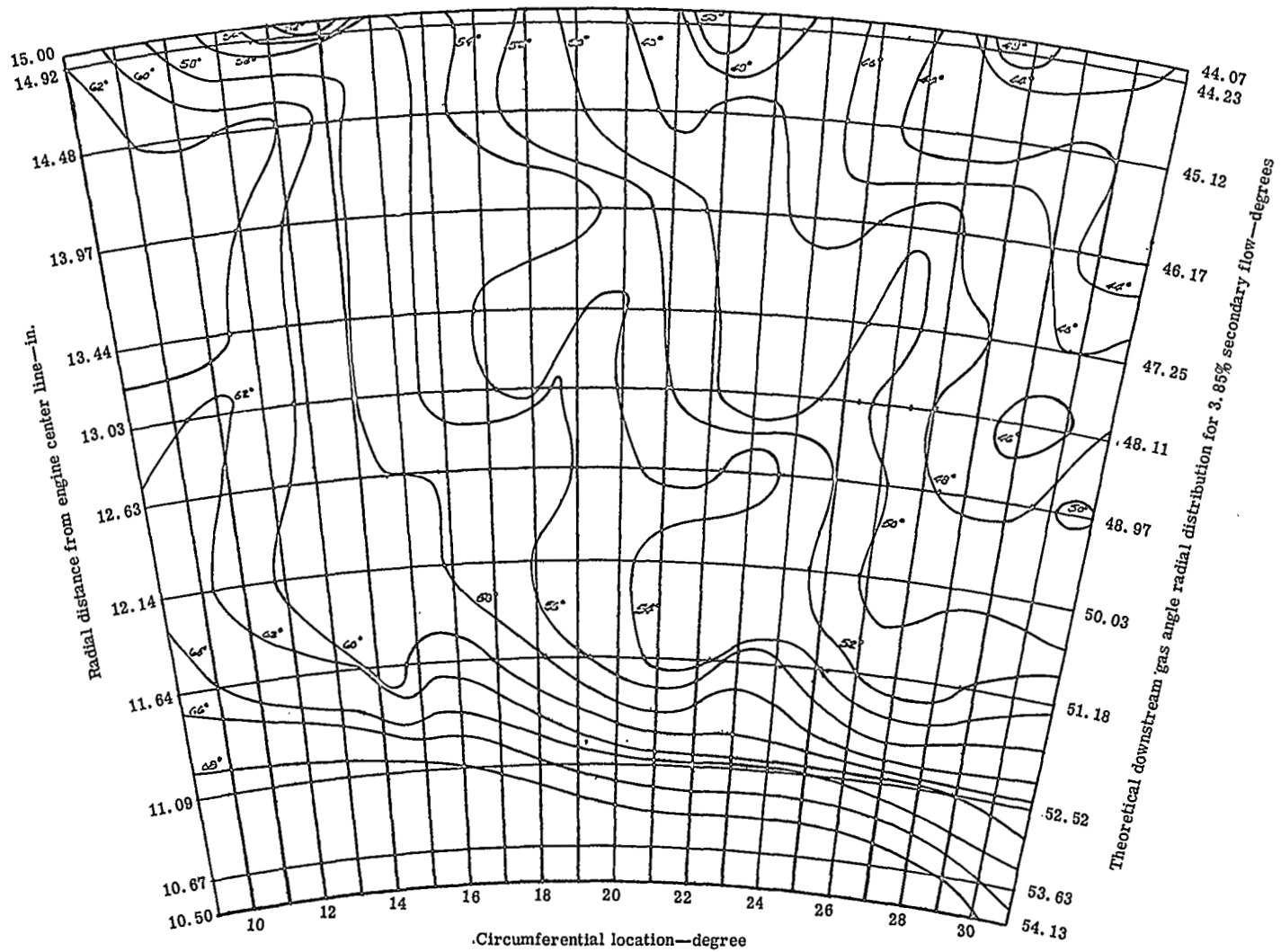
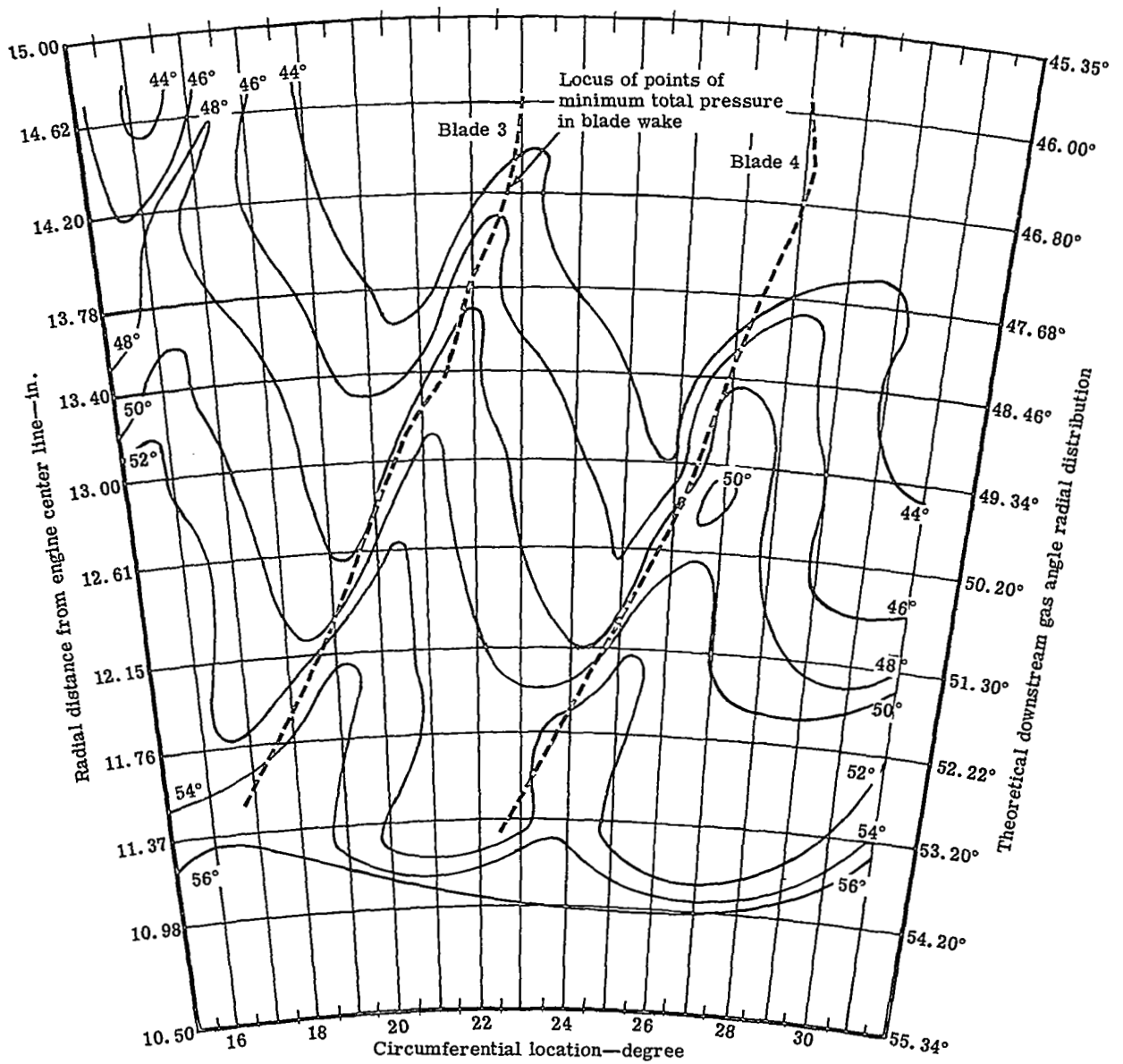


Figure 68. Contours of downstream gas angle measured from axial for the jet-flap blade (0.040-in. slot and 3.08% \dot{m}_j/\dot{m}_p).



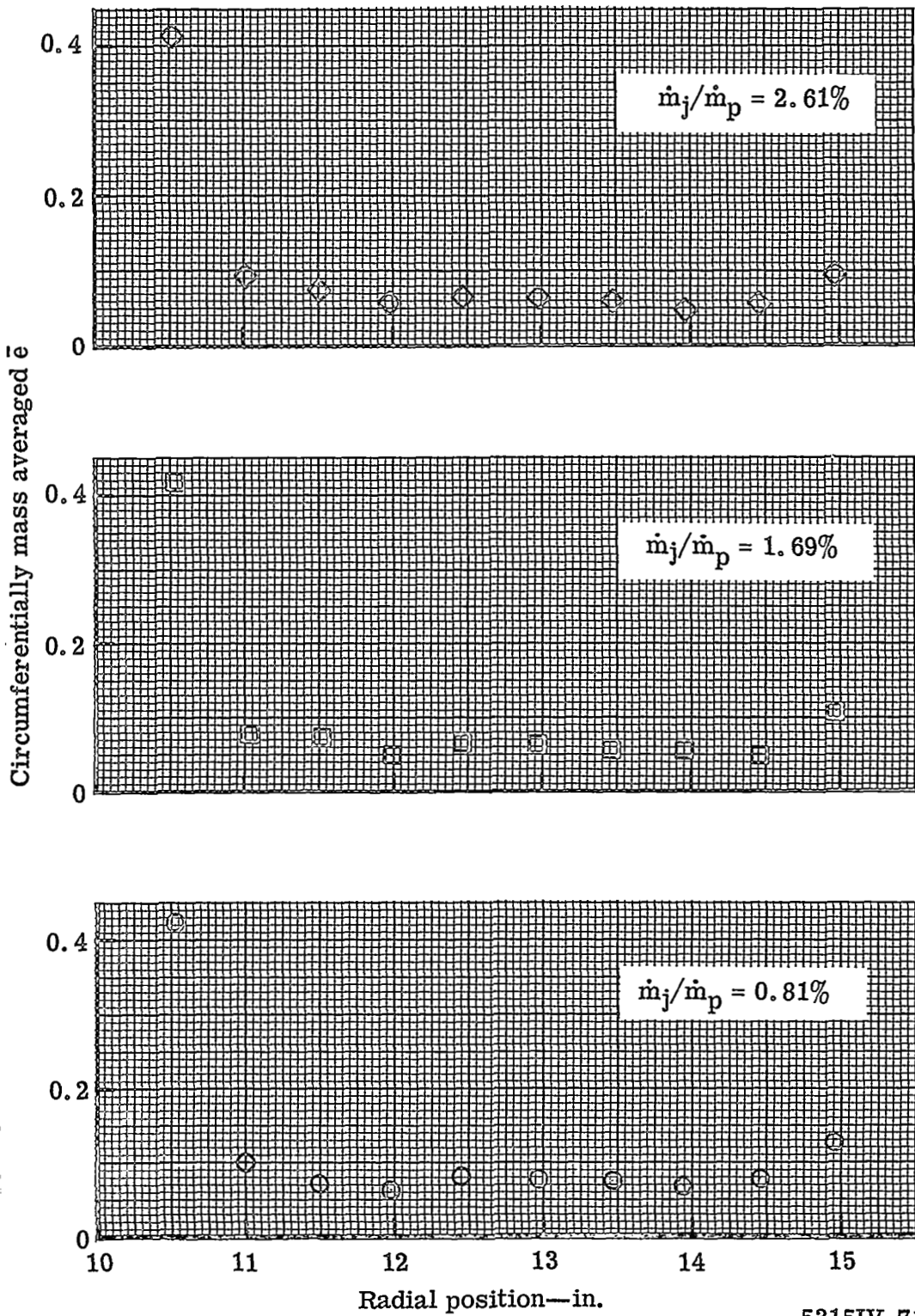
5315IV-69

Figure 69. Contours of downstream gas angle measured from axial for the jet-flap blade (0.040-in. slot and 3.85% \dot{m}_j/\dot{m}_p).



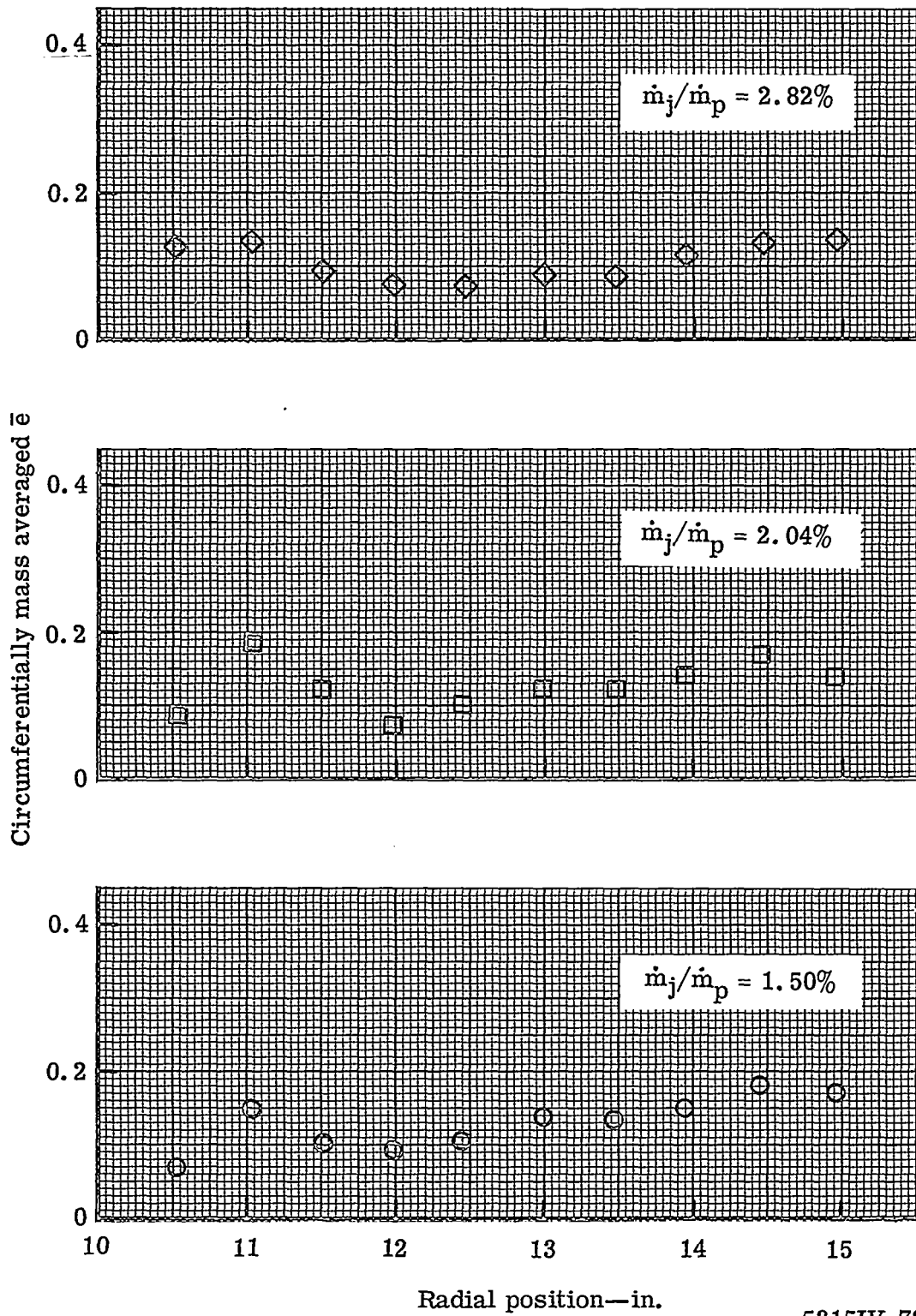
5315

Figure 70. Contours of downstream gas angle measured from axial for the plain blade at Station 4.



5315IV-71

Figure 71. Radial variation of circumferentially mass averaged \bar{e} at Station 3-0.022-in. slot.



5315IV-72

Figure 72. Radial variation of circumferentially mass averaged \bar{e} at Station 3—0.031-in. slot.

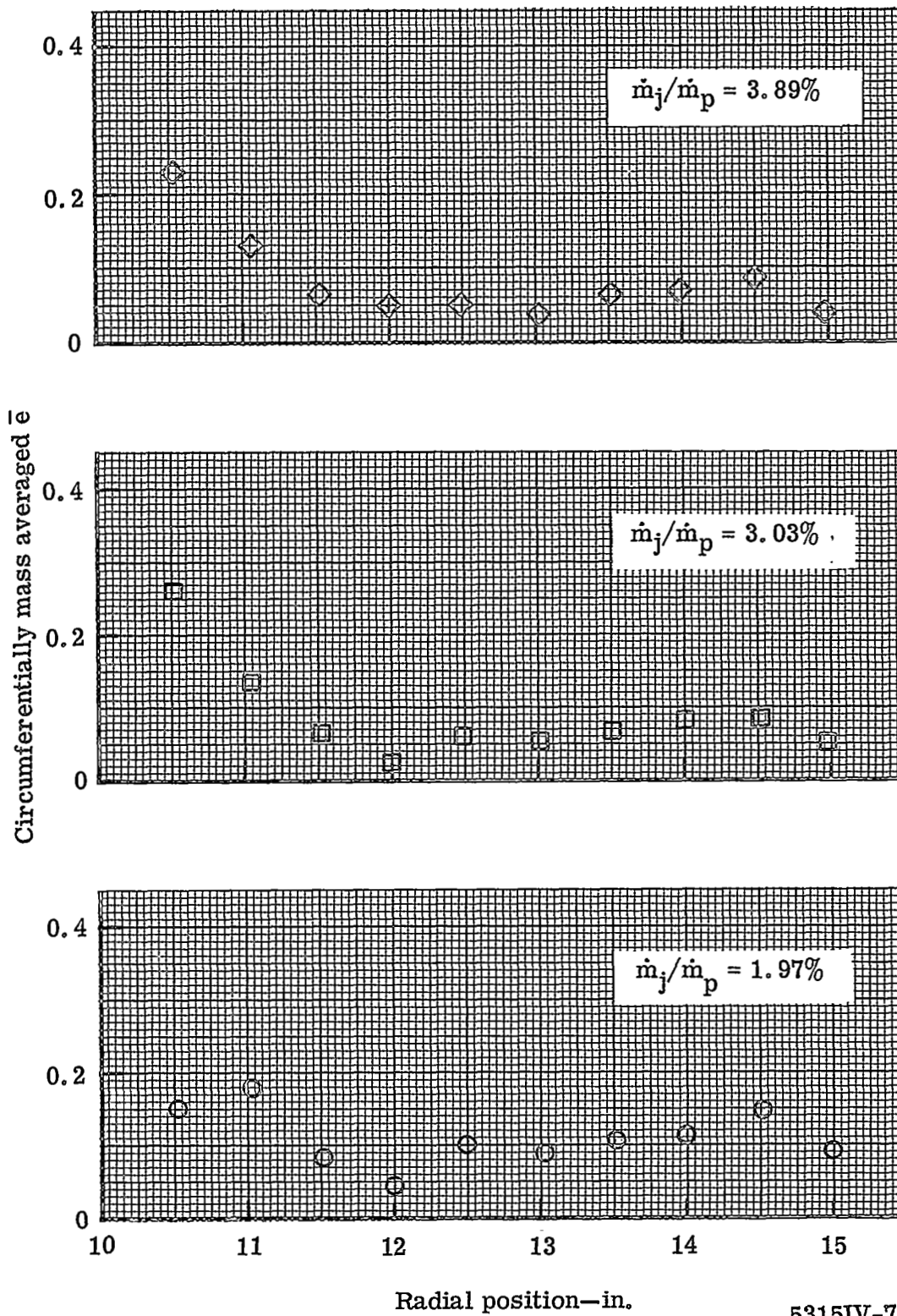


Figure 73. Radial variation of circumferentially mass averaged \bar{e} at Station 3—0.040-in. slot.

5315IV-73

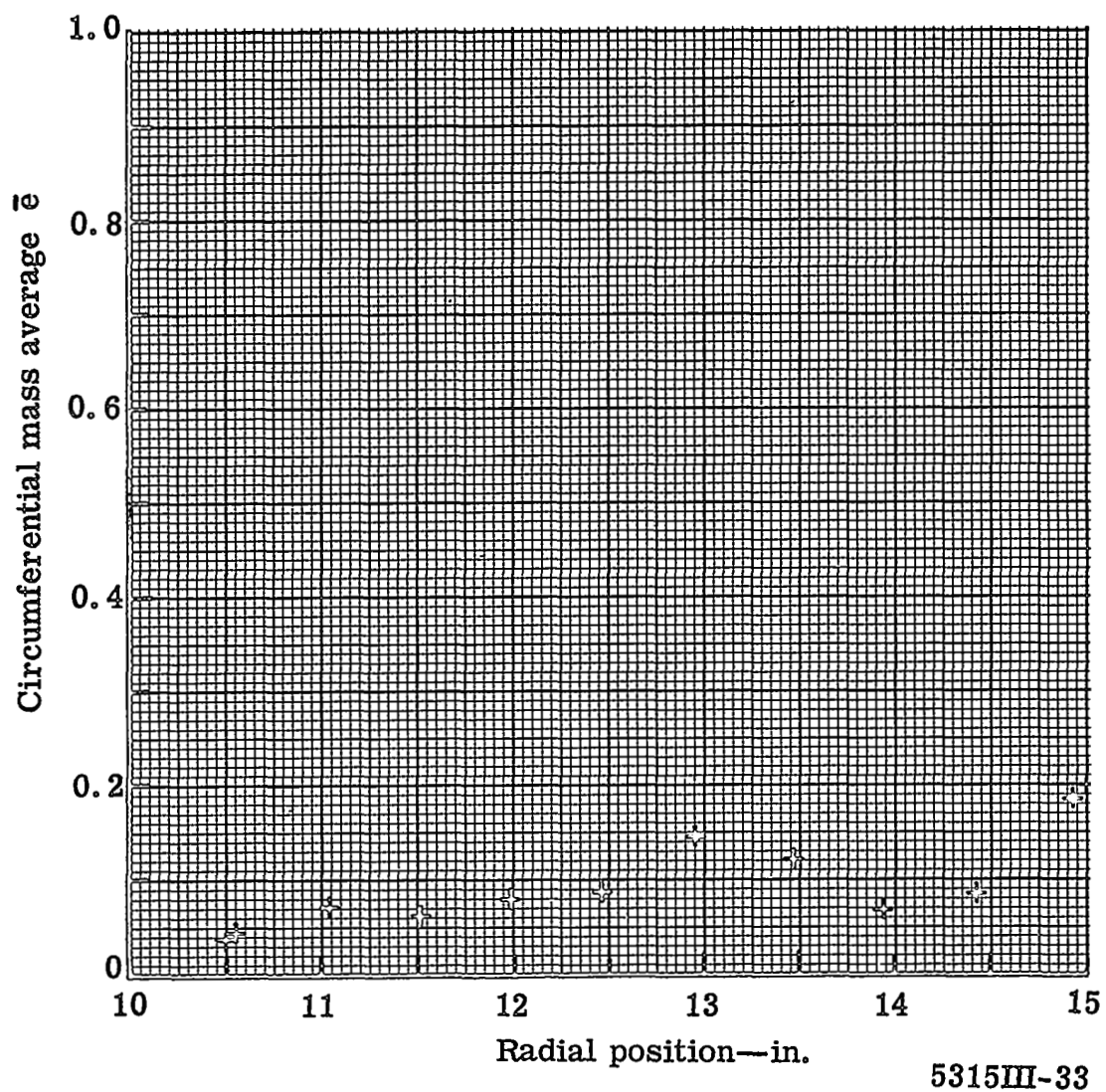
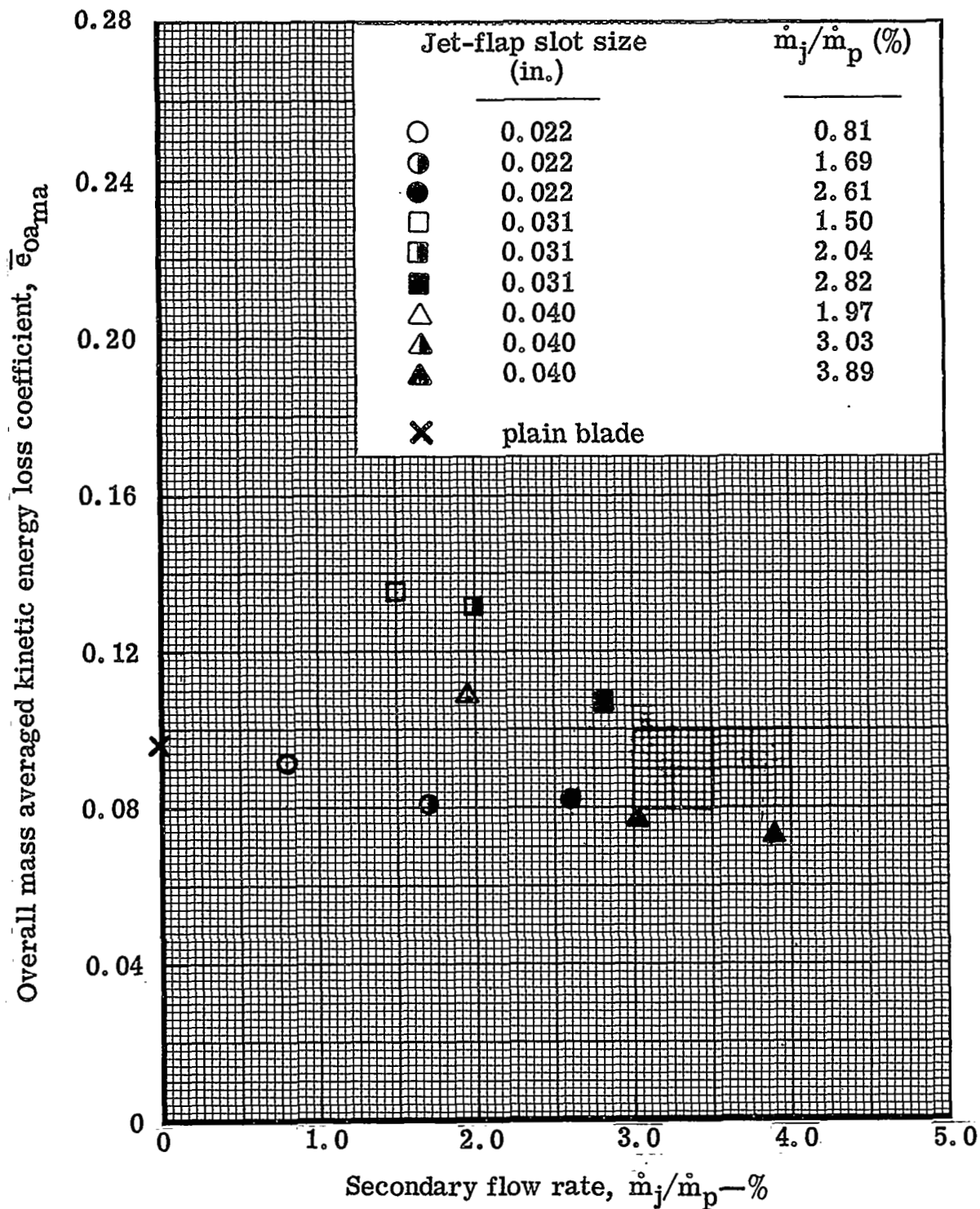


Figure 74. Radial variation of circumferentially mass averaged \bar{e} at Station 3—plain blade.



5315IV-75

Figure 75. Variation of overall mass averaged kinetic energy loss coefficient with percent secondary flow rate at the jet-flapped blade trailing edge.

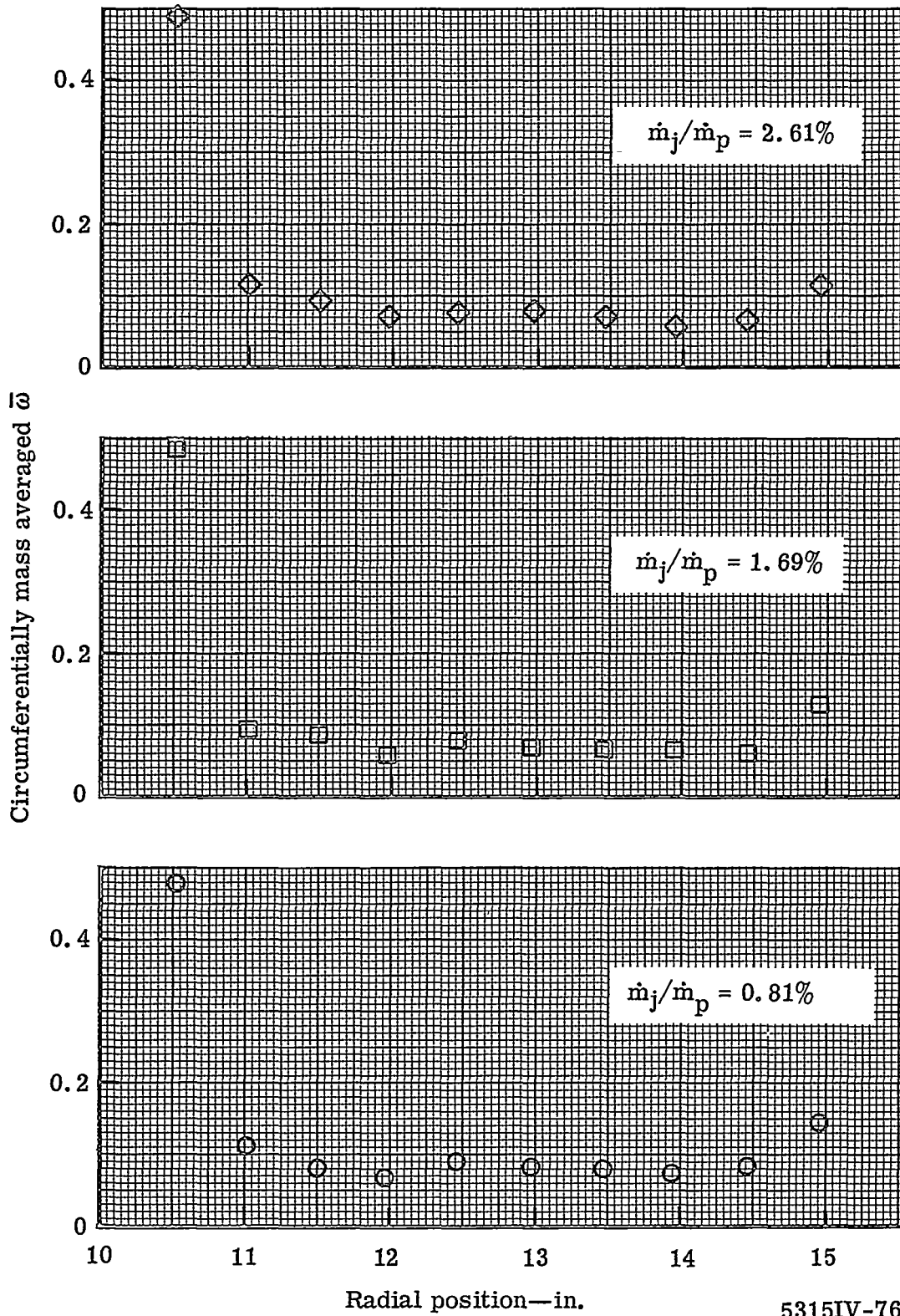
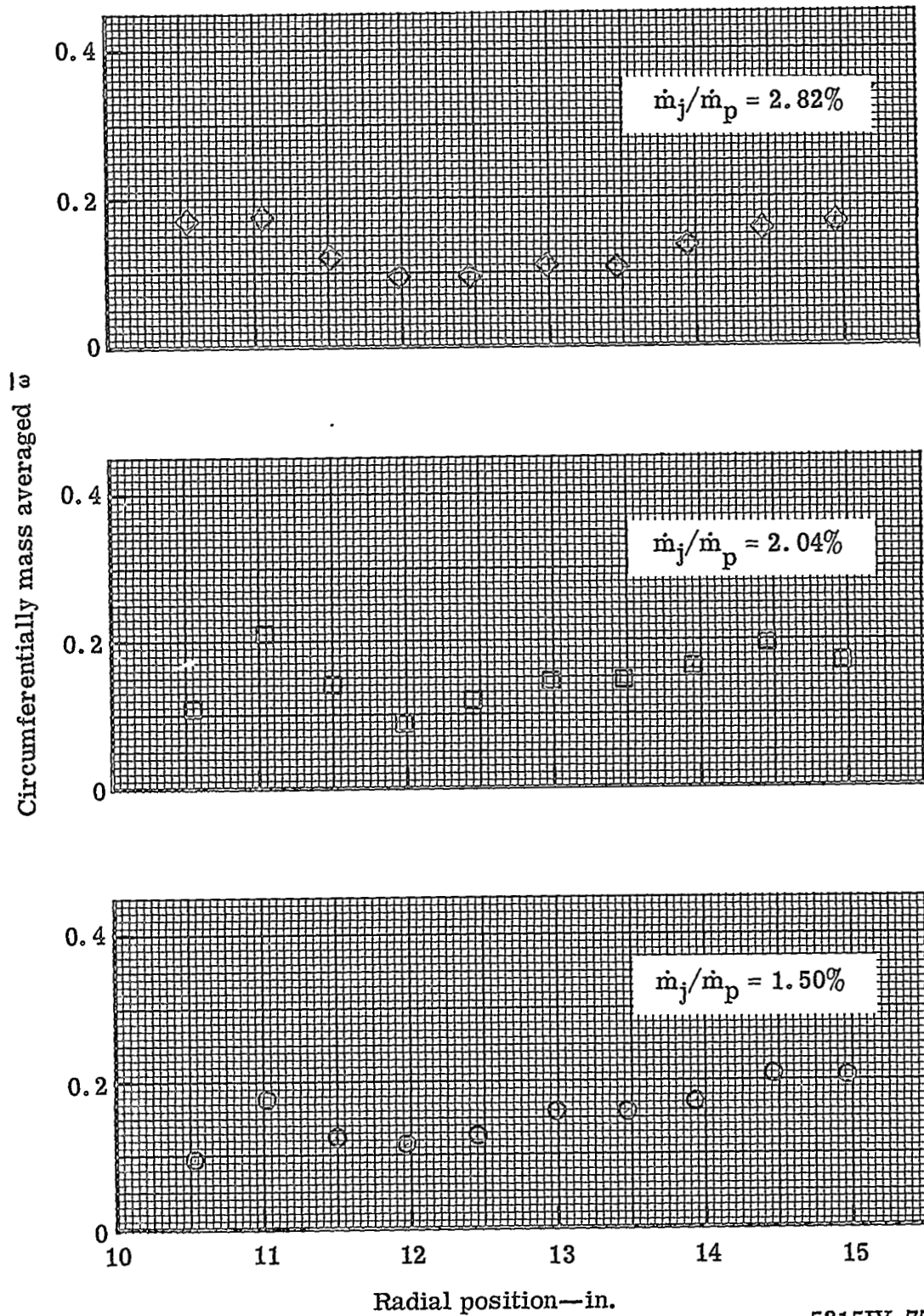
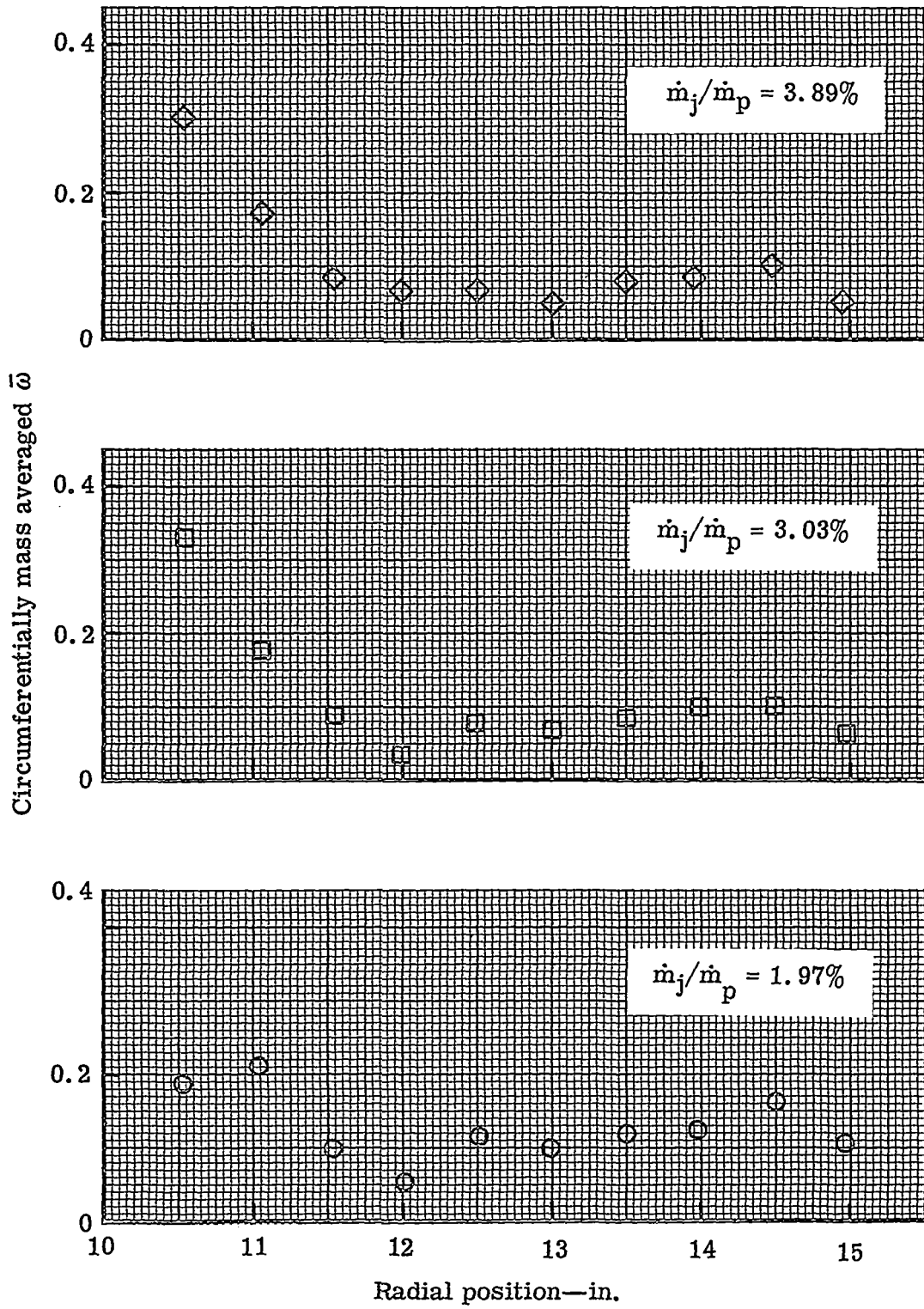


Figure 76. Radial variation of circumferentially mass averaged $\bar{\omega}$ at Station 3—0.022-in. slot.

5315IV-76



5315IV-77
 Figure 77. Radial variation of circumferentially mass averaged $\bar{\omega}$
 at Station 3—0.031-in. slot.



5315IV-78

Figure 78. Radial variation of circumferentially mass averaged $\bar{\omega}$ at Station 3—0.040-in. slot.

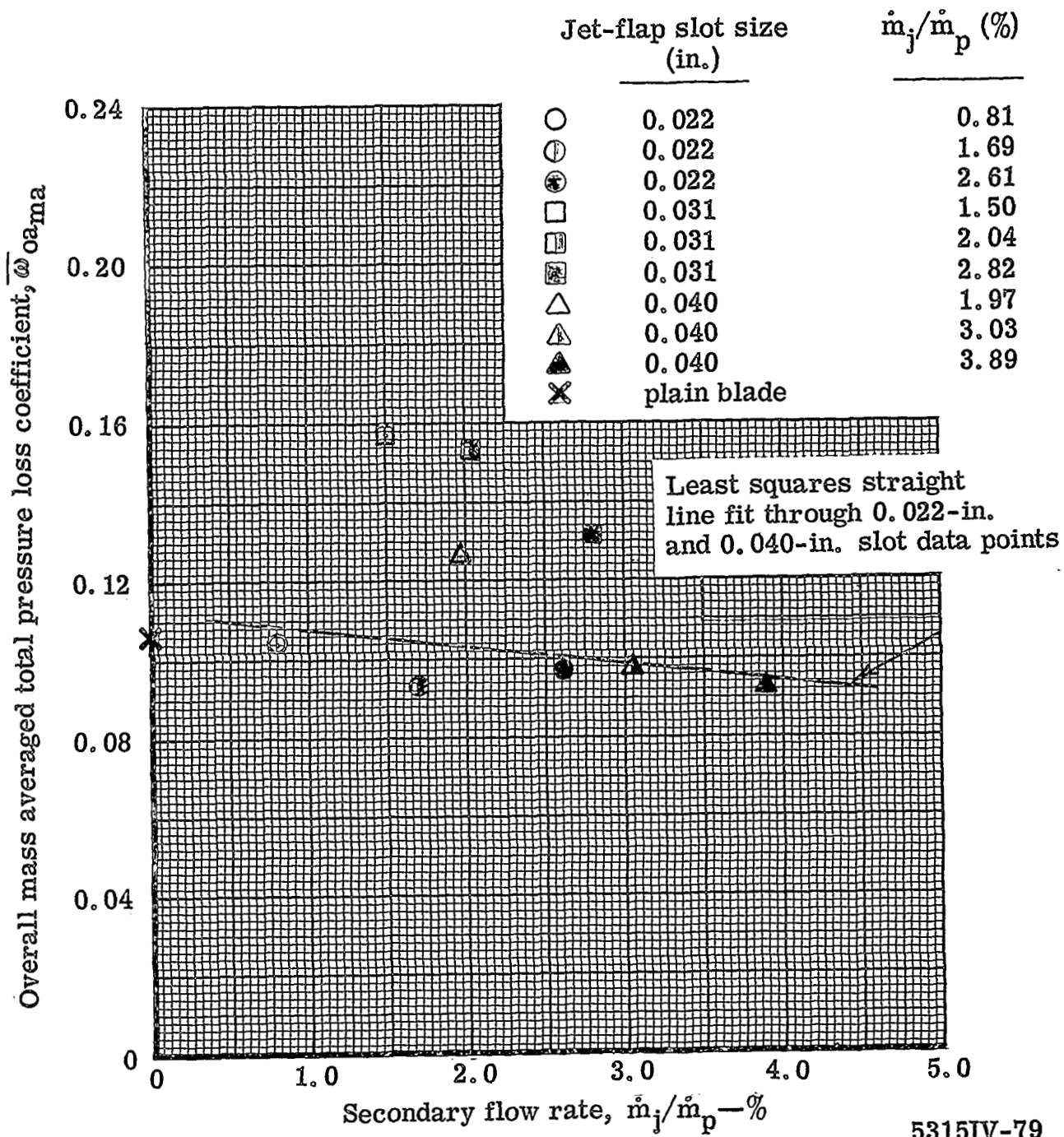
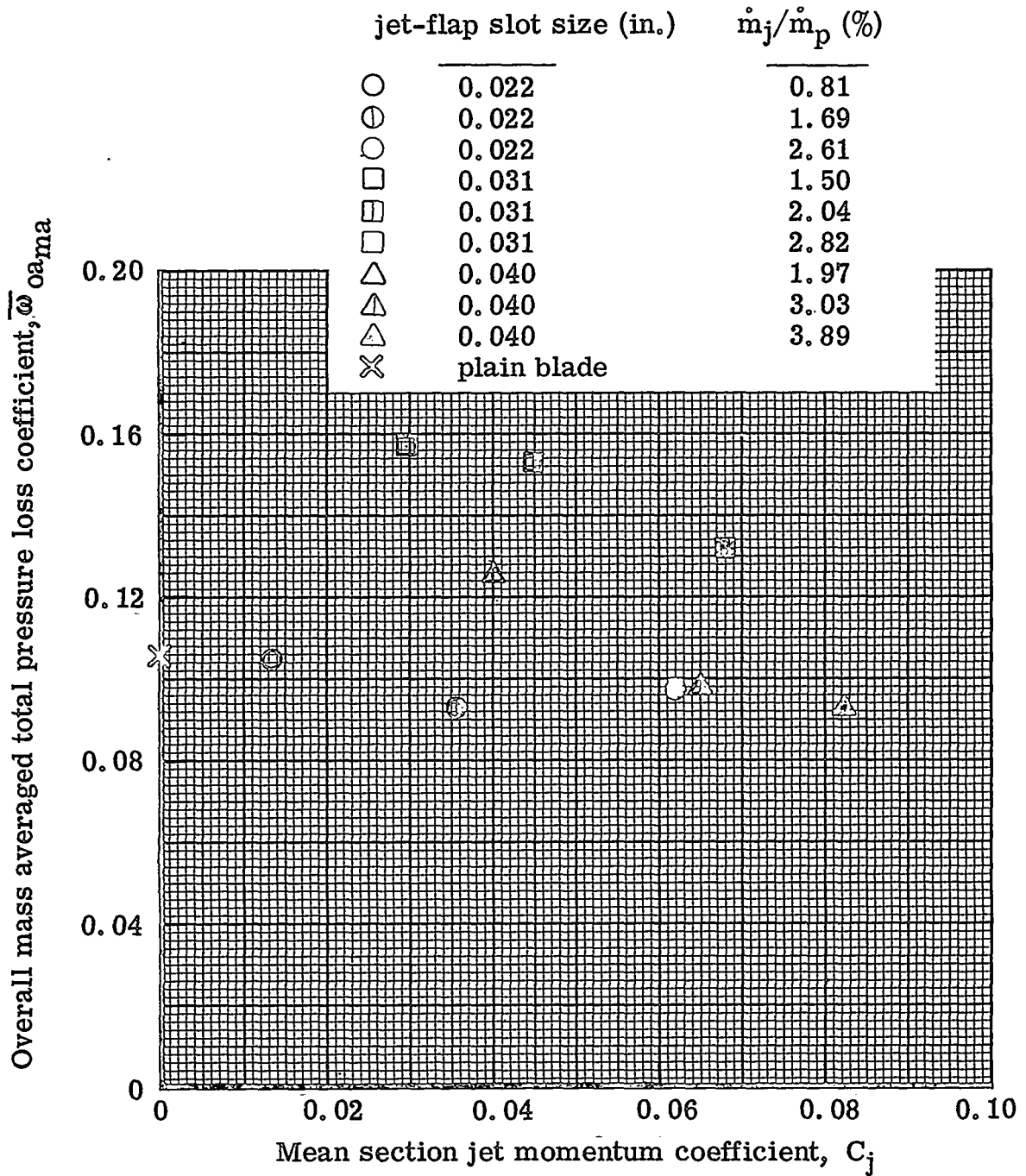


Figure 79. Variation of overall mass averaged total pressure loss coefficient with percent secondary flow rate at the jet-flapped blade trailing edge.



5315IV-80

Figure 80. Variation of trailing edge (Station 3) overall mass averaged total pressure loss coefficient with mean section jet momentum coefficient.

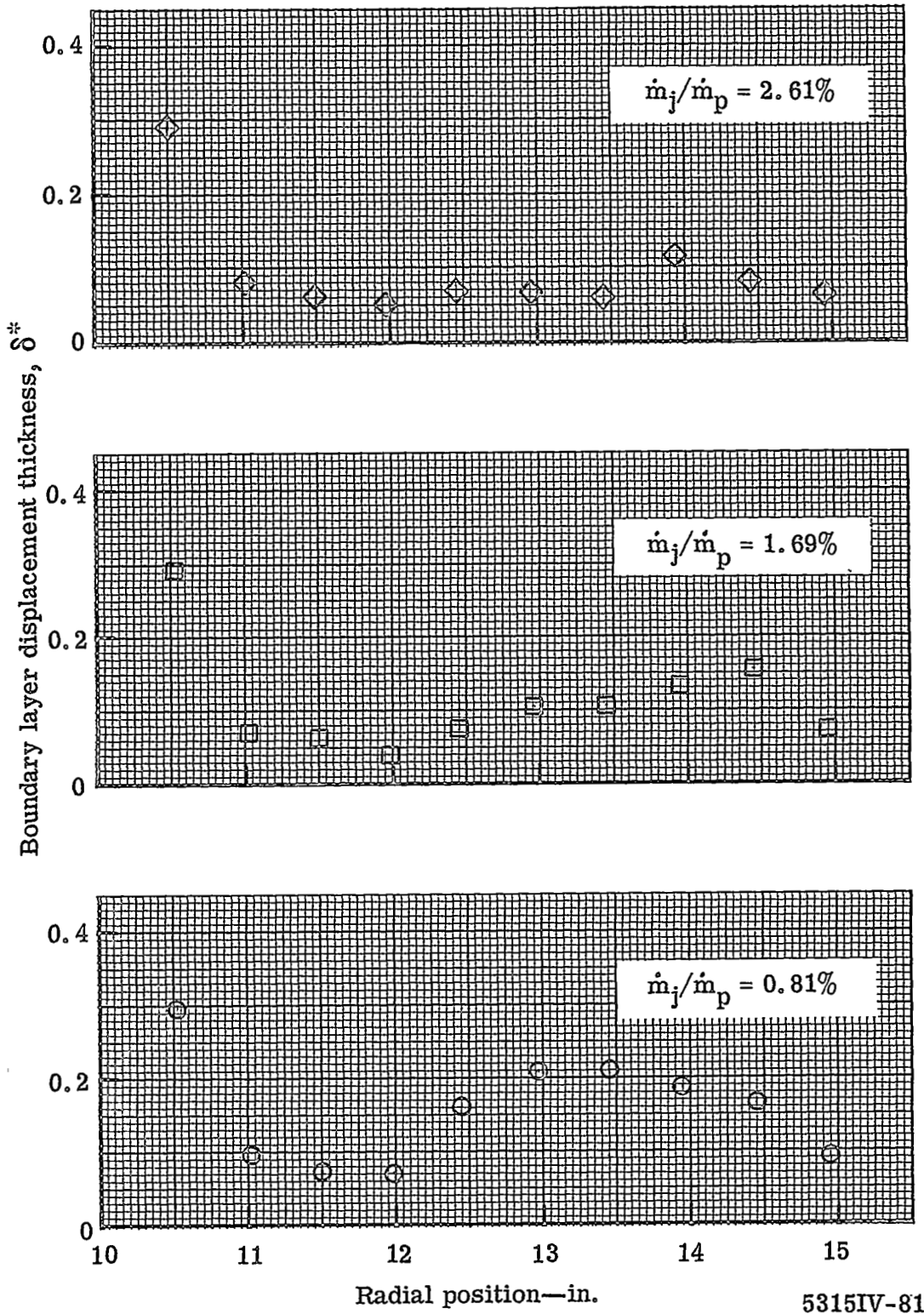
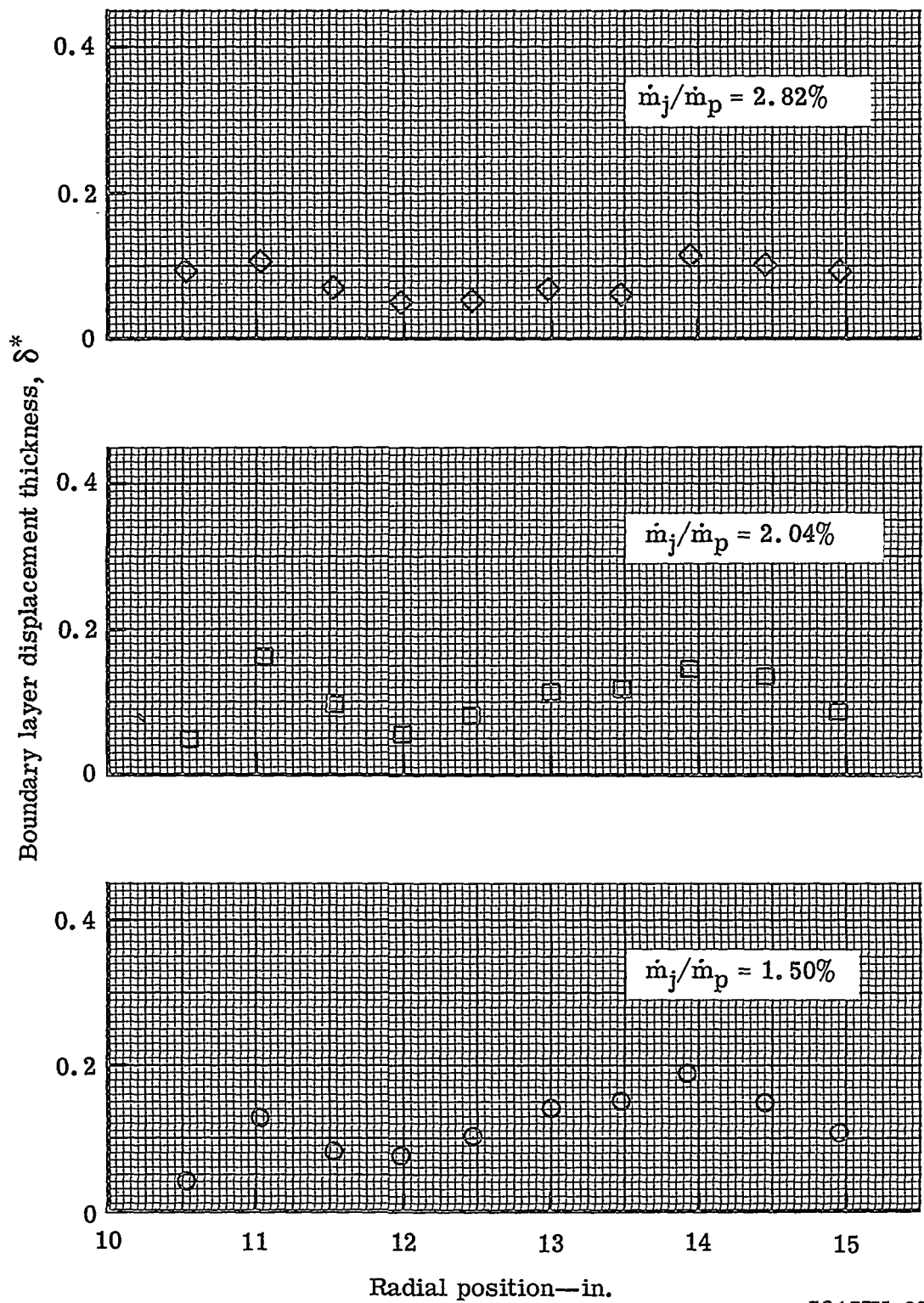


Figure 81. Radial variation of boundary layer displacement thickness at Station 3—0.022-in. slot.

5315IV-81



5315IV-82

Figure 82. Radial variation of boundary layer displacement thickness at Station 3—0.031-in. slot.

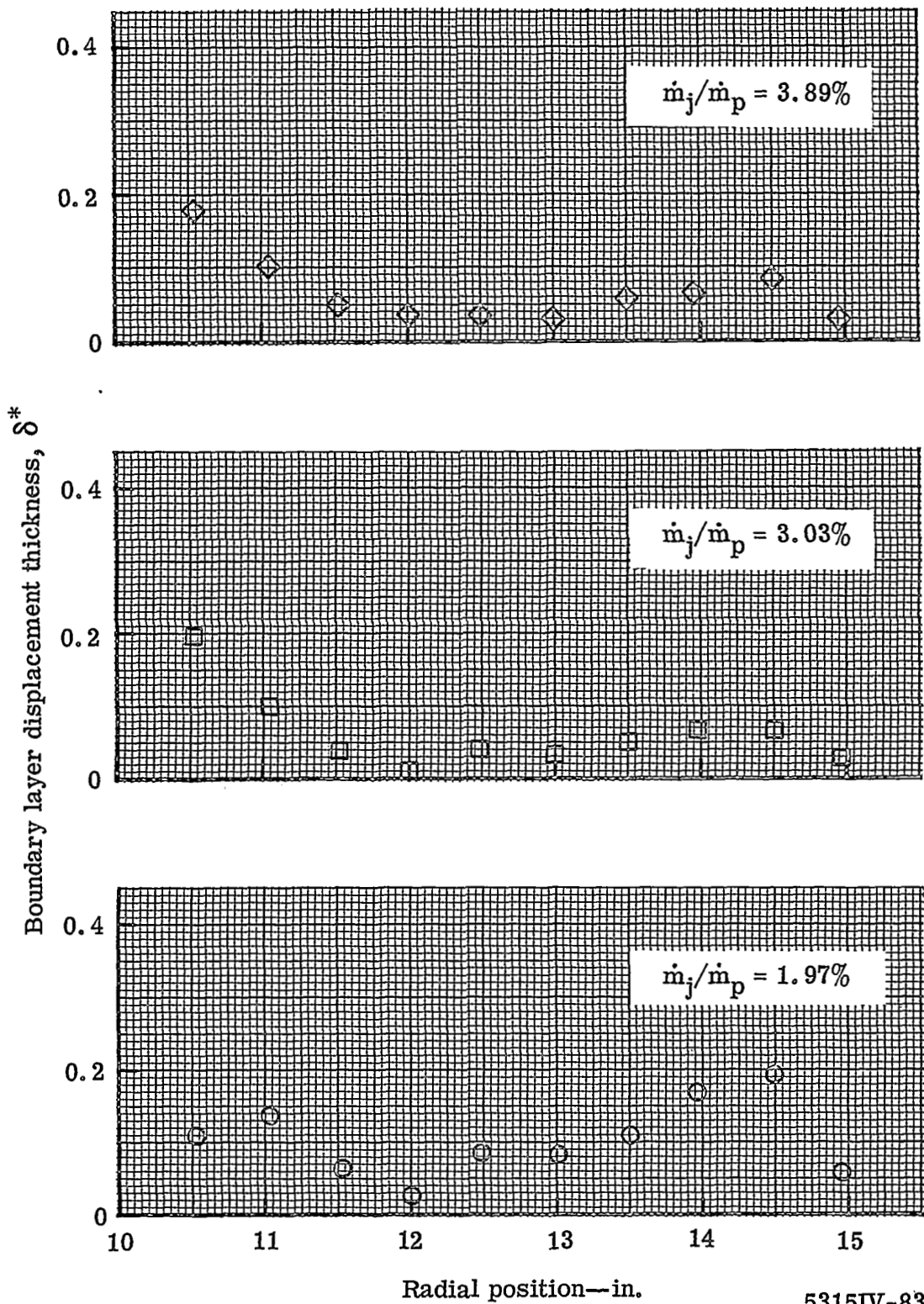
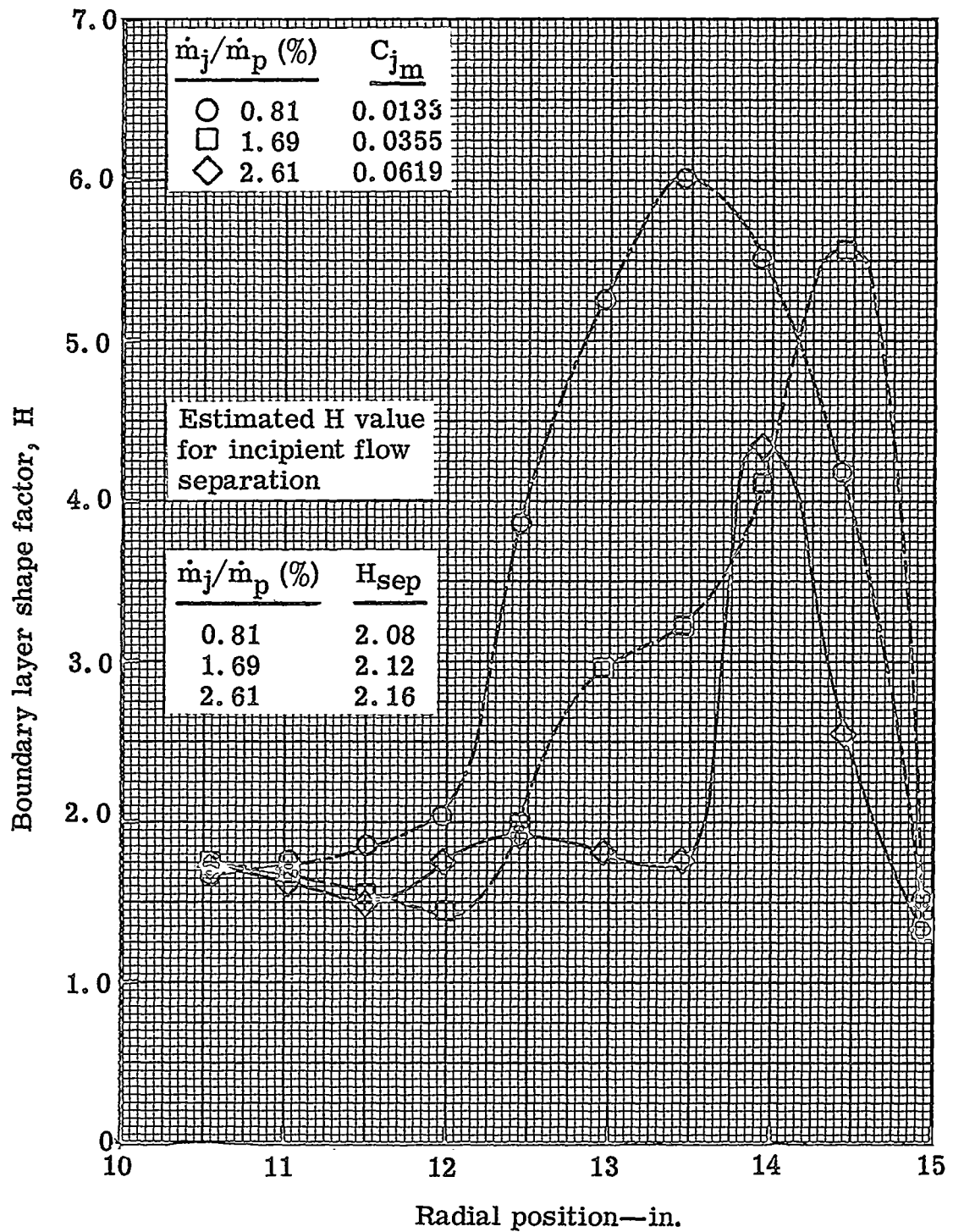


Figure 83. Radial variation of boundary layer displacement thickness at Station 3—0.040-in. slot.



5315IV-84

Figure 84. Shape factor distribution at Station 3—0.022-in. slot.

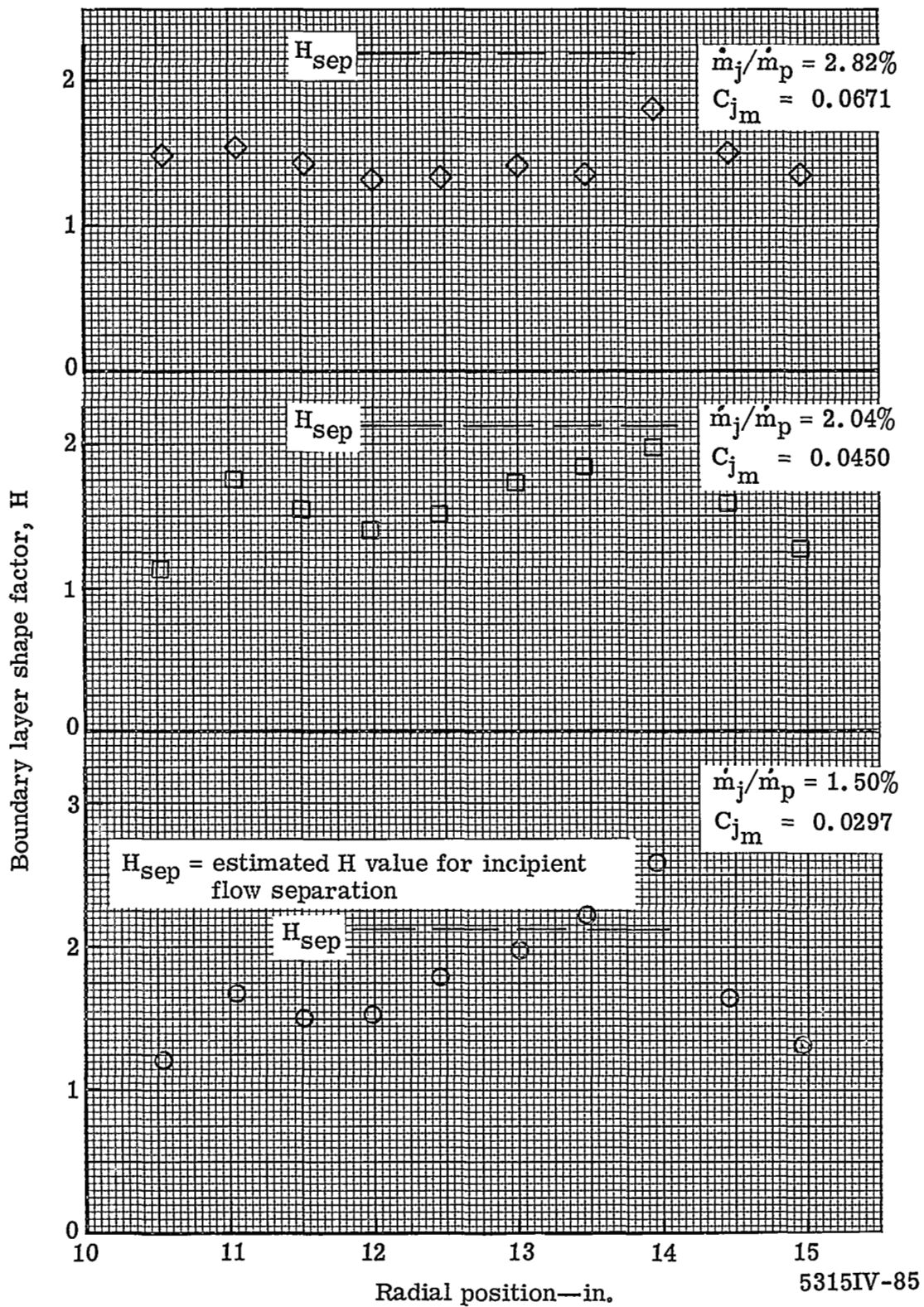


Figure 85. Radial variation of boundary layer shape factor at Station 3—0.031-in. slot.

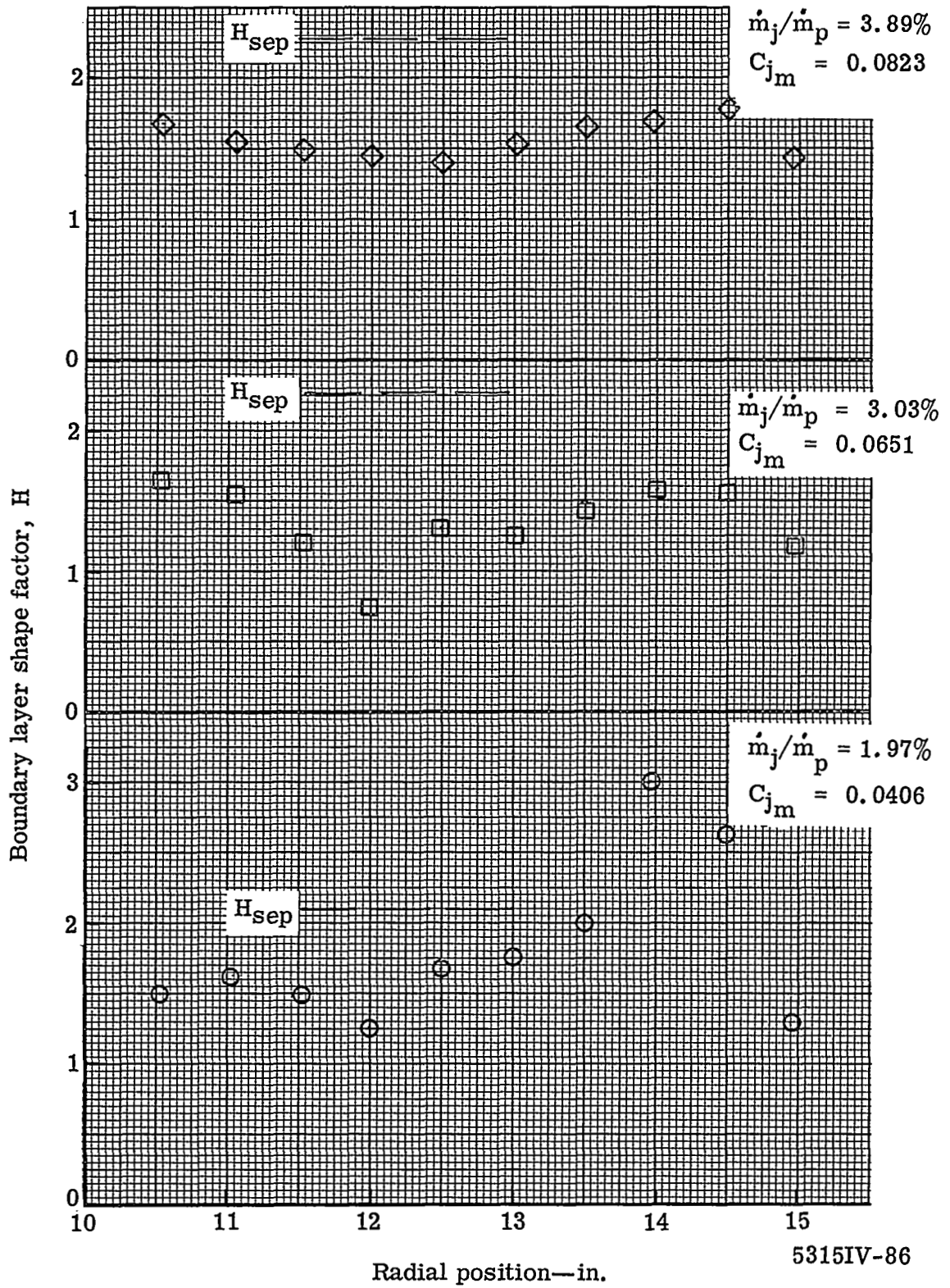
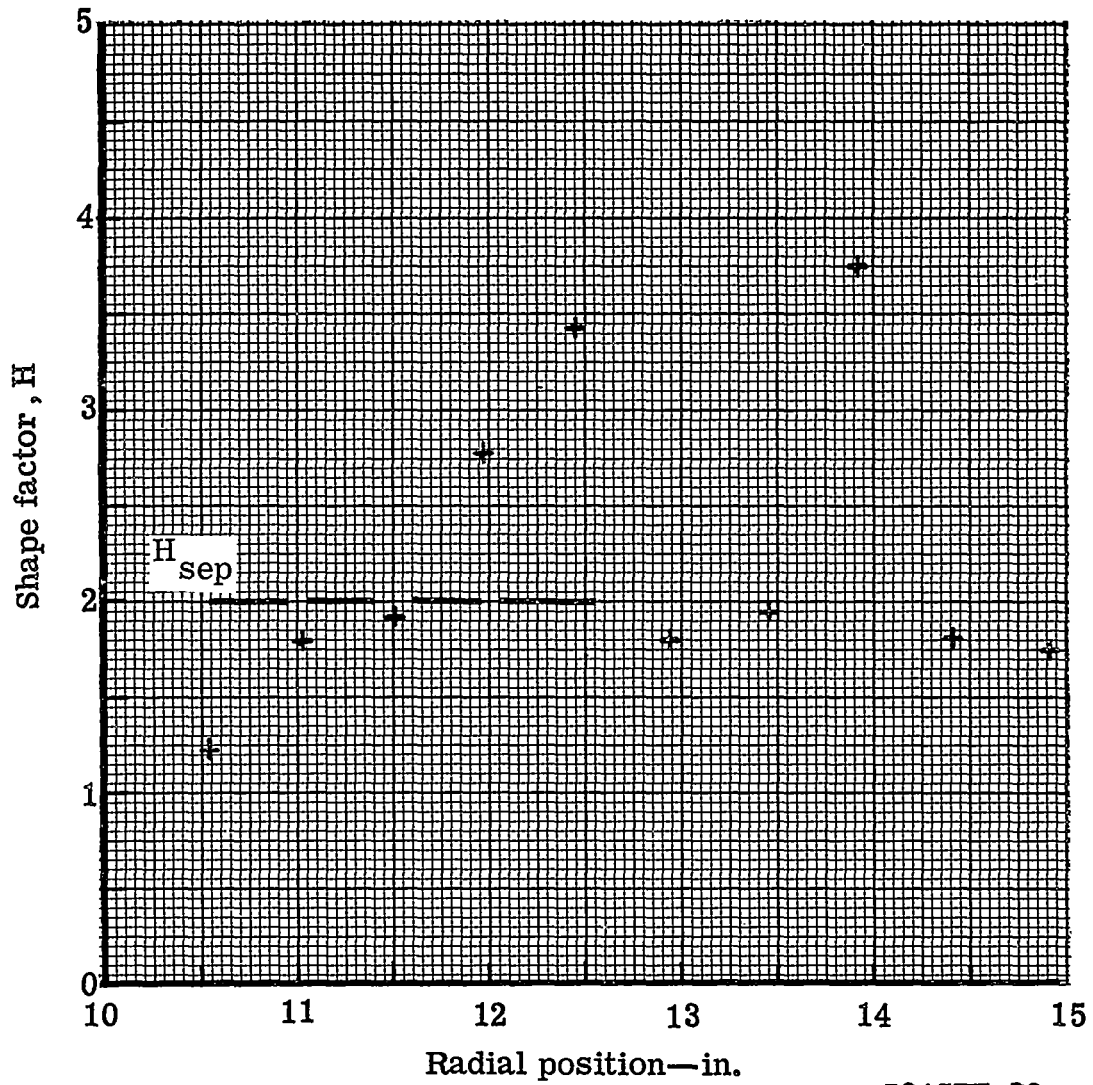
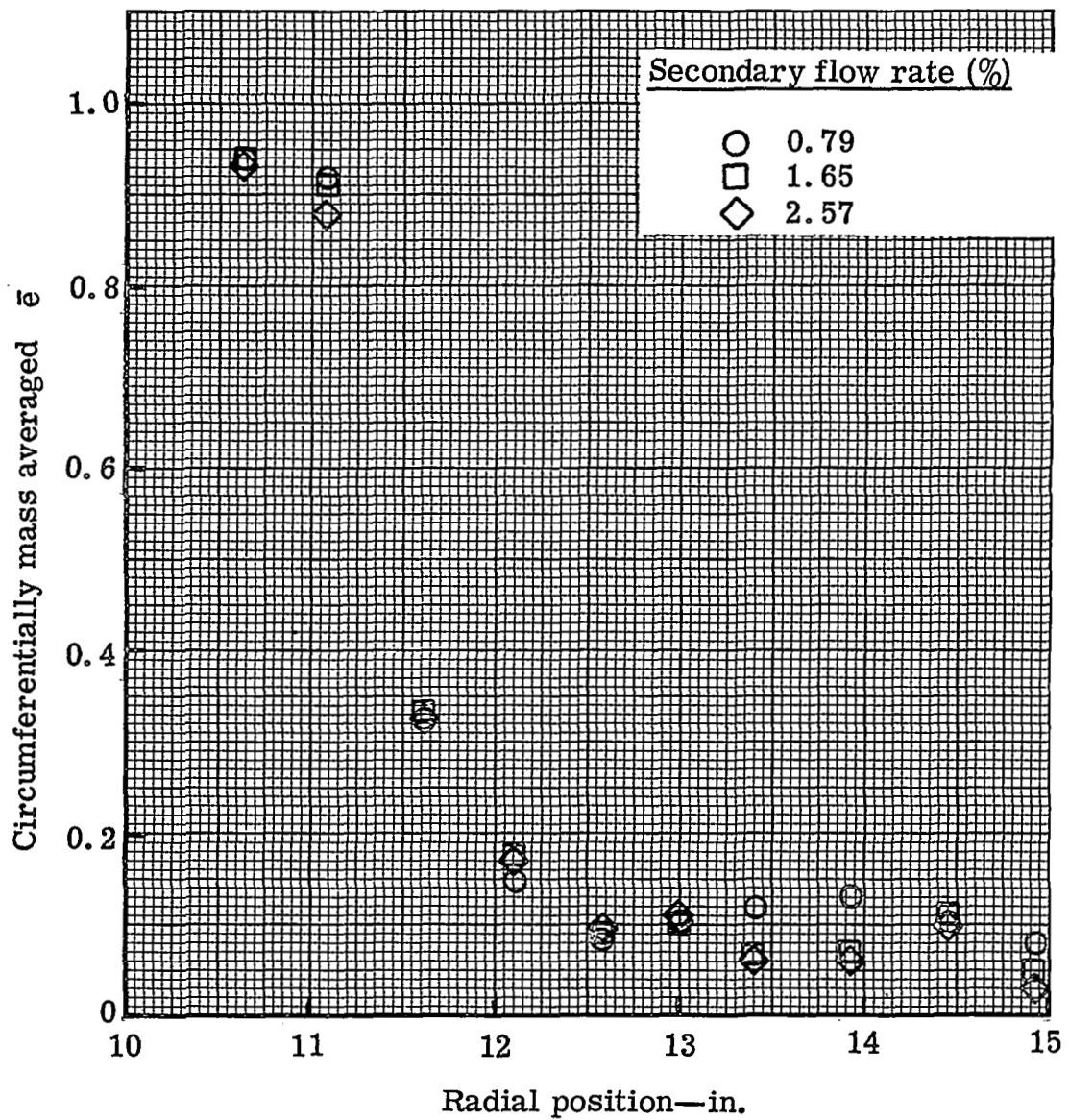


Figure 86. Radial variation of boundary layer shape factor at Station 3—0.040-in. slot.



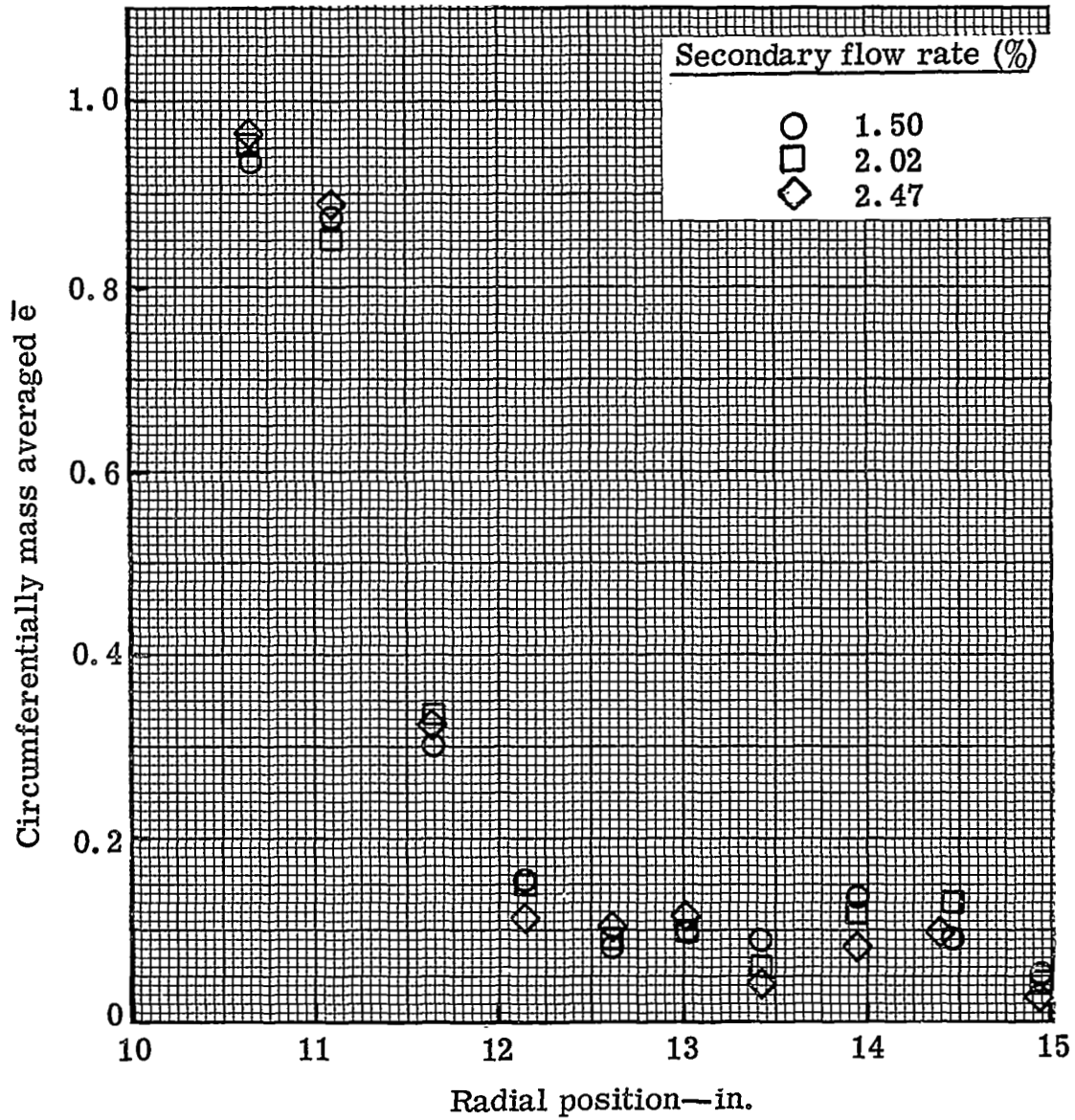
5315III-38

Figure 87. Radial variation of boundary layer shape factor at Station 3—plain blade.



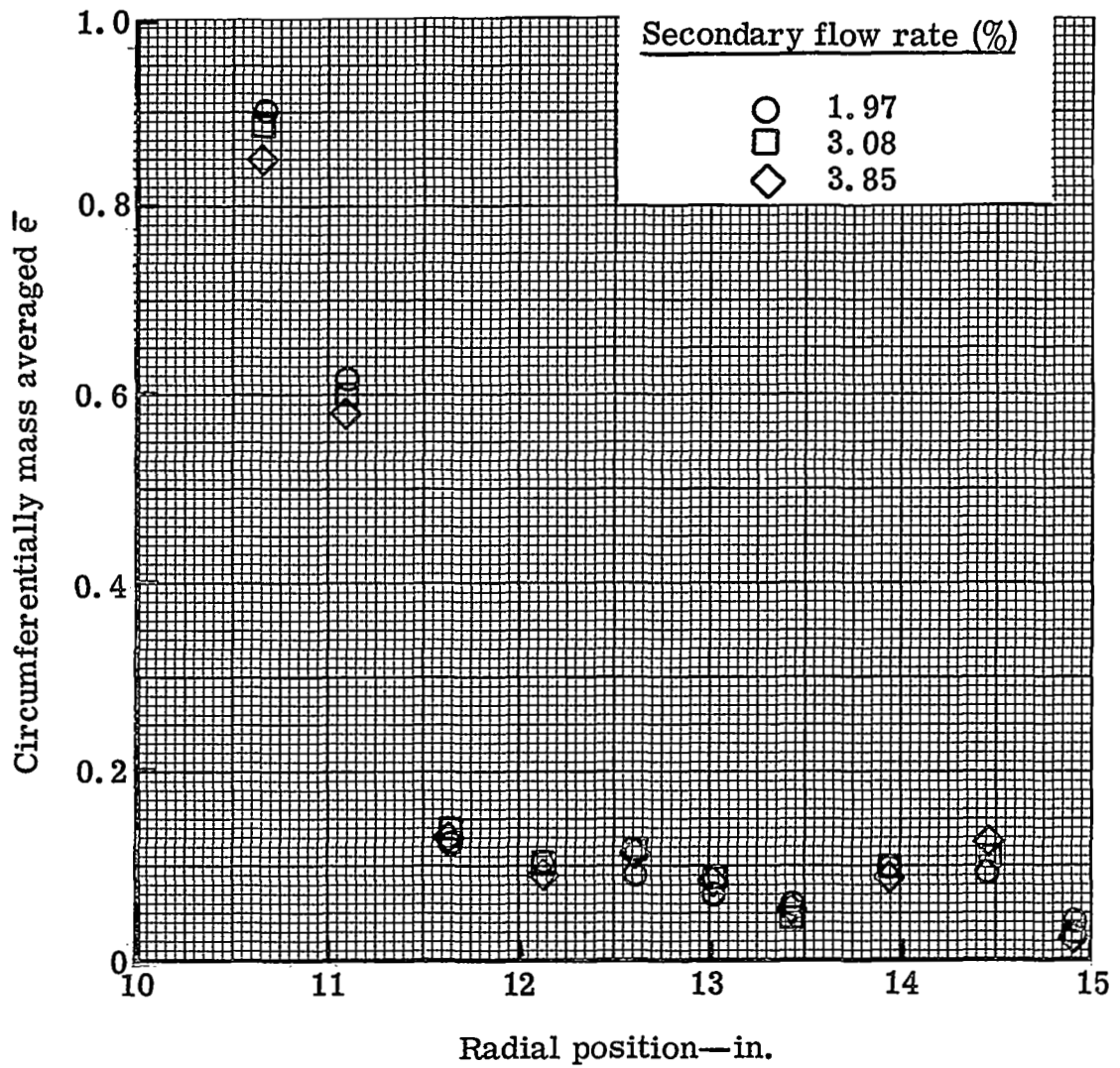
5315IV-88

Figure 88. Circumferentially mass averaged kinetic energy loss coefficient distribution at Station 4—0.022-in. slot.



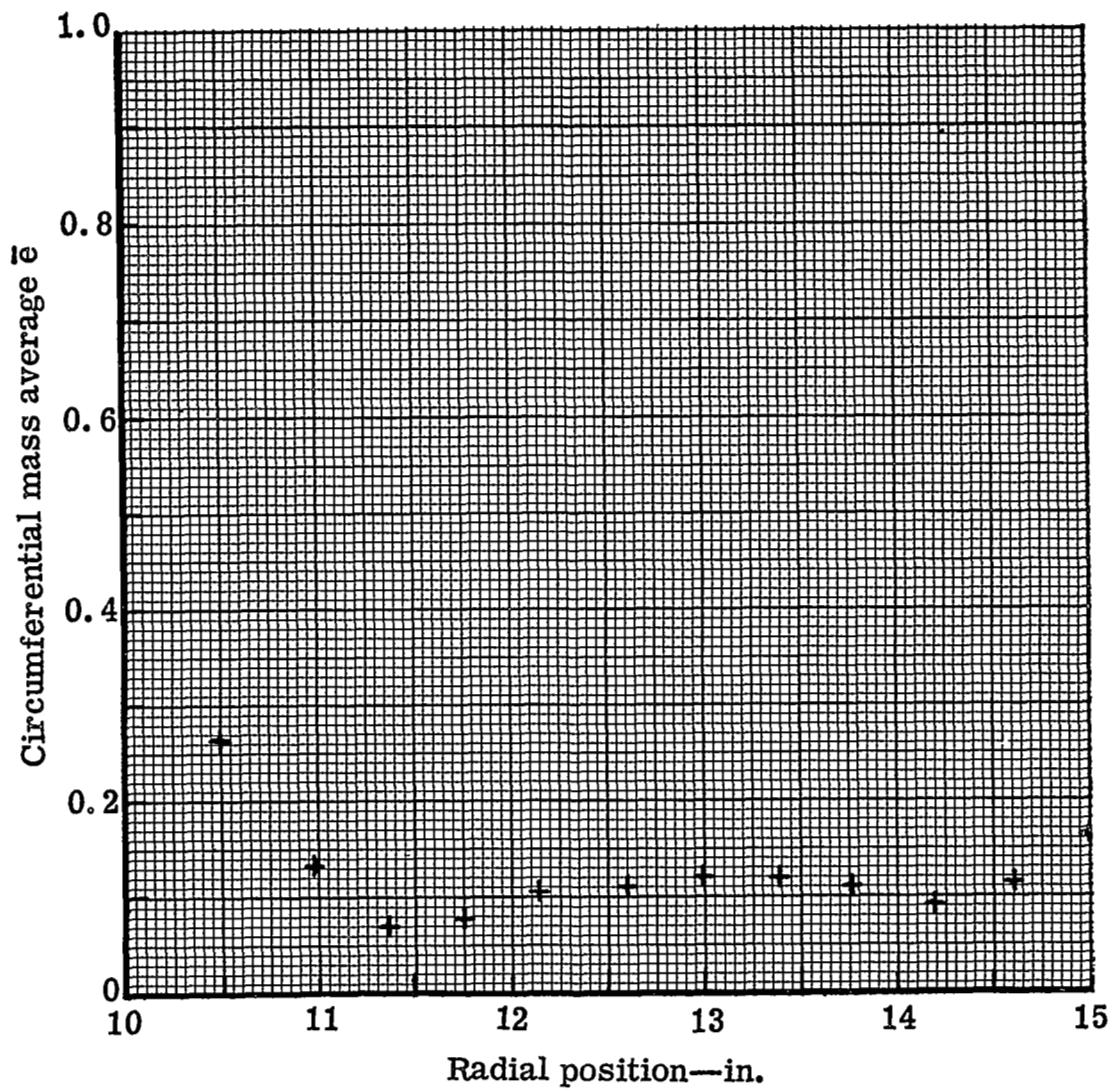
5315IV-89

Figure 89. Circumferentially mass averaged kinetic energy loss coefficient distribution at Station 4—0.031-in. slot.



5315IV-90

Figure 90. Circumferentially mass averaged kinetic energy loss coefficient distribution at Station 4—0.040-in. slot.



5315III-40

Figure 91. Circumferentially mass averaged kinetic energy loss coefficient distribution at Station 4—plain blade.

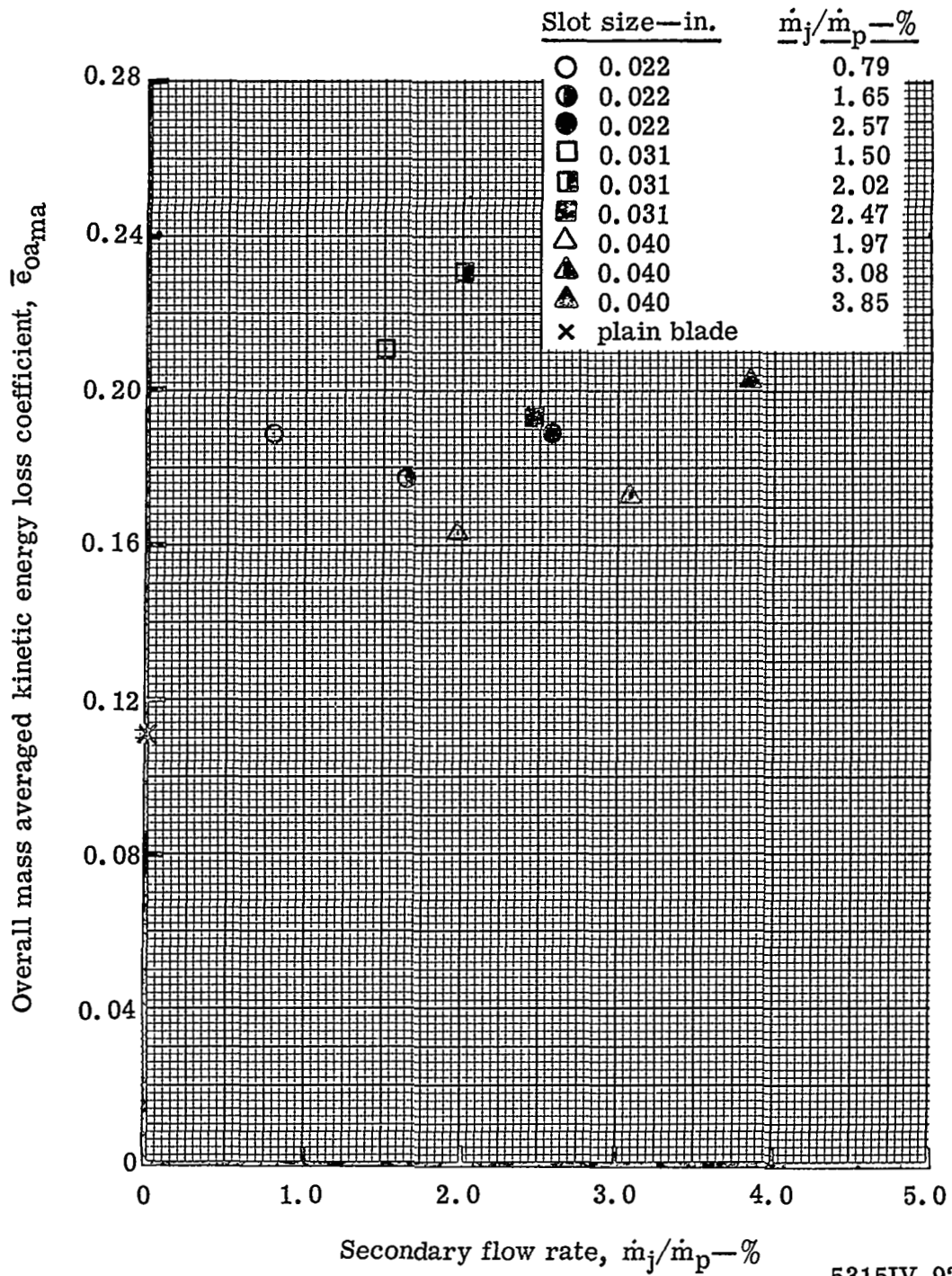
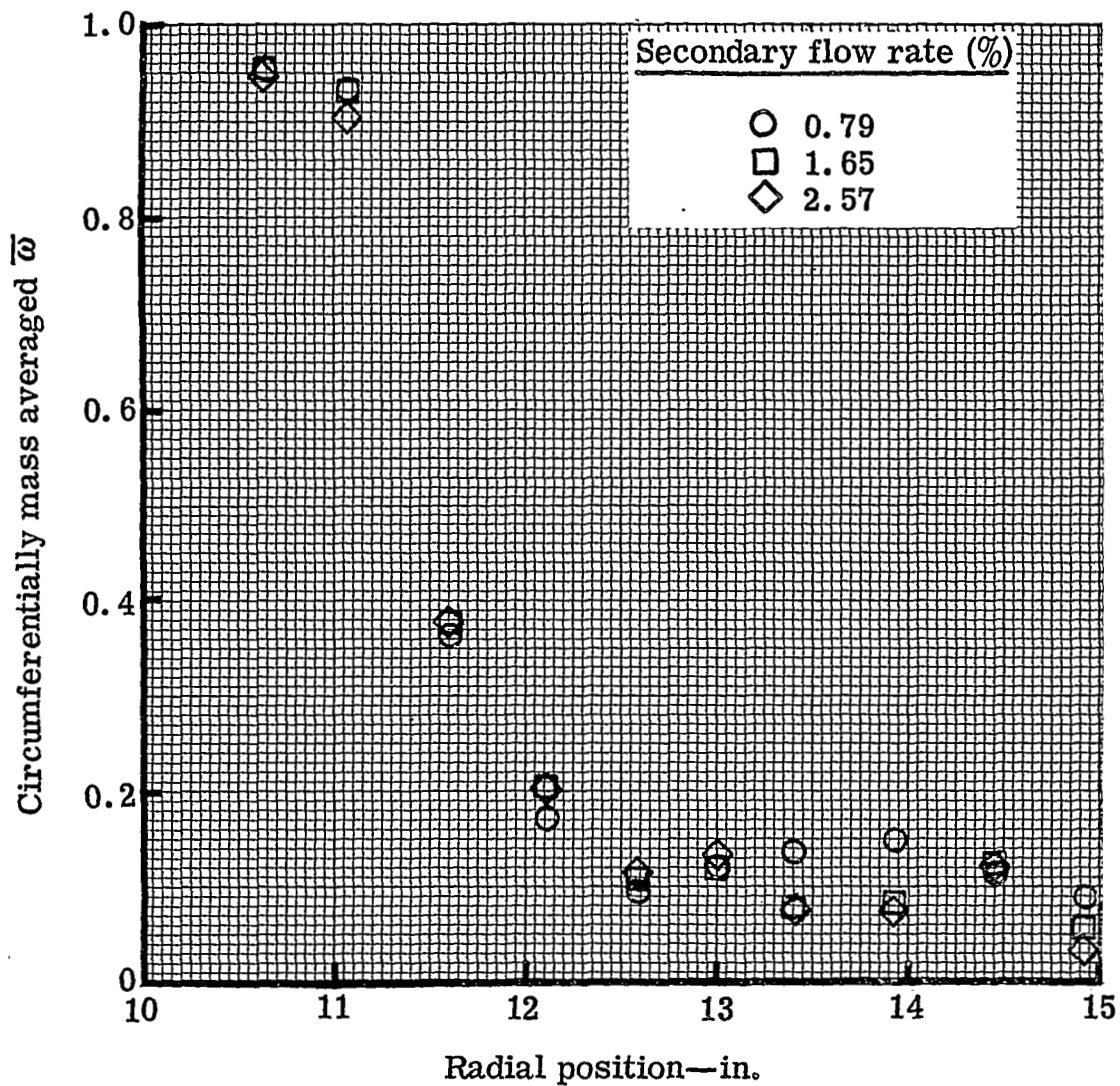
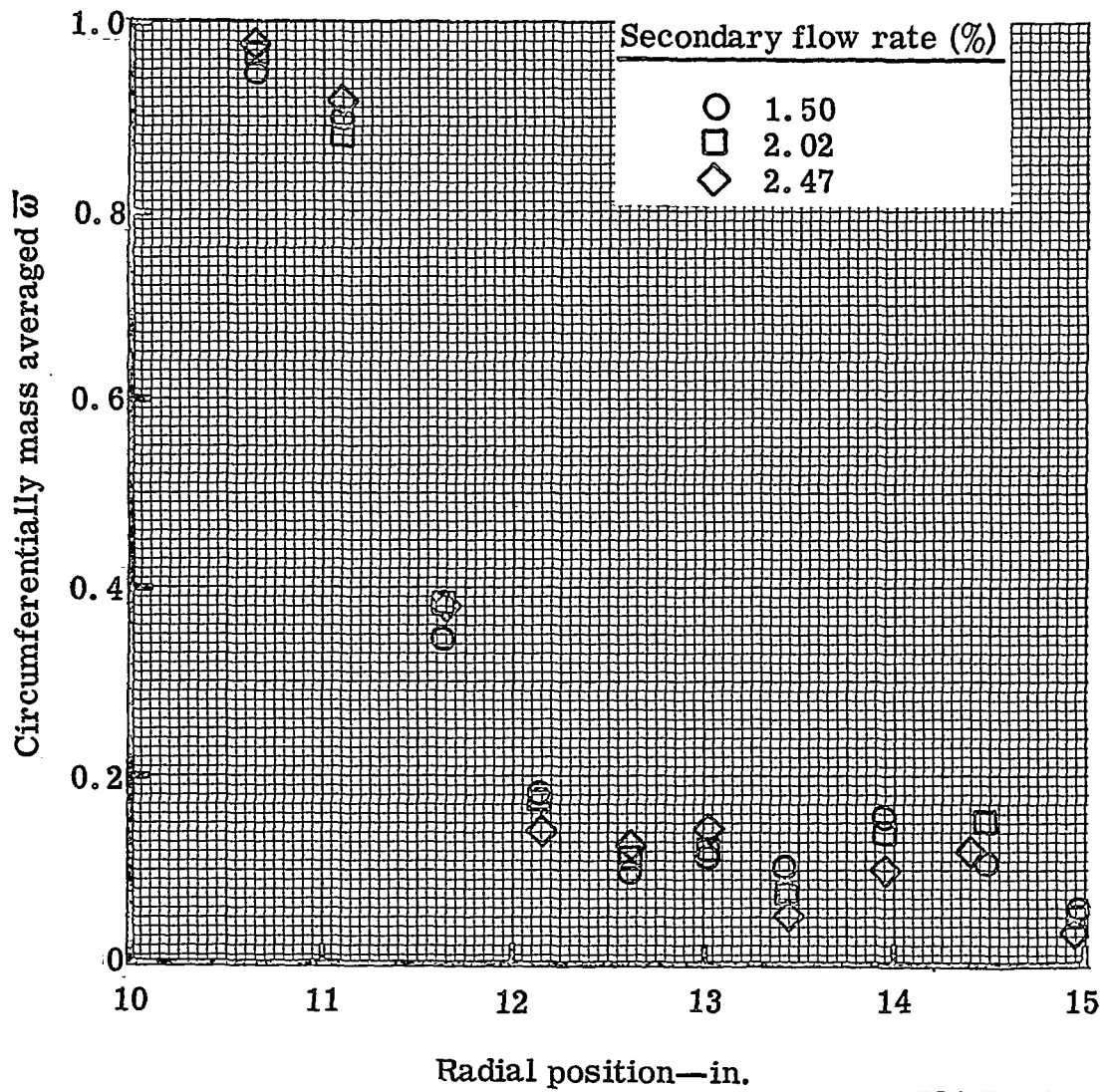


Figure 92. Variation of overall mass averaged kinetic energy loss coefficient with percent secondary flow rate at Station 4 (2 in. downstream of blade trailing edge).



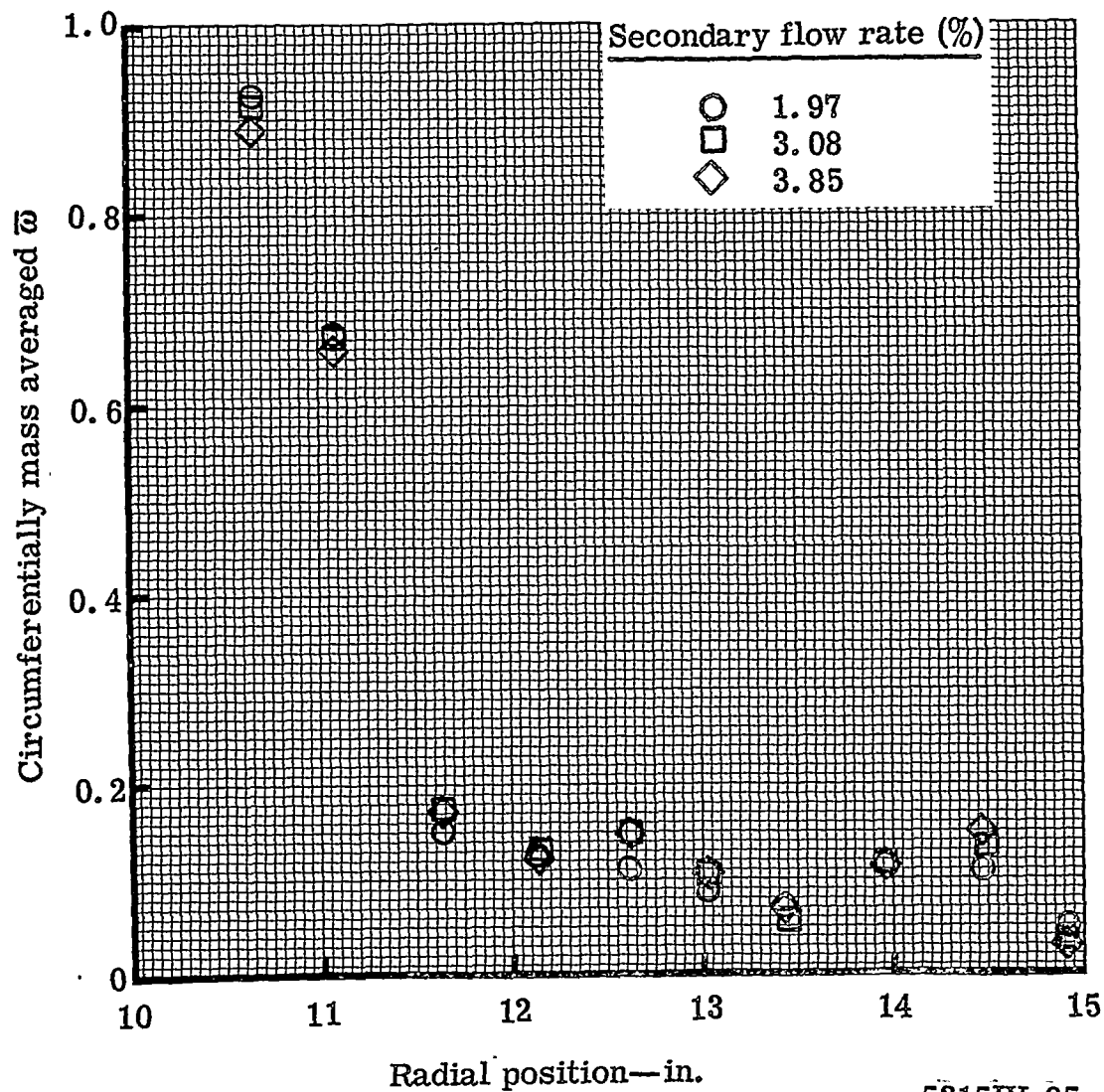
5315IV-93

Figure 93. Circumferentially mass averaged total pressure loss coefficient distribution at Station 4—0.022-in. slot.



5315IV-94

Figure 94. Circumferentially mass averaged total pressure loss coefficient distribution at Station 4—0.031-in. slot.



5315IV-95

Figure 95. Circumferentially mass averaged total pressure loss coefficient distribution at Station 4—0.040-in. slot.

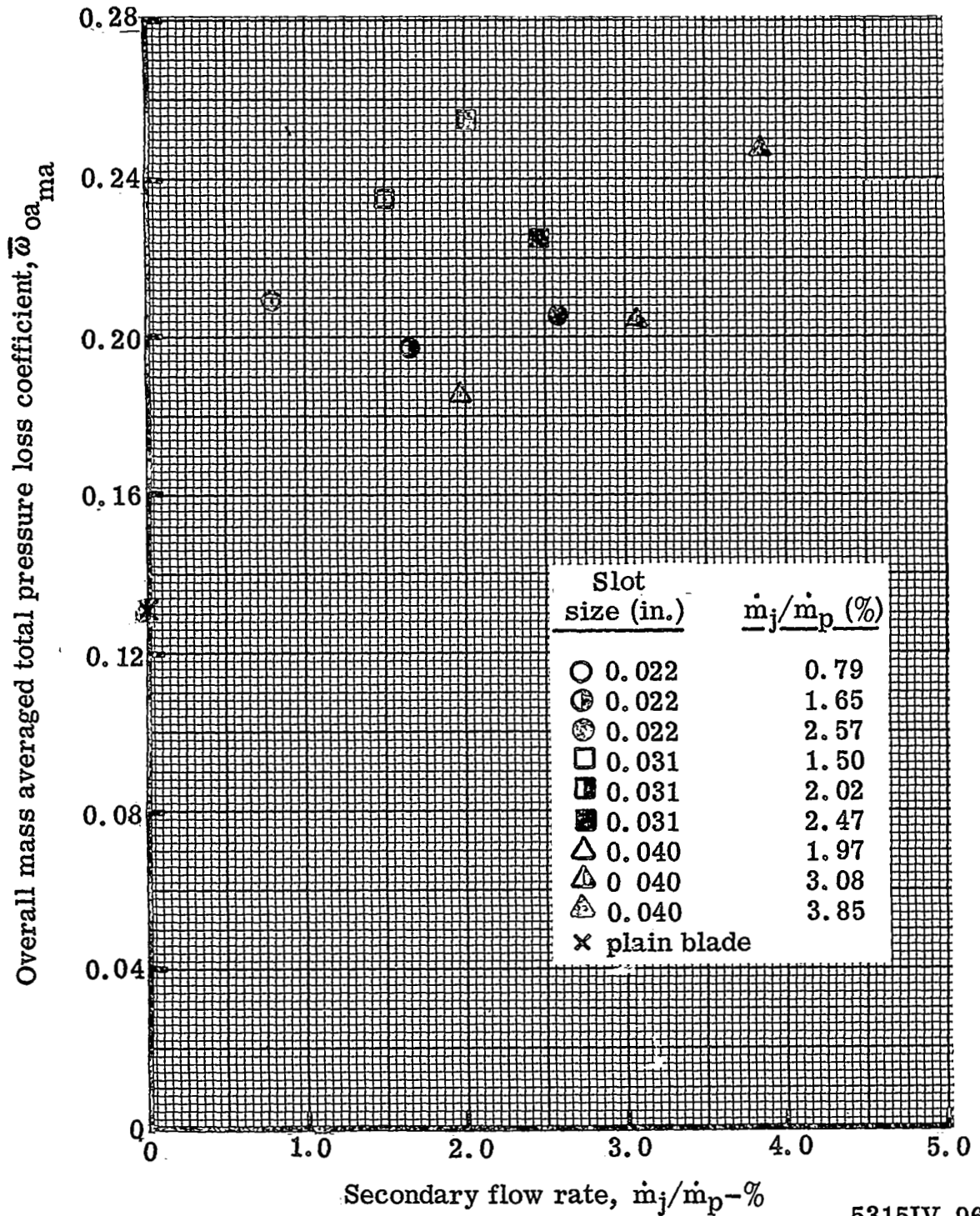
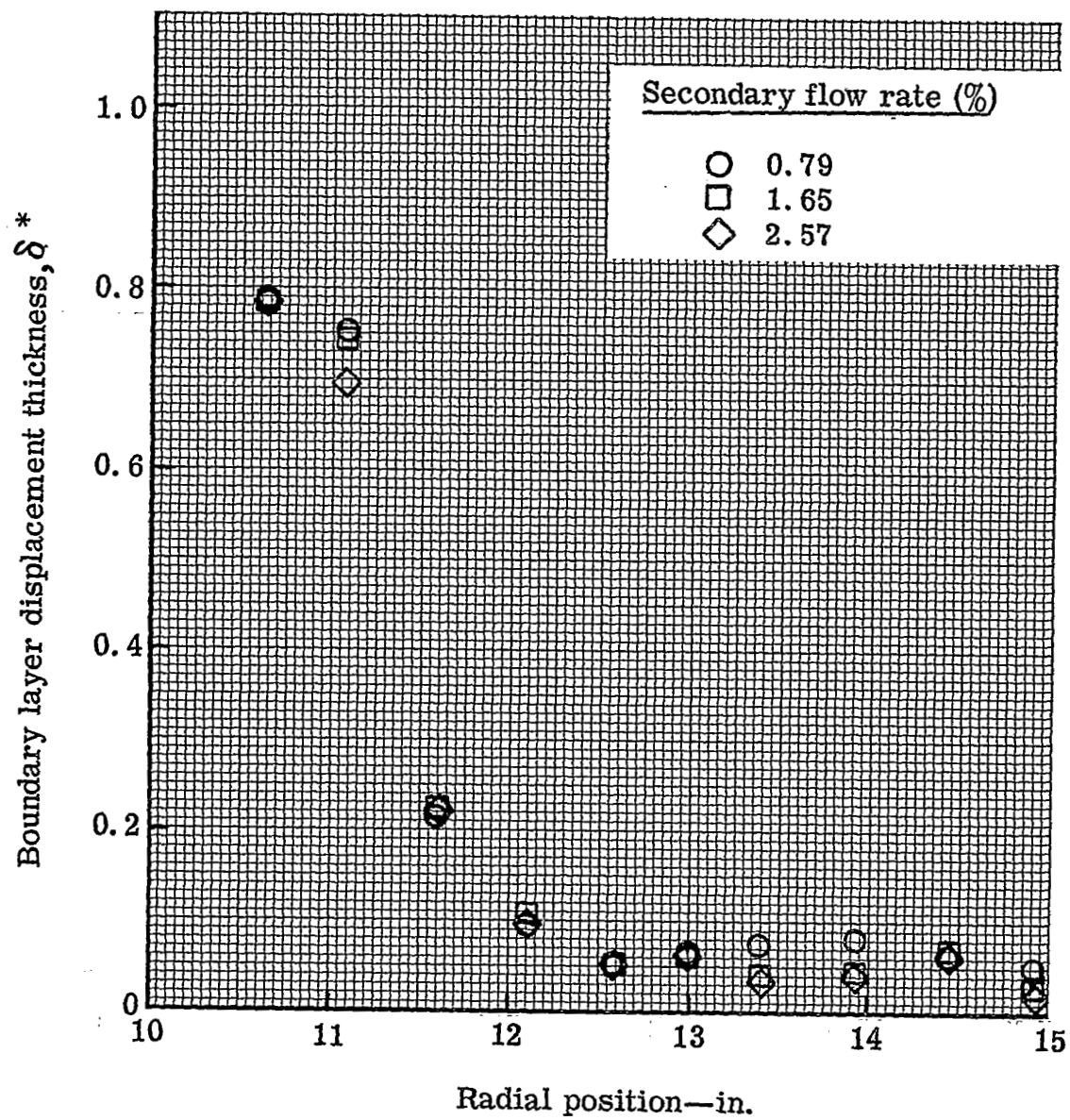
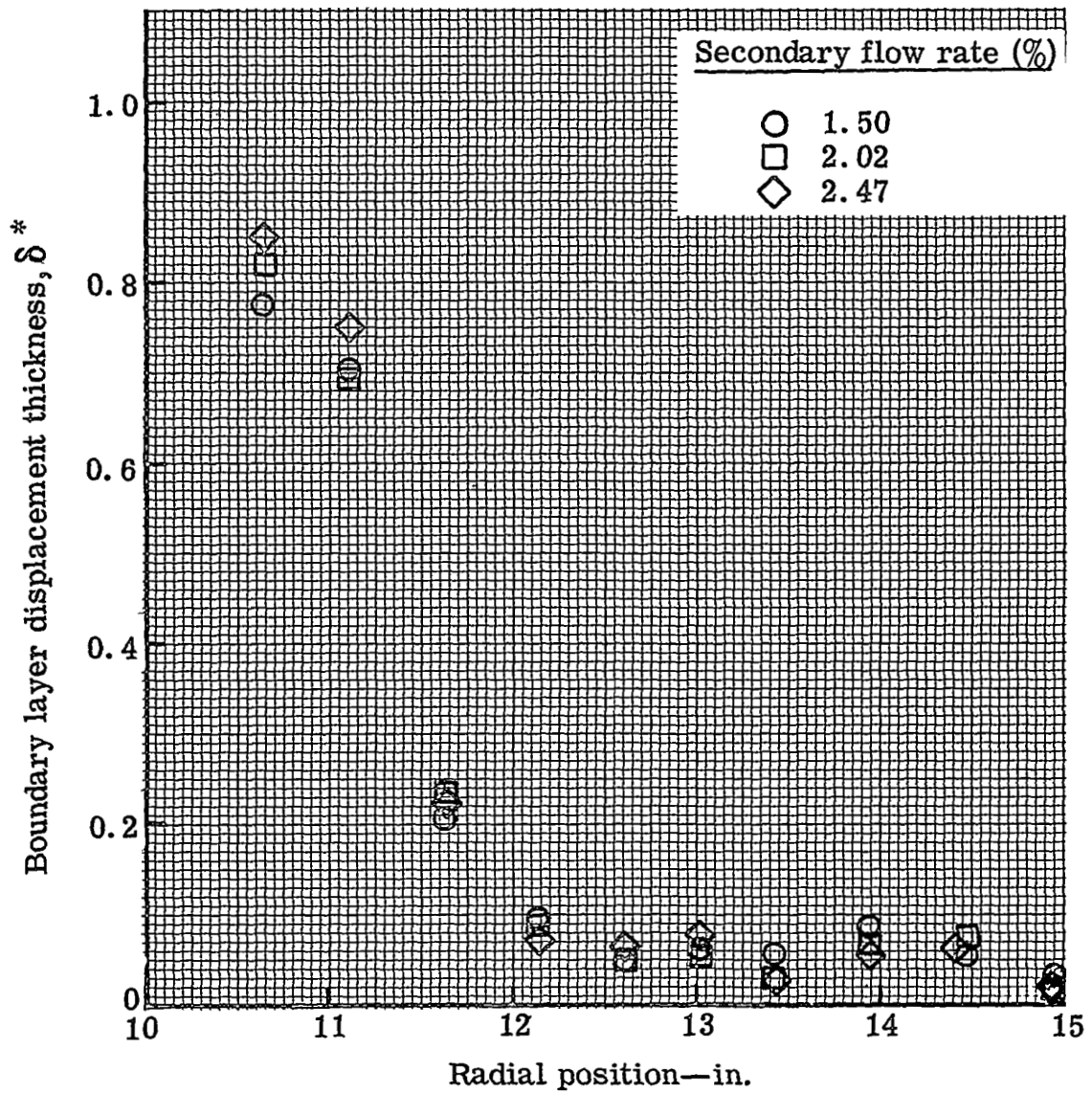


Figure 96. Variation of overall mass averaged total pressure loss coefficient with percent secondary flow rate at Station 4 (2 in. downstream of blade trailing edge).



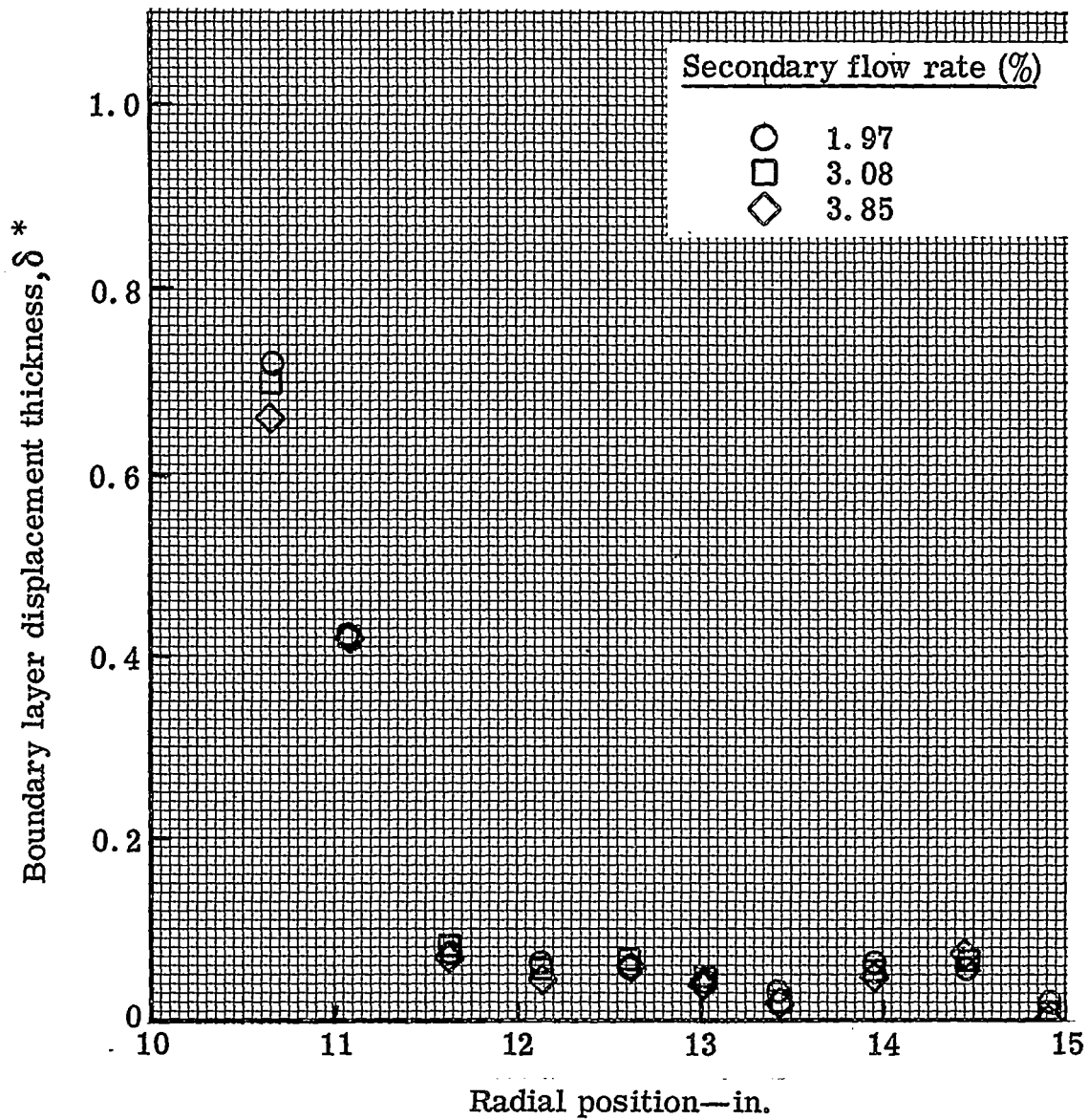
5315IV-97

Figure 97. Radial variation of boundary layer displacement thickness at Station 4—0.022-in. slot.



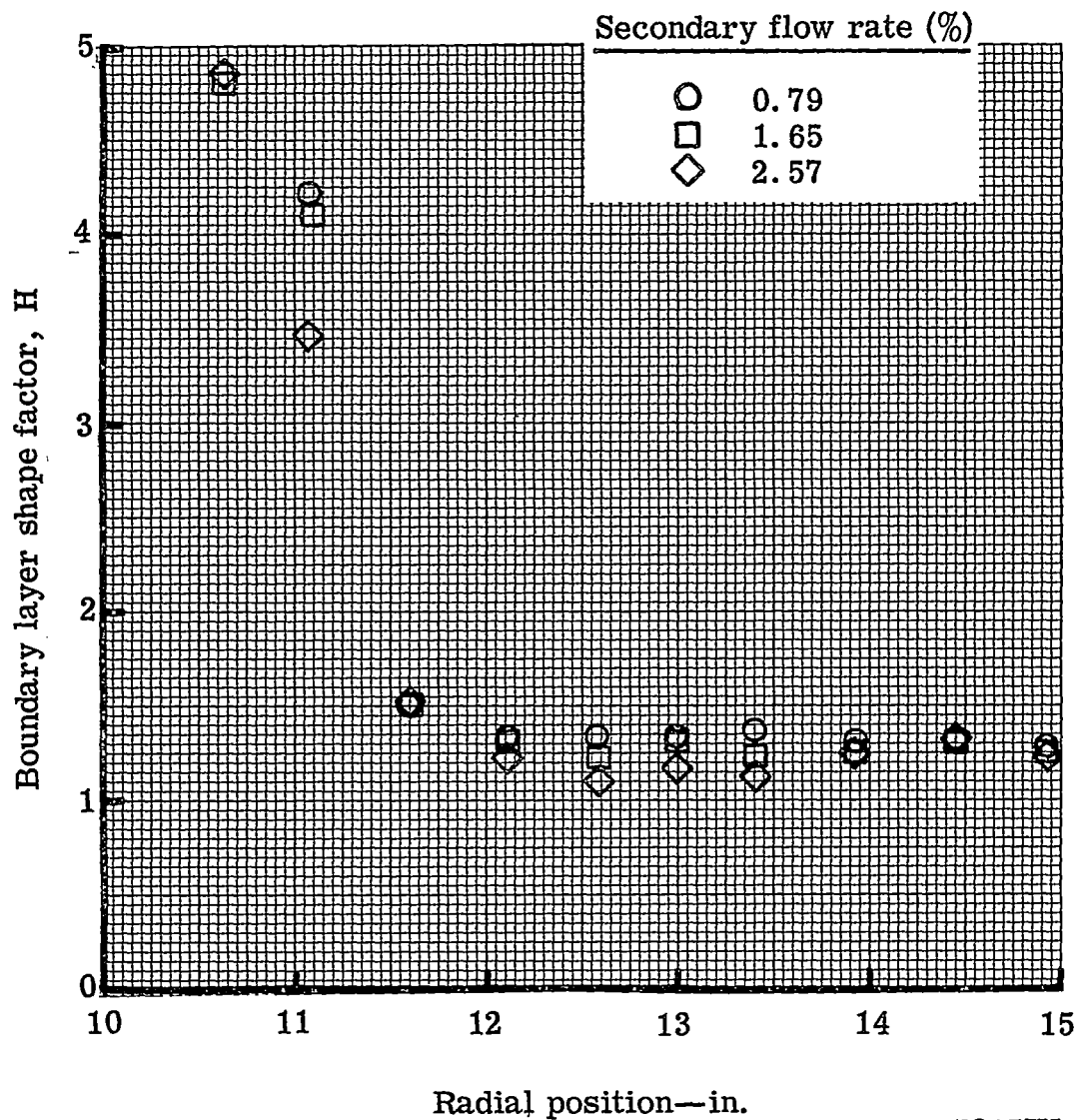
5315IV-98

Figure 98. Radial variation of boundary layer displacement thickness at Station 4—0.031-in. slot.



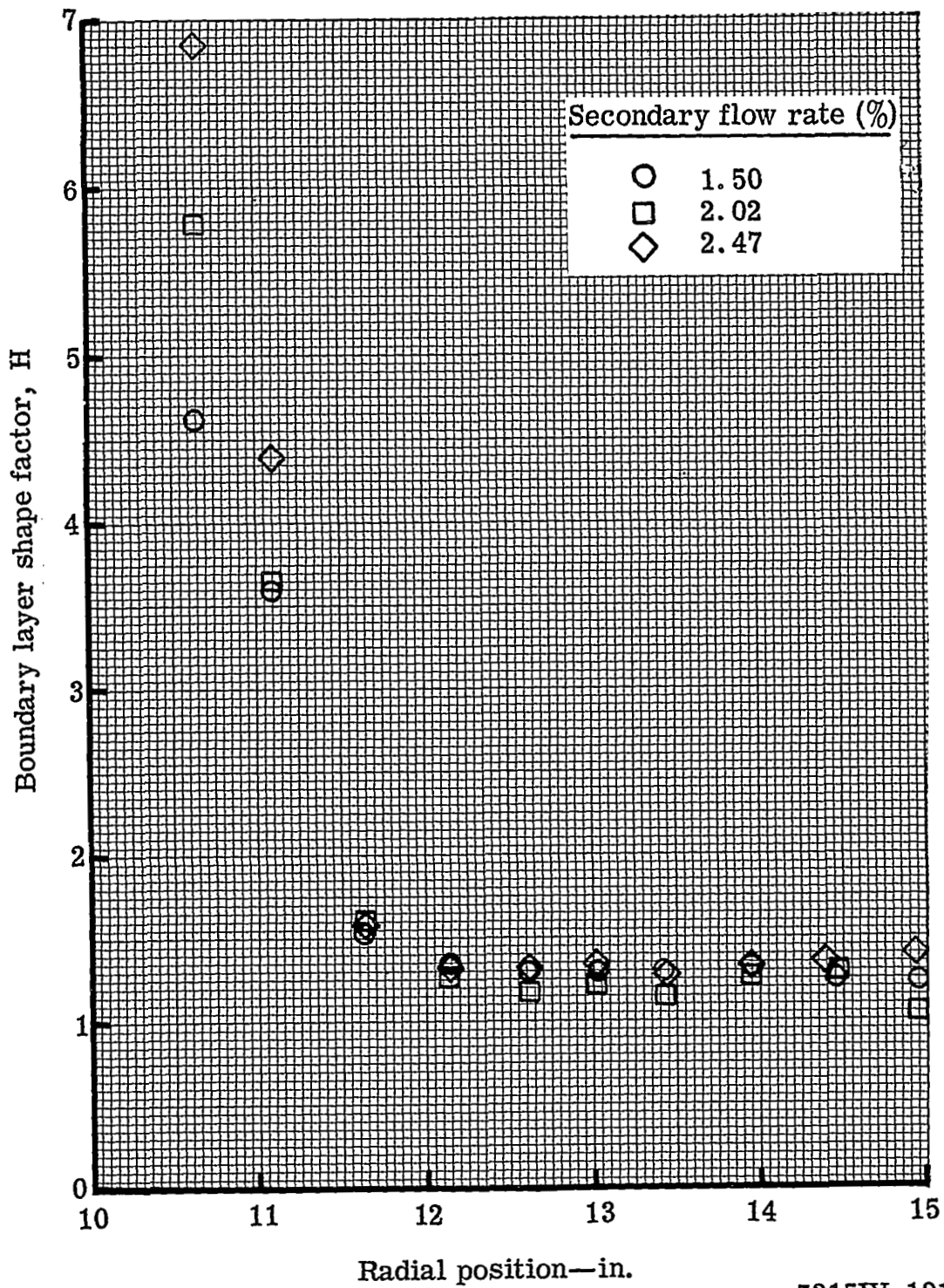
5315IV-99

Figure 99. Radial variation of boundary layer displacement thickness at Station 4—0.040-in. slot.



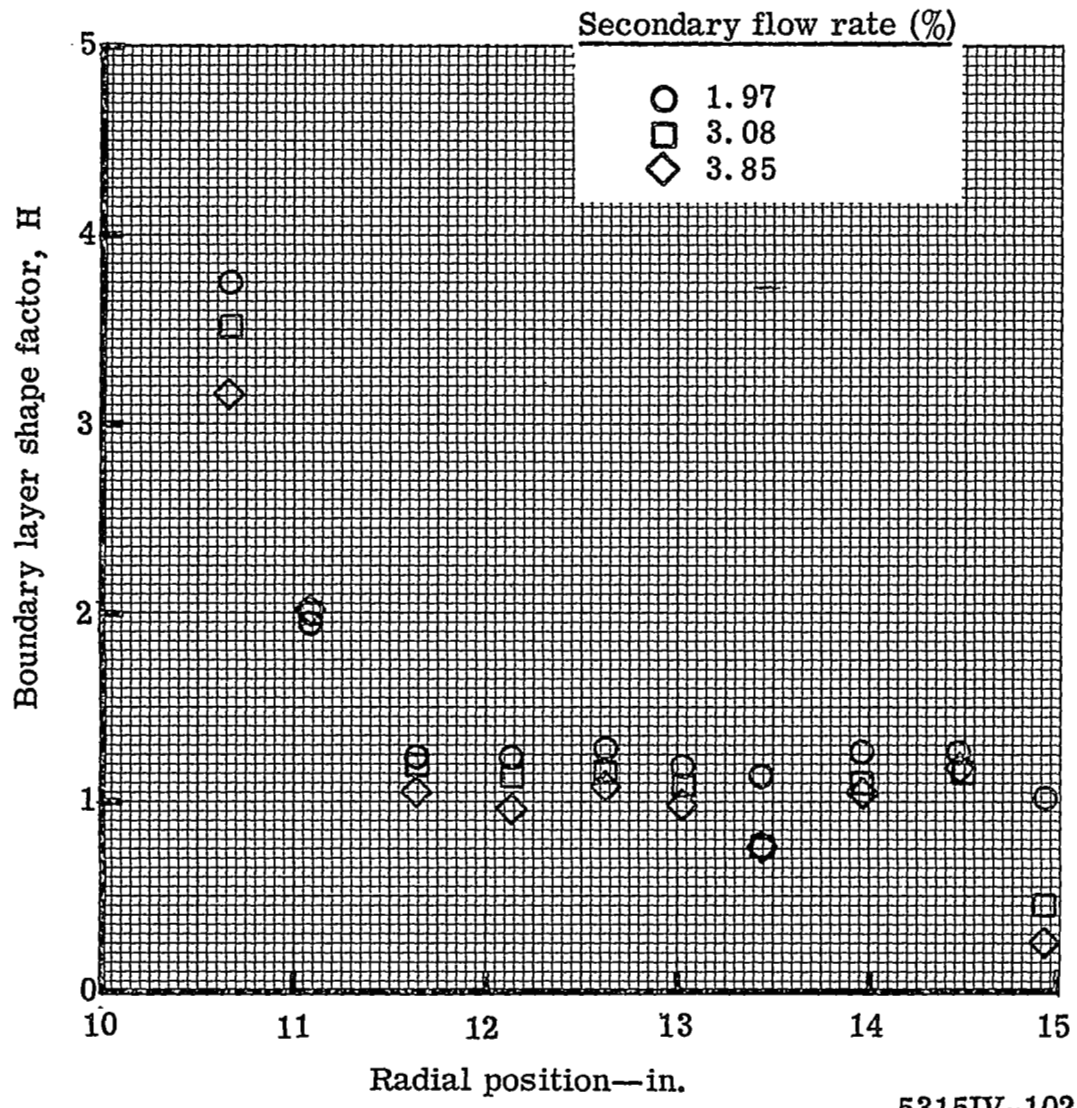
5315IV-100

Figure 100. Radial variation of boundary layer shape factor at Station 4-0.022-in. slot.



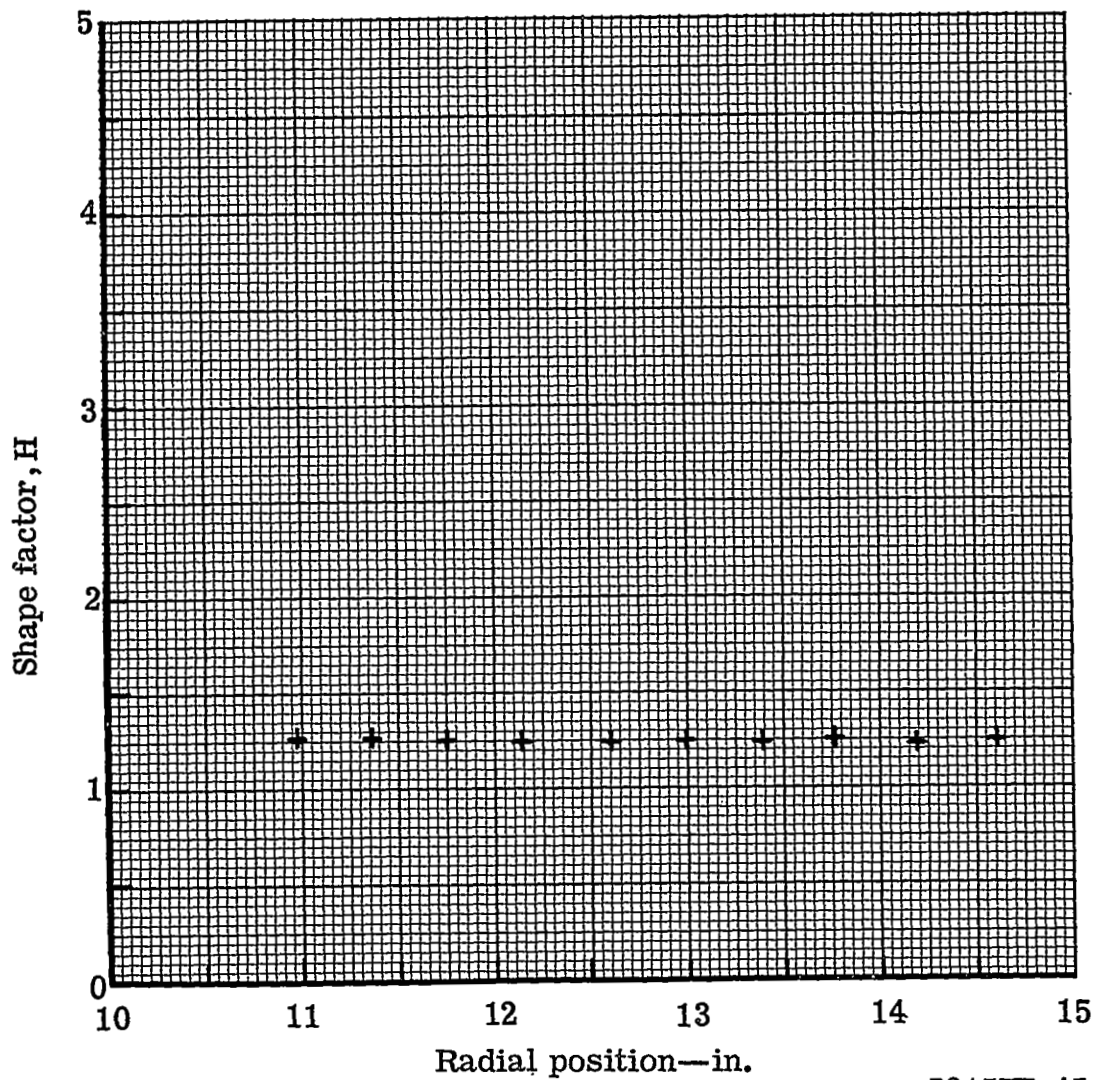
5315IV-101

Figure 101. Radial variation of boundary layer shape factor at Station 4— 0.031-in. slot.



5315IV-102

Figure 102. Radial variation of boundary layer shape factor at Station 4—0.040-in. slot.



5315III-45

Figure 103. Radial variation of boundary layer shape factor at Station 4—plain blade.